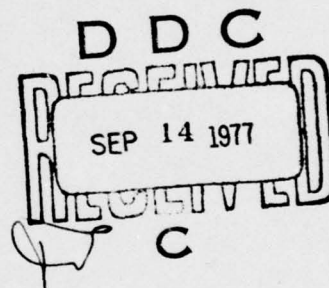AFAL-TR-77-60

OPTICAL WAVEGUIDE LENSES, II

ROCKWELL INTERNATIONAL CORPORATION
ELECTRONICS RESEARCH CENTER
3370 MIRALOMA AVENUE
ANAHEIM, CALIFORNIA 92803

D D C

SEP 14 1977

C

JUNE 1977

TECHNICAL REPORT AFAL-TR-77-60
Final Report for Period 1 December 1975 − 1 December 1976

DDC FILE COPY

AIR FORCE AVIONICS LABORATORY
AIR FORCE WRIGHT AERONAUTICAL LABORATORIES
AIR FORCE SYSTEMS COMMAND
WRIGHT-PATTERSON AIR FORCE BASE, OHIO 45433

NOTICE

When Government drawings, specifications, or other data are used for any purpose other than in connection with a definitely related Government procurement operation, the United States Government thereby incurs no responsibility nor any obligation whatsoever; and the fact that the government may have formulated, furnished, or in any way supplied the said drawings, specifications, or other data, is not to be regarded by implication or otherwise as in any manner licensing the holder or any other person or corporation, or conveying any rights or permission to manufacture, use, or sell any patented invention that may in any way be related thereto.

This report has been reviewed by the Information Office (IO) and is releasable to the National Technical Information Service (NTIS). At NTIS, it will be available to the general public, including foreign nations.

This technical report has been reviewed and is approved for publication.

MICHAEL C. HAMILTON
Project Engineer
Electro-Optics Techniques and
    Applications Group
Electro-Optics Technology Branch

KENNETH R. HUTCHINSON, Chief
Electro-Optics Techniques and
    Applications Group
Electro-Optics Technology Branch
Electronic Technology Division

WILLIAM C. SCHOONOVER, Chief
Electro-Optics Technology Branch
Electronic Technology Division

ACCESSION for
NTIS   White Section
DDC   B ff Section
UNANNOUNCED
JUSTIFICATION

BY
DISTRIBUTION/AVAILABILITY CODES
Dist.   SPECIAL

A

AIR FORCE/56780/6 September 1977 — 100

A 027214

REPORT DOCUMENTATION PAGE		READ INSTRUCTIONS BEFORE COMPLETING FORM
1. REPORT NUMBER AFAL-TR-77-60	2. GOVT ACCESSION NO.	3. RECIPIENT'S CATALOG NUMBER
4. TITLE (and Subtitle) OPTICAL WAVEGUIDE LENSES, II.		5. TYPE OF REPORT & PERIOD COVERED Final Technical Report 75 Dec 01 - 76 Dec 01
		6. PERFORMING ORG. REPORT NUMBER C76-1187.13/501
7. AUTHOR(s) D. B. Anderson, R. R. August R. L. Davis W. H. Southwell J. T. Boyd, C. L. Chen V. G. Kreismanis		8. CONTRACT OR GRANT NUMBER(s) F33615-76-C-1040
9. PERFORMING ORGANIZATION NAME AND ADDRESS Rockwell International Corporation Electronics Group; 3370 Miraloma Avenue Anaheim, CA 92803		10. PROGRAM ELEMENT, PROJECT, TASK AREA & WORK UNIT NUMBERS 62204F 2001-02-35
11. CONTROLLING OFFICE NAME AND ADDRESS Air Force Avionics Laboratory Air Force Wright Aeronautical Laboratory Air Force Systems Command Wright-Patterson Air Force Base; Dayton, OH 45433		12. REPORT DATE June 1977
		13. NUMBER OF PAGES 276
14. MONITORING AGENCY NAME & ADDRESS(if different from Controlling Office)		15. SECURITY CLASS. (of this report) Unclassified
		15a. DECLASSIFICATION/DOWNGRADING SCHEDULE None

16. DISTRIBUTION STATEMENT (of this Report)

Approved for public release; distribution unlimited.

17. DISTRIBUTION STATEMENT (of the abstract entered in Block 20, if different from Report)

18. SUPPLEMENTARY NOTES

19. KEY WORDS (Continue on reverse side if necessary and identify by block number)

Thin-Film Waveguide, Generalized Luneburg Lenses, Beam Expansion, Lens Systems, Fourier Transform Lens, Cleaved Reflectors, Waveguide Coupled Photodetector Array with CCD Readout, and Multilayer Thin-Film Waveguide

20. ABSTRACT (Continue on reverse side if necessary and identify by block number)

The results of an effort to further improve thin-film waveguide lens elements for implementation of the optical Fourier transform as may be employed for real-time RF spectral analysis is delineated. Thin-film waveguide positive inhomogeneous refractors identified as generalized Luneburg lenses were investigated calculating the performance and demonstrating their operation with quantitative measurement of the diffraction patterns. They were assembled as inverting beam expanders and lenses were used with retroreflectors for folding.

DD FORM 1473   EDITION OF 1 NOV 65 IS OBSOLETE
1 JAN 73

i

The effort included the demonstration of waveguide coupled photodetector arrays for application in the spatial frequency plane of the transform lens. Charge coupled readout mechanization of the detectors was demonstrated. This latter waveguide coupled photodetector array was performed by the Department of Electrical and Computer Engineering at the University of Cincinnati.

The approach emphasized the application of Ta_2O_5 as the high index film, together with Corning 7059 as a waveguide, all of which were deposited upon thermally-grown SiO_2 as an isolation layer on a substrate. This structure permits the integration of the optical components with their electronic counterpart on a single substrate. The problem with scattering and its effect upon the dynamic range and resolution of the Fourier transform received consideration which, in part, led to the choice of this preferred material-structure because the thermally-grown oxide has yielded the smoothest low-scattering surface thus far identified upon which to deposit thin-film optical components.

A numerical procedure was developed to compute the performance of thin-film waveguide generalized Luneburg lenses and lens systems. Using the waveguide lens thickness profile, ray traces through the inhomogeneous lens can be determined together with the ray intercept in the image plane to provide wavefront phase error to determine the resulting intensity diffraction pattern. The procedure allows the introduction of various waveguide thickness profile errors.

Luneburg lenses having F/D extended from 0.5 to 10 have been fabricated. Representative patterns characterizing their performance have been included. Various shapes of deposition masks have been employed to control the radial lens thickness profile. Some measured diffraction spot widths approach 5µ. The measurements employ a reimaging technique external to the waveguide-lens structure with its prism couplers. Collimated beam expanders of X3 and X90 were demonstrated. Cleaved reflectors utilizing total internal reflection were demonstrated with transform lenses.

Application considerations, comparative lens technology, waveguide coupled photodetector technology, and the computational procedures for inhomogeneous lenses have been delineated for publication elsewhere and are reproduced herein. These preprints, publication and manuscript submissions derived from this program are:

D. B. Anderson, J. T. Boyd, M. C. Hamilton, and R. R. August, "An Integrated Optical Approach to the Fourier Transform"

D. B. Anderson, R. L. Davis, J. T. Boyd, and R. R. August, "Comparison of Optical Waveguide Lens Technologies"

J. T. Boyd and C. L. Chen, "Integrated Optical Waveguide and Charge Coupled Device Image Array"

C. L. Chen and J. T. Boyd, "Linear Charge Coupled Device Detector Array for Imaging Light Propagating in an Integrated Thin-Film Optical Waveguide"

W. H. Southwell, "Inhomogeneous Optical Waveguide Lens Analysis"

W. H. Southwell, "Index and Waveguide Thickness Profiles for Generalized Luneburg Lenses"

FOREWORD

This document is the final technical report by Rockwell International Corporation, Electronics Research Center, Anaheim, California under Air Force Contract No. F33615-76-C-1040 under Project 2001, Task 02. It delineates the effort performed from 1 December 1975 through 1 December 1976. The authors submittal date was February 28, 1977. The Program Manager and Co-Principal Investigator was Mr. D. B. Anderson with Mr. R. L. Davis as Co-Principal Investigator. During this effort Professor J. T. Boyd, University of Cincinnati, served as a consultant.

A part of this effort was performed by the Department of Electrical and Computer Engineering at the University of Cincinnati under a sub-contract carried out under the direction of Professor Boyd and by Mr. C. L. Chen.

Sincere appreciation is expressed here to Mr. R. R. August of the Rockwell Electronics Research Center and to Mr. M. C. Hamilton, Air Force Avionics Laboratory, who jointly recognized and stimulated the application of thermally oxidized silicon as a new substrate for thin-film optical waveguide lenses.

The initial effort under this contract relating to telephoto lens systems, their field of view and field curvature, carried out by Mr. R. E. Eisele by geometric optical ray analysis, was included in Appendix B of the prior contractual final report "Optical Waveguide Lenses, I", AFAL-TR-76-54, and therefore is not included herein.

Stimulating discussions with Capt. W. J. Miceli (AFAL/DHO), Air Force Project Engineer, and Mr. M. C. Hamilton, AFAL, are greatly acknowledged. Capt. Miceli, who served as the Air Force Project Engineer for most of the contract's duration, has been transferred to the Air Force Cambridge Research Laboratory. Mr. Hamilton has fulfilled the Project Engineer responsibilities during the completion phase.

TABLE OF CONTENTS

TABLE OF CONTENTS (CONTINUED)

PAGE

TABLE OF CONTENTS (CONTINUED)

TABLE OF CONTENTS (CONCLUDED)

LIST OF ILLUSTRATIONS

LIST OF ILLUSTRATIONS (CONTINUED)

LIST OF ILLUSTRATIONS (CONTINUED)

LIST OF ILLUSTRATIONS (CONTINUED)

LIST OF ILLUSTRATIONS (CONTINUED)

LIST OF ILLUSTRATIONS (CONTINUED)

LIST OF ILLUSTRATIONS (CONTINUED)

LIST OF ILLUSTRATIONS (CONTINUED)

xviii

LIST OF ILLUSTRATIONS (CONTINUED)

LIST OF ILLUSTRATIONS (CONTINUED)

LIST OF ILLUSTRATIONS (CONTINUED)

LIST OF ILLUSTRATIONS (CONCLUDED)

xxii

I. INTRODUCTION

A. BACKGROUND

The development of <u>electronic</u> integrated circuits and their application to our defense systems has led to increased reliability and life; reduced cost, size and weight; and reduced primary power requirements. The example set by this development has provided the justification for a corresponding effort addressed to an integrated <u>optical</u> circuit technology with the expectation of realizing some of the same benefits for optical computers, sensors and communication systems, while simultaneously providing an increased information handling capacity.

One important application of integrated optics is in the field of coherent signal processing employing the Fourier transform.[1,2] Optical signal processing is admirably suited to perform linear analog operations such as matrix products, the Fourier transform integration and related correlation and convolution.[3-5] The process employs a coherent source, modulation function(s) and the detection function to be performed throughout the signal spatial field with one or more Fourier transform lenses between. The optical signal processing function is *usually* performed for a two-dimensional image, whereas an integrated optics format will limit the processing to a single transverse dimension as a function of time.

For an application such as spectral analysis of microwave signals extending over a broad expanse of the spectrum, this one-dimensional characteristic is not a limitation. The optical Fourier transform applied to spectral analysis of microwave signal is attractive because it provides "wide open" continuous response.[2] The schematic diagram of Figure 1 illustrates the essential components of an optical Fourier transform process applied to spectral analysis. An integrated optics implementation of the spectrum analyzer will contain a coherent source (presumably a (GaAl)As distributed-feedback laser)[6,7] coupled to a thin-film optical waveguide,[8] an assortment of thin-film waveguide lenses performing the beam expansion and the transform functions, together with a spatial modulator[9-14] (presumably a surface elasto-optic interaction within a

1
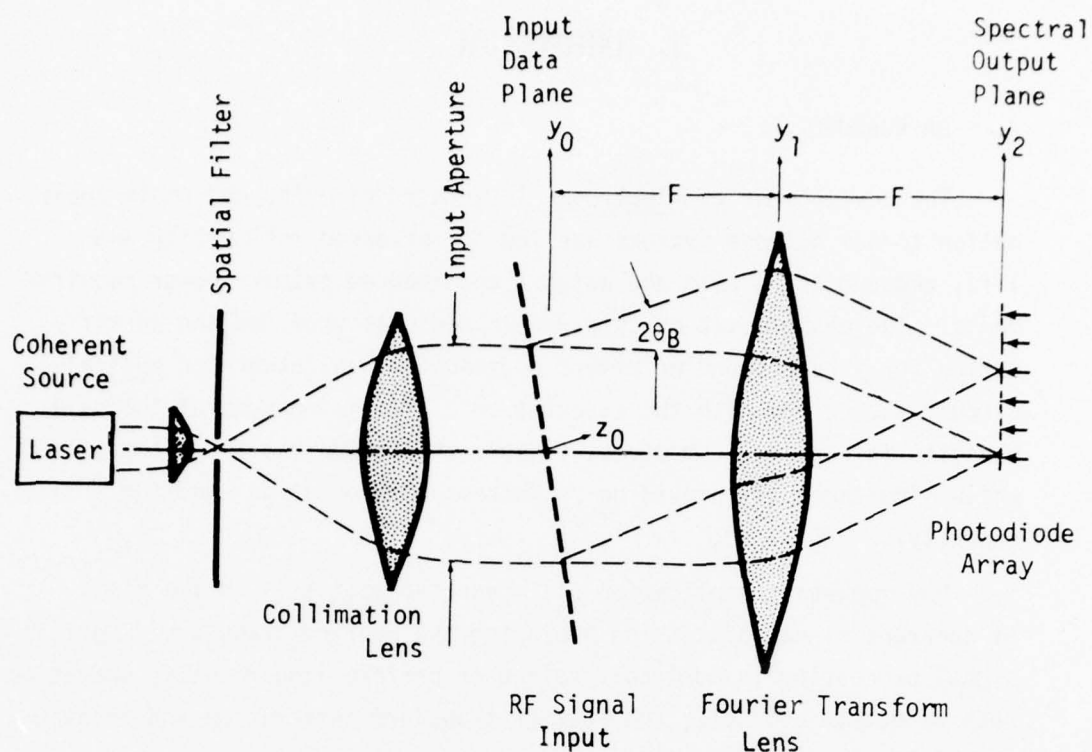
Figure 1. Real-Time Spectrum Analyzer Implemented by Coherent Optical Fourier Transform

common thin-film) and a thin-film detector array[15] responsive to the laser with a temporal bandwidth encompassing the down-converted convolved microwave signal. The microwave signal is temporarily "stored" as a waveform in the spatial modulator which is simultaneously accessed in its entirety by the optical field and transformed into various spectral components spatially separated by the lens and detected in an array. Use of the integrated optics format for the spectrum analyzer on a single substrate provides the necessary mechanical structure to obtain rigidity between the various optical elements. It also provides the potential for a substantial reduction in size and weight of optical signal processing systems.

The optical Fourier transform process requires a series of lenses with sufficient aperture and resolution to encompass the time-spatial-

2

bandwidth-product system requirements. Near diffraction-limited lens
performance and low scattering are necessary to obtain a useful resolu-
tion and dynamic range. Lens systems designed to fulfill these re-
quirements using conventional optical elements in three dimensions is
a highly developed art.[5] The corresponding implementation of lenses
in two-dimensional thin-film waveguides constitutes a developing
technology of which this report constitutes a second year's effort
sponsored by the Air Force Avionics Laboratory. The first year's effort[16]
addressed various approaches to lenses, lens systems and reflectors,
as may be required for implementation of the optical Fourier trans-
form function in an integrated optics format, whereas this second
effort has addressed a most promising approach and has proceeded towards
its optimization.

B.   PROGRAM OBJECTIVE

Basic to the development of an integrated optics technology are
the requirements for (1) a coherent source (2) the general modulation
function, both temporal and spatial (3) the detection function and (4)
a waveguide technology to appropriately interconnect these components,
all of which must be implemented as a planar structure compatible with
various thin-film processes used in the semiconductor industry. It is
the optimization of thin-film waveguide lenses, lens systems and reflectors
for use in a real-time spectrum analyzer to which this program is
addressed.

Optical lens elements within a thin-film waveguide media have
several additional design freedoms and some restrictions when compared
with conventional optical systems. First, the lens system is entirely
immersed in the thin-film waveguide which has an effective refractive index
determined by the choice of materials and film thickness. The ambient
waveguide effective refractive index may be greater than, or less than,
the index employed for the lenses. The available range of refractive
indices is restricted to values greater than that of the substrate bulk
refractive index to preserve wave binding within the thin-film waveguide.
Second, the use of nonplanar substrates permits the formation of lenses
of uniform refractive index by changes of the path length because the rays
traverse geodesics. The maximum refractive index is usually limited by

3

the thin-film waveguide material except for geodesics where the path length increase synthesizes the larger value. Third, inhomogeneous lens elements are feasible using homogeneous dielectrics and may be produced by graded waveguide film thickness. Consideration of these various ramifications was included in the initial effort, Optical Waveguide Lenses, I.[16] One important conclusion derived from this initial effort suggested that generalized thin-film Luneburg lenses were a favored approach for optimization in integrated optics format.

Referring to Figure 1, the essential lens elements include a beam expansion system and a Fourier transform lens. In addition to the requirement for near diffraction-limited performance and low scattering, the design of these lenses must consider the length of the optical axis because the Fourier transform "chip" substrate area is limited. Reasonable substrate dimensions are comparable to that employed in the electronic circuit industry. Therefore, consideration of the telephoto effect so as to reduce the physical focal length of the Fourier transform lens received attention during the initial program, Optical Waveguide Lenses, I. The required large compression of the physical focal length, field of view and field curvature negated further consideration of the telephoto effect in preference to a folded optical system. It was also necessary to develop plane refractors for folding so as to minimize the substrate area employed.

Characterization of optical element performance is essential for design and applications requiring near diffraction-limited performance. Various techniques are available to characterize conventional three-dimensional lens systems. However, new techniques were necessary to characterize the performance of thin-film optical elements because they are imbedded within the film and, therefore, their development has been included and applied.

C. TECHNICAL APPROACH

Based upon the result of the preceding program, Optical Waveguide Lenses, I, this current effort, Optical Waveguide Lenses, II, reported herein, addresses inhomogeneous thin-film waveguide lenses, lens systems and reflectors which are apposite to the optical Fourier transform function continuing the emphasis upon waveguide material-structures with compatible

4

planar processes. The basic refractive element considered is the positive generalized Luneburg lens (with arbitrary axial foci equal to, or greater than, the lens diameter). Two of these lenses with comparatively short focal length are employed for the beam expansion while a single lens with a longer focal length is employed for the Fourier transform function using reflectors for folding.

Specific considerations during the current effort have included (1) optimization of inhomogeneous lens radial refractive index profile to more closely approach the diffraction-limited performance, (2) reduction of scattering losses due to the waveguide films, substrate isolation layers and optical element boundaries, (3) establishment of lens reproducibility, alignment and positioning without regard to the specific profiles and (4) suppression of mode conversion within optical elements. As a result, the capability to fabricate generalized Luneburg lenses with specific parameters has been established, together with the means to characterize and predict their performance.

Motivated by the potential advantages of integration of both optical and electronic components, a new waveguide material-structure was identified, developed and used to create the deliverable lens systems. The new waveguide material-structure exploits thermally-oxidized silicon as an isolation layer between the waveguide and the supporting silicon substrate. Typical Luneburg lenses employ Ta_2O_5 as an overlayer or underlayer in conjunction with Corning 7059 glass employed as the waveguide. The thermally-oxidized substrate with appropriate careful processing has proven to yield the lowest scattering substrate thus far identified. All of the effort reported herein has utilized this waveguide material-structure. It should be noted this structure is also compatible with the waveguide coupled detector array and spatial modulator requirements for the optical Fourier transform "chip" using an overlayer of ZnO as the piezoelectric[17-22]

A part of this program has been directed to the waveguide coupled photodetector array for use in the spatial frequency plane of the optical Fourier transform "chip." Lenses and waveguide have been formed and characterized using the thermally-grown SiO_2 on Si substrate where the

SiO_2 isolation layer has been removed for coupling of the waveguide to the photodetector using the evanescent field. This waveguide photo-detector array investigation has been carried out by the Department of Electrical and Computer Engineering at the University of Cincinnati under a subcontract under the direction of Professor J. T. Boyd.

The following Technical Discussion is organized by subdivisions into the reporting of specific results complemented by a series of appendices constituting scientific papers in the process of publication in the open literature. The appendices include:

(A) D. B. Anderson, J. T. Boyd, M. C. Hamilton, and R. R. August, "An Integrated Optical Approach to the Fourier Transform," to be published, IEEE Journal of Quantum Electronics Special Issue, Integrated Optics, April, 1977.

(B) D. B. Anderson, R. L. Davis, J. T. Boyd, and R. R. August, "Comparison of Optical Waveguide Lens Technologies," to be published, IEEE Journal of Quantum Electronics Special Issue, Integrated Optics, April, 1977.

(C) J. T. Boyd and C. L. Chen, "Integrated Optical Waveguide and Charge Coupled Device Image Array," to be published, IEEE Journal of Quantum Electronics Special Issue, Integrated Optics, April, 1977.

(D) C. L. Chen and J. T. Boyd, "Linear Charge Coupled Device Detector Array for Imaging Light Propagating in an Integrated Thin-Film Optical Waveguide," Proceedings Conference on Charge Coupled Device Technology and Applications, sponsored by the National Aeronautics and Space Administration, November 30 - December 2, 1976, Washington, D. C.

(E) W. H. Southwell, "Inhomogeneous Optical Waveguide Lens Analysis," to be published, Journal of Optical Society of America, Aug. 1977.

(F) W. H. Southwell, "Index and Waveguide Thickness Profiles for Generalized Luneburg Lenses," to be published, Journal of Optical Society of America, Aug. 1977.

An effort has been made to avoid duplication between the Technical Discussion and the various appendices. Therefore, reading of the appendices is

6

suggested prior to delving into the technical discussion section in
depth. Appendix (A) introduces the optical Fourier transform design
considerations with supplementary details provided in the following
section. Appendix (B) compares various thin-film waveguide lens
technologies largely encompassing the work of the prior effort, Optical
Waveguide Lenses I. Appendices (C) and (D) are the result of this effort
which has been performed at the University of Cincinnati. Appendices
(E) and (F) are also the result of this effort directed to the compu-
tation of lens performance to provide a tolerance analysis, more fully
developed in the following section.

7

II. TECHNICAL DISCUSSION

A. GENERAL

Some general properties of optical Fourier transform signal processing are delineated herein prior to detailed discussion of thin-film optical waveguide lenses, reflectors and lens systems. The following analyses should be considered simultaneously with Appendix A, "An Integrated Optical Approach to the Fourier Transform." Both of these analyses consider various aspects of the spectrum analyzer theory of operation which is essential background for the development of thin-film optical waveguide lenses, reflectors and lens systems delineated herein because the optical performance of these elements has direct impact upon spectrum analysis.

The optical Fourier transform as an electronic spectrum analyzer is illustrated in Figure 1. Coherent laser light propagating in a thin-film waveguide is expanded and collimated prior to being incident on a surface elastic wave which has been excited by the incoming electrical signal. Diffraction of light by the surface elastic wave occurs in such a way that light is diffracted at different angles corresponding to different electrical signal frequency components. For a range of signal frequencies and surface elastic wave intensities, the deflection angle is linearly proportional to the signal frequency, and the diffracted light amplitude is linearly proportional to the signal surface elastic wave amplitude. A waveguide lens is then positioned so as to perform a one-dimensional Fourier transform. Signal spectral information which is represented by the angular composition of light emerging from the surface elastic wave region then becomes represented by the transverse spatial variation of light in the Fourier transform plane. The intensity of the light spatial distribution in the transform plane corresponds to the signal power density spectrum and can then be converted to an electrical signal by means of a detector array.

1. Spectrum Analyzer Theory of Operation

Considering the optical waveguide geometry shown in Figure 1, the field amplitude $E(y_2)$ in the transform plane is related to the field amplitude in the input plane $E(y_1)$ according to[23]

$$E(y_2) = b \int_{-\infty}^{\infty} E(y_0) e^{i \frac{kN_e(m)y_2}{F} y_0} dy_0 \quad , \tag{1}$$

where y is oriented along the waveguide surface perpendicular to the
axis of wave propagation (z axis) and the x axis is normal to the wave-
guide surface. The x dependence of the field contains the form of the
waveguide modes and will generally be suppressed for conciseness in the
present development. However, its effect on Bragg diffraction is in-
corporated.[10] In (1), F is the lens focal length, $N_e(m)$ is the thin-
film waveguide mode effective refractive index for the mth order mode,
$k = 2\pi/\lambda$ where λ is the optical wavelength, and b is a complex constant.
As use of the optical Fourier transform for spectral analysis in an inte-
grated optical format dictates minimizing substrate area, the separation
of the lens and the input plane should approach zero. The resulting phase
quadrature term in the Fourier transform[23] is of no consequence since only
the signal power density spectrum is detected. If a uniform plane wave
over an aperture D is present at the input, the output has the familiar
form:

$$E_0(y_2) = bD \, \text{Sinc} \left(\frac{kN_e(m)Dy_2}{2F} \right) \quad , \tag{2}$$

where $\text{sinc} x = \sin x / x$. The 1/2 width between nulls of this diffraction
pattern is

$$\Delta y_2 = \frac{\lambda F}{N_e(m)D} \quad \cdot \quad \text{(Plane Wave)} \tag{3a}$$

For the more realistic situation of a Gaussian transverse dependence
truncated to the 1/e value, the corresponding diffraction pattern width
is given as:[24]

$$\Delta y_2 = 1.41 \frac{\lambda F}{N_e(m)D} \quad \cdot \quad \text{(Truncated Gaussian)} \tag{3b}$$

Similar expressions can be obtained for other transverse field distri-
butions. For a given transverse field distribution, expressions of the
form given in (3) determine the smallest resolvable distance in the
Fourier transform.

10

The optical axis in Figure 1 and the surface elastic wave propagation axis are oriented so as to satisfy the Bragg condition at the signal center frequency. The z axis in Figure 1 is thus at an angle $2\theta_B$ with respect to the optical axis of the incident wave which we denote as z_i, where θ_B is the Bragg angle defined as

$$\text{Sin}\theta_B = \frac{\lambda f_{so}}{2N_e(m)v_r} \quad , \tag{4}$$

where f_{so} is the signal center frequency and v_r is the Rayleigh wave velocity. We now consider both the optical wave incident on the surface elastic wave and the diffracted optical wave to have the form:

$$E_i(y_i, z_i, t) = \iint A_i(\omega_i, \overline{k}_i)e^{i(\omega_i t - \overline{k}_i \cdot \overline{r}_i)} d\omega_i d\overline{k}_i \tag{5a}$$

$$E_d(y, z, t) = \iint A_d(\omega_d, \overline{k}_d)e^{i(\omega_d t - \overline{k}_d \cdot \overline{r}_d)} d\omega_d d\overline{k}_d \quad , \tag{5b}$$

where the subscript i refers to the incident wave and the subscript d refers to the diffracted wave and $k_{i,d} = \omega_{i,d} N_e/c$. The coordinates (y, z) without subscripts apply to the diffracted wave. The surface elastic wave field has the form:

$$g(y, z) = \iint G(f_s, \overline{k}_s)e^{i(2\pi f_s t - \overline{k}_s \cdot \overline{r})} df_s d\overline{k}_s \quad , \tag{6}$$

where

$$k_s = 2\pi f_s/v_r \text{ and } \omega_d = 2\pi f_s + \omega_1 \quad .$$

The variation of the elastic wave amplitude along the propagation axis of the elastic wave $g(y, z)$ represents the time variation of the applied electronic signal so that we can write

11

$$g(y, z) \Big|_{\substack{\text{Propagation} \\ \text{axis}}} \equiv g(t) \tag{7}$$

where $g(t)$ is the signal function for spectral analysis. By following the procedure described by a number of authors,[11,25,26] substituting the above field expansions into the electromagnetic wave equation and making the usual assumption of neglecting the spatial second derivatives of the optical field amplitudes $A_{i,d}$, the following equation can be derived for A_d:

$$\frac{dA_d}{dz} = i\eta_d \iint e^{i\overline{\Delta k} \cdot \overline{r}} G(f_s, \overline{k}_s) A_i(\omega_i, \overline{k}_i) d\overline{k}_s d\overline{k}_i \tag{8}$$

where

$$\overline{\Delta k} = \overline{k}_d - \overline{k}_s - \overline{k}_i \tag{9}$$

$$\eta_d = \frac{\omega_d N_e^3 p S_o}{4c} Q \tag{10}$$

In (10), p is the photoelastic constant and N_e the refractive index of the waveguide, S_o is the maximum value of the elastic strain, $G(f_s, \overline{k}_s)$ is normalized so that its maximum value is unity, c is the velocity of light, and Q is an overlap integral given elsewhere [10] which is a measure of the strength due to coupling for the suppressed x dependence of the fields.

We now assume that the input optical wave is composed of only a single plane wave component. Furthermore, the surface elastic wave consists of uniformly-weighted plane wave components within diffraction angle $\delta\phi$ and no components beyond $\delta\phi$, i.e.,

$$A(\omega_i, \overline{k}_i) = A_{io} \delta(\overline{k}_i - \overline{k}_{io}) \tag{11a}$$

12

$$G(f_s, \overline{k}_s) = \begin{cases} G(f_s) & k_s \text{ within } \delta\phi, \\ \\ 0 & \text{otherwise} \end{cases} \tag{11b}$$

where $\delta\phi$ is assumed sufficiently large so that the elasto-optic band-width is limited by the transducer bandwidth [10] . In (11b), $G(f_s)$ is the Fourier transform of the input electric signal $g(t)$. The assumption (11b) concerning the angular spectrum of the surface elastic wave can be closely approximated over large signal bandwidths through the use of tilted transducer arrays.[12,27] The assumptions (11) correspond to the case in which the optical beam spread is much less than the surface elastic beam spread. For this case, the optical beam spread will not be significantly altered by the elasto-optic interaction.[13,28,29] We further restrict our attention to the Bragg regime so as to eliminate the possibility of ambiguities caused by multiple scattering. Furthermore, as noted by Giallorenzi and Milton,[13] second-order multiple scattering is avoided if $k_{s\,max} < 2\,k_{s\,min}$, where $k_{s\,min}$ and $k_{s\,max}$ are the minimum and maximum values of k_s over the range of the signal band. Using (11), the equation governing the amplitude, (8) reduces to

$$\frac{dA_d}{dz} = i\,n_d\,A_{io}\,G(f_s) \int_{\overline{k}_s \subset \delta\phi} e^{i\Delta\overline{k}\cdot\overline{r}}\,d\overline{k}_s \quad. \tag{12}$$

If we restrict our attention to the region of operation in which the incident wave is not depleted, then the diffracted amplitude is readily obtained by a simple integration. Operation of the spectrum analyzer requires a linear relationship between the diffracted field amplitude and the signal amplitude spectrum, which is achieved by limiting the surface elastic wave intensity. Cumulative and thus efficient energy transfer from the signal input to the diffracted optical beam only occurs when momentum conservation is satisfied, i.e., $\overline{\Delta k} = 0$.[14] Restricting our attention to only the surface elastic wave angular component which causes $\overline{\Delta k} = 0$ and using the solution of (12) for a nondepleted incident wave, we obtain from (5b):

13

$$E_d\ (y,\ z,\ t) = a e^{i(\omega_d t - k_{do}z)} \int G(f_s) e^{-i\frac{2\pi}{v_r}(f_s - f_{so})\cos\theta_B y}$$

$$e^{i\frac{2\pi}{v_r}|f_s - f_{so}|\sin\theta_B z}\ df_s\ . \tag{13}$$

where

$$k_{do} = |\overline{k}_{io} + \overline{k}_{so}| \tag{14}$$

and a is a collection of constants and $k_{so} = 2\pi f_{so}/v_r$.

The transverse portion of the spatial field distribution (13) emerging from the surface elastic wave propagation region is then Fourier transformed by the optical waveguide lens according to (1). Letting $z = 0$ be the transform input plane and substituting the spatial portion of (13) into (1) gives

$$E(y_2) = ab \int\limits_{-\infty}^{\infty}\int\limits_{-\infty}^{\infty} G(f_s)\ w(y_0) e^{-i\frac{2\pi}{v_r}(f_s - f_{so})\cos\theta_B y_0}$$

$$e^{i\frac{kN_e y_2}{f}y_0}\ dy_0\ df_s\ , \tag{15}$$

where $w(y_1)$ is a window function defined such that

$$w(y_1) \begin{cases} \neq 0, & |y_0| < D/2 \\ = 0, & |y_0| > D/2\ . \end{cases} \tag{16}$$

The Fourier transform result (15) corresponds to the starting point, i.e., Equation (5A) in the paper "An Integrated Optical Approach to the Fourier Transform" reproduced in Appendix A of this report. In that paper, we show that (5A) above reduces to the usual truncated Fourier transform relation; that is, the convolution of the signal spectrum with

14

the Fourier transform of the window function (7A). The above paper then proceeds to point out that this convolution will yield an accurate mapping of the Fourier transform of the input signal in the output optical transverse plane if the time-bandwidth product of that portion of the surface elastic wave delay line traversing the input optical aperture is much greater than one. Thus, as in other Fourier transform techniques, the appropriate time-bandwidth product serves as a figure of merit for measuring the fidelity of the spectrum analysis process.

The paper, "An Integrated Optical Approach to the Fourier Transform," then proceeds to develop various design considerations of the spectrum analyzer indicating how the lens aperture and focal length determine the time-bandwidth-product and the spectrum analyzer resolution where a surface elasto-optic Bragg type spatial modulator is employed and where a discrete set of photodetectors are employed in an array. The center frequency of the spatial modulator and the photodetector array spatial resolution are determined by the lithographic art employed which determines the minimum practical dimensions realizable with reasonable yield. Figures 3A and 4A of Appendix A indicate these functional relationships which have served as the base for this effort, "Optical Waveguide Lenses II."

The spectrum analyzer requires a beam expansion lens system with a large expansion ratio ($\sim$ 90) confined to a minimum of substrate area ($\sim$2 cm). The Fourier transform lens requires a field of view on the order of 3 degrees and an f-number in the range of.5-10. The original intent to employ a telephoto system was abandoned because of the difficulty of realizing the field of view without excessive field curvature. Thus, a single Luneburg lens with a retroreflector was substituted to minimize the substrate area required and to obtain a comparatively flat field with a long folded focal length. The spectrum analyzer also requires a detector array coupled to the thin-film waveguide containing the Fourier transform lens. The results of the investigation relating to these optical elements for the spectrum analyzer follow.

15

2. Optical Wavelength

Several considerations dictate the preference for an optical wavelength in the far red or near infrared for use in the integrated optical Fourier transform "chip." The emission wavelength of the electron injection laser is in the vicinity of 0.9 microns. Its characteristics of small size, efficiency, and adaptability for hybrid coupling to thin-film waveguide optics are compatible with the integration concept. Incorporation of distributed feedback will provide the requisite narrow emission linewidth and emission wavelength stability.

Another important consideration is the waveguide materials, structures and associated processes that must yield low-loss waveguide because scattering can degrade the Fourier transform's dynamic range and degrade its resolution. Some oxide thin films have been demonstrated to exhibit comparatively low loss in the far red and near infrared. Because Rayleigh scattering is inversely proportional to the fourth power of wavelength, it becomes essential to emphasize the near infrared to minimize scattering. Use of the longer wavelength relaxes the tolerances required for thin films to obtain reproducible controlled waveguide effective refractive indices. Waveguide lens aberrations are also wavelength dependent.

Although 0.9μ is recognized as the preferred wavelength, most experiments reported herein have employed 0.633μ radiation from a He/Ne gas laser for experimental convenience.

3. Waveguide Materials Compatible with Silicon Technology

During the preceding program, Optical Waveguide Lenses I,[16] various types of homogeneous and inhomogeneous refractors were investigated using a variety of thin films and substrates. Planar and geodesic lenses were included. As a result and recognizing the requirements for the optical Fourier transform function, this current effort, Optical Waveguide Lenses II, has emphasized a single lens-waveguide structure formed by processes which yield relatively low losses. All refractors considered herein have employed multilayer thin films to form generalized Luneburg lenses. The waveguide-lens material-structure universally employed

16

consists of Ta_2O_5 on Corning 7059 waveguide on thermally-grown SiO_2 on a single crystal silicon substrate.

Several factors have led to placement of emphasis upon the use of Ta_2O_5 on 7059 on thermally-grown SiO_2 on Si. First, thermally-grown SiO_2 has proven to yield the lowest loss, low-scattering substrate surface as an isolation layer between the waveguide and the substrate. The thermal growth process and resulting film resemble that of ultra low-loss fibers implying that it is reasonable to expect comparable results due to this substrate structure for integrated optical circuits. Second, single-crystal wafers of silicon have sufficient dimensions to encompass all optical elements for integration on a single "chip." They are available at reasonable cost, and its associated processing is a mature technology. Third, an integrated optical circuit may be formed on the oxide isolation layer while integrated electronic circuits may be formed under the layer with coupling between established by removal of the oxide.[15] Some optical circuits will require the presence of a piezoelectric to initiate a surface elasto-optic or electro-optic interaction. RF-sputter-deposited ZnO on the SiO_2 can fulfill this requirement.[17] An optical circuit may be integrated with the electronic counterpart providing for its simultaneous exploitation.

The formation of a generalized Luneburg lens is a simple process. Three different cross sections of waveguide Luneburg lens structures are illustrated in Figure 2. The lenses are circular symmetric and are formed by deposition through a suitably shaped mask. The transverse electric mode of the lowest order (TE_0) is normally employed in the waveguide.

The overlay lens structure (a) has been employed for most experiments for expedience whereas the overlay structure (c) is better because it suppresses scattering at the feathered edge of the Ta_2O_5. Cross sections (a) and (c) are asymmetrical and, therefore, can potentially excite the next higher order mode, TE_1 or TM_1. The waveguide lens (b) is the pre-ferred structure because it is nearly symmetrical and because the feathered edge is immersed. This structure only minimally excites the TE_1 mode but may excite the TE_2 and higher orders if sufficiently thick, a condition to be avoided. Because the Luneburg lens derives its inhomogeneity by

17

(a) Lens Overlay - Asymmetrical Waveguide

Ta$_2$O$_5$

7059

SiO$_2$

Si
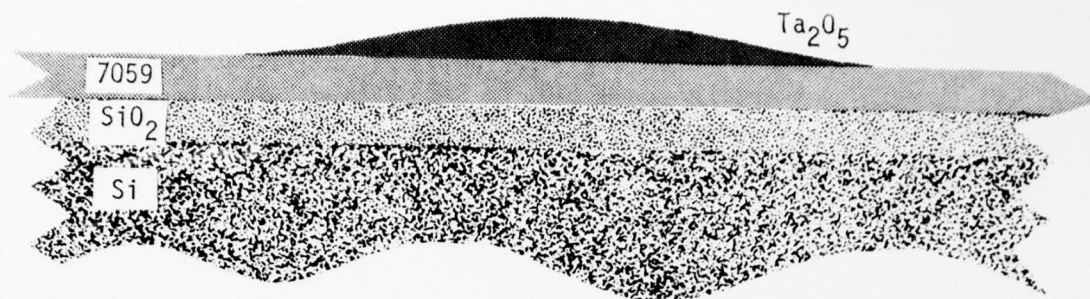
(b) Lens Interleave - Symmetrical Waveguide
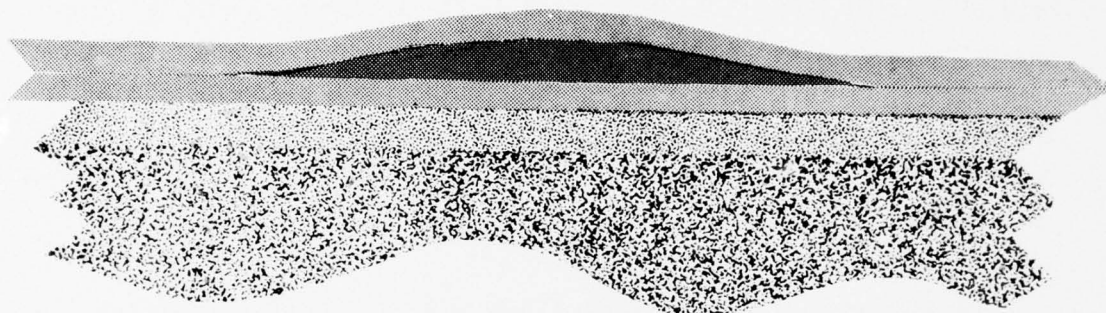
(c) Lens Underlay - Asymmetrical Waveguide
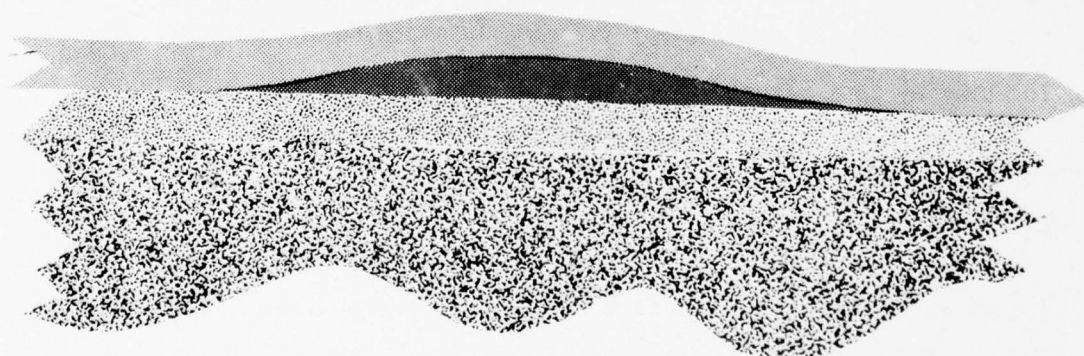
Figure 2. Three Cross Sections of Waveguide Luneburg Lens Which Result in Different Degrees and Different Types of Mode Conversion.

18

changes of waveguide thickness, it will exhibit an inherent chromatic aberration.

The losses encountered in optical waveguide propagation are due to absorption and scattering, the latter of which is important because it may limit the spectrum analyzer dynamic range and resolution. Aside from the waveguide material absorption, a structure employing an isolation layer may also exhibit additional losses due to the penetration of the evanescent field through the isolation layer into the substrate. The calculated[30] waveguide attenuation due to evanescent field absorption in a silicon substrate for three waveguide thicknesses of 7059 as a function of the thermally-grown SiO_2 isolation layer thickness is depicted in Figure 3. Observe that a waveguide with a thickness comparable to the wavelength or less with an isolation layer, more than a wavelength thick, suppresses the absorption due to the evanescent field to a trivially small value.

During this program, considerable effort was devoted to the suppression of Mie and Rayleigh scattering because it constitutes the one major factor that may compromise the exploitation of a thermally-oxidized silicon substrate. Sufficient evidence has now been obtained to show that the scattering may be suppressed, although its consistent realization is sometimes elusive. The transmission of He/Ne radiation at 6328Å through Corning 7059 waveguide is depicted in Figure 11B, Appendix B, and in Figure 4. In each case, a collimated beam resembling a Gaussian was employed. The measured input beam profile is included in the figures. The observed output transverse profile, after propagation through 9 cm of 7059 waveguide using input and output prism couplers (Ti_2O), is shown in Figure 4. The beam width and profile are essentially the same except for fine-grain, spatial noise. The residual scattering level of both the input and output beam distributions at approximately -28 dB is an electronic instrumentation limit of the beam profile probe and recording system. Relatively long sections of 7059 waveguide have been produced on thermally-grown SiO_2 for which the scattering trace is not apparent to the eye. Typical Corning 7059 waveguide absorption and scattering loss is on the order of 1 dB/cm. While some specimens are in the 0.3 dB/cm regime, these depositions degrade with time with the attachment of atmospheric particulates, which
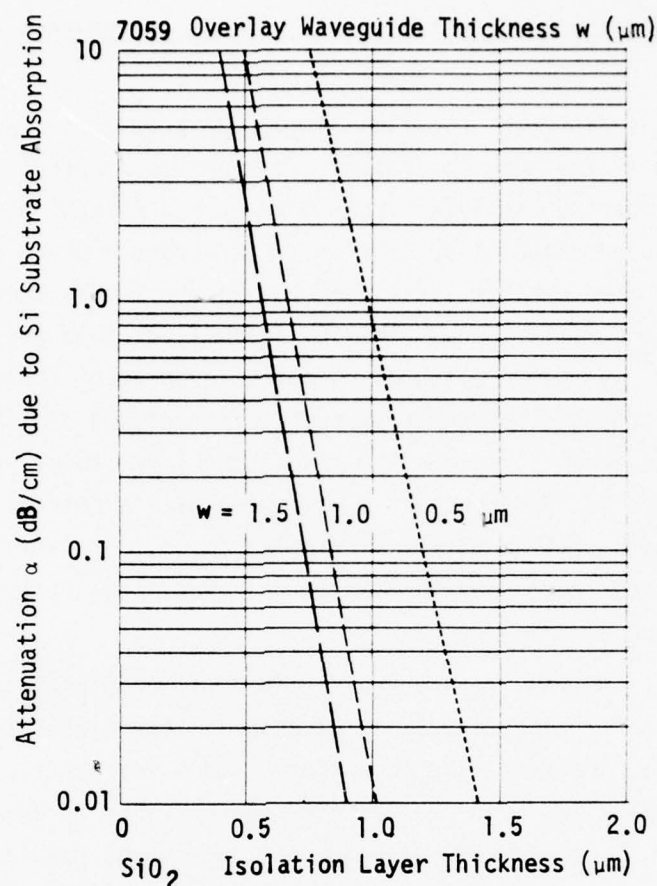
Figure 3.   Thin-Film Waveguide Attenuation Due to Evanescent Field
Absorption in Silicon Substrate for Three Corning 7059
Overlay Waveguide Thicknesses as a Function of the Thermally-
Grown SiO_2 Isolation Layer Thickness (After Chen).[30]

suggests the use of a superstrate isolation layer, possibly an organic
deposited from solution.

Tantalum pentoxide[31-33] and Nb_2O_5 have been employed to form homogeneous
and inhomogeneous thin-film lenses.[35] Their losses are in the 0.5-3 dB/cm
range depending upon the deposition process.   The larger value is usually
obtained for very thin layers on Corning 7059 and a lower value may be
obtained when immersed or in thicker cross sections.   All of the experi-
mental results, depicting lens performance photographically, have employed
the overlay structure and thus exhibit the larger loss.   The photograph

20
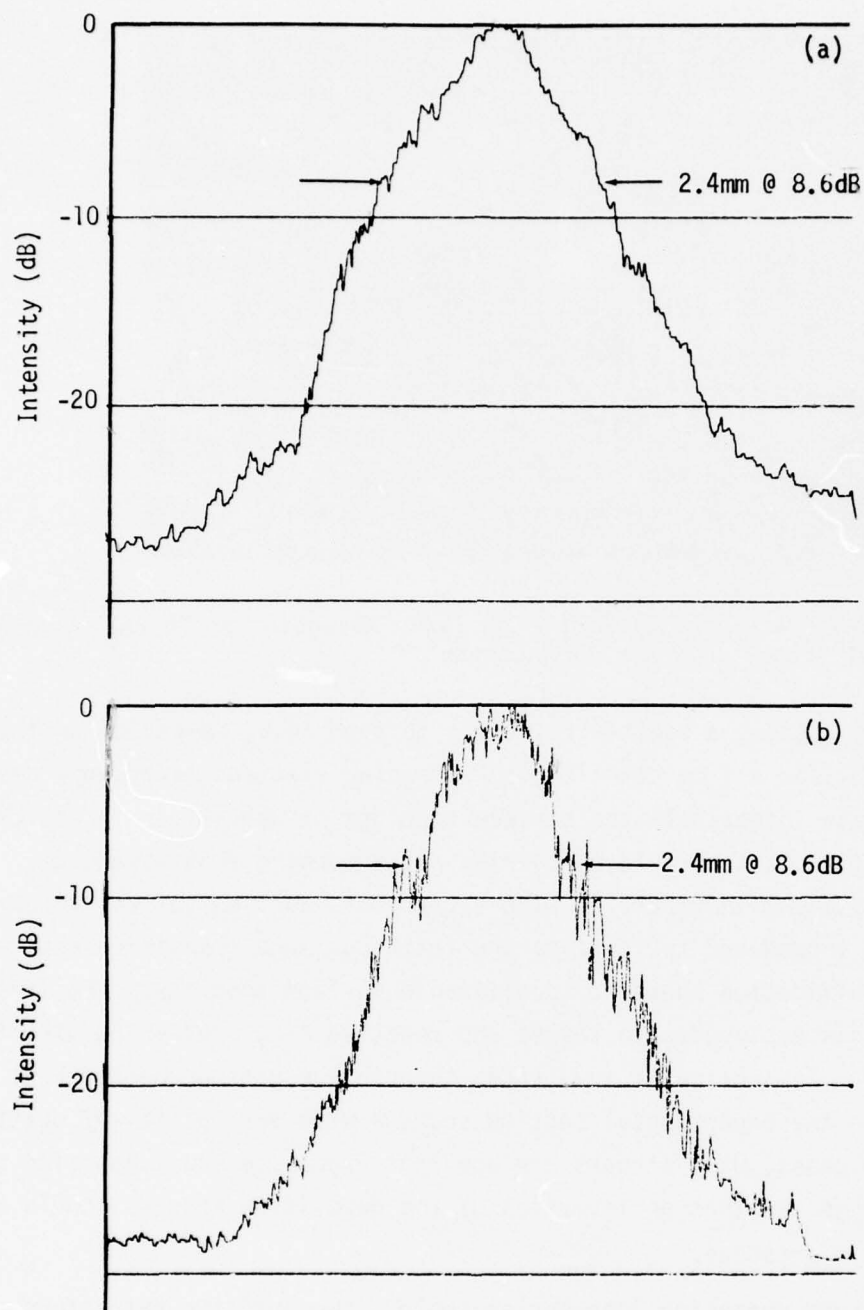
Figure 4. Intensity Distribution of 6328Å Laser Radiation (a) Input
Beam to Prism Coupler and (b) Output Beam From Prism Coupler
After the Beam Has Traversed Through 9 cm of 7059 Waveguide
on Thermally-Grown SiO_2.

21

Wafer Edge

Prism
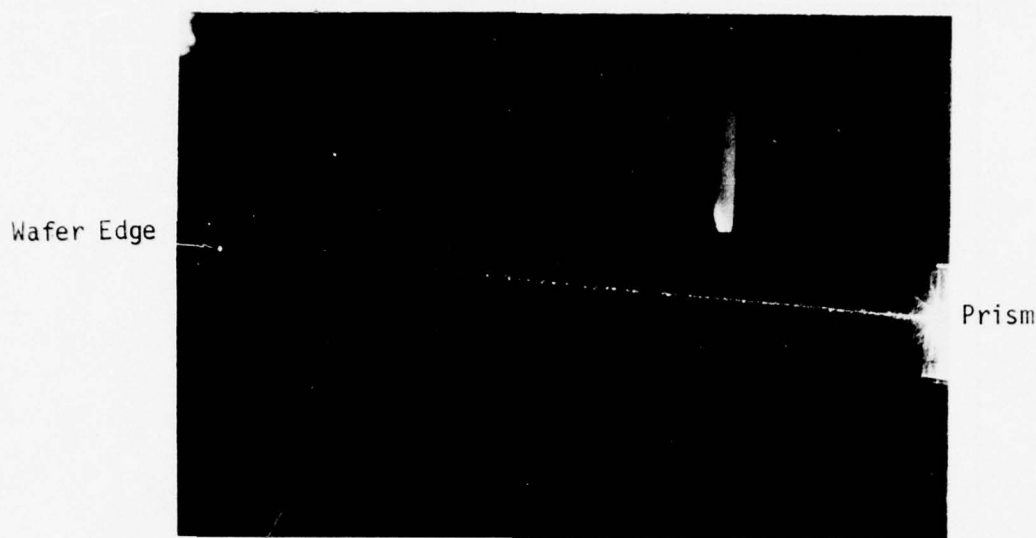
Figure 5. Ray Trace of 6328 Å Through Ta_2O_5 Waveguide on Thermally-Grown SiO_2 on Si, 7 cm Path Length

of Figure 5 shows a scatter ray trace through Ta_2O_5 waveguide on thermally-grown SiO_2 for a 7 cm path length. Scanning electron microscopy has been employed to investigate the surface topology of waveguides in the transition region between a Ta_2O_5 overlay and a Corning 7059 waveguide. A result is shown in Figure 6. The artifact in Section (a) was intentionally introduced to identify the feathered edge transition region. High magnification shows no identifiable surface topology. The lens overlay has employed a Ta target and reactive $A-O_2$ sputtering directed downward. Inspection of ray traces through the various photographs contained in the experimental section shows a wide variability of scattering. In a few cases, dark streaks are apparent from some Mie scattering centers. It is suggested that an inversion of the deposition process should minimize their presence.

The beam expansion lens system employs two positive refractors producing inversion and, therefore, the source radiation comes to a focus in the waveguide. Thus far, no optical damage has been observed in Corning 7059 waveguide on thermally-oxidized silicon. This waveguide safely handles at least 0.4×10^6 watts/cm^2 continuously with no apparent photo-induced refraction effects such as appear in $LiNbO_3$.
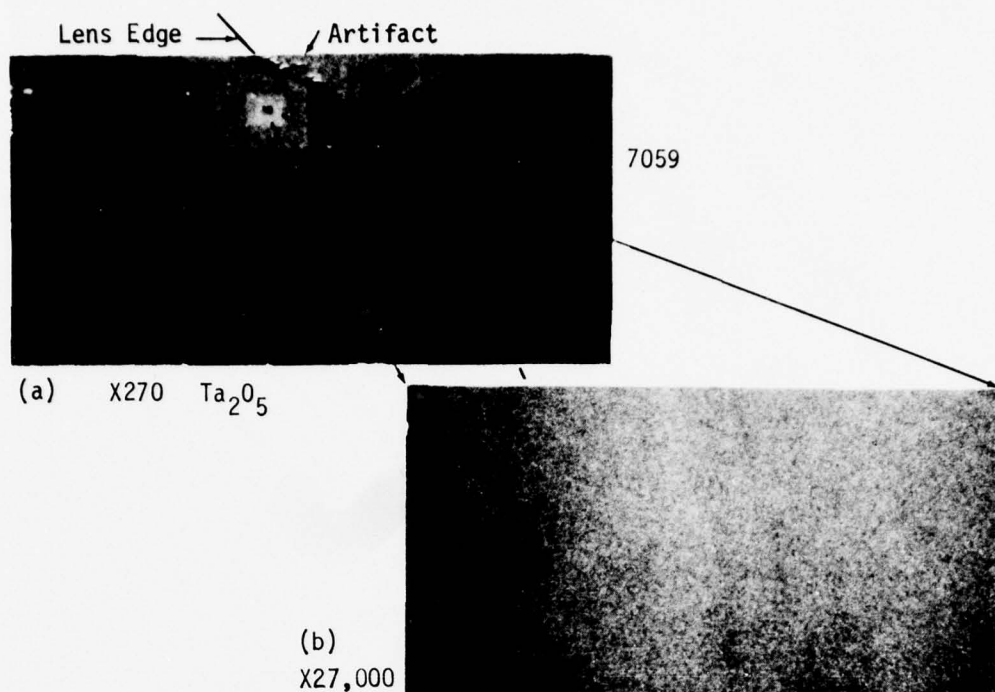
Figure 6. Scanning Electron Micrograph of Luneburg Lens Surface: (a) Transition Region (Edge), Magnification 270X with Artificial Artifact and Scan Outline, (b) Magnification 27,000X.

In conclusion, scattering, particularly Mie, is an important characteristic which must be suppressed for Ta_2O_5 and Corning 7059 waveguides to be a viable competitive structure applicable to an integrated optical Fourier transform "chip". Experimental evidence shows that it is possible to realize low-scattering-loss waveguides competitive with other thin film approaches. The problem remaining is of consistent reproducibility over large areas.

B. MULTILAYER THIN-FILM WAVEGUIDES

To provide a basis for direction of optical lenses formed in thin-film
waveguide, we will briefly summarize some of the more important properties
of bound modes in dielectric waveguide.[34] In particular, we will consider
the four-layer structure illustrated in Figure 7. It consists of a sub-
strate having a refractive index of n_4 and superstrate having a refractive
index of n_1, each with an infinite extent with one or two thin films be-
tween which serve as the optical waveguides or as a waveguide with isolation
layer. The planar structure considered also has infinite extent in y with
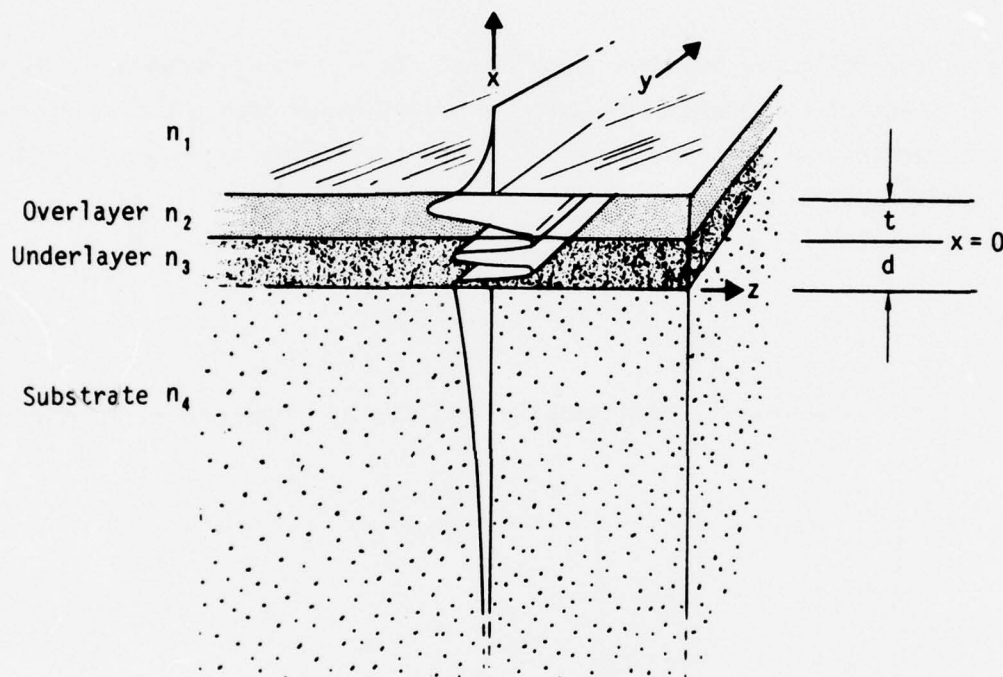
Figure 7. Cross Section of Asymmetrical Multilayer Planar Dielectric
Waveguide Showing Fourth Order Mode With Evanescent Field

optical propagation in the z-direction. For wave binding, it is necessary
that (n_2 and/or n_3) be greater than (n_1 and n_4). We will not consider the modes
bound to the substrate when it is of limited extent. The modes bound to this
type of structure may be either transverse electric (TE_m) or transverse mag-
netic (TM_m) of order m. A transverse field component bounded to both layers
(overlayer and underlayer) is illustrated in Figure 7, showing the fourth
order with the evanescent field extending into the superstrate and substrate.
It is possible that the refractive index and the film thickness of these layers

25

be such that wave binding occurs only in that region which has the highest
index with an evanescent component in the other layers.

1.   Dielectric Waveguide Modes

   The transverse electric modes (TE) are the eigensolutions of the field
equation where the time variation $e^{i\omega t}$ has been suppressed

$$\left[\frac{\partial^2}{2x^2} + \frac{\partial^2}{2z^2} + \omega^2 \varepsilon(x)\mu_0\right] E_y(x,z) = 0 \tag{17}$$

subject to the following boundary conditions: $E_y \rightarrow 0$ as x approaches $\pm \infty$,
and the tangential components of E and H are continuous across the boundaries.
The z dependence will be the same in all four regions for a given mode and
can be written as

$$e^{-i\beta_m Z} \tag{18}$$

where m is the mode order. Additionally $\varepsilon(x)$ can be expressed as follows

$$\varepsilon(x) = \begin{cases} n_1^2 \varepsilon_0 & x z t \\ n_2^2 \varepsilon_0 & t > x > 0 \\ n_3^2 \varepsilon_0 & 0 > x > -d \\ n_4^2 \varepsilon_0 & -d \geq x \end{cases} \tag{19}$$

Applying the boundary conditions on E to the solutions of (17) the fields
in the four regions can be written as

$$E_{m1} = A_m e^{-P_m(x-t)} \sin(h_m t + \phi_m) \sin \gamma_m e^{-i\beta_m Z} \tag{20a}$$

$$E_{m2} = A_m \sin(h_m x + \phi_m) \sin \gamma_m e^{-i\beta_m Z} \tag{20b}$$

$$E_{m3} = A_m \sin(\ell_m x + \gamma_m) \sin \phi_m e^{-i\beta_m Z} \tag{20c}$$

26

$$E_{m4} = A_m \, e^{q_m(x+d)} \, Sin \, (-\ell_m d + \gamma_m) \, Sin \, \phi_m \, e^{-i\beta_m Z} \tag{20d}$$

where A_m is a normalization constant, and P_m, h_m, ℓ_m and q_m are the transverse components of the propagation vector in regions 1, 2, 3, 4 respectively. P_m, h_m, ℓ_m, q_m and β_m are related by the following dispersion equations

$$P_m = (\beta_m^2 - k^2 \, n_1^2)^{1/2} \tag{21a}$$

$$h_m = (k^2 \, n_2^2 - \beta_m^2)^{1/2} \tag{21b}$$

$$\ell_m = (k^2 \, n_3^2 - \beta_m^2)^{1/2} \tag{21c}$$

$$q_m = (\beta_m^2 - k^2 \, n_4^2)^{1/2} \tag{21d}$$

Application of the boundary conditions on H yields

$$\tan(h_m t + \phi_m) = -h_m/P_m \tag{22}$$

$$\tan \phi_m = (h_m/\ell_m) \tan \gamma_m \tag{23}$$

$$\tan(-\ell_m d + \gamma_m) = \ell_m/q_m \tag{24}$$

These equations when combined lead to the following transcendental equation

$$\frac{1}{\ell_m} \, \tan\!\left(\ell_m d + \tan^{-1} \frac{\ell_m}{q_m}\right) + \frac{1}{h_m} \, \tan\!\left(h_m t + \tan^{-1} \frac{h_m}{P_m}\right) = 0 \tag{25}$$

The roots of this equation are the allowed values of the propagation constants.

27

The transverse magnetic modes (TM) are the eigensolutions of the field equation

$$\left[\frac{\partial^2}{\partial x^2} + \frac{\partial^2}{\partial z^2} + \omega^2 \, \epsilon(x) \, \mu_o \right] Hy(x,z) = 0 \qquad (26)$$

The development of the TM modes is identical to that for the TE modes and again the allowed values of the propagation constants are roots of a trans-cendental equation, which is

$$\frac{n_3^2}{\ell_m} \tan\left(\ell_m d + \tan^{-1} \left[\frac{n_4^2}{n_3^2} \frac{\ell_m}{q_m} \right] \right) +$$

$$\frac{n_2^2}{h_m} \tan\left(h_m t + \tan^{-1} \left[\frac{n_1^2}{n_2^2} \frac{h_m}{p_m} \right] \right) = 0 \qquad (27)$$

2. Thin-Film Waveguide Dispersion Data

Tantalum pentoxide and Corning 7059 glass have been universally employed to form waveguides and lenses on thermally-grown SiO_2 substrates because they exhibit comparatively low scattering loss and may be deposited with reproducible properties and thickness profiles. Therefore, the dispersion for each has been calculated and the dispersion when combined to form refractive lens elements has also been calculated. Dispersion data is also presented for the multi-layer structure when the field is trapped in only the dense layer and when it is trapped in both layers.

The single layer thin-film waveguide dispersion of Ta_2O_5 structure on 7440 glass is shown in Figure 8 for both TE and TM modes as a function of the normalized film thickness. The thin-film waveguide dispersion of a Corning 7059 glass structure on an SiO_2 substrate is shown in Figure 9 for both TE and TM modes as a function of the normalized thickness. The effective refractive index approaches the bulk value for thick films and approaches the substrate for thin films. Each of these thin-film waveguide modes exhibit a cutoff

28

where $n_e(m) = 1.53$ for Figure 8 and $n_e(m) = 1.47$ for Figure 9 in a dielectric waveguide structure. Cutoff means the lack of wave binding to the film. An asymmetric dielectric structure cutoff leads to refraction into the substrate.

The dispersion for a two-layer structure for only the transverse electric modes is shown in Figures 10 and 11 where Ta_2O_5 is employed as the <u>overlayer</u> of variable thickness T and where the <u>underlayer</u> normalized thickness is constant (kt = 2.37 π) which is equivalent to a 7059 layer having a thickness of 0.75 microns and an optical wavelength of 0.63 microns. Each of the dispersion curves of Figures 10 and 11 exhibit an inflection representing the transition region where wave binding occurs to only the dense overlayer and where wave binding occurs in both layers. Figure 11 is an expansion of Figure 10 in the region where wave binding occurs in both layers showing the effect of substrate refractive index.

The dispersion for a two-layer structure for only the transverse electric modes where 7059 is employed as the <u>overlayer</u> of fixed thickness and where the <u>underlayer</u> of Ta_2O_5 of variable thickness T is shown in Figures 12 and 13. The fixed thickness waveguide (kt = 2.37 π) is equivalent to a 7059 layer having a thickness of 0.75 microns for the optical wavelength of 0.63 microns. Each of the dispersion curves of Figures 12 and 13 again exhibit an inflection representing the transition region where wave binding occurs to only the dense underlayer and wave binding occurs in both layers. Figure 13 is an expansion of Figure 12 in the region where wave binding occurs in both layers showing the effect of substrate refractive index for the same three values of refractive index.

This dispersion data is sufficient for design of homogeneous and inhomogeneous refractors, reflectors and geodesic lens systems. In general, only transverse electric modes are employed in the lowest order to minimize loss. Restriction to the TE mode is achieved by input coupling polarization. The thickness of some lenses will permit the presence of a multiplicity of mode orders, however, most transitions are sufficiently gradual to minimize excitation of higher order modes. Location of the highest index layer adjacent to the substrate minimizes conversion to the next higher order mode which is odd. It is also possible to prohibit mode conversion by symmetry, that is, by interleaving the denser film between two separate halves of the waveguide.

29
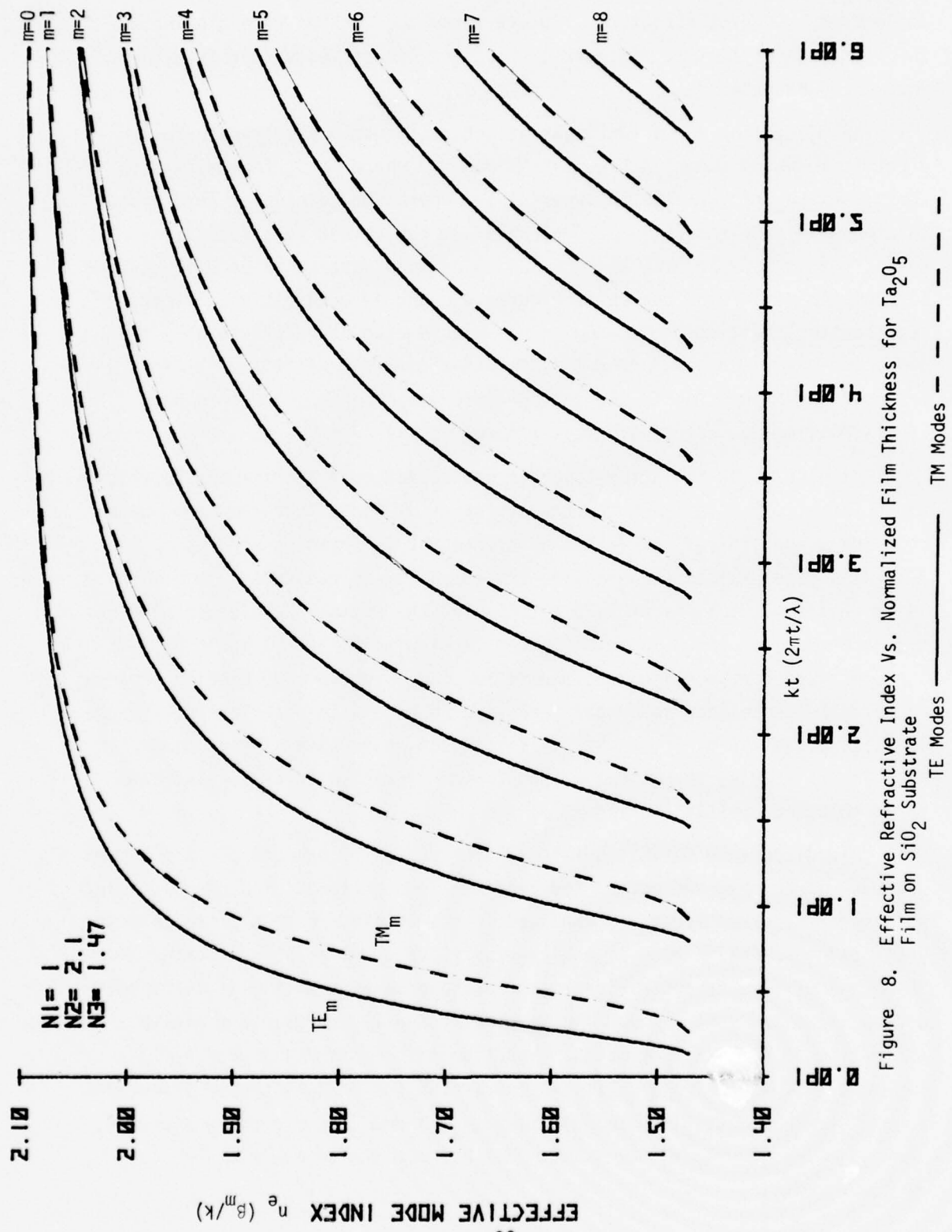
Figure 8. Effective Refractive Index Vs. Normalized Film Thickness for Ta_2O_5 Film on SiO_2 Substrate

TE Modes ———   TM Modes – – – –
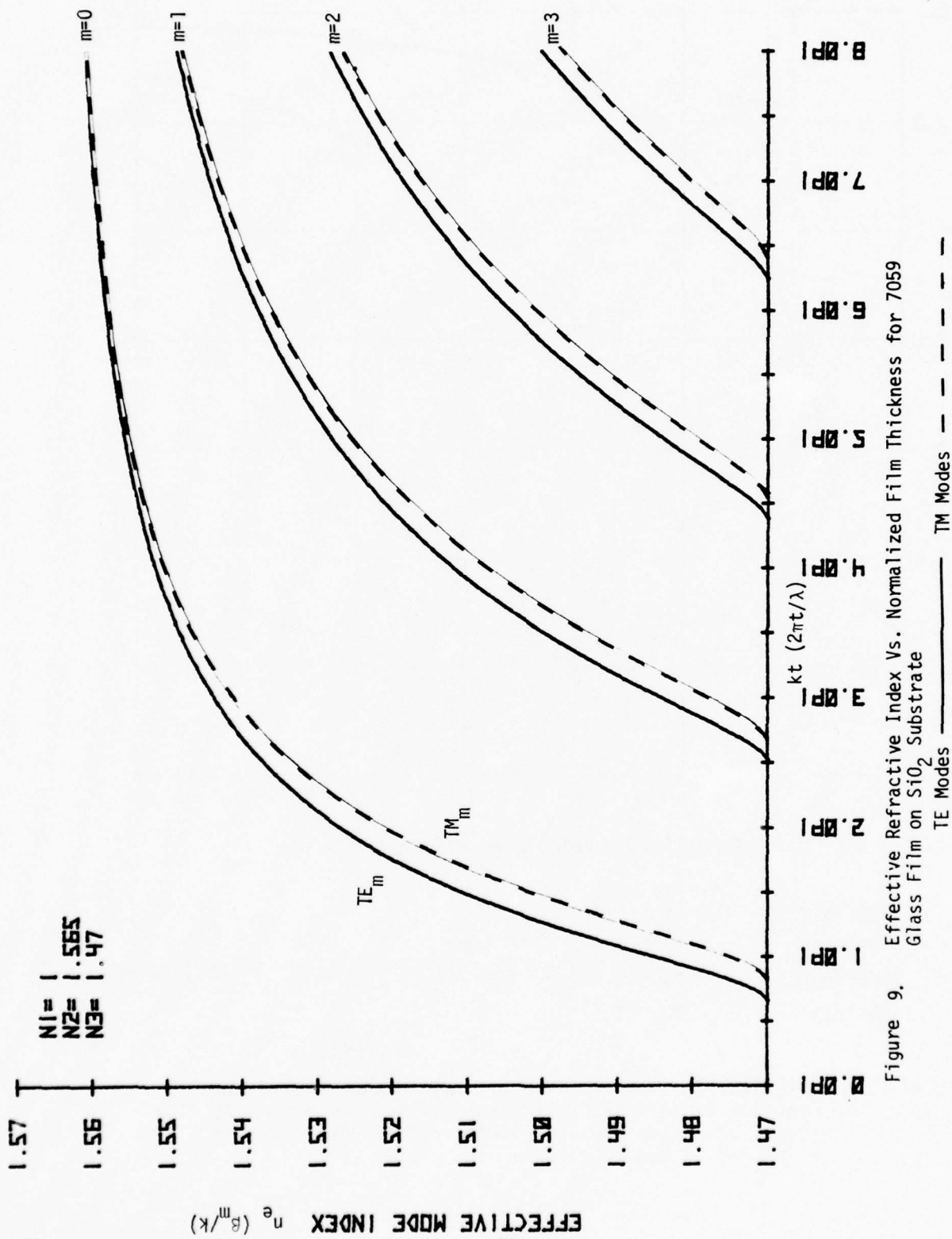
Figure 9. Effective Refractive Index Vs. Normalized Film Thickness for 7059 Glass Film on SiO$_2$ Substrate

TE Modes ——————

TM Modes — — — —

N1= 1
N2= 1.565
N3= 1.47

EFFECTIVE MODE INDEX n_e (β_m/k)

kt ($2\pi t/\lambda$)

31

Figure 10.   Effective Refractive Index of Composite Structure as a Function of Normalized Thickness of the Dense Overlay Film (Lens) Where the Overlay Film Normalized Thickness kt = 2.37π for TE Modes Only

32

Effective Refractive Index (n_e)

m = 0

m = 1

1.53

m = 2

1.497

1.47

Normalized Lens Thickness $2\pi T/\lambda$
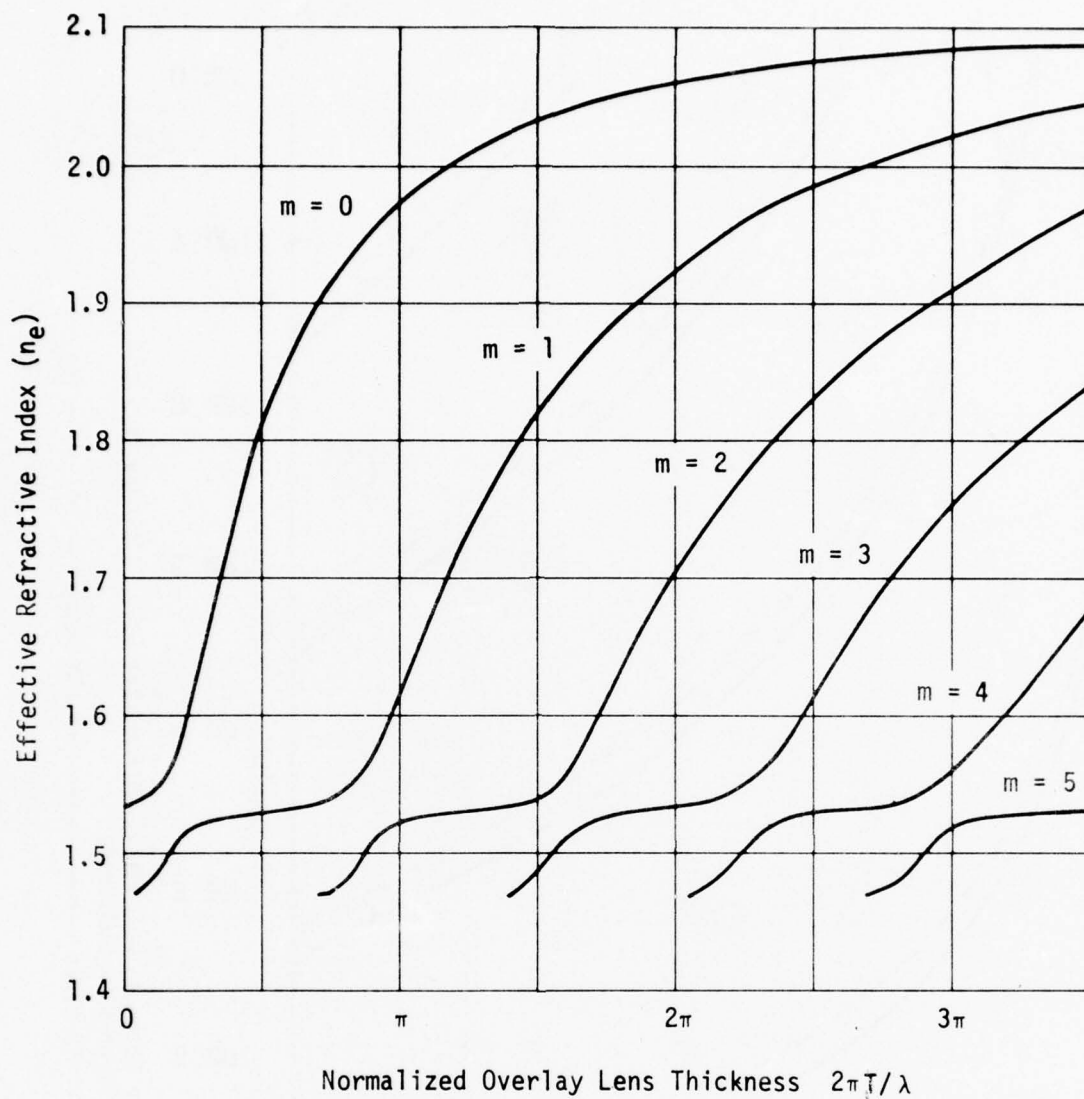
Superstrate	$n_1 = 1.0$
Overlayer	$n_2 = 2.1$ kT Lens
Underlayer	$n_3 = 1.565$ kt = 2.37π (t = .75μ @ λ = .63μ) Waveguide
Substrate	$n_4 = 1.47, 1.497, 1.53$

Figure 11.   Expanded Scale of Figure 10 Showing the Effect of Three
Substrates for TE Modes Only

33

Figure 12. Effective Refractive Index of Composite Structure as a Function of Normalized Thickness of the Dense Underlay Film (Lens) Where the Underlay Film Normalized Thickness $kt = 2.37\pi$ for TE Modes Only

34

Figure 13. Expanded Scale of Figure 12 Showing the Effect of Three Substrates for TE Modes Only

The figure axes:
- Y-axis: Effective Refractive Index (n_e), from 1.46 to 1.60
- X-axis: Normalized Lens Thickness $2\pi T/\lambda$, from 0 to $3\pi/2$

Curves labeled m = 0, m = 1, m = 2, with values 1.53, 1.497, 1.47.
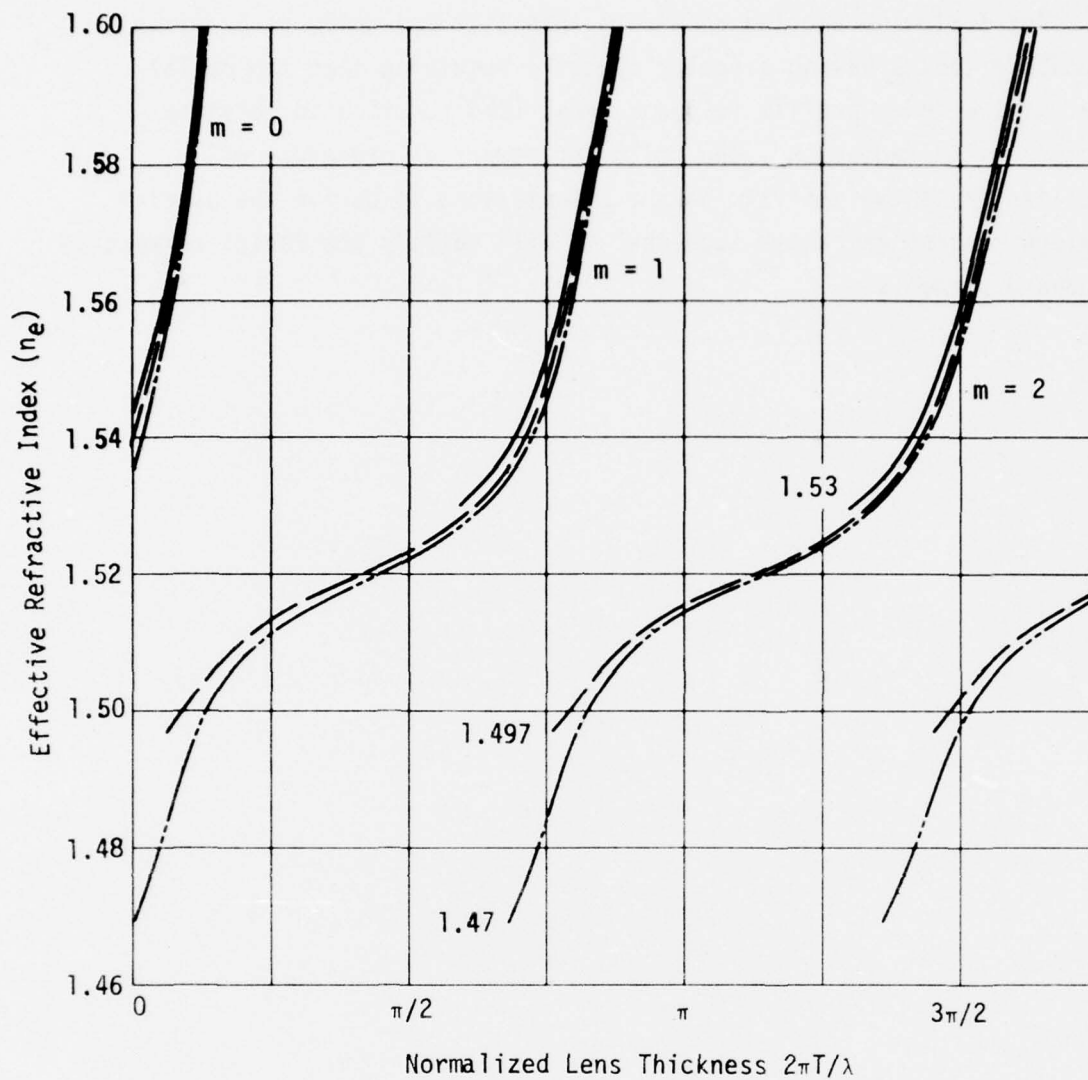
Superstrate	$n_1 = 1.0$
Overlayer	$n_2 = 1.565$ kt = 2.37π (t = .75μ @ λ = .63μ) Waveguide
Underlayer	$n_3 = 2.1$ kT Lens
Substrate	$n_4 = 1.47, 1.497, 1.53$

35

The following section considers thin-film waveguide generalized
Luneburg lenses having circular symmetry requiring that the radial
refractive index profile follow a prescribed function to obtain a
focus of the radiation. The following numerical procedure will
utilize the above analysis in the computations to derive the overlay
waveguide-lens thickness such that it will satisfy the radial refractive
index dependents.

36

C. INHOMOGENEOUS REFRACTIVE WAVEGUIDE LENS SYSTEMS

Conventional optical lens systems employ homogeneous dielectric and spherical surfaces in various combinations to correct aberrations. In general, inhomogeneous materials are avoided, particularly when perturbations are randomly distributed. Generally, the perturbations are weak except for certain processes applicable to surfaces. Lenses requiring the large refractive inhomogeneities obeying prescribed functions such as Maxwell's fish-eye[36] and the Luneburg lens[37] have not been realized in the optical portion of the spectrum. Thin-film optical waveguide provides the opportunity to produce thin-film inhomogeneous dielectric sections using homogeneous materials by variation of the film thickness.

1. "Classical" Luneburg Lens [37]

Luneburg lens is an inhomogeneous positive refractor with radial symmetry which images a plain wave front to a microscopic hemispherical spot located on the opposite boundary of the refractor. Interest in the Luneburg lens arises because of its 4π field of view and because it is free of all aberrations except field curvature. For integrated optics, its simplicity of fabrication in a thin-film structure realized reproducibly is an important attribute.[35] The circular symmetry is of particular interest where the substrate area is limited because folding of the optical axis may use the same lens for several purposes. The waveguide Luneburg lens has a further advantage that all refractive index variations are continuous, smooth and slow functions with respect to the optical wavelength. Mode conversion in the lens is suppressed by the graded thickness profile and by symmetry.

A generalized Luneburg lens will form a perfect geometric image of two given concentric circles on each other.[38] The perfect focusing property may be achieved in various regions. If one of the circles is of infinite radius, the lens may be designed to focus on another circle outside of, at the boundary, or inside of, the Luneburg lens. Luneburg found a solution for the refractive index function which had a conjugate foci for two given points outside of the lens. The solution for a parallel beam array which focuses on the opposite lens interface requires

37

that the refractive index $n(r,m)$

$$n(r,m) = n_e(m) \sqrt{2 - (r/r_0)^2} \qquad r \le r_0 \quad , \qquad (28)$$

where n_e is the refractive index of the medium surrounding and lens, r_0 is the lens radius, and r is the radial coordinate for mode (m). The trajectory of rays through a "classic" Luneburg lens is illustrated in Figure 14.
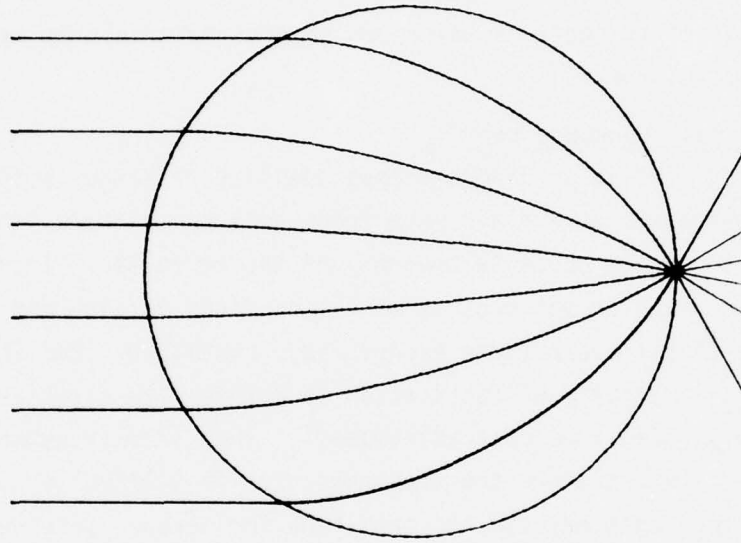
Figure 14. Ray Trajectory Through Luneburg Lens Where f-Number = 0.5, S=1.

The technique of ray tracing through an inhomogeneous refractor is delineated in Appendix E by Southwell entitled, "Inhomogeneous Optical Waveguide Lens Analysis."

2. Generalized Luneburg Lenses

The "classic" Luneburg lens has been generalized by Morgan[38] developing a radial refractive index profile which will focus one circle on another in the region beyond the edge of the lens radius r_0. The

38

r_1

Perfect Ray Trace

Drawing For
S=4

α

y

r_0

Imperfect Ray Trace

y'

Luneburg Lens
Outline

Pupil Plane
Phase Reference

F
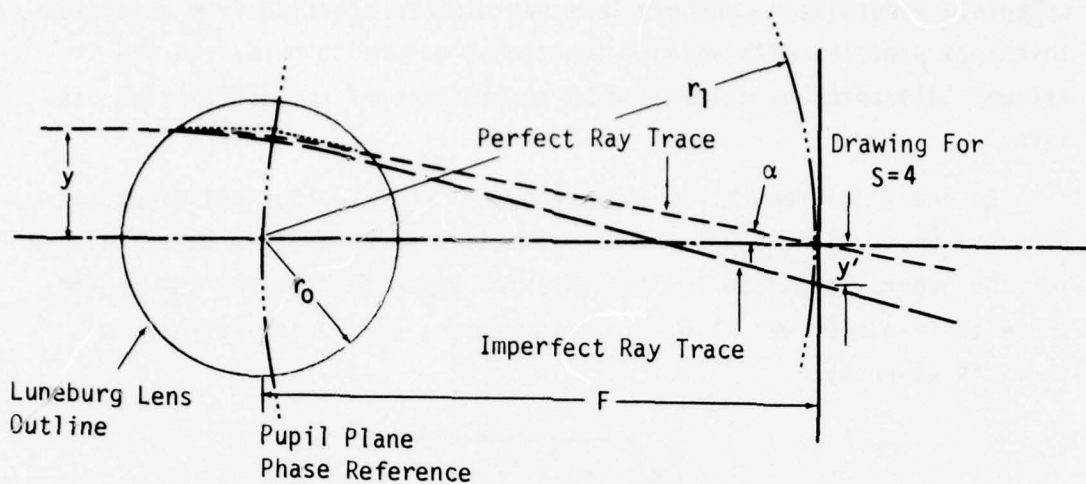
"Classic"
  $F=r_0$, $f=F/r_0=1/2$, $S=1$, $\alpha=90°$

Generalized
  $F>r_0$, $f>1/2$, $S=2f>1$, $\alpha<90°$

y'

y
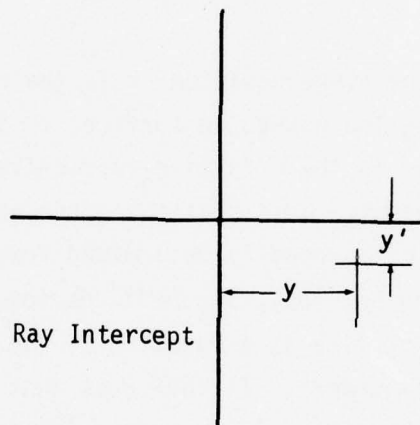
Ray Intercept

Figure 15. Ray Trace Geometry Through Luneburg Lens and Ray Trace
Intercept Plot.

increased focal length reduces the range of refractive index variation
required to form the lens. Extending the focus outside of the lens
region increases the f-number and thus the diffraction pattern width in
the focal region.

The geometry of a generalized Luneburg lens is depicted in Figure 15
showing a perfect ray trace from which a ray intercept plot is developed
which is also included in the figure. In the following section, numer-
ous ray traces are calculated yielding the ray intercept plot from which
the phase wavefront has been derived followed by the calculated inten-
sity diffraction pattern. This procedure has provided the means to

39

calculate generalized Luneburg lens performance starting from waveguide thickness profiles with various functional errors to determine the allowed tolerances as determined by degradation of the diffraction pattern.

In the final report for the preceding program, "Optical Waveguide Lenses I[16]," the functional radial refractive index profile was developed for the generalized case for the paraxial approximation for the regime where the f-number was >1.5. In this region, the radial refractive index is given by

$$n(r,m) = n_e(m) \, \exp \left(\sqrt{\frac{n_e(m)^2 r_o^2 - r^2 n^2(r,m)}{\pi n_e(m) r_1}} \right). \tag{29}$$

In the above equation, r is the radial coordinate from the lens center along the waveguide surface, r_o is the radius of the lens region, $r_1 = F$ an $n_e(m)$ is the effective refractive index for the waveguide mode (m) of interest. Note that the above equation is not solved for $n(r,m)$, but $n(r,m)$ is readily determined from Eq. (29) numerically as a function of r_1 Using Eq. (29), Figure 16 depicts the normalized effective refractive index profile as a function of the normalized lens radius for several values of f-numbers. It indicates that the transverse profile becomes more uniform having a lower refractive index over a larger central region of the lens as the focal length is increased. Figure 17 depicts the minimum required effective refractive index at the center of the lens relative to its ambient waveguide effective refractive index as the lens focal length is increased. For the classic Luneburg lens $n(o,o) = \sqrt{2}$, a high index layer like Ta_2O_5 or Nb_2O_5 is required on Corning 7059 for F/D = 0.5. Generalized Luneburg lenses may be formed with these materials using thinner films or using films with lower index and thicker layers. Generalized Luneburg lenses have been realized using an "all" 7059 thin film when F/D>6. Lenses which are formed from a single composition by changes of the layer thickness exhibit substantially less scattering and further suppress the excitation of higher order modes.

40
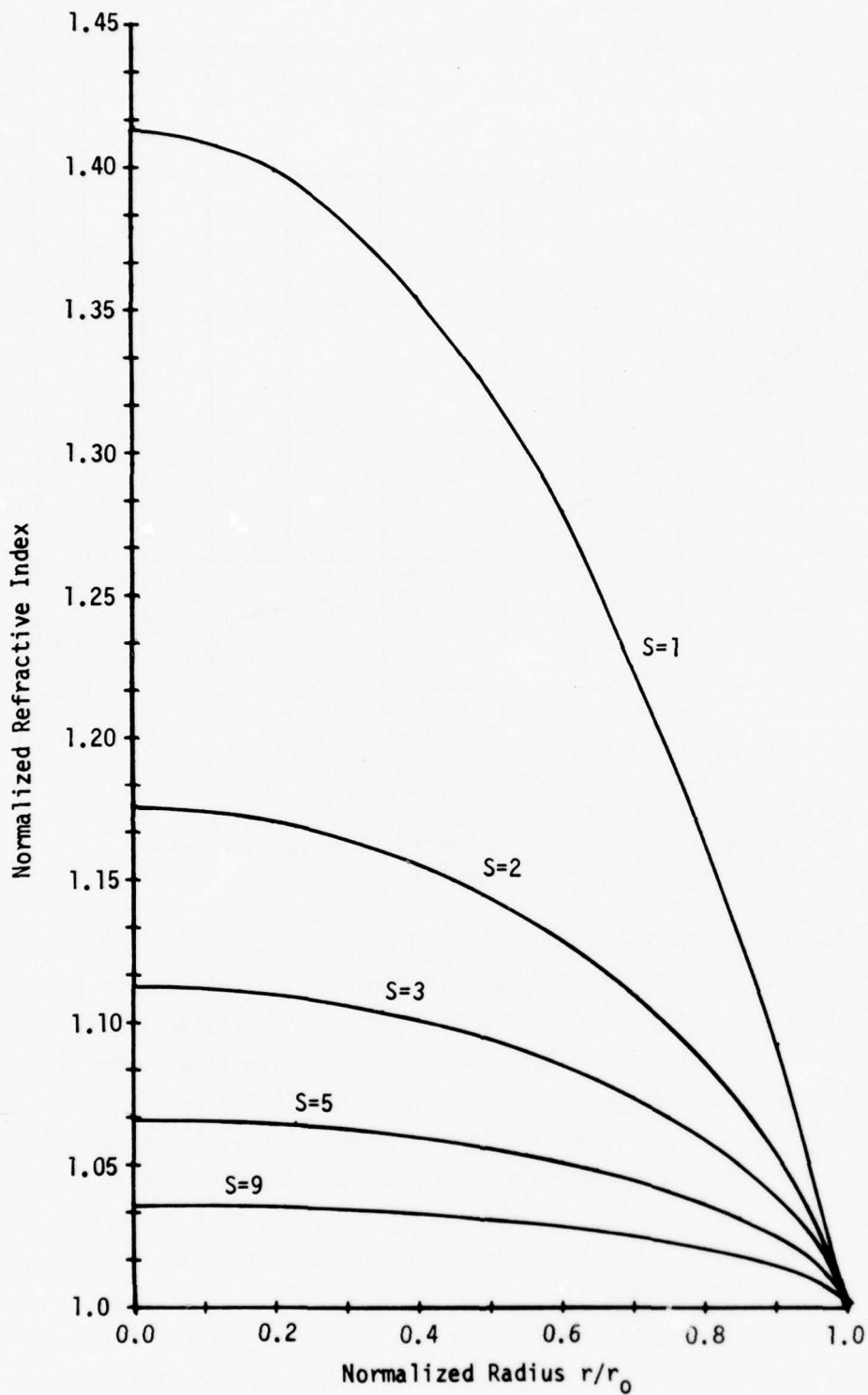
Figure 16. Normalized Refractive Index Profile for Generalized Luneburg Lenses for Various S-Parameters Listed by Morgan and Southwell (f-Number = S/2).

41
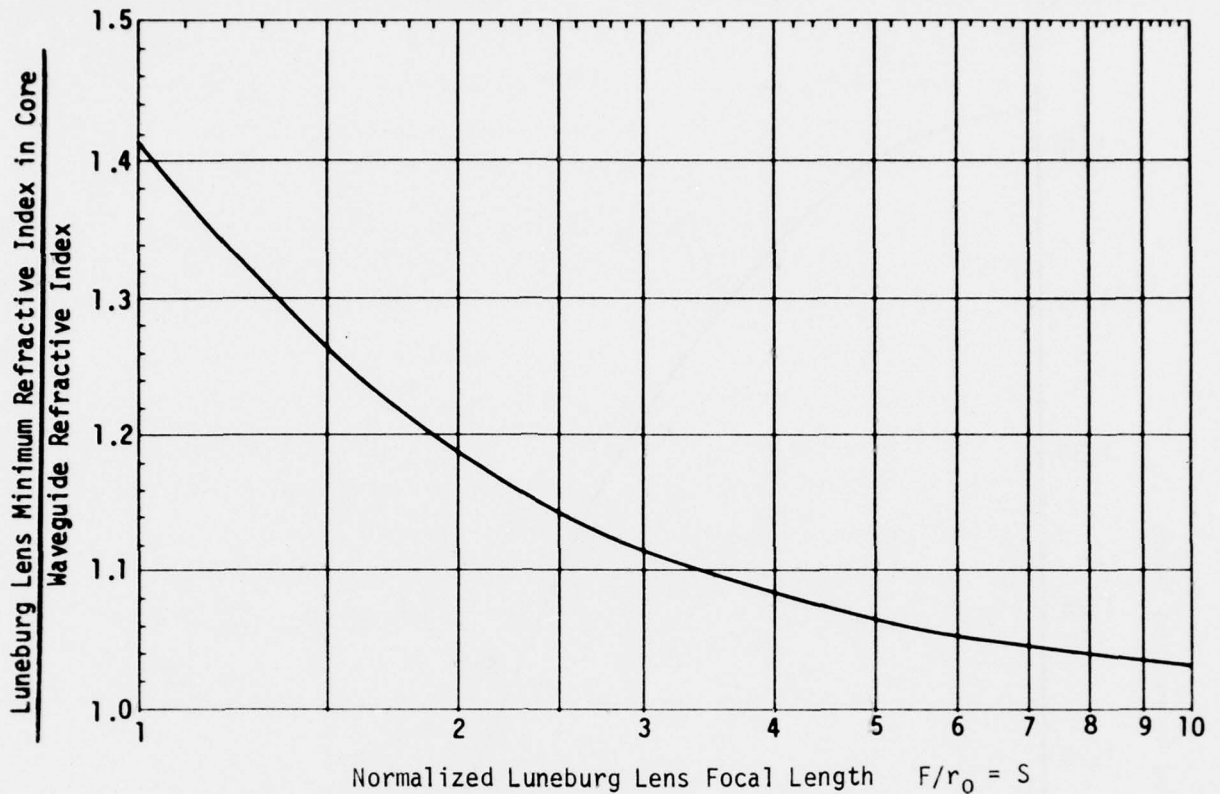
Figure 17. Thin-Film Waveguide Luneburg Lens Design Requirement (the
Minimum Ratio of Refractive Indices at Center Perimeter
Versus Normalized Focal Length $F/r_0 = S$)

3. Generalized Luneburg Lens Analytical Data

During this effort, the procedure to numerically evaluate the per-
formance of inhomogeneous lenses has developed in three stages. To
complement the experimental effort and provide constructive guidance
shaping the generalized Luneburg lens profile and to determine the
various allowed tolerances, it has been necessary to develop pro-
cedures to ray trace through these lenses and to determine the re-
sulting diffraction pattern. It was deemed desirable that the pro-
cedure utilize either experimentally determined thin-film lens thickness
profiles or utilize mathematical functions descriptive of profiles which
could be altered to adjust the focal length and to adjust the radial
functional dependence so as to be related to masks employed for lens
depositions. The first analytical procedure for ray tracing through
Luneburg lenses represented the radial thickness profile by a series

42

of stepped refractive index annuli. Snell's law was applied at the step between each annulus. It was found that 500-2000 annuli were necessary to obtain ray traces which pictorially represent a classic Luneburg lens using the Hewlett-Packard 9830 computer with graphical display. The procedure proved to be relatively slow with questionable accuracy for the marginal rays.

A second method of ray tracing through waveguide lenses was developed by Southwell and further refined yielding accurate results with considerable reduction of computational time in the H-P 9830 without exceeding its capacity. The procedure was extended to determine the ray intercepts from which the wavefront could be determined and, thus, the resulting intensity diffraction pattern. Only this latter procedure and its refinement will be delineated herein. Specific mathematical development of the procedure is contained in Appendices E and F by W. H. Southwell entitled, "Inhomogeneous Optical Waveguide Lens Analysis," and "Index and Waveguide Thickness Profiles for Generalized Luneburg Lenses." The procedure is briefly summarized here, followed by an ensemble of data. This data illustrates how various Luneburg lens refractive index profiles and errors of same influence the diffraction patterns. In several cases, the numerically devised results can be related to the experimental results of the following section.

The Southwell procedure essentially traces the wavefront normal by way of a numerical solution to the differential equation governing the fields because no closed-form solutions are available. Taylor series expansions are used for both the wave vector and the ray-position vector. Terms up to the second and third order are retained. The expansion derivatives are thus expressed in terms of the ray path, curvature and rate of change of the curvature. The major factor saving computational time results from a new extrapolation algorithm. Basically, the technique employs the well-known Richardson extrapolation except that the higher order terms are included to account for changes due to curvature. As each incremental step of the ray trace is taken, a test is taken to see whether the new ray trace position will fall within the waveguide lens region. If it does not, it becomes necessary to locate the precise position of the boundary along the ray path. An iterative technique, using Newton's method, was developed.

43

To evaluate the accuracy of this ray trace algorithm prior to ex-
trapolation, a "classical" Luneburg refractive index profile was used
to trace several errors. The results, using Southwell's procedure and
an H-P 9830 computer, are shown in Figure 18. The classical profile
was chosen because it is known to produce perfect focusing at a point
on the opposite edge of the lens. The actual ray trace intercept
represents ray trace errors because the rays should intercept at zero.
The computational time to trace rays through the lens is inversely pro-
portional to the step size used in the expansion. A plot of this ray
intercept error vs step size is shown in Figure 4 of Appendix E.

For near diffraction-limited optical systems, ray tracing does not
provide a direct comparison between the computer results and the measurements
which appear as diffraction patterns. An algorithm for deriving the pupil
function $P(x,y)$ is:

$$P(x,y) = exp \left[\frac{i2\pi}{\lambda} W(x,y) \right] , \qquad (30)$$

where $W(x,y)$ is the wave front error over the pupil coordinates x and y.
The purpose for obtaining the pupil function (30) is so that it may then
be Fourier transformed to provide the diffraction pattern in the specified
image plane. The theory for this pupil function derivation from ray trace
data is based upon solutions to "characteristic equations" which are, in
turn, based upon the optical Eikonal Equation.[39] An intermediate curve-
fitting step is employed which tends to keep the number of rays to a
minimum. A plot of the phase error across the aperture as a wave front
traverses the classical Luneburg lens of Figure 14 is shown in Figure 18.
The presence of non-zero phase error for the "perfect" classical Luneburg
lens indicates the residual computational error in the algorithm. The
maximum computational phase error in Figure 18 is $\lambda/25$. This residual error
is a function of the computational time and may be made arbitrarily small.

When the pupil function has been evaluated, the digital fast Fourier
transform is used to obtain the diffraction pattern. Figure 18 is the

44
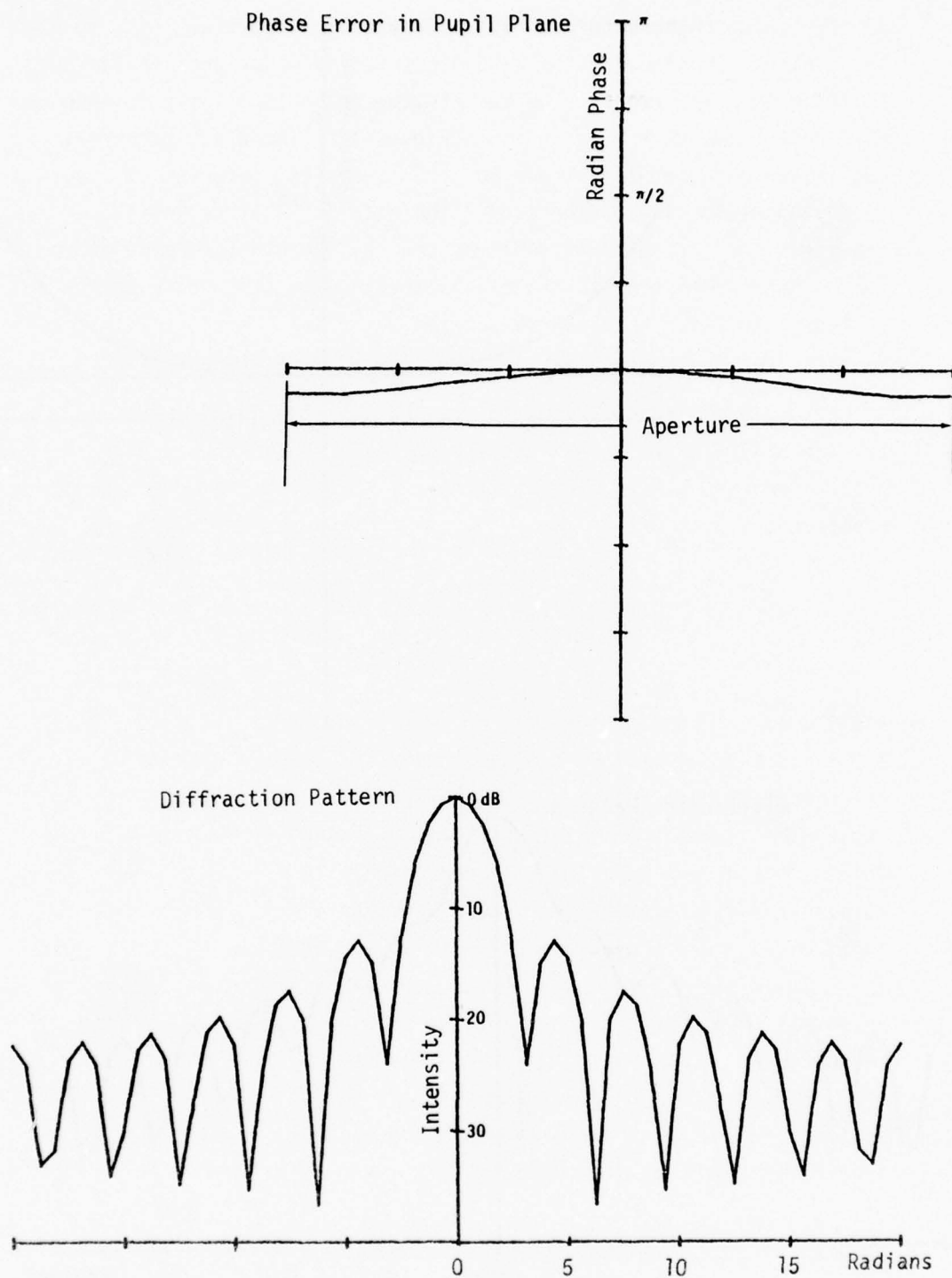
Figure 18. Wavefront Phase Error and Corresponding Intensity Diffraction Pattern for "Classic" Geodesic Lens Ray Traced in Figure 14 for Perfect Radial Profile.

45

Phase Error in Pupil Plane
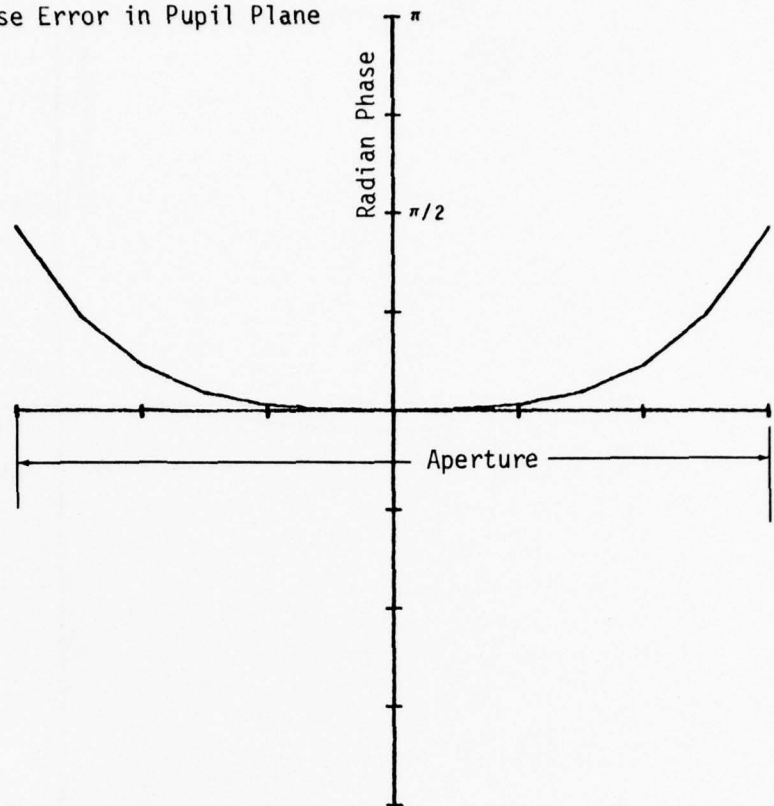
Diffraction Pattern
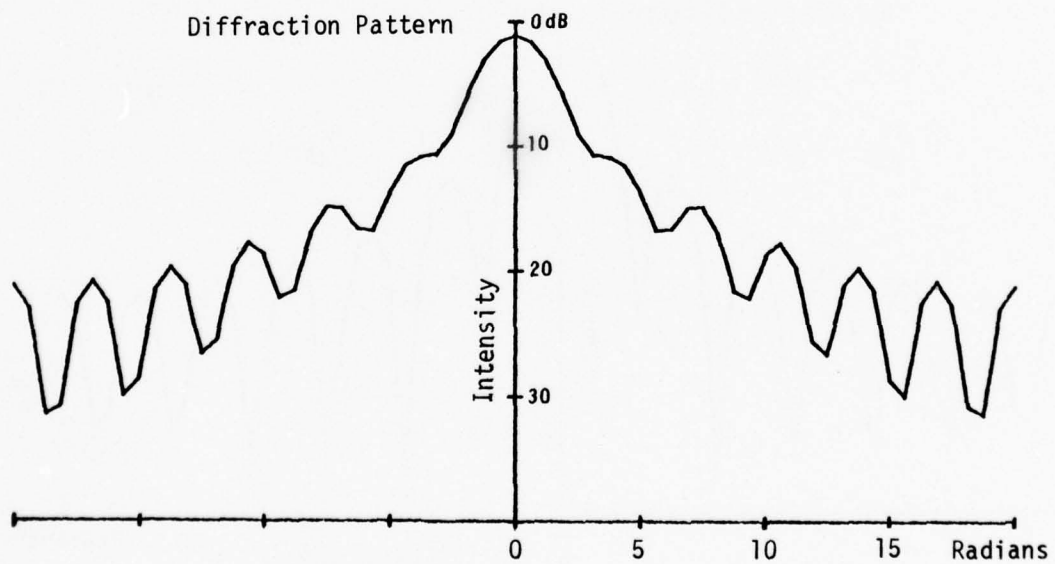
Figure 19. Wavefront Phase Error and Corresponding Intensity Diffraction Pattern for "Classic" Geodesic Lens Ray Traced in Figure 14 for Perfect Radial Profile Where the Image Plane Has Been Displaced by .5μ Yielding the Defocus Aberration.

46

Phase Error in Pupil Plane
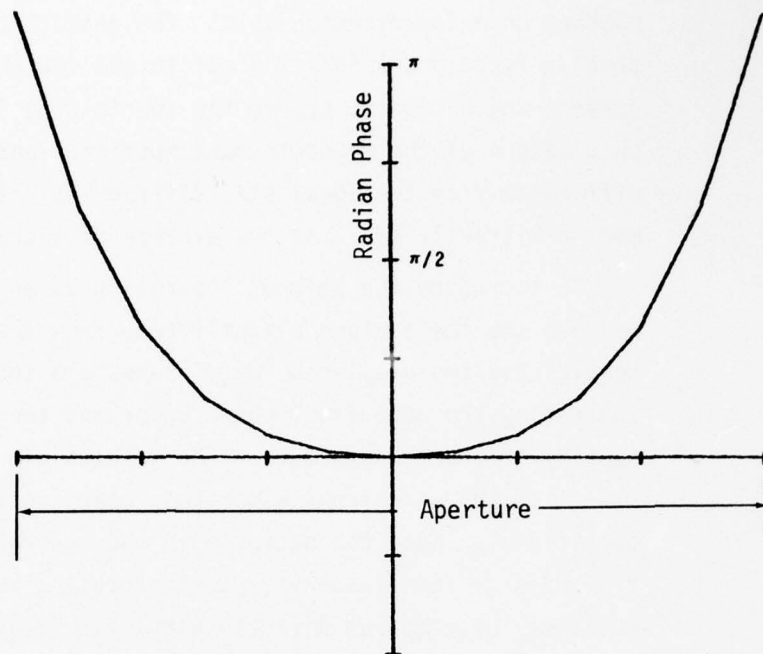
Diffraction Pattern
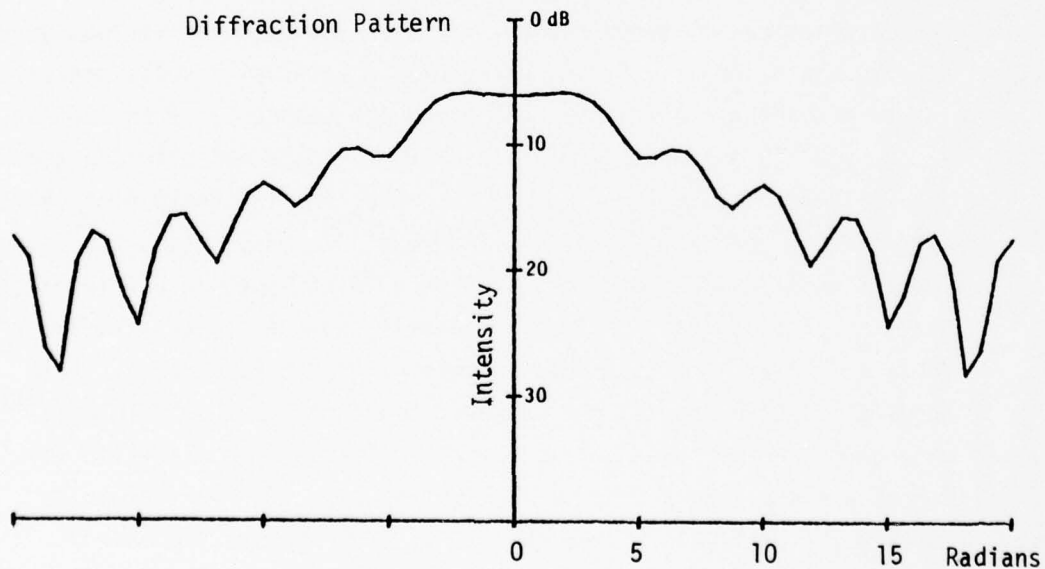
Figure 20. Wavefront Phase Error and Corresponding Intensity Diffraction Pattern for "Classic" Geodesic Lens Ray Traced in Figure 14 for Perfect Radial Profile Where the Image Plane Has Been Displaced by 1.0μ Yielding the Defocus Aberration.

47

diffraction pattern for the "classical" Luneburg lens at the focus plotted on a logarithmic scale. The pattern is identical to the $sinc^2 x$ functions (sin^2x/x^2) out to the fourth side lobe. The difference which results beyond the fourth side lobe is due to the periodic nature of the discrete fast Fourier transform algorithm. The difference from the ideal sinc diffraction pattern can likewise be made arbitrarily small at the expense of increased computational time.

To introduce the defocus aberration in an otherwise perfect system, we move the image plane slightly away from the edge of the lens. The results for two displaced image planes are shown in Figures 19 and 20 indicating the wave front phase error and the resulting defocused intensity diffraction pattern. The results are as expected which indicate that the wave front algorithm, starting from the ray trace, is operational. Note the decrease in the central peak intensity and the rise of side lobe imagery as the defocusing is increased. These results may be compared directly with experiments (see Figures 68 and 69) and the microwave literature.[40]

This numerical ray tracing procedure, which allows determination of the ray intercepts, the wave front phase error and the intensity diffraction pattern, as verified for the classic Luneburg lens yielding diffraction-limiting results, has been employed for various generalized Luneburg lenses. First, using Boyd's paraxial results contained in the preceding effort, "Optical Waveguide Lenses I," AFAL TR76-54, (Figure 36), a best-fit simulation of Boyd's data was obtained for a generalized Luneburg lens f-number 2. The lens thickness profile was simulated by $cosine^{0.18}$, $cos^{0.211}$ and $cos^{0.25}$. Ray traces for each of these simulations are depicted in Figure 10 of Appendix E which suggests that the profile $cos^{0.211}$ is a reasonable representation yielding a good focus so far as it is possible to determine from ray traces. This best-fit focused generalized Luneburg lens thickness profile ($cos^{0.211}$) was used as a reference for tolerance analysis. The resulting ray traces are depicted in Figure 21, Section (a). The ray traces in Section (b) of Figure 21 are the result of a uniform increase of thickness by 10 percent as may be obtained by increasing the deposition time. Note that the increased thickness results in a shorter focal length and the onset of spherical aberration because the marginal rays

48
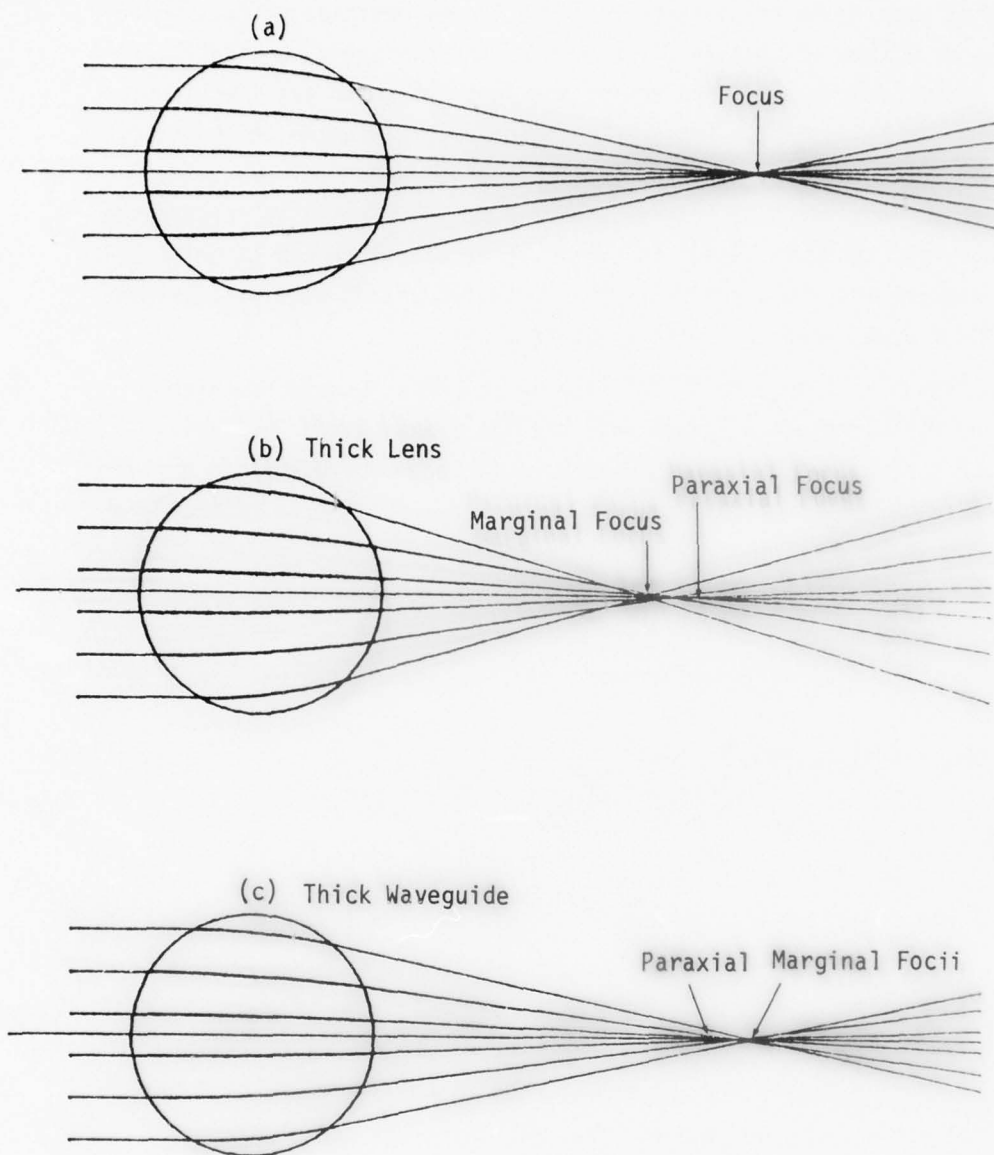
Figure 21. Comparison of Computer Ray Traces for Luneburg Lens With f-Number of 2 for Refractive Index Profile $\cos^{0.211}$ Where (a) Thicknesses are Correct, (b) the Lens Thickness Has Been Increased by 10 Percent and (c) Underlying Waveguide Thickness Has Been Increased by 10 Percent.

focus at even a shorter length. The ray traces depicted in Section (c) of Figure 21 are the result of increasing the ambient waveguide thickness by 10 percent without altering the lens thickness profile, i.e., Section (a). These ray traces for an increased waveguide thickness show an increased focal length and the onset of spherical aberration by further increasing of the marginal ray focus. Thus, the performance of thin-film Luneburg lenses is sensitive to the thickness of both the lens and ambient waveguide. Errors of the deposition time will affect the focal length and the onset of aberrations.

Although the use of $\cos^{0.211}$ profile yields a focused ray trace, this profile simulation is not sufficiently exact to obtain a well-defined diffraction pattern. Therefore, it became necessary to derive more exact expressions for the refractive index profile of generalized Luneburg lenses. We extended the work of Morgan[38] and Luneburg[37] which is fully delineated in Appendix F by Southwell entitled, "Index and Waveguide Thickness Profiles for Generalized Luneburg Lenses." The normalized index profile is given in terms of a transcendental equation

$$n/n_0 = \exp[\omega(\rho,S)], \tag{31}$$

where

$$\omega(\rho,S) = p_1(1-\rho)^{1/2} + p_2(1-\rho)^{3/2} + p_3(1-\rho)^{5/2} + p_4(1-\rho)^{7/2} + p_5(1-\rho)^{9/2} \tag{32}$$

where $\rho=rn/r_0 n_0$ and where Morgan's parameter $S=2f=2F/r_0$. Eq. (32) is a parametric generalization of the data that has been tabulated in Morgan and in Appendix F with several additional significant figures. From these profiles, we generate the lens thickness profile in terms of waveguide parameters delineated in Section B.

Using this procedure, a series of figures have been generated for generalized Luneburg lenses having perfect and various types of defective profiles where the defects have been introduced as changes of the p_n parameter. Most of the data has been calculated for the s parameter value of 2 and several cases for 3 and 5 where the lens f-number is 1/2 of S.

These figures depict the overlay waveguide thickness profile for a standard set of waveguide parameters. An overlay lens of Ta_2O_5 having a refractive index $n_1=2.1$ has been assumed for all cases. The waveguide

50

effective refractive index has been assumed to be 1.535 for all cases which can be derived from a Corning 7059 thin film n_w=1.565 having a thickness t=1.0665μ using 0.9μ radiation. The substrate, in all cases, is SiO$_2$ having a refractive index of n_s=1.47.

Ray traces for each lens waveguide thickness profile is included in the figures together with the ray intercepts in the image plane where the ray intercept is defined in Figure 15. The ray trace intercept utilizes "x" marks corresponding to individual ray trace calculations to which a smooth curve has been fitted for subsequent calculation. Deviations from the abscissa represent the blur width in the image plane corresponding to the ray traces.

Together with each tabulation of generalized Luneburg lens parameters included in these figures is a companion set of figures containing wave front phase error and the corresponding intensity diffraction pattern. In certain cases, more than one wave front error and diffraction pattern is included. These additional figures represent adjustment of the image plane to obtain a better focus by inspection of the ray intercept slope.

Figures 22 and 23 illustrate the case for a perfect generalized Luneburg lens S=2 showing the overlay waveguide lens thickness profile, lens ray traces, ray intercepts, wave front phase error, and corresponding intensity diffraction pattern. Note that the intensity diffraction pattern is the expected sinc^2 x function which is nearly identical to Figure 18 except for the residual computational errors. Figure 24 utilizes the parameters in Figure 22 with an intentional shift of the image plane to depict the effect of defocusing in the same manner as Figure 19. This figure is included because it is representative of one experimental result discussed later.

The effect of altering the p parameters (p_1'=.95p_1, p_2'=.7p_2) so as to increase the lens thickness in the central zone (1/3) and decrease the lens thickness in the outer annular zone in the region of r/r_o=2/3 is illustrated in Figure 25. This type of defective profile can arise from an incorrectly shaped deposition mask. The wave front and corresponding diffraction pattern are illustrated in Figure 26. This type of profile defect is excessive

51

Overlay Waveguide Thickness Profile   PERFECT GENERALIZED LUNEBURG LENS

Overlay Lens Thickness (Microns)

Using Ta_2O_5 on 7059 Waveguide

0.2

0.1

0.0

0.0   0.5   1.0

Normalized Radius r/r_0

$S = 2$ $P_1 = .2356878353$
$P_2 = -.07475003583$
$P_3 = 6.728944762 \times 10^{-3}$
$P_4 = -5.14447054 \times 10^{-3}$
$P_5 = -9.892996612 \times 10^{-4}$

Lens Ray Traces

$+ \lambda f/D$

Blur Width

×—×—×—×—×—×—×—×—×|—×   ×—×—×—×—×—×—×—×—×—×—×|
|←————————Full Aperture|of Ray Traces————————→|

$- \lambda f/D$

Lens Overlay Ta_2O_5 $n_1 = 2.1$
Waveguide $n_{eff} = 1.535$
   Corning 7059 $n_w = 1.565$
   Thickness $t = 1.0665\mu$, $\lambda = 0.9\mu$
Substrate SiO_2 $n_s = 1.47$

Ray Trace Intercepts
in Image Plane

Figure 22. Tabulation of Generalized Luneburg Lens Parameters with
          Corresponding Overlay Waveguide Lens Thickness Radial Profile,
          Ray Traces through this Lens and the Intercept Error in the
          Image Plane (Perfect Luneburg Lens).

52

Phase Error in Pupil Plane

Diffraction Pattern

Figure 23. Wavefront Phase Error and Corresponding Intensity Diffraction
Pattern for Generalized Luneburg Lens Delineated in Figure 22
(Perfect Luneburg Lens).

53

Phase Error in Pupil Plane

Radian Phase

+ π

+ π/2

Aperture

- π/2

- π

Diffraction Pattern

0 dB

-10

-20

Intensity

-30

0   5   10   15   Radians

Figure 24. Wavefront Phase Error and Corresponding Intensity Diffraction Pattern for Generalized Luneburg Lens Delineated in Figure 22 (Perfect Luneburg Lens) Where Defocusing Has Been Introduced to Create a π/4 Phase Error Across the Aperture.

54

because it destroys the focus. Inspection of the ray trace intercept or wave front error suggests that stopping down the aperture to remove some marginal rays and refocusing will improve the diffraction pattern. Figure 27 contains the same type of defective profile, however, with a much less distortion, ($p_1'=.995p_1$, $p_2'=.997p_1$). The same characteristic wave front error shape is observed with a similar degradation of the diffraction pattern, both of which are less than that of Figure 26; however, of serious consequence. Therefore, the radial weighting is an important parameter to be determined by the deposition mask.

The effects of another type of defect in the overlay waveguide lens thickness profile is shown in Figures 28 and 29 where the zone in the region of $r/r_0=0.5$ is excessively thick ($p_1'=1.04p_1$, $p_4'=10p_4$). For this case, the desired single-lobed diffraction pattern at the focus is completely destroyed. Note that stopping down the lens will remove some marginal rays which contribute to the excessive blur width. Again, reducing this type of distortion by altering the p parameters ($p_1'=1.0004p_1$, $p_4'=1.1p_1$), similar wave front errors of lesser magnitude are observed in Figure 30 while the principal lobe is somewhat restored. Again, the radial weighting is an important parameter in determining the deposition mask shape.

We will now consider the case of an accurately shaped profile where the deposition time has been allowed to increase producing a uniform radial percentage error, thus, the p parameters are ($p_1'=1.02p_1$, $p_2'=1.02p_2$, $p_3'=1.02p_3$, and $p_4'=1.02p_4$). The resulting overlay waveguide thickness profile lens ray traces and ray trace intercept are depicted in Figure 31 with the resulting wave front error and intensity diffraction pattern depicted in Figure 32. The intensity diffraction pattern has been taken in the same position as in the previous distorted cases. Inspection of the ray trace intercept shows that the beam is defocused and, therefore, the image plane should be shifted. The effect of a lesser degree of overlay waveguide lens thickness percentage error is shown in Figures 33 and 34 ($p_1'=1.0002p_1$, $p_2'=1.0002p_2$, $p_3'=1.0002p_3$, and $p_4'=1.0002p_4$). Again, the

55

Overlay Waveguide Thickness Profile

GENERALIZED LUNEBURG LENS

S = 2

$P_1 = .2239034435$

$P_2 = -.052325025$

$P_3 = 6.728944762 \times 10^{-3}$

$P_4 = -5.14447054 \times 10^{-3}$

$P_5 = -8.39925916 \times 10^{-3}$

Perfect Profile

Defective Profile

Overlay Lens Thickness (Microns)

Using Ta_2O_5 on 7059 Waveguide

0.2

0.1

0.0

0.0   0.5   1.0

Normalized Radius r/r_0

Lens Ray Traces

Blur Width

$+ 300 \lambda f/D$

Full Aperture of Ray Traces

$- 300 \lambda f/D$

Lens Overlay Ta_2O_5 $n_1 = 2.1$

Waveguide $n_{eff} = 1.535$

Corning 7059 $n_w = 1.565$

Thickness $t = 1.0665\mu$, $\lambda = 0.9\mu$

Substrate SiO_2 $n_s = 1.47$

Ray Trace Intercepts in Image Plane

Figure 25. Tabulation of Generalized Luneburg Lens Parameters with Corresponding Overlay Waveguide Lens Thickness Radial Profile, Ray Traces through this Lens and the Intercept Error in the Image Plane (.95 P_1, .7 P_2, 8.4901 P_5).

56

Phase Error in Pupil Plane

Diffraction Pattern

Fourier Transform Sampling
Error May Be Present

Figure 26. Wavefront Phase Error and Corresponding Intensity Diffraction
Pattern for Generalized Luneburg Lens Delineated in Figure 25

57

Phase Error in Pupil Plane

GENERALIZED LUNEBURG LENS

$S = 2$ $P_1 = .2355699914$
         $P_2 = -.0745257856$
         $P_3 = 6.728944762 \times 10^{-3}$
         $P_4 = -5.14447054 \times 10^{-3}$
         $P_5 = 1.063399332 \times 10^{-3}$

Diffraction Pattern

Figure 27. Wavefront Phase Error and Corresponding Intensity Diffraction Pattern for Generalized Luneburg Lens Delineated in Figure 25 (.9995 P_1, .997 P_2, -1.0749 P_5).

58

same shape wave front phase error is observed with substantially less distortion while the diffraction pattern is diffused and the principal lobe identifiable. Inspection of the ray trace intercept shows that the beam is defocused and, therefore, the image plane should be shifted. This has been done for Figure 34 by reducing the focal length 4μ. The resulting refocused wave front phase error and diffraction pattern correspond to the results of the idealized profile as exemplified in Figure 23.

Figures 31 through 34 are applicable to lens thickness profiles having uniform percentage increase or a uniform thickness decrease of the underlying waveguide. The following five figures are applicable to overlay waveguide thickness profiles having a uniform percentage less than the perfect profile or due to the underlying waveguide having an excessive thickness. Figures 35 and 36 are applicable for the p parameters ($p_1'=.98p_1$, $p_2'=.98p_2$, $p_3'=.98p_3$, and $p_4'=.98p_4$). Note that the ray intercept and wave front phase error indicate the opposite effects to that in the preceding four figures. Inspection of the ray intercept plot and wave front phase error suggests movement of the image plane to obtain re-focusing. This has been done in Figure 37 by increasing the focal length 375μ. This refocusing has substantially reduced the quadratic wave front distortion and defocusing to a somewhat excessive length leaving higher order spatial phase errors.

Reduction of the uniform distortion in the same manner as before for p parameters ($p_1'=.9998p_1$, $p_2'=.9998p_2$, $p_3'=.9998p_3$, and $p_4'=.9998p_4$) yields the wave front error and diffraction pattern shown in Figure 38. In-spection of the ray intercept plot shows that the image plane should be repositioned. This has been done and the result illustrated in Figure 39 by increasing the focal length 4μ. The result is, thus, identical to the perfect profile shown in Figure 23 and the refocused profile shown in Figure 34. Thus far, these results indicate that the focal length may be adjusted by altering the waveguide thickness or the deposition time through a mask having the shape capable of producing the correct profile.

59

Overlay Waveguide Thickness Profile GENERALIZED LUNEBURG LENS

Overlay Lens Thickness (Microns)

Using Ta_2O_5 on 7059 Waveguide

0.2

0.1

0.0

Perfect Profile

Defective Profile

0.0   0.5   1.0

Normalized Radius r/r_0

$S = 2$

$P_1 = .2451153437$

$P_2 = -.07475003583$

$P_3 = 6.728944762 \times 10^{-3}$

$P_4 = -5.14447054 \times 10^{-2}$

$P_5 = .0358834217$

Lens Ray Traces

Blur Width

$+ 300\lambda f/D$

Full Aperture of Ray Traces

$- 300\lambda f/D$

Ray Trace Intercepts
in Image Plane

Lens Overlay Ta_2O_5 $n_1 = 2.1$

Waveguide $n_{eff} = 1.535$

Corning 7059 $n_w = 1.565$

Thickness $t = 1.0665\mu$, $\lambda = 0.9\mu$

Substrate SiO_2 $n_s = 1.47$

Figure 28. Tabulation of Generalized Luneburg Lens Parameters with
Corresponding Overlay Waveguide Lens Thickness Radial
Profile, Ray Traces through this Lens and the Intercept
Error in the Image Plane $(1.04\ P_1,\ 10\ P_4, -36.2715\ P_5)$.

60

Phase Error in Pupil Plane

Diffraction Pattern
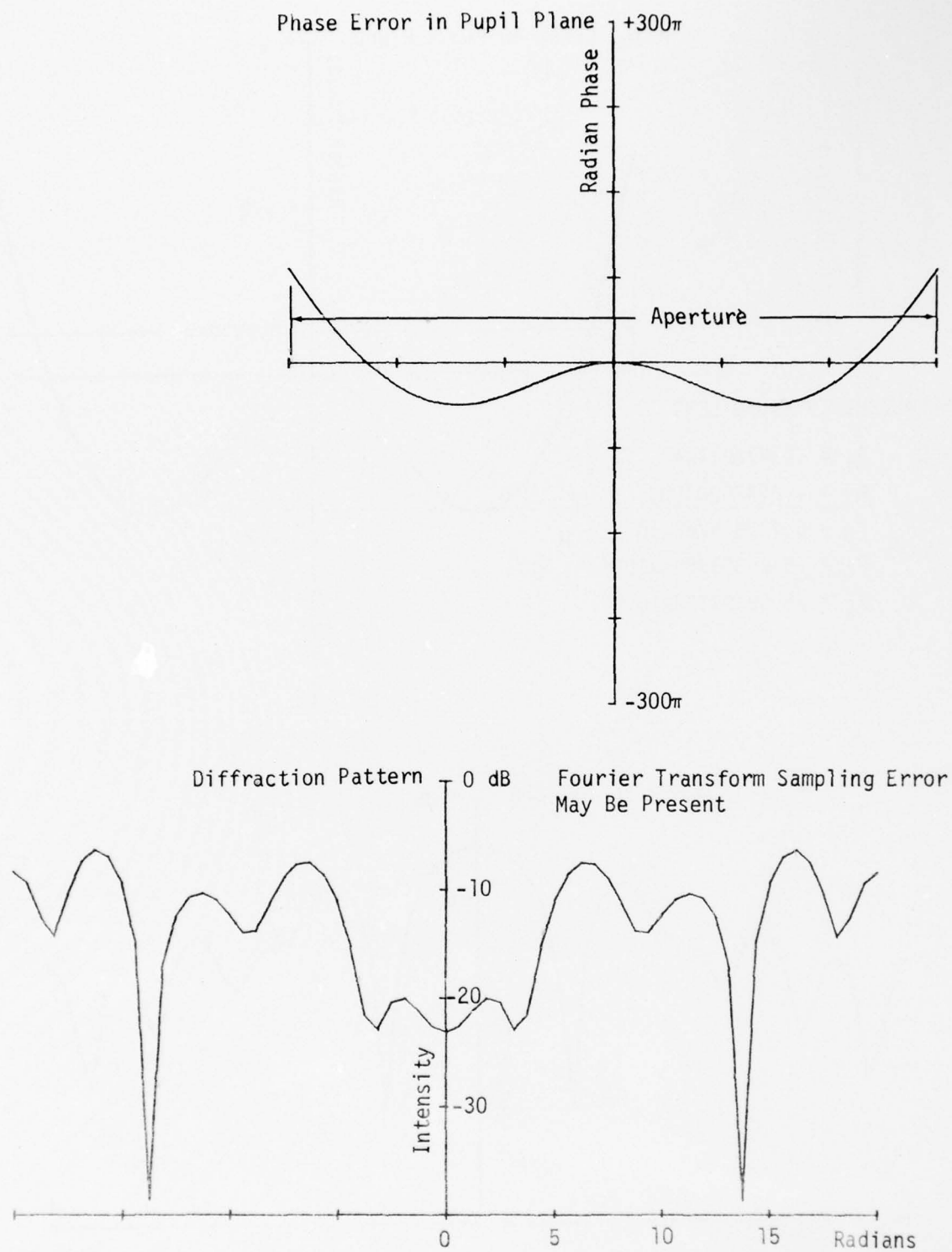
Figure 29. Wavefront Phase Error and Corresponding Intensity Diffraction
Pattern for Generalized Luneburg Lens Delineated in Figure 28

61

Phase Error in Pupil Plane

Radian Phase

+ π

+ π/2

Aperture

- π/2

- π

GENERALIZED LUNEBURG LENS

$S = 2$ $P_1 = .2357821104$

$P_2 = -.07475003583$

$P_3 = 6.728944762 \times 10^{-3}$

$P_4 = -5.658917594 \times 10^{-3}$

$P_5 = -5.69127768 \times 10^{-4}$

Diffraction Pattern   0 dB

-10

Intensity

-20

-30

0   5   10   15   Radians

Figure 30. Wavefront Phase Error and Corresponding Intensity Diffraction
Pattern for Generalized Luneburg Lens Delineated in Figure 28
$(1.0004 \ P_1, \ 1.1 \ P_4, \ .5752 \ P_5)$.

62

Another type of defective profile considered employs a central zone (1/2) of reduced thickness and an outer zone in the region of $r/r_0=3/4$ of increased thickness by lesser value is illustrated in Figures 40 and 41 for the p parameters ($p_1'=1.05p_1$, $p_2'=1.35p_1$). This type of distortion is similar to that of Figures 25 and 26, however, producing the opposite effects.

Similarly, Figures 42 and 43 having the opposite zonal distortion to that of Figures 28 and 29 are illustrated in Figures 42 and 43 for the p parameters ($p_1'=.96p_1$, $p_4'=-10p_4$). Similarly, this type of defect has been reduced using the p parameter ($p_1'=0.996p_1$, $p_4'=-1.1p_4$) which corresponds to the opposite effect of Figure 44, however, in each of these cases, producing ill-defined single lobe diffraction pattern. Thus, for each of the cases involving zonal distortions of the ideal profile, severe aberrations occur which destroy the desired single-lobed well-defined diffraction pattern inherent from perfect profiles. All of the above data has pertained to a generalized Luneburg lens with s=2.

The overlay waveguide lens thickness profile, lens ray traces, ray intercepts, wave front phase error, and intensity diffraction pattern for a perfect generalized Luneburg lens having s=3 is depicted in Figures 45 and 46. Similarly, for the perfect generalized Luneburg lens having s=5, the results are depicted in Figures 47 and 48. Introduction of defects in these latter longer focal length lenses has not been executed. However, the trends indicated for the s=2 case should carry over.

Some of the diffraction patterns contain the note that an error may be present due to the Fourier transform sampling. The transform as implemented to derive these figures has utilized 64 "data" points to economize the computational time. Therefore, when the wavefront phase error fluctuates through wide excursions, the sampling error may distort the diffraction pattern. This is not considered a handicap because such large phase errors do not usually produce a well-defined principle lobe diffraction pattern. An improvement could be obtained with additional

Overlay Waveguide Thickness Profile   GENERALIZED LUNEBURG LENS

Overlay Lens Thickness (Microns)

Using Ta_2O_5 on 7059 Waveguide

0.2

Perfect Profile

Defective Profile

0.1

0.0

0.0   0.5   1.0

Normalized Radius r/r_o

$S = 2$

$P_1 = .240401592$
$P_2 = -.0762450365$
$P_3 = 6.863523657 \times 10^{-3}$
$P_4 = -5.247359951 \times 10^{-3}$
$P_5 = -1.009085654 \times 10^{-3}$

Lens Ray Traces

$+ 300\lambda f/D$ Blur Width

Full Aperture of Ray Traces

$- 300 \lambda f/D$

Ray Trace Intercepts
in Image Plane

Lens Overlay Ta_2O_5 $n_1 = 2.1$
Waveguide $n_{eff} = 1.535$
    Corning 7059 $n_w = 1.565$
    Thickness $t = 1.0665\mu$, $\lambda = 0.9\mu$
Substrate SiO_2 $n_s = 1.47$

Figure 31. Tabulation of Generalized Luneburg Lens Parameters with
Corresponding Overlay Waveguide Lens Thickness Radial
Profile, Ray Traces through this Lens and the Intercept
Error in the Image Plane ($1.02 P_1$, $1.02 P_2$, $1.02 P_3$,
$1.02 P_4$, $1.02 P_5$).

64
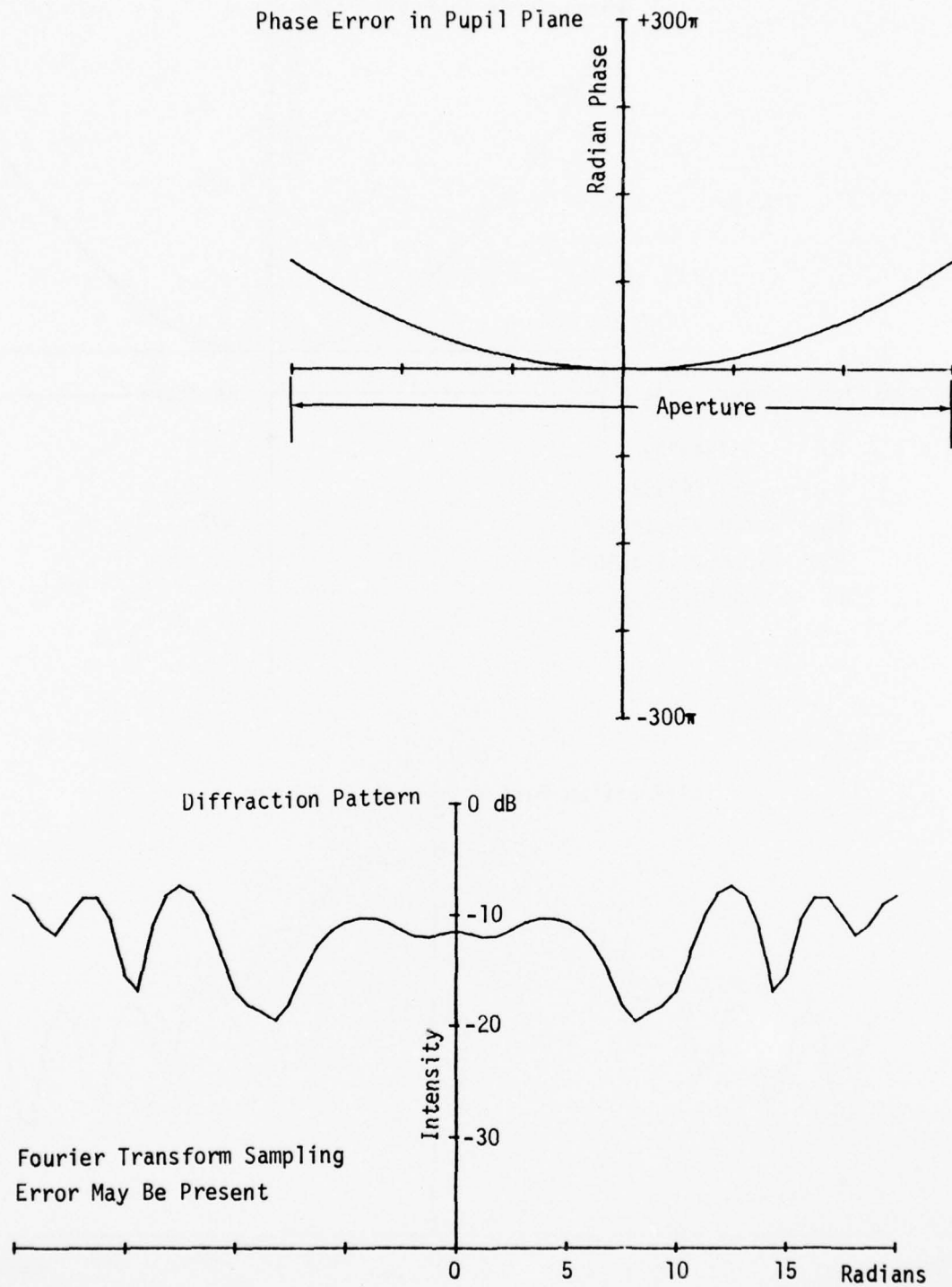
Figure 32. Wavefront Phase Error and Corresponding Intensity Diffraction Pattern for Generalized Luneburg Lens Delineated in Figure 31

Phase Error in Pupil Plane

Radian Phase

$+ \pi$

$+ \pi/2$

Aperture

$- \pi/2$

$- \pi$

GENERALIZED LUNEBURG LENS

$S = 2$ $P_1 = .2357349729$

$P_2 = -.0747649858$

$P_3 = 6.730290551 \times 10^{-3}$

$P_4 = -5.145499434 \times 10^{-3}$

$P_5 = -9.894975211 \times 10^{-4}$

Diffraction Pattern   0 dB

-10

-20

Intensity

-30

0   5   10   15   Radians
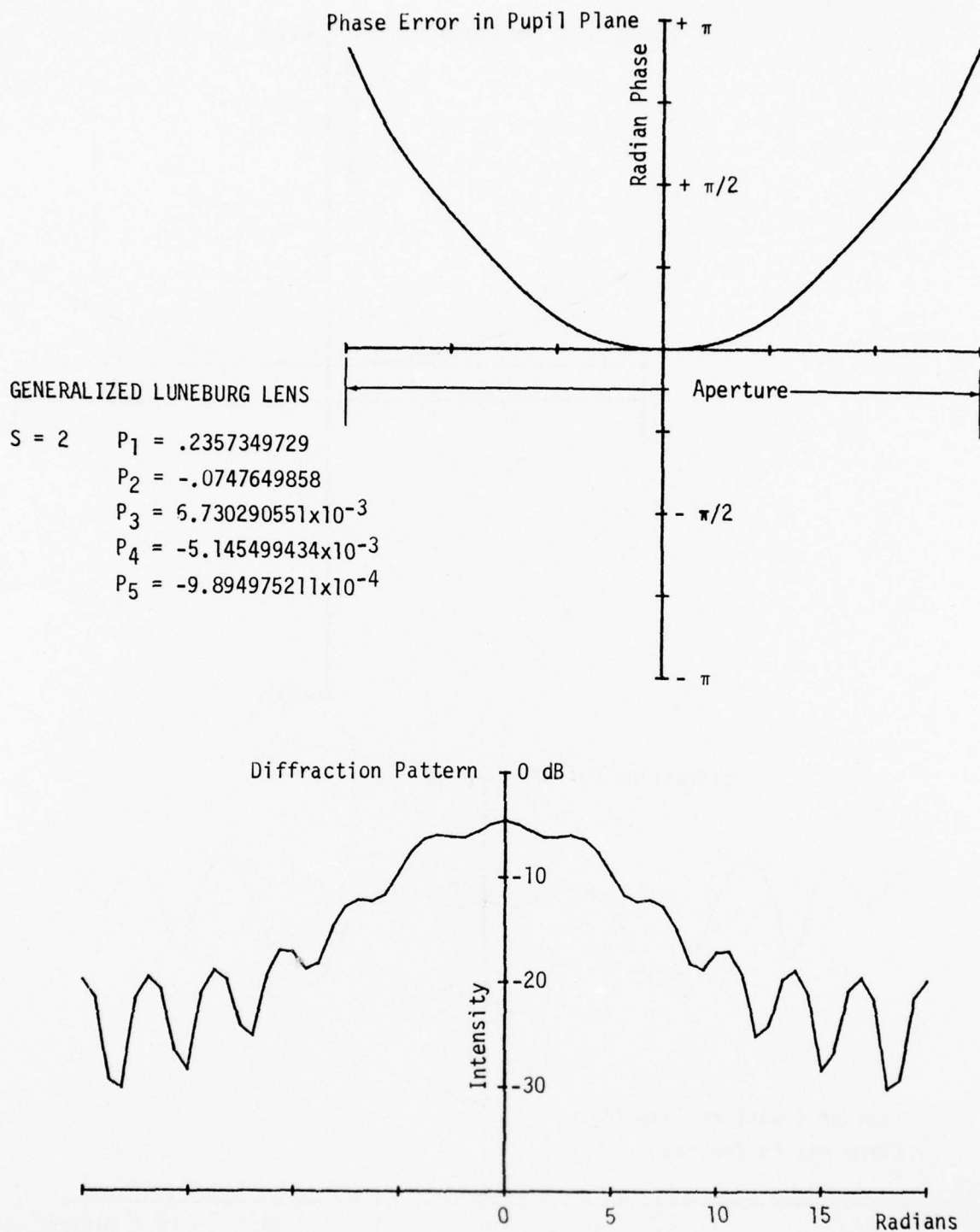
Figure 33.   Wavefront Phase Error and Corresponding Intensity Diffraction
Pattern for Generalized Luneburg Lens Delineated in Figure 31
$(1.0002\ P_1,\ 1.0002\ P_2,\ 1.0002\ P_3,\ 1.0002\ P_4,\ 1.0002\ P_5)$.

66

Phase Error in Pupil Plane

Radian Phase

$+ \pi$

$+ \pi/2$

Aperture

$- \pi/2$

$- \pi$

GENERALIZED LUNEBURG LENS

$S = 2$ $P_1 = .2357349729$

$P_2 = -.0747649858$

$P_3 = 6.730290551 \times 10^{-3}$

$P_4 = -5.145499434 \times 10^{-3}$

$P_5 = -9.894975211 \times 10^{-4}$

Refocused Diffraction Pattern

0 dB

-10

-20

Intensity

-30

0   5   10   15   Radians
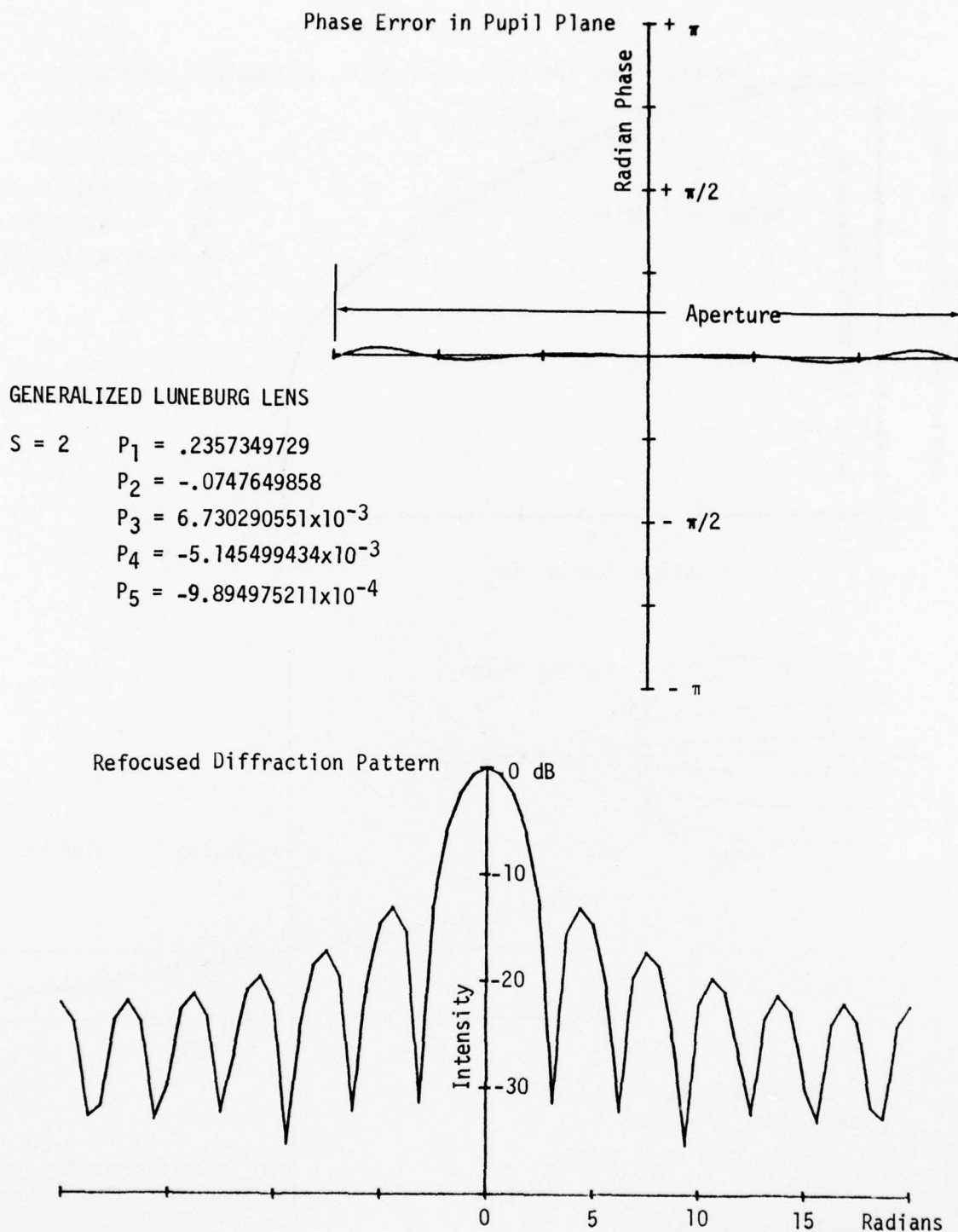
Figure 34. Wavefront Phase Error and Corresponding Intensity Diffraction
Pattern for Generalized Luneburg Lens Delineated in Figure 31
$(1.0002 \ P_1, 1.0002 \ P_2, 1.0002 \ P_3, 1.0002 \ P_4, 1.0002 \ P_5)$,
New Focal Length -4μ.

67

Overlay Waveguide Thickness Profile   GENERALIZED LUNEBURG LENS

Overlay Lens Thickness (Microns)

Using Ta$_2$O$_5$ on 7059 Waveguide

0.2

0.1

0.0

Perfect Profile

Defective Profile

S = 2   P$_1$ = .2309740786

P$_2$ = -.073255035

P$_3$ = 6.594365867x10^{-3}

P$_4$ = -5.041581129x10^{-3}

P$_5$ = -9.69513668x10^{-4}

0.0   0.5   1.0

Normalized Radius r/r$_0$

Lens Ray Traces

+ 300λf/D   Blur Width

Full Aperture of Ray Traces

- 300λf/D

Ray Trace Intercepts
in Image Plane

Lens Overlay Ta$_2$O$_5$ n$_1$ = 2.1
Waveguide n$_{eff}$ = 1.535
    Corning 7059 n$_w$ = 1.565
    Thickness t = 1.0665μ, λ = 0.9μ
Substrate SiO$_2$ n$_s$ = 1.47

Figure 35. Tabulation of Generalized Luneburg Lens Parameters with
           Corresponding Overlay Waveguide Lens Thickness Radial
           Profile, Ray Traces through this Lens and the Intercept
           Error in the Image Plane (.98 P$_1$, .98 P$_2$, .98 P$_3$, .98 P$_4$,
           .98 P$_5$).

68
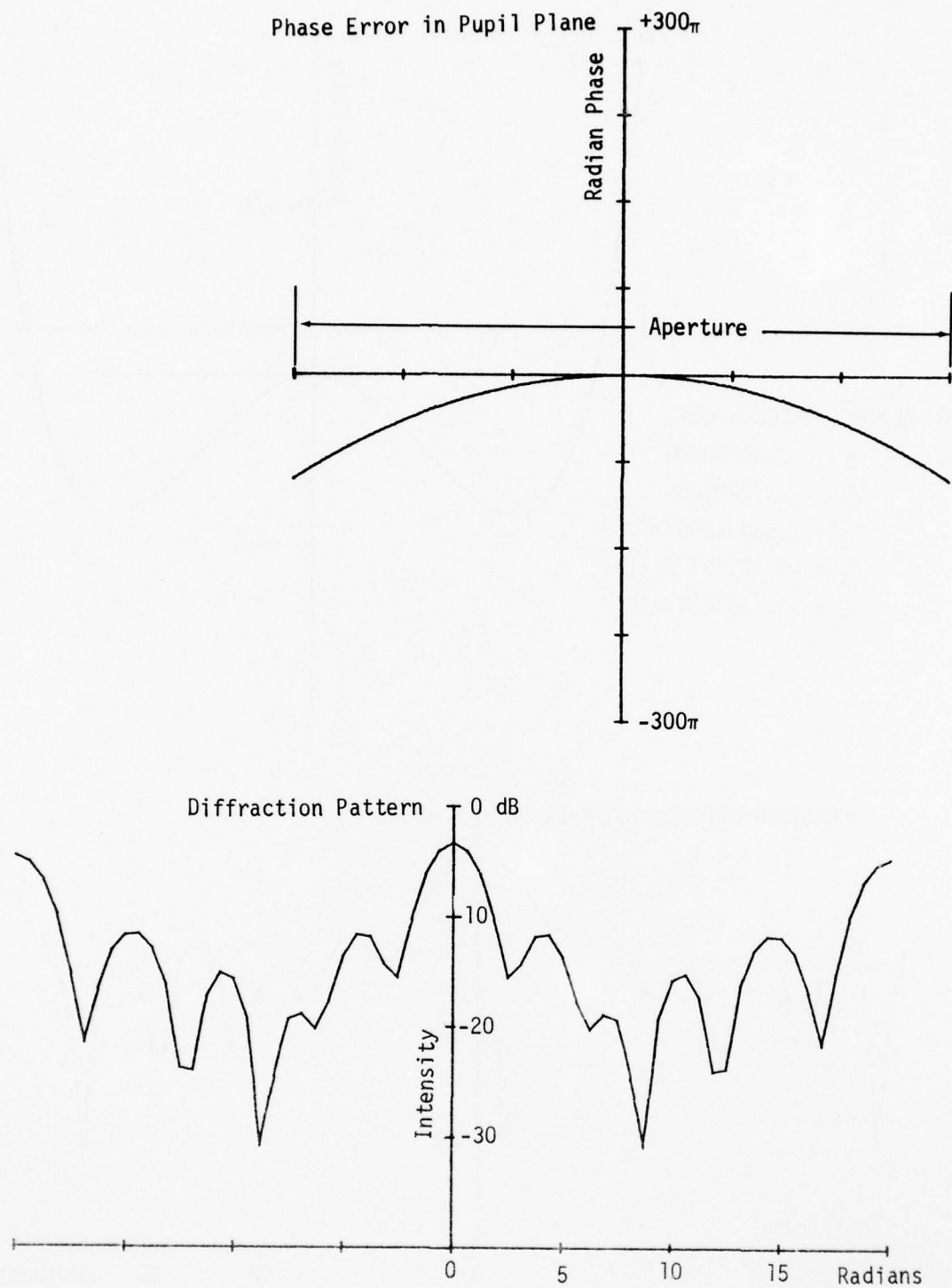
Figure 36. Wavefront Phase Error and Corresponding Intensity Diffraction Pattern for Generalized Luneburg Lens Delineated in Figure 35.

69

Phase Error in Pupil Plane

GENERALIZED LUNEBURG LENS

$S = 2$ $P_1 = .2309740786$

$P_2 = -.073255035$

$P_3 = 6.594365867 \times 10^{-3}$

$P_4 = -5.041581129 \times 10^{-3}$

$P_5 = -9.69513668 \times 10^{-4}$

Refocused Diffraction Pattern
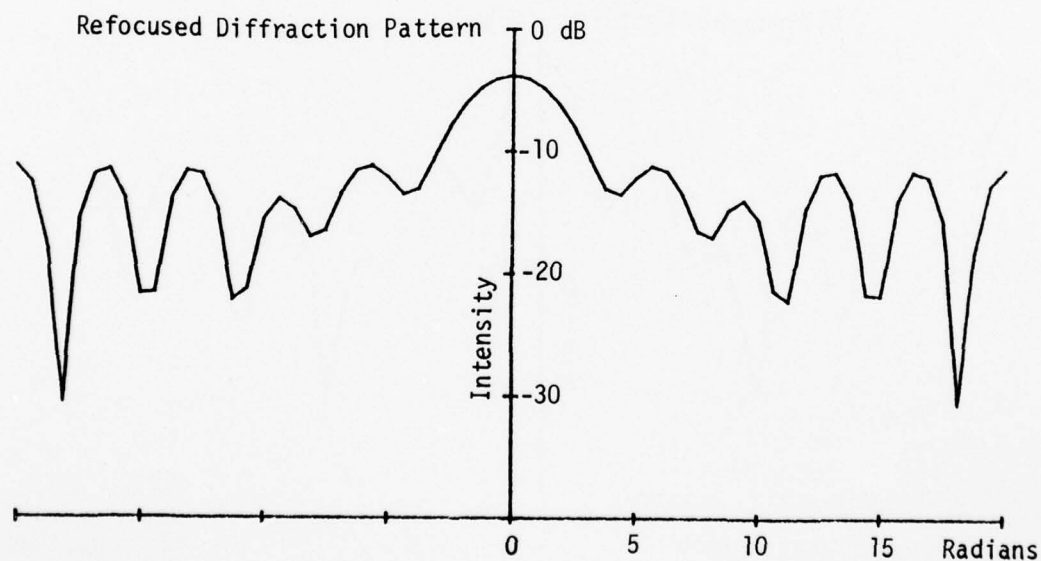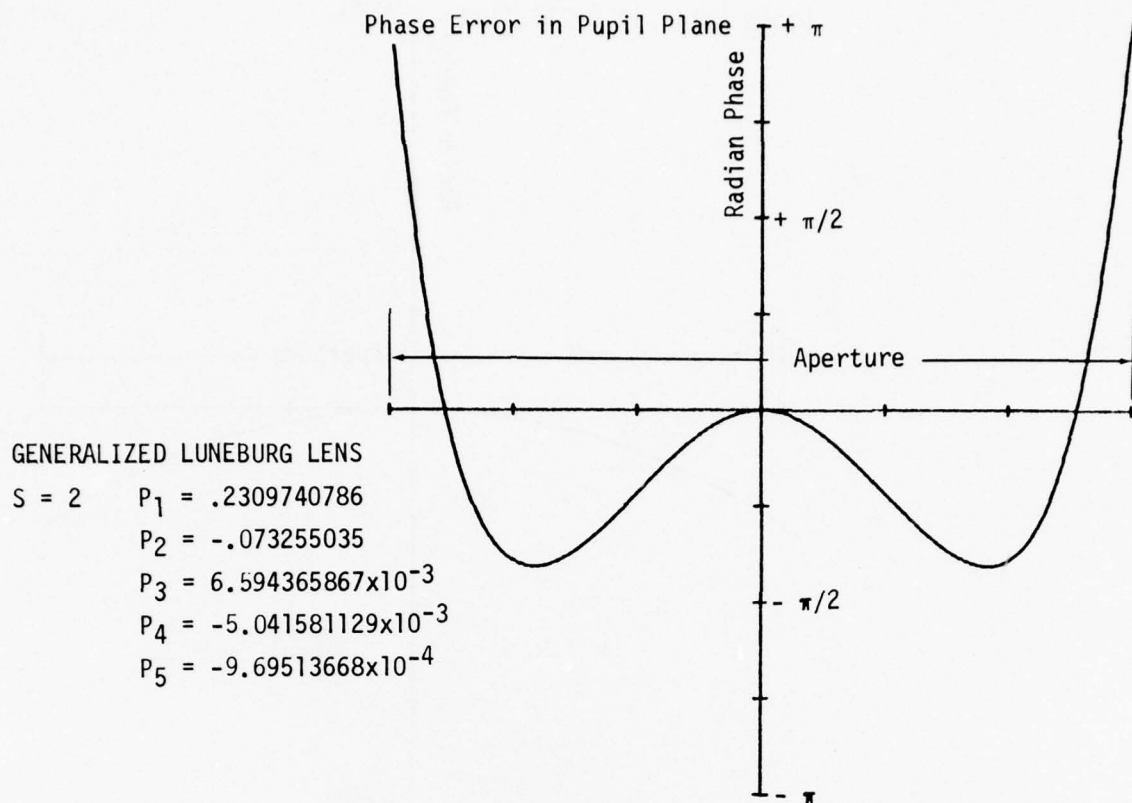
Figure 37. Wavefront Phase Error and Corresponding Intensity Diffraction Pattern for Generalized Luneburg Lens Delineated in Figure 35 (.98 P_1, .98 P_2, .98 P_3, .98 P_4, .98 P_5), New Focal Length +375μ.

70

Phase Error in Pupil Plane

GENERALIZED LUNEBURG LENS

$S = 2$ $P_1 = .2356406977$

$P_2 = .0747350857$

$P_3 = 6.727598973 \times 10^{-3}$

$P_4 = -5.143441646 \times 10^{-3}$

$P_5 = -9.891018013 \times 10^{-4}$

Radian Phase

$+ \pi$

$+ \pi/2$

Aperture

$- \pi/2$

$- \pi$

Diffraction Pattern

0 dB

-10

-20

-30

Intensity

0   5   10   15   Radians
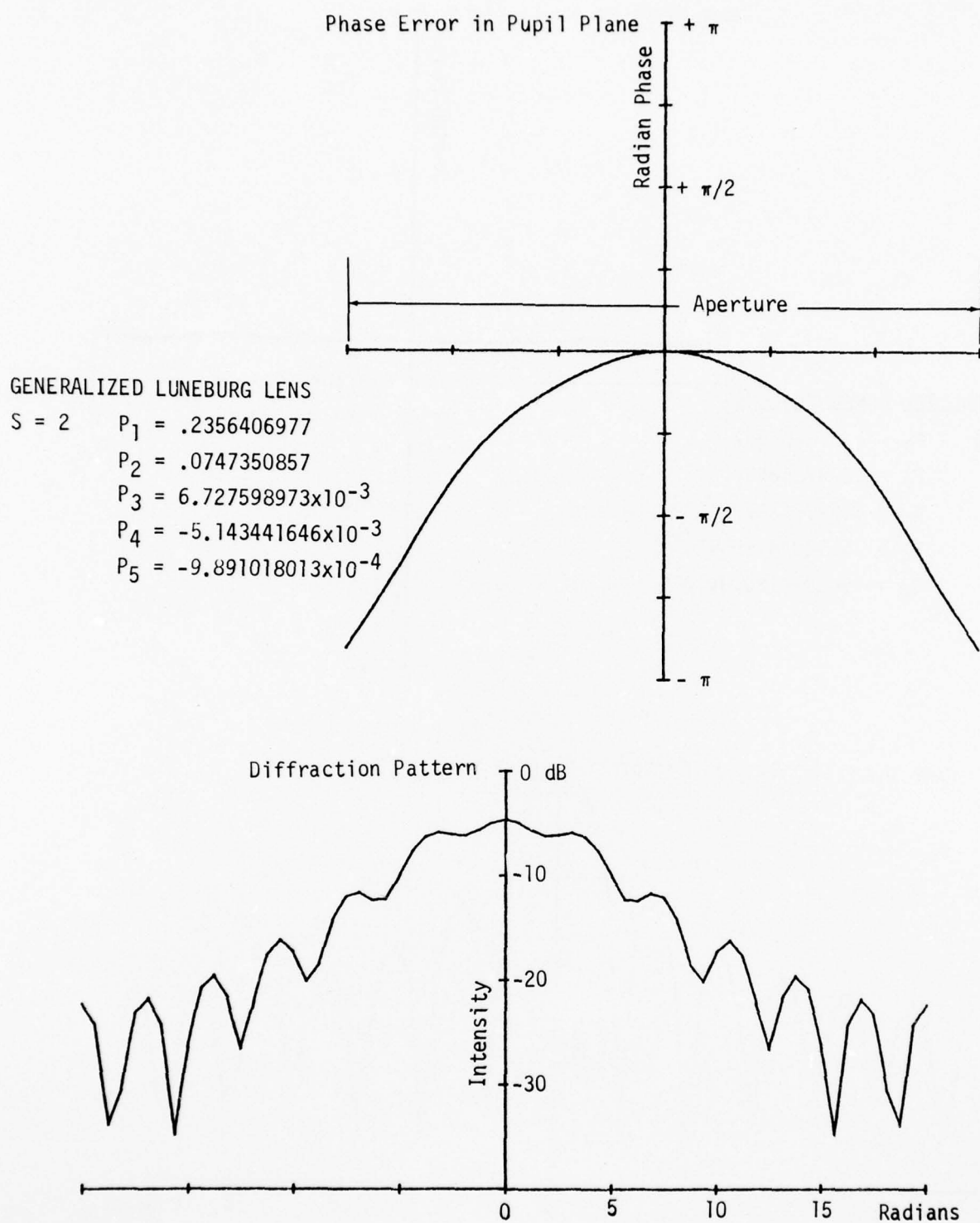
Figure 38. Wavefront Phase Error and Corresponding Intensity Diffraction
Pattern for Generalized Luneburg Lens Delineated in Figure 35
(.9998 P_1, .9998 P_2, .9998 P_3, .9998 P_4, .9998 P_5).

71

Phase Error in Pupil Plane

Radian Phase

$+ \pi$

$+ \pi/2$

GENERALIZED LUNEBURG LENS

Aperture

S = 2 P_1 = .2356406977

P_2 = .0747350857

P_3 = $6.727598973 \times 10^{-3}$

P_4 = $-5.143441696 \times 10^{-3}$

P_5 = $-9.891018013 \times 10^{-4}$

$- \pi/2$

$- \pi$

Refocused Diffraction Pattern

0 dB

-10

-20

Intensity

-30

0   5   10   15   Radians
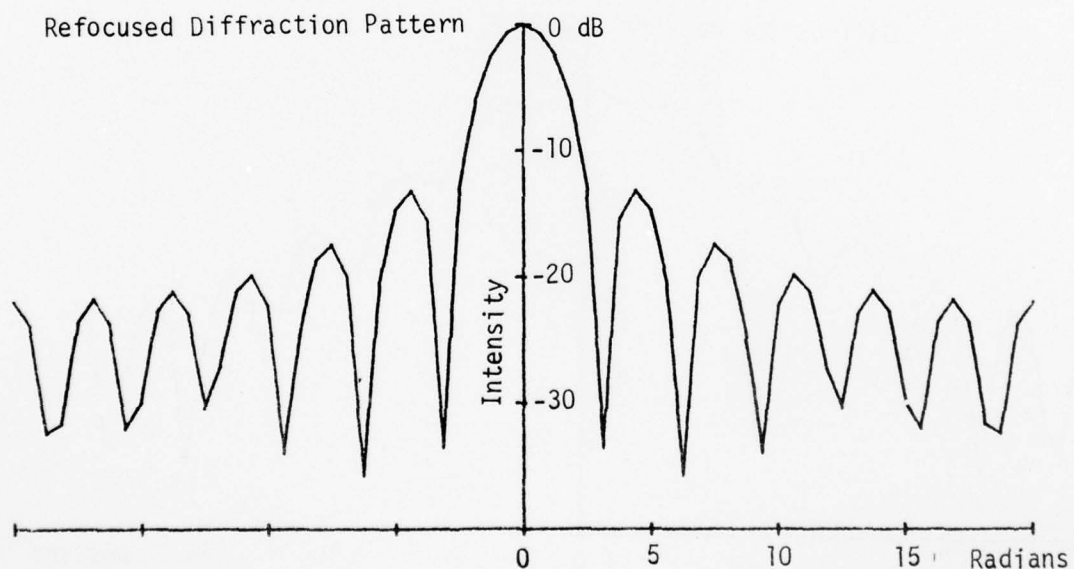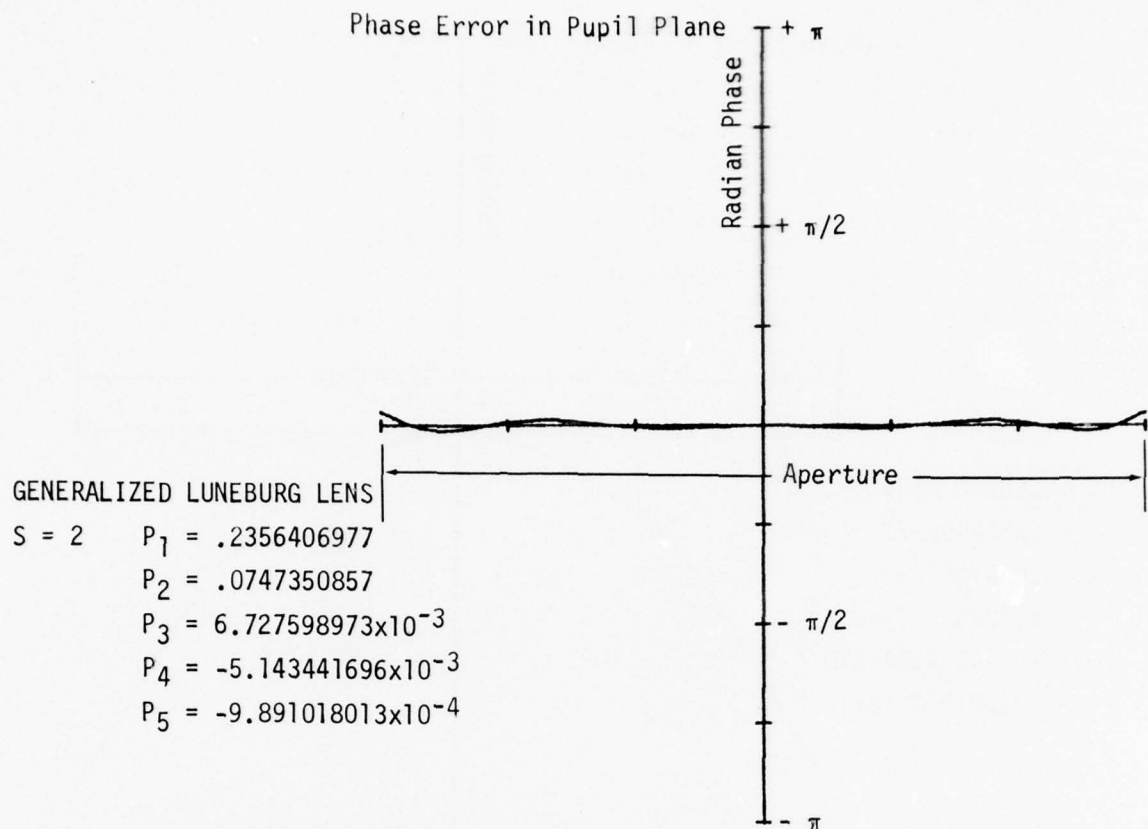
Figure 39. Wavefront Phase Error and Corresponding Intensity Diffraction
Pattern for Generalized Luneburg Lens Delineated in Figure 35
(.9998 P_1, .9998 P_2, .9998 P_3, .9998 P_4, .9998 P_5),New Focal
Length +4μ.

72

data points at the expense of additional computational time. It should be remembered that these computations are based upon only 19 ray traces through the lens and that the resulting transform computations are based upon a curve-fit for these data points.

An error analysis of these lenses could be performed utilizing established techniques deriving the optical transfer function or modulation transfer function as currently utilized for characterizing the performance of lens systems used with incoherent radiation. It would require an extension to include consideration for coherent radiation, however, the above procedure is considered more direct and exact (within the computational time allowed). It provides the intensity diffraction pattern starting with thin-film waveguide radial profiles, each of which are experimentally determinable factors relating the analysis with measured lens performance in its ultimate application, the optical Fourier transform "chip". The data presented has incorporated various types of error perturbations in the ideal radial profile. It has indicated the type of errors allowed and correctable by refocusing and the errors which may be compensated by apodization or limiting of the useful aperture. Some further effort is required to more accurately refine the deposition process so that the radial waveguide thickness profile may be more closely matched to the ideal profile. It should be remembered that this match must be solved by each lens having different focal lengths.

Overlay Waveguide Thickness Profile GENERALIZED LUNEBURG LENS

Perfect Profile

Defective Profile

$S = 2$ $P_1 = .2474722271$
$P_2 = -.1009125483$
$P_3 = 6.728944762 \times 10^{-3}$
$P_4 = -5.14447054 \times 10^{-3}$
$P_5 = .0101581614$

Overlay Lens Thickness (Microns)

Using Ta_2O_5 on 7059 Waveguide

0.2

0.1

0.0

0.0   0.5   1.0

Normalized Radius r/r_o

Lens Ray Traces

Blur Width

$+ 300\lambda f/D$

Full Aperture of Ray Traces

Lens Overlay Ta_2O_5 $n_1 = 2.1$
Waveguide $n_{eff} = 1.535$
   Corning 7059 $n_w = 1.565$
      Thickness $t = 1.0665\mu$, $\lambda = 0.9\mu$
Substrate SiO_2 $n_s = 1.47$

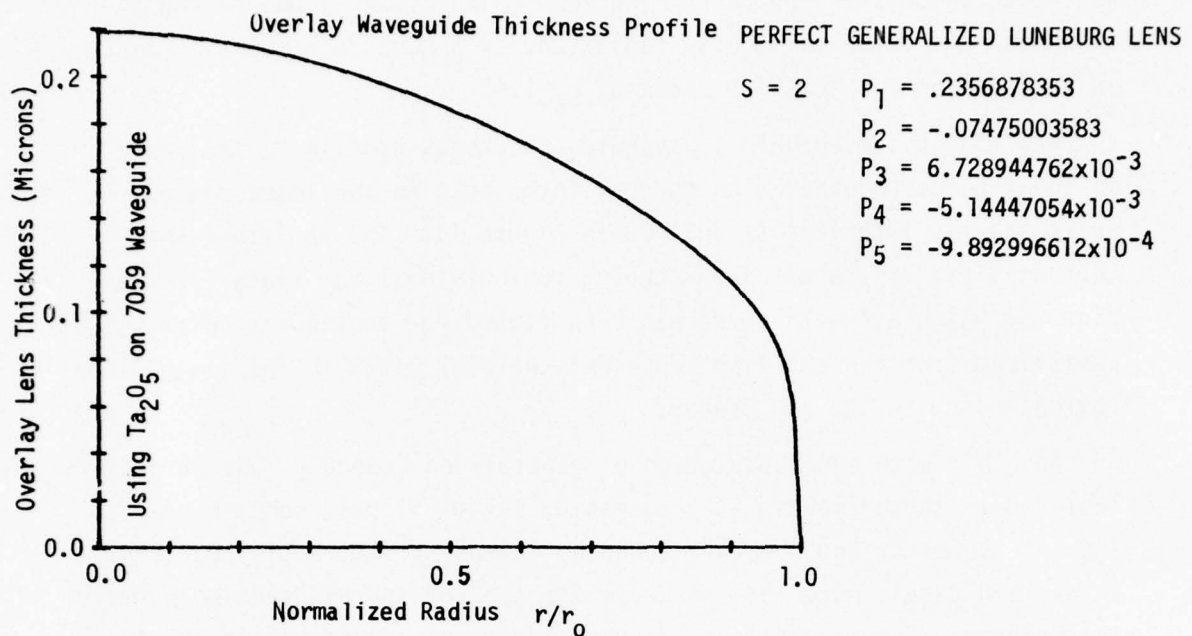Ray Trace Intercepts
in Image Plane

Figure 40. Tabulation of Generalized Luneburg Lens Parameters with
           Corresponding Overlay Waveguide Lens Thickness Radial
           Profile, Ray Traces through this Lens and the Intercept
           Error in the Image Plane ($1.05 P_1$, $1.35 P_2$, P_3, P_4, $10.2680 P_5$).

74

Phase Error in Pupil Plane $+300\pi$

Radian Phase

Aperture

-300π

Diffraction Pattern   0 dB

Intensity

-20

-30

Fourier Transform Sampling
Error May Be Present

0   5   10   15   Radians
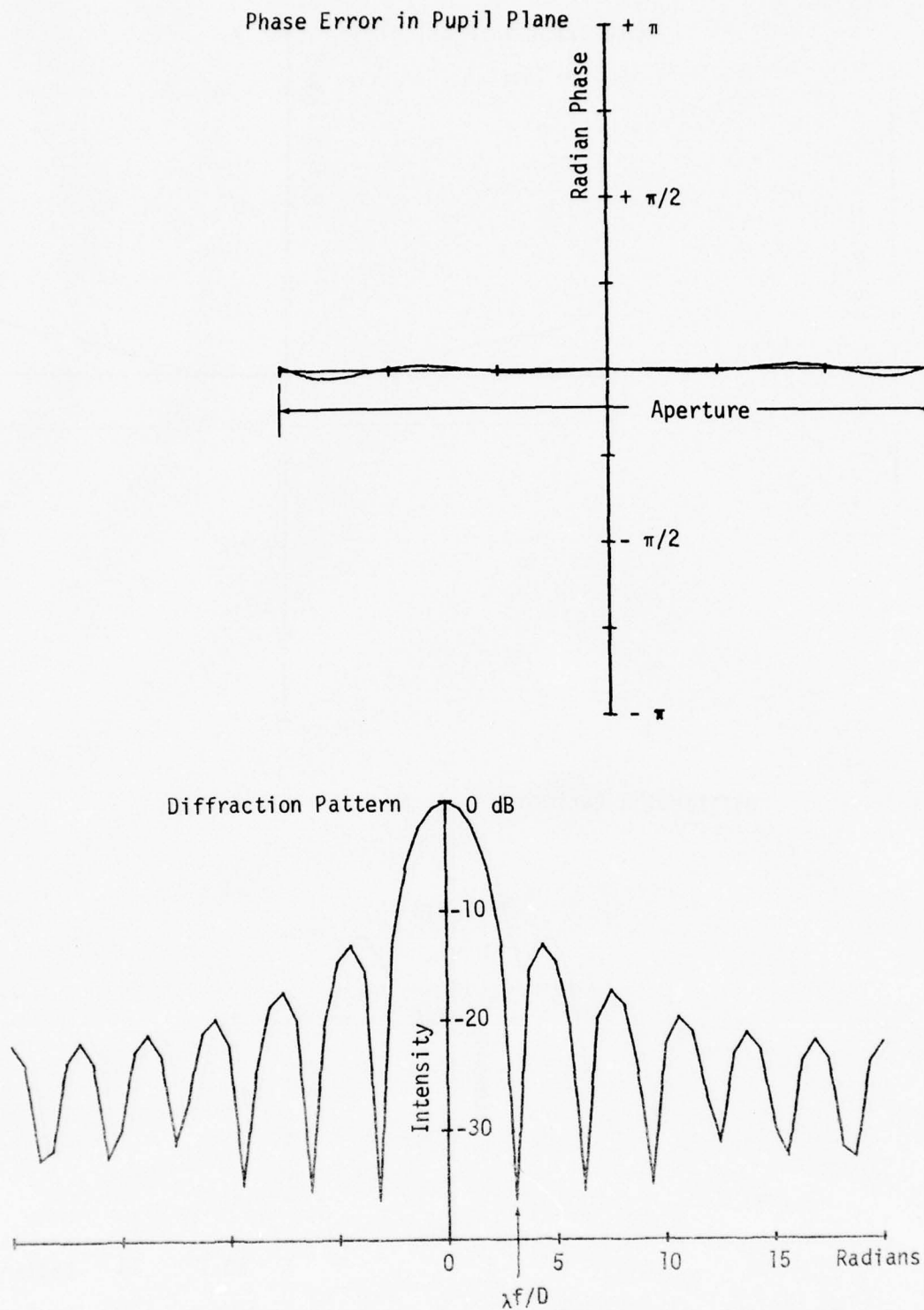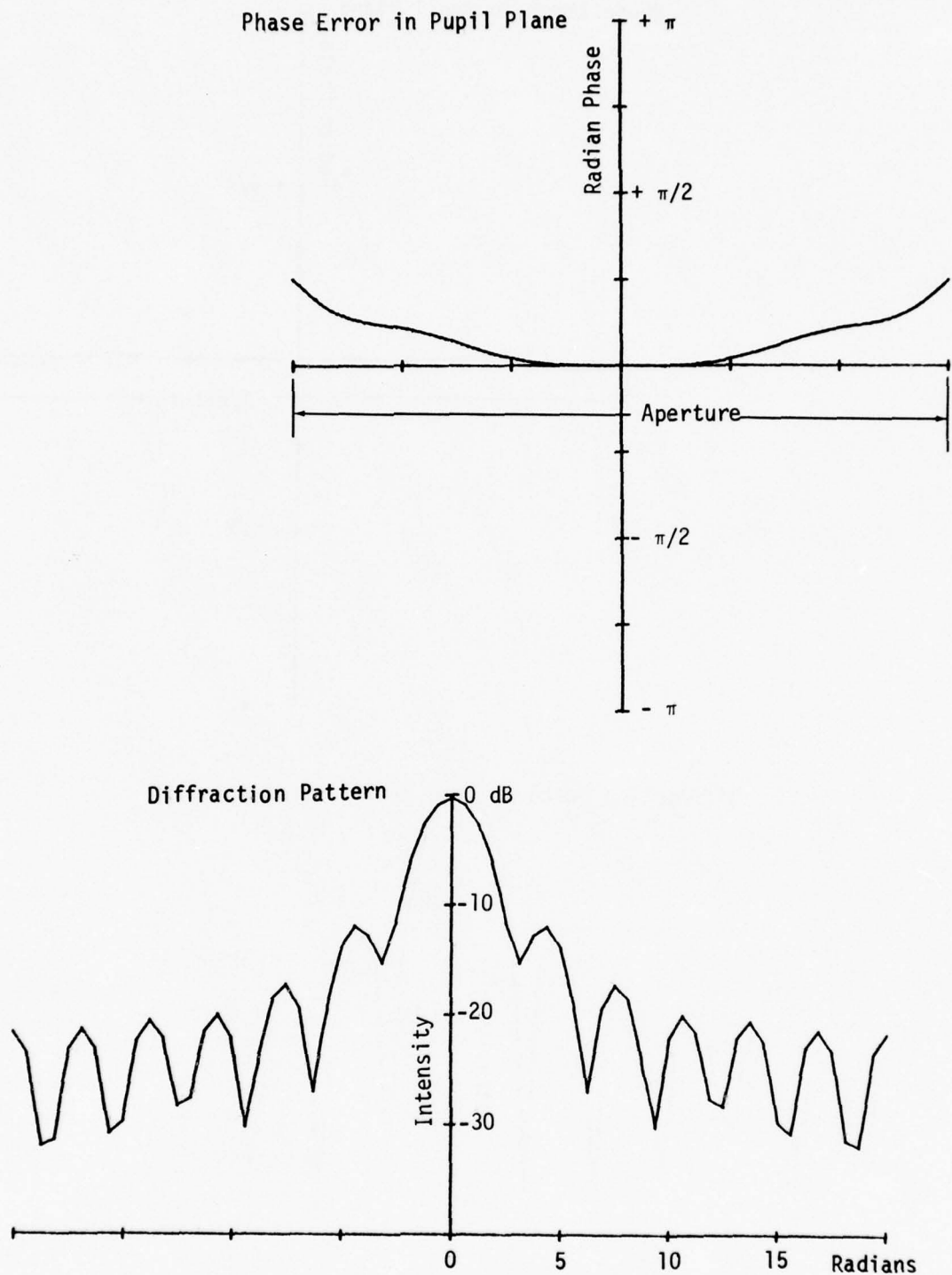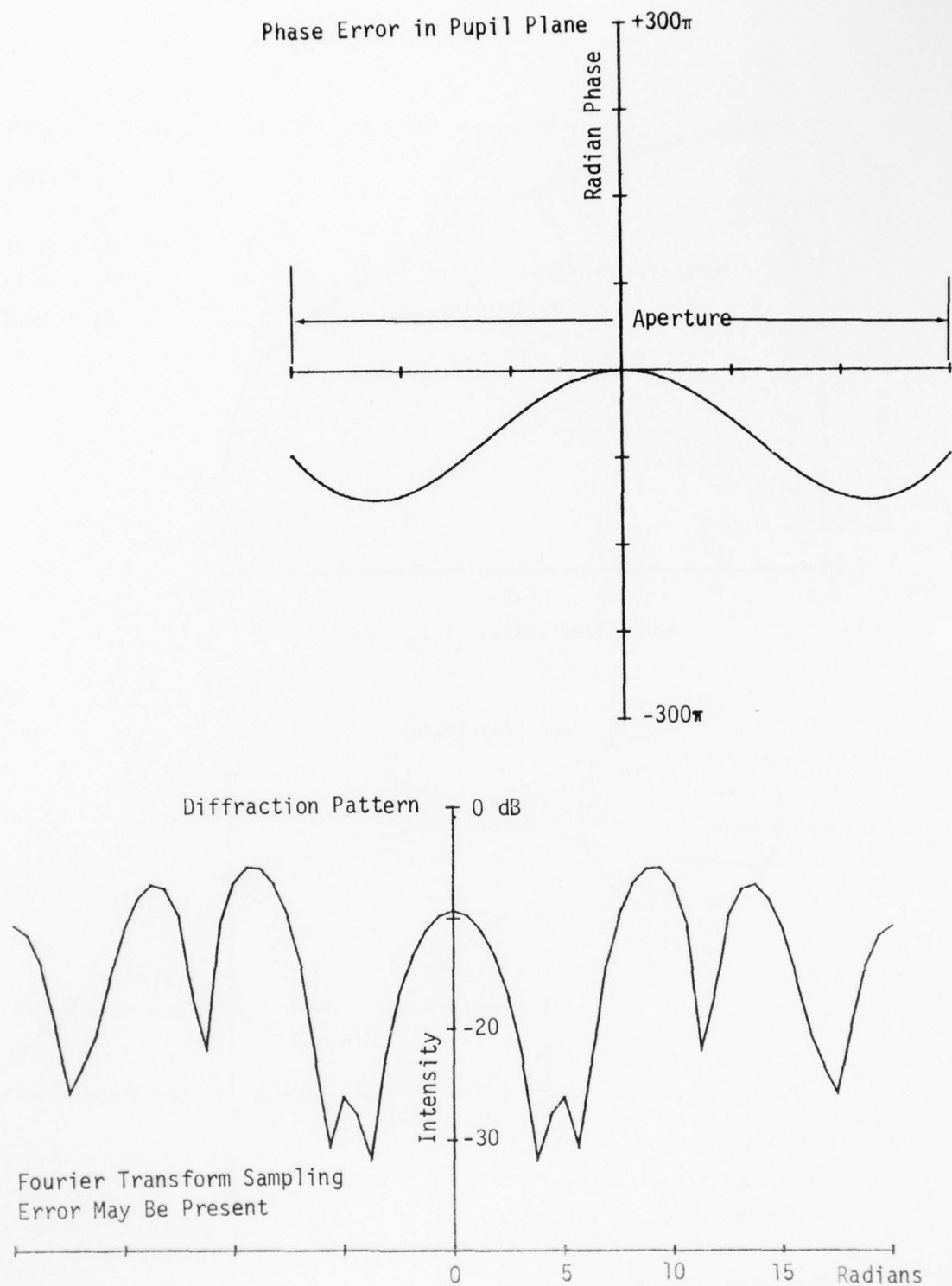
Figure 41. Wavefront Phase Error and Corresponding Intensity Diffraction
Pattern for Generalized Luneburg Lens Delineated in Figure 40.

75
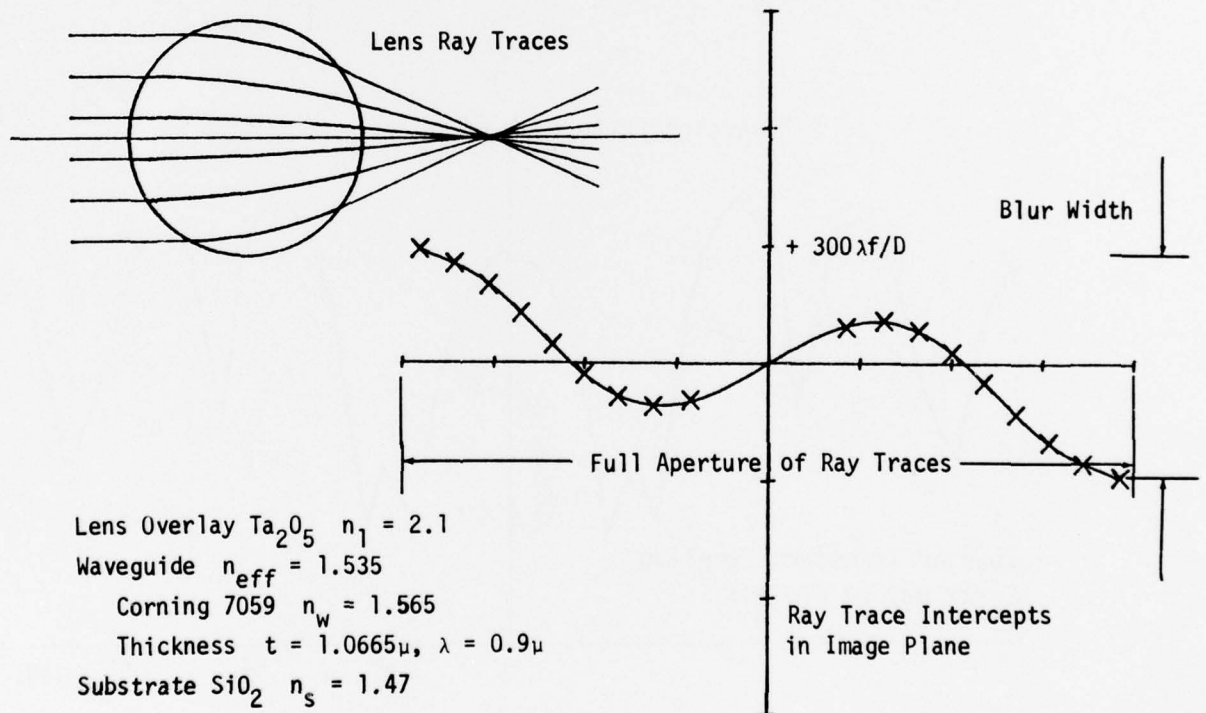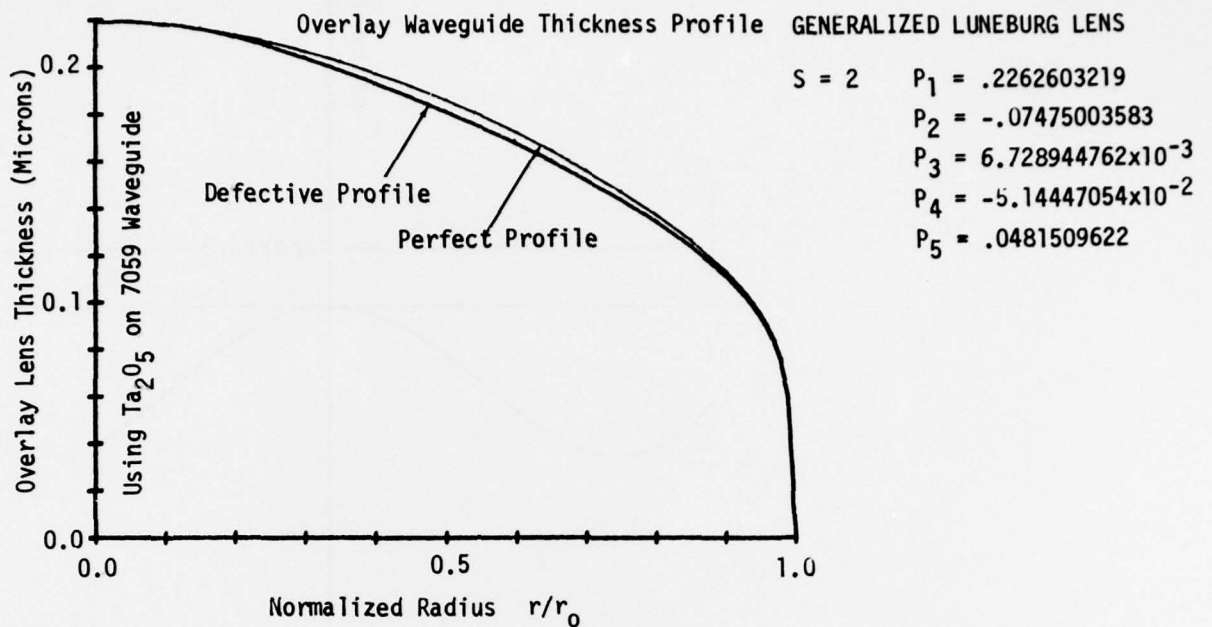
Figure 42. Tabulation of Generalized Luneburg Lens Parameters with Corresponding Overlay Waveguide Lens Thickness Radial Profile, Ray Traces through this Lens and the Intercept Error in the Image Plane (.96 P_1, P_2, P_3, -10 P_4, 48.6717 P_5).

76
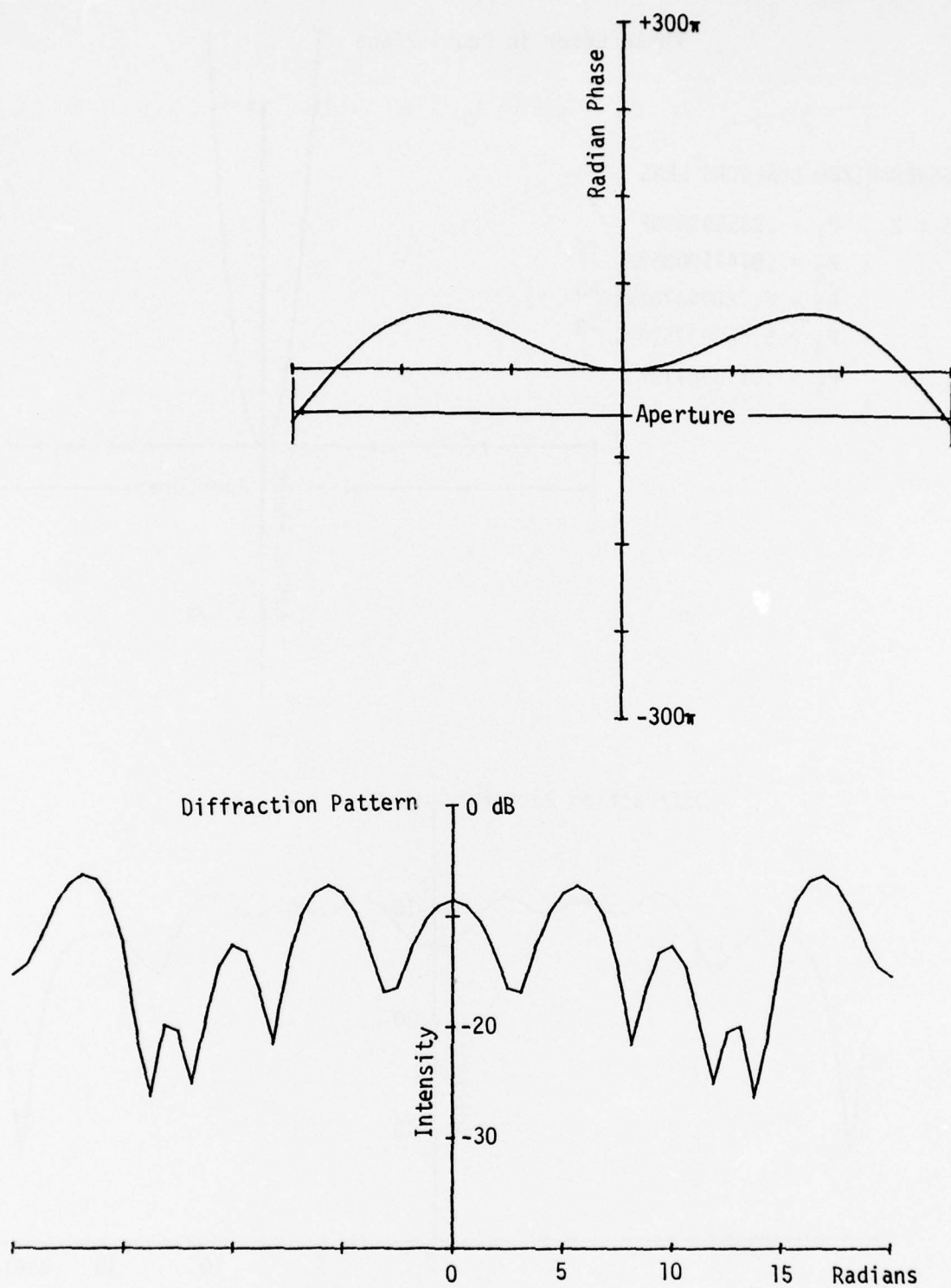
Figure 43. Wavefront Phase Error and Corresponding Intensity Diffraction Pattern for Generalized Luneburg Lens Delineated in Figure 42.

77

Phase Error in Pupil Plane

GENERALIZED LUNEBURG LENS

$S = 2$ $P_1 = .2355935602$
$P_2 = .07475003583$
$P_3 = 6.728944762 \times 10^{-3}$
$P_4 = 5.658917594 \times 10^{-3}$
$P_5 = .0116984127$

$+ \pi$

Radian Phase Aperture

$- \pi/2$

Diffraction Pattern — 0 dB

-10

-20

Intensity

-30

0   5   10   15   Radians
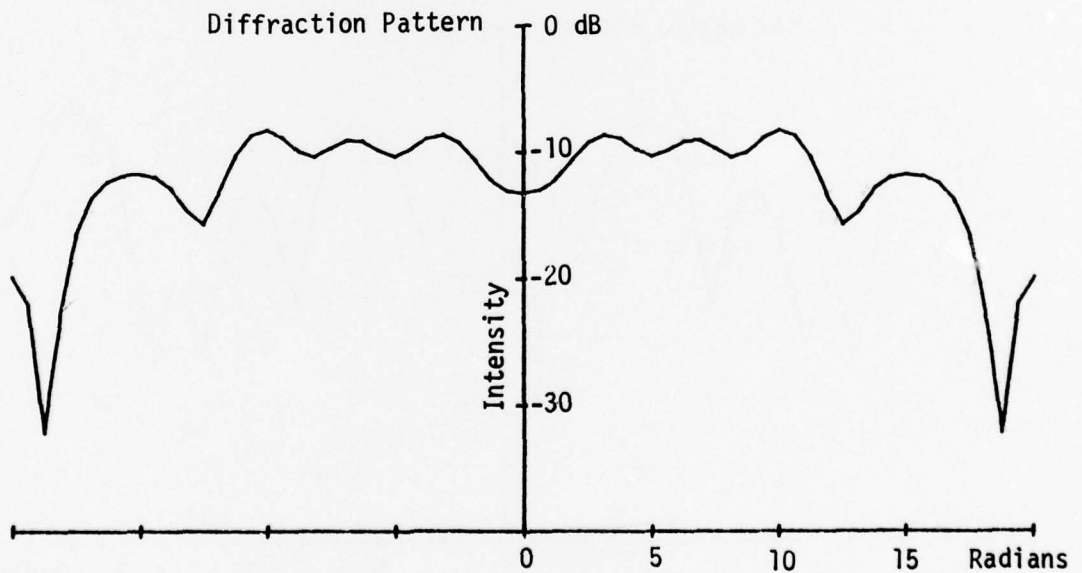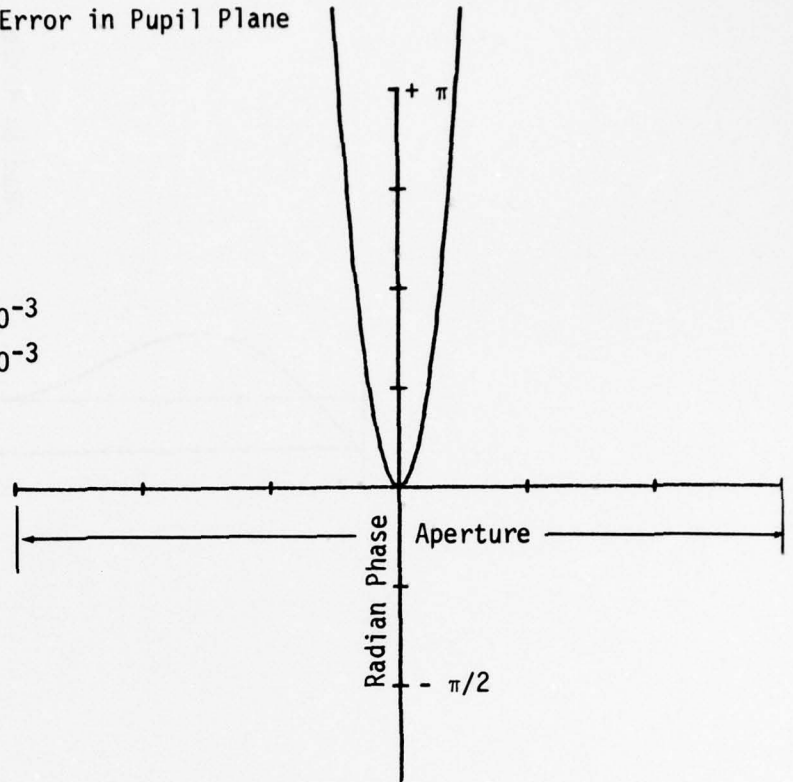
Figure 44. Wavefront Phase Error and Corresponding Intensity Diffraction Pattern for Generalized Luneburg Lens Delineated in Figure 42 (.9996 P_1, P_2, P_3, -1.1 P_4, 11.8249 P_5).

78

The above delineated numerical analysis procedure computes ray traces through a circular symmetric inhomogeneous refractor providing the ray intercept, wave front phase error, and intensity diffraction pattern for a single lens. The optical Fourier transform "chip" requires a beam expander, lens system and a transform lens matching the source aperture and the signal input aperture to be transformed. The computer program has been modified to include a second lens coupling rays through both lenses providing for magnitication. Ray traces through a beam expander of unity, X2 and X4 magnification, are depicted in Figure 49. It will be necessary to add a third lens using the above procedures to fully synthesize the optical Fourier transform "chip." When this task is completed, it will be possible to introduce defective waveguide lens profiles in any of the three lenses. Thus far, all of the preceding numerical analysis has assumed a uniform illuminated aperture which will produce the $\text{sinc}^2 x$ diffraction pattern. It will, however, be desirable to include an apodization to improve the spatial distribution of the diffraction pattern by suppressing side lobes which compromise the system dynamic range and can lead to ambiguities.
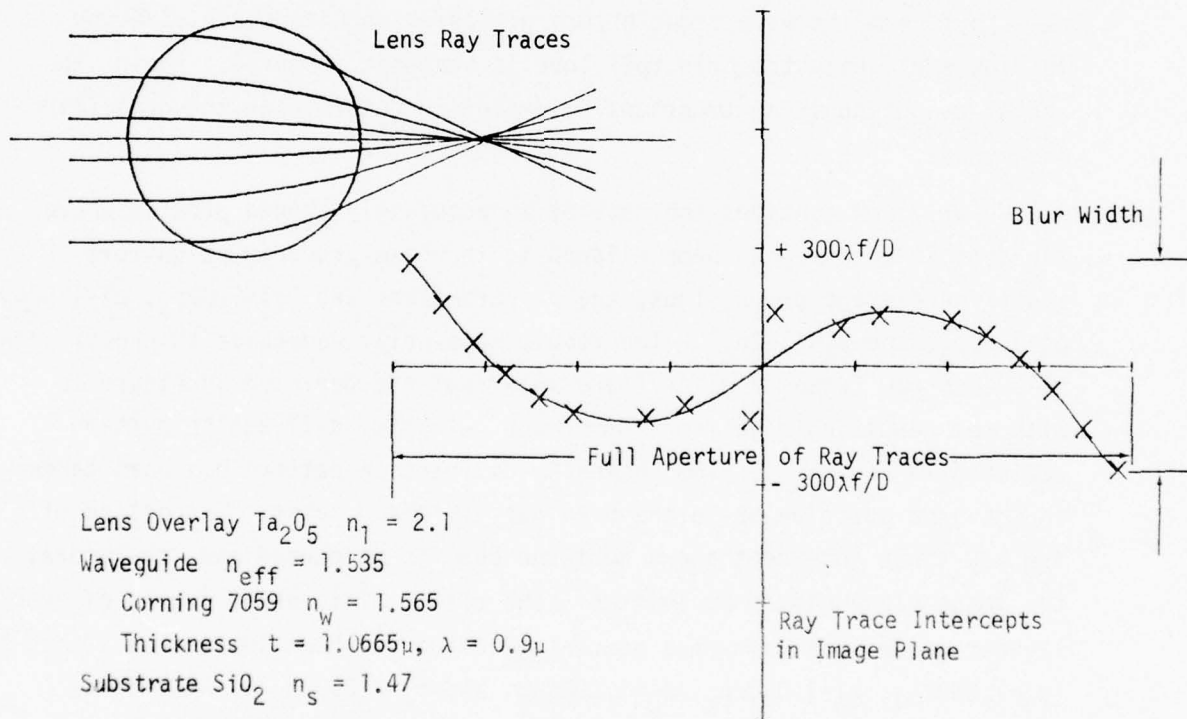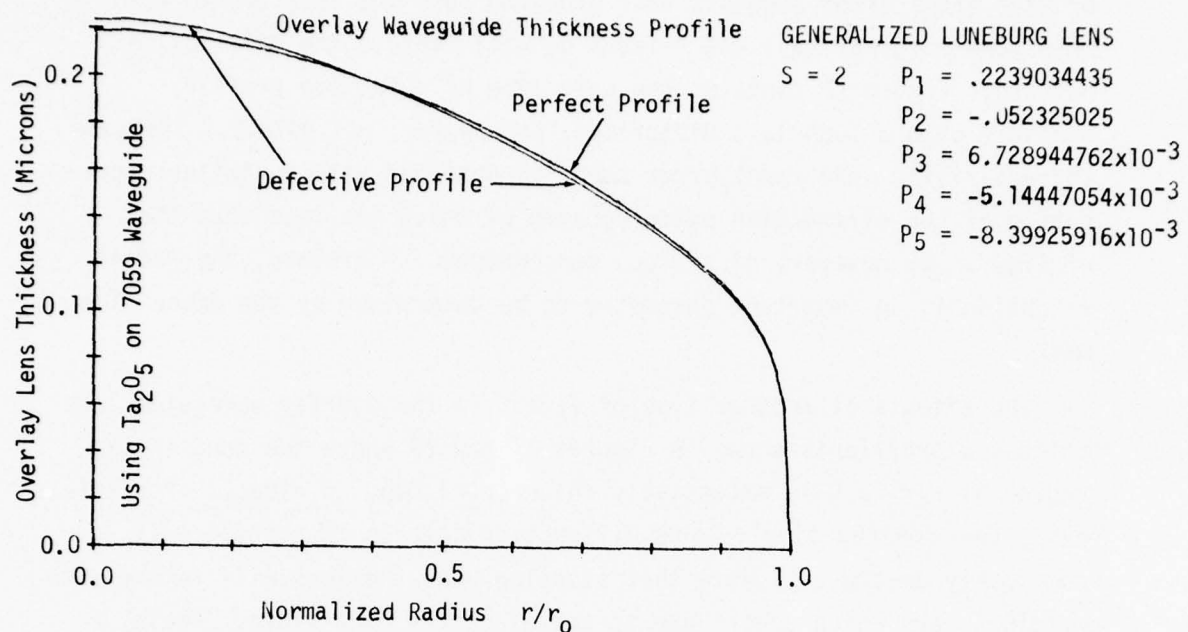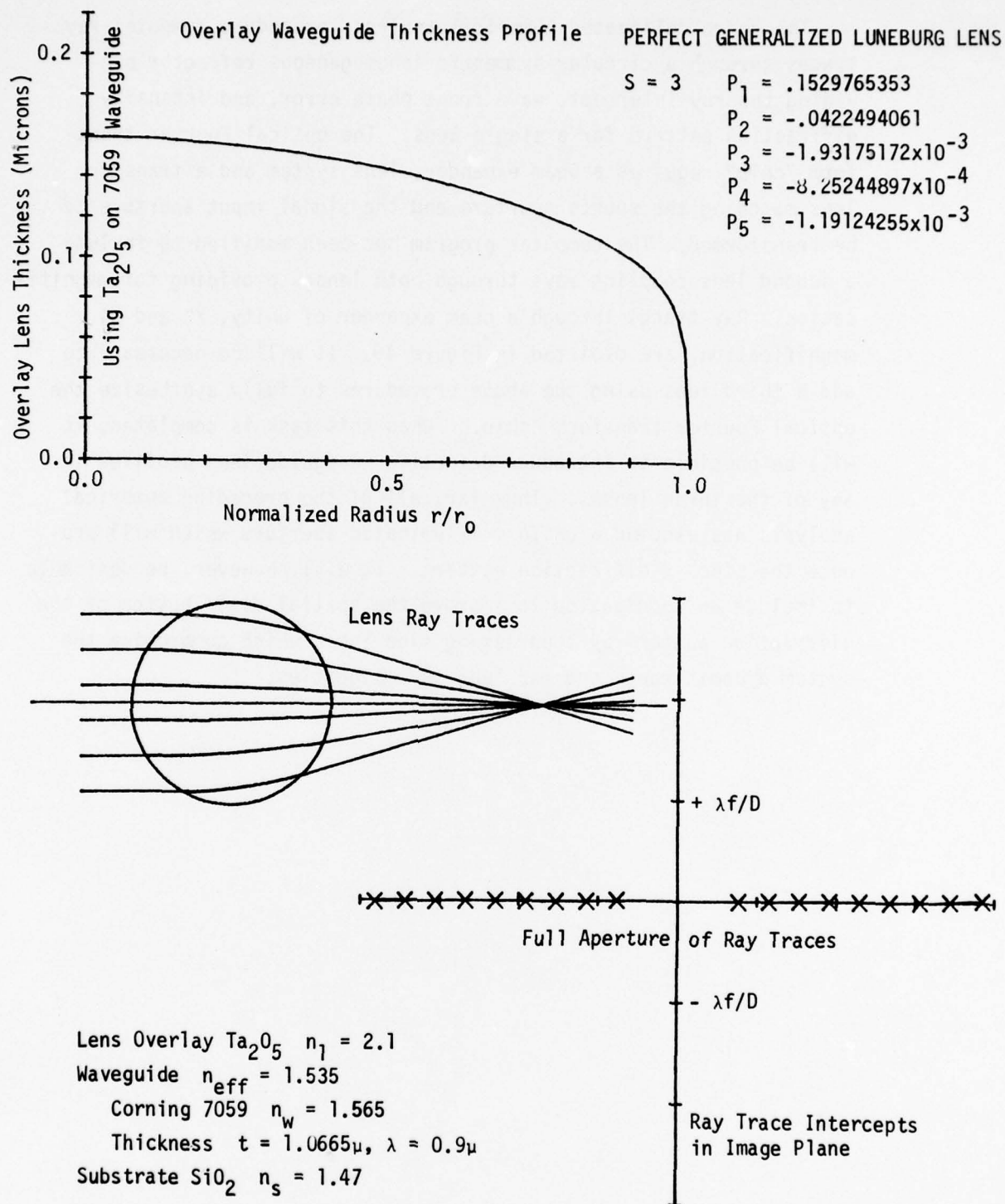
Figure 45. Tabulation of Generalized Luneburg Lens Parameters with Corresponding Overlay Waveguide Lens Thickness Radial Profile, Ray Traces through this Lens and the Intercept Error in the Image Plane (Perfect Luneburg Lens).

80

Phase Error in Pupil Plane

Radian Phase

+ π

+ π/2

Aperture

- π/2

- π

Diffraction Pattern
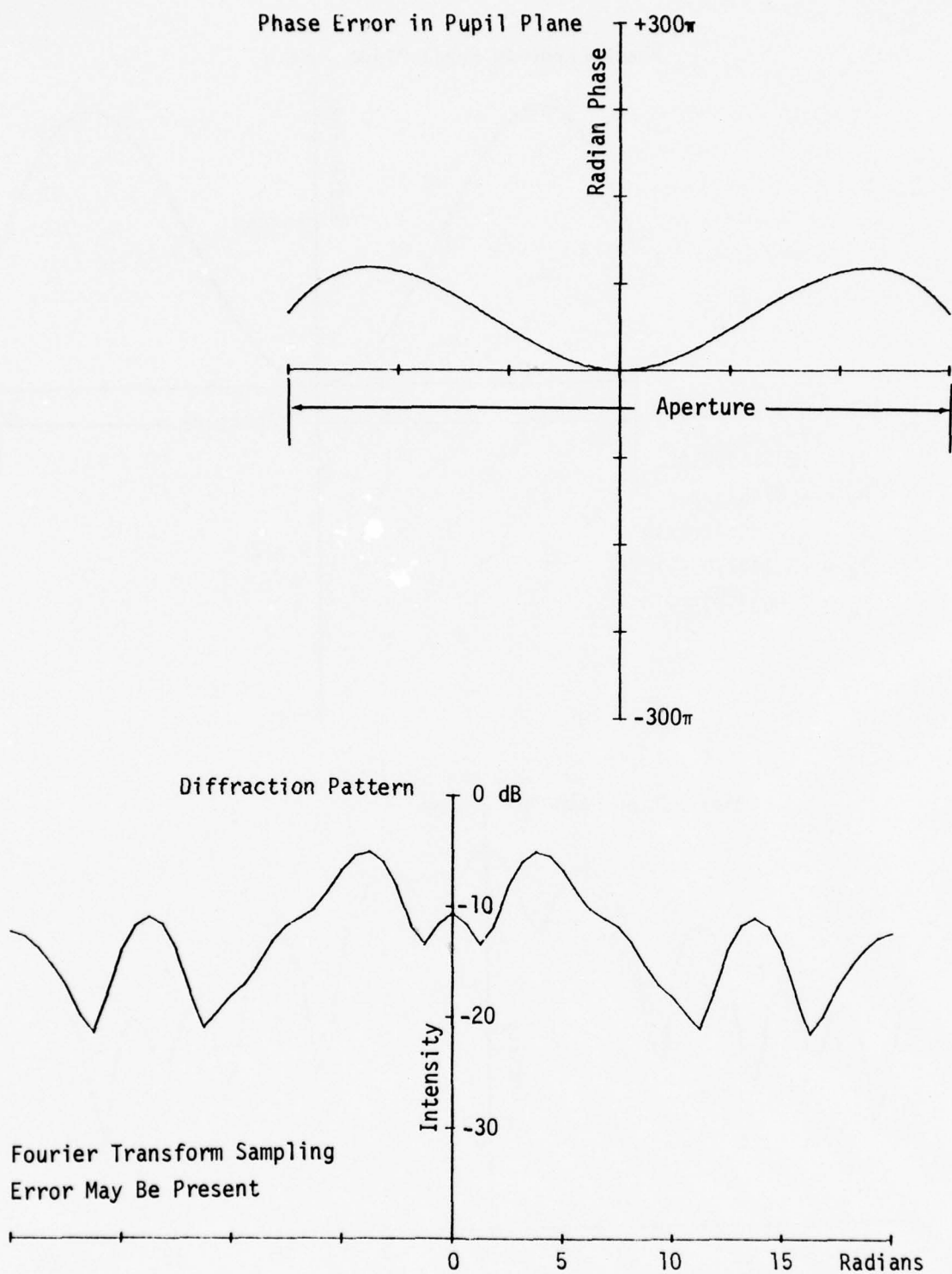
0 dB

-10

Intensity

-20

-30

0   5   10   15   Radians

λf/D
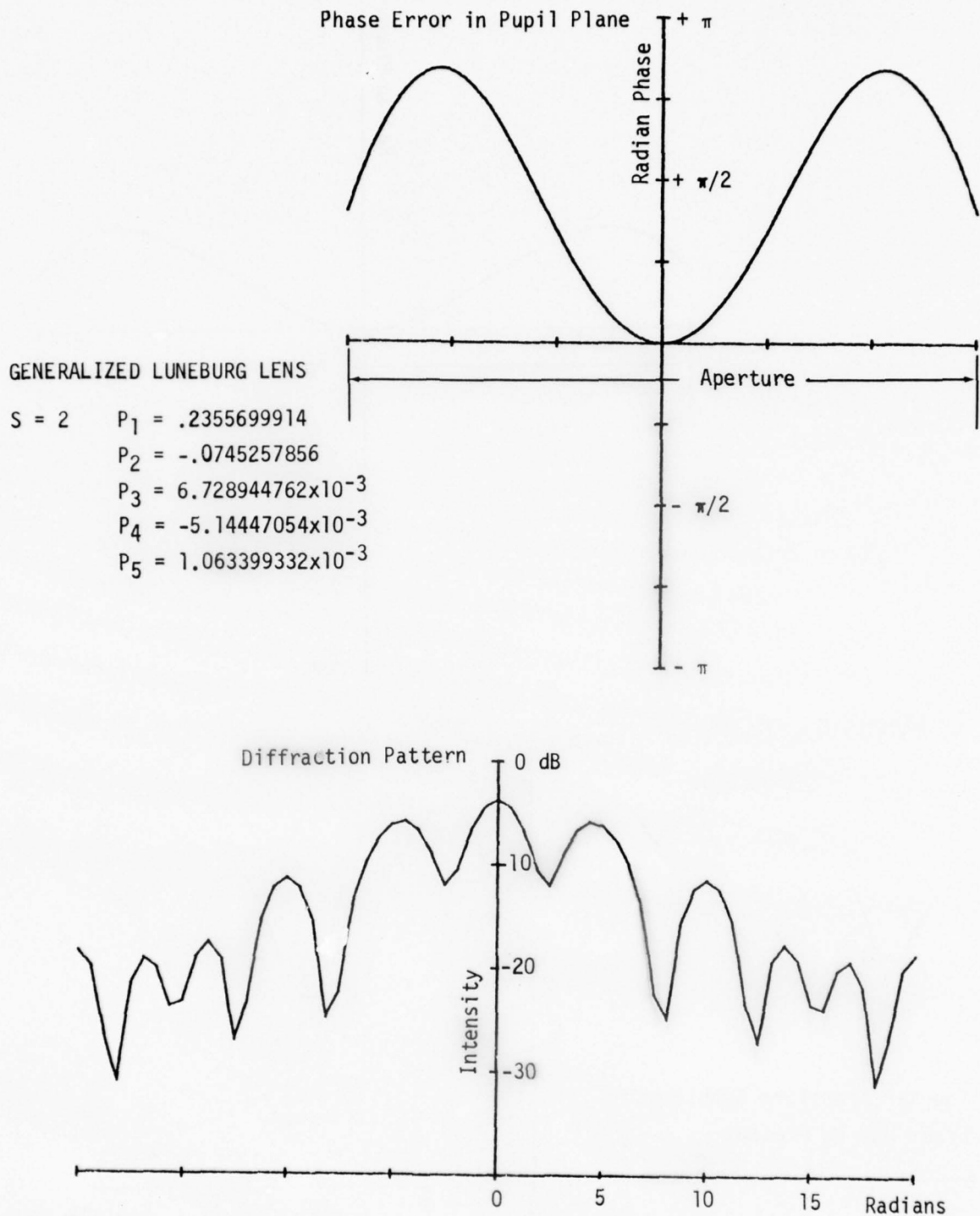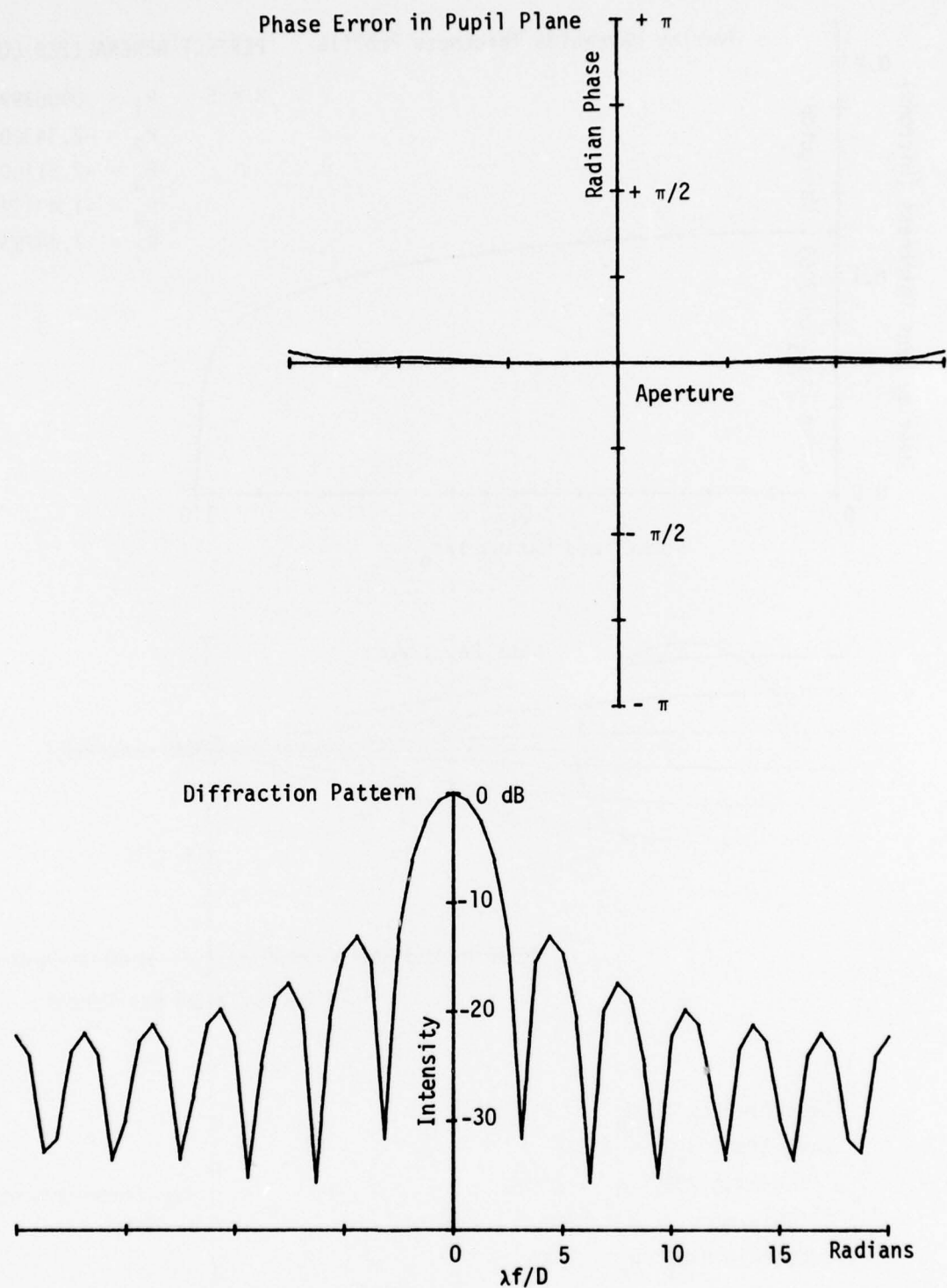
Figure 46. Wavefront Phase Error and Corresponding Intensity Diffraction
Pattern for Generalized Luneburg Lens Delineated in Figure 45
(Perfect Luneburg Lens).

81

Overlay Waveguide Thickness Profile   PERFECT GENERALIZED LUNEBURG LENS

Overlay Lens Thickness (Microns)

0.2

0.1

0.0

Waveguide
Using Ta_2O_5 on 7059

0.0   0.5   1.0
Normalized Radius r/r_o

$S = 5$ P_1 = .0906399959
P_2 = $-2.34300068 \times 10^{-2}$
P_3 = $-2.51100017 \times 10^{-3}$
P_4 = $-1.49192458 \times 10^{-4}$
P_5 = $-7.44793717 \times 10^{-4}$

Lens Ray Traces

$+ \lambda f/D$

Full Aperture of Ray Traces

$- \lambda f/D$

Ray Trace Intercepts
in Image Plane

Lens Overlay Ta_2O_5 n_1 = 2.1
Waveguide n_{eff} = 1.535
    Corning 7059 n_w = 1.565
    Thickness   t = 1.0665μ, λ = 0.9μ
Substrate SiO_2 n_s = 1.47

Figure 47.   Tabulation of Generalized Luneburg Lens Parameters with
Corresponding Overlay Waveguide Lens Thickness Radial
Profile, Ray Traces through this Lens and the Intercept
Error in the Image Plane (Perfect Luneburg Lens).

82

Phase Error in Pupil Plane

Radian Phase

+ π

+ π/2

Aperture

- π/2

- π

Diffraction Pattern

0 dB

-10

-20

-30

Intensity

0   5   10   15   Radians

λf/D
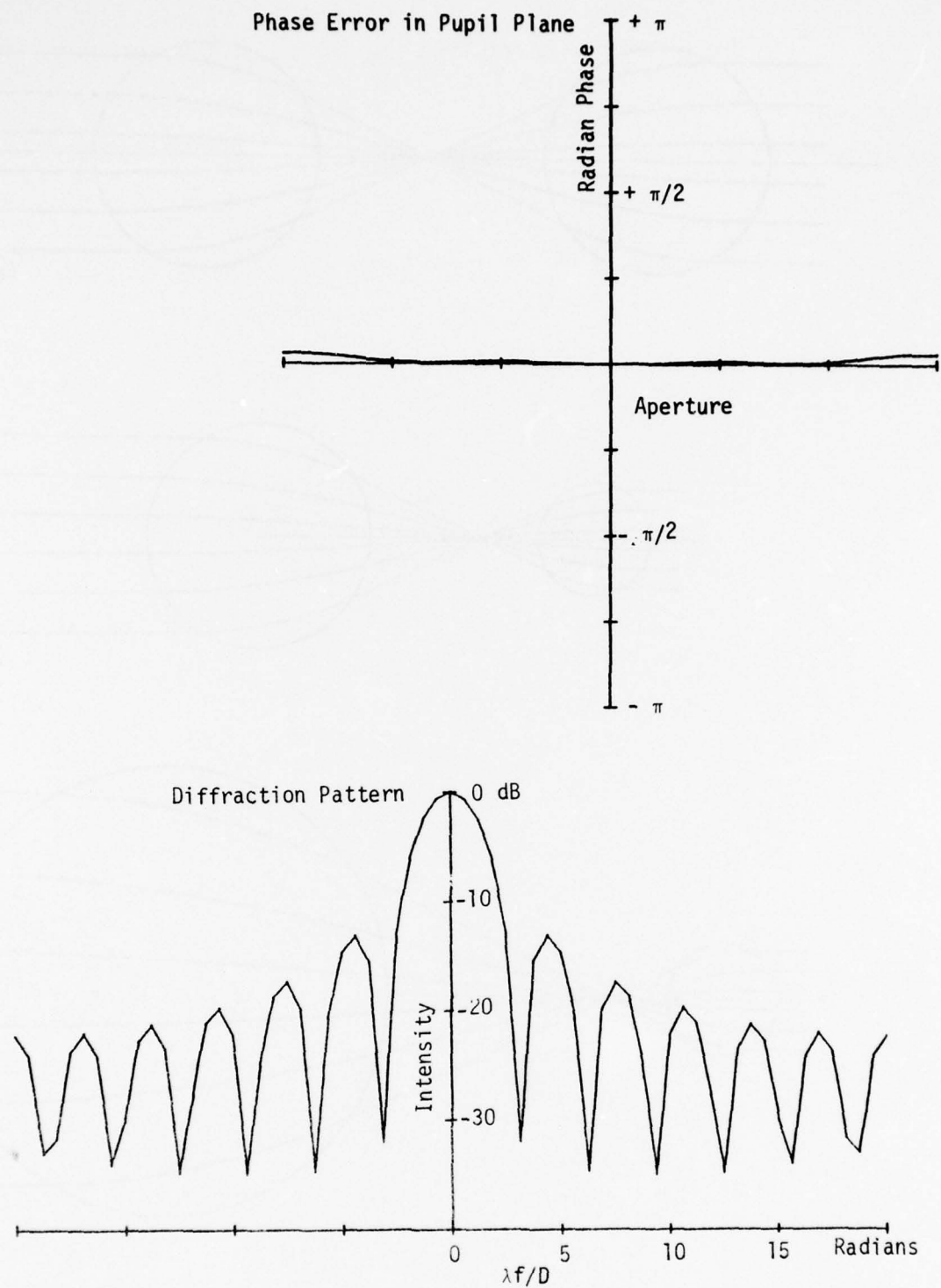
Figure 48.   Wavefront Phase Error and Corresponding Intensity Diffraction
Pattern for Generalized Luneburg Lens Delineated in Figure 47
(Perfect Luneburg Lens).

83
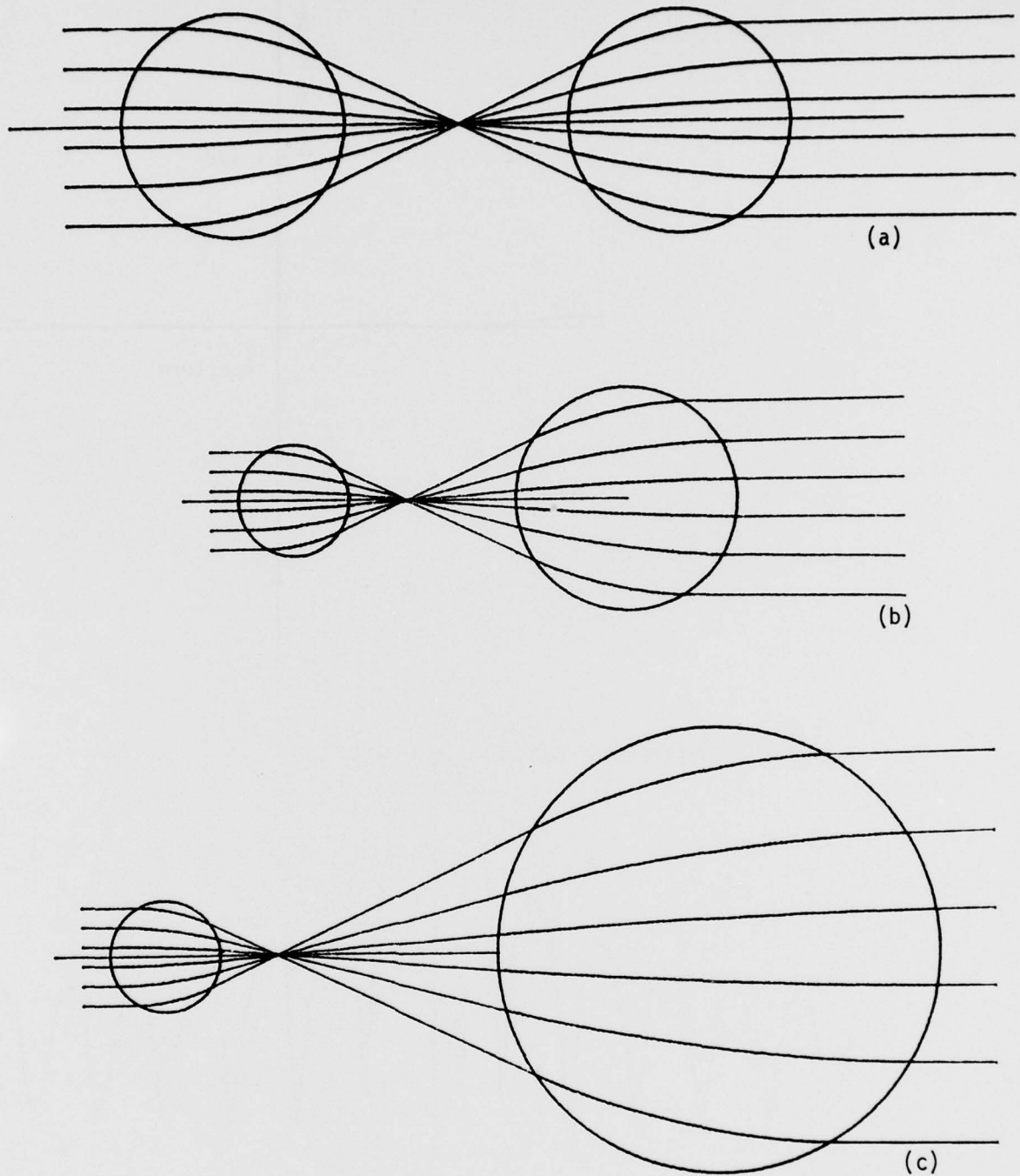
Figure 49. Computer-Generated (HP9830) Ray Traces Through Beam
Expansion System for (a) Unity Magnification, (b)
X2 Magnification, and (c) X4 Magnification.

84

4. Waveguide Generalized Luneburg Lenses and Lens Systems Experimental Data

Two methods have been employed to characterize the performance of thin-film waveguide Luneburg lenses and lens systems. One method, yielding quantitative data, utilizes the lenses and waveguide with input and output couplers and apparatus to probe, scan and record the resulting diffraction pattern via a reimaging technique using magnification. These results are therefore a convolution of the coupling prisms, the waveguide, thin-film lenses, reimaging lens, and probe aperture. When diffraction-limited results are required, aberrations of the associated apparatus become an important factor. The other method has employed photography of the sc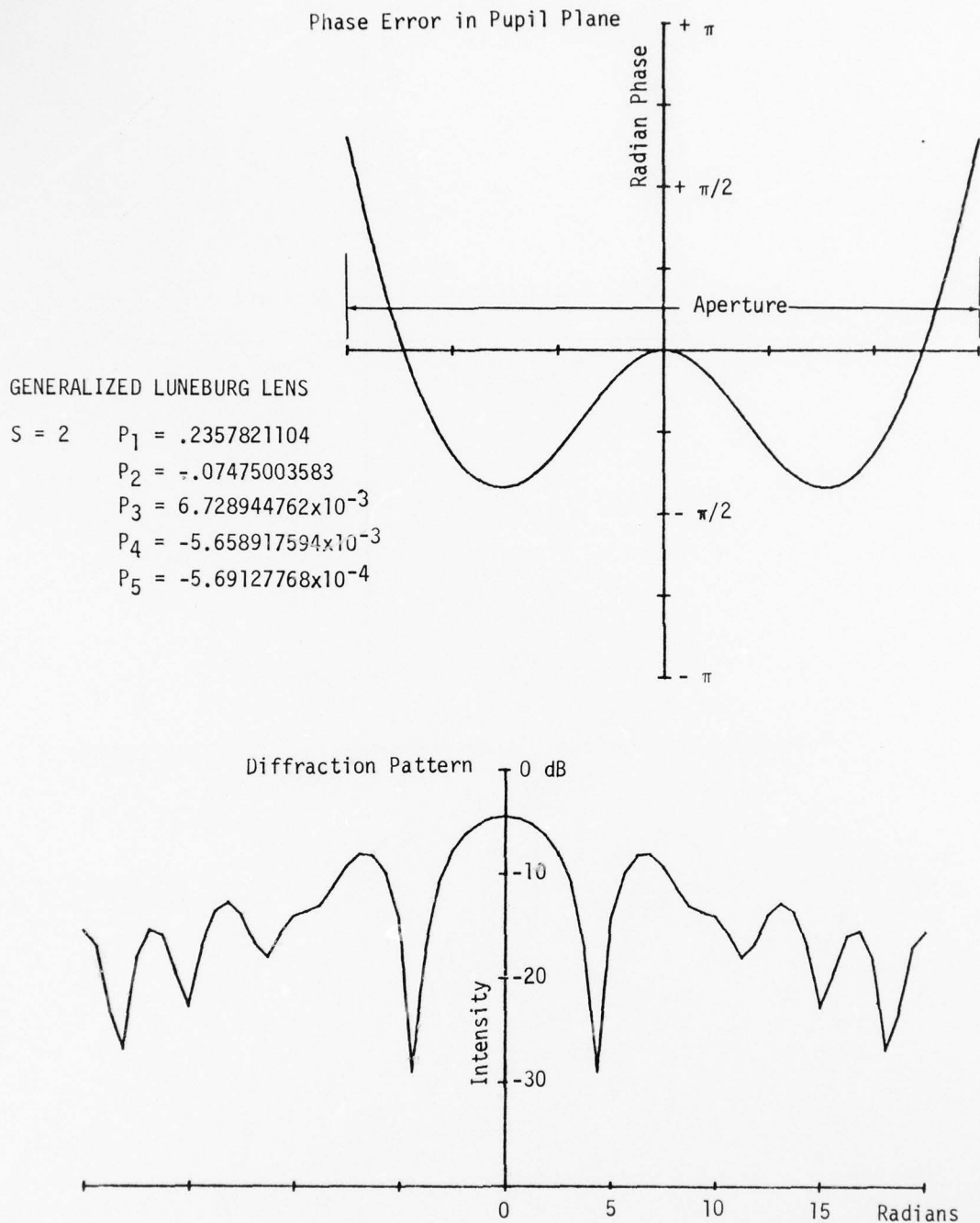attered wide-angle radiation associated with propagation through lossy waveguides. It readily identifies defects through the propagation path which affect the measured diffraction pattern. In general, good low-scattering waveguide is not observable in this manner without excessive exposure time. Although numerous photographs are employed herein, it should be remembered that their dynamic range is limited by sensitivity and saturation to somewhat more than one order of magnitude. The use of individual ray traces in these photographs has proven to be useful for the identification of multiple modes of propagation and for the identification of scattering defects.

All the waveguide lenses reported herein have employed Ta_2O_5 as the highest refractive index material used for forming lenses. All the waveguides have employed Corning 7059 glass on thermally-grown SiO_2 on Si as a substrate. Most of the lenses have utilized the dense overlay. All the lenses have been deposited by an RF sputter technique starting with metallic Ta and using a reactive process with $Ar-O_2$ to form the deposition through a circular symmetric mask with an appropriately shaped aperture. A semi-cross-section of the mask, lens, waveguide, isolation layer and substrate are illustrated in Figure 50. A conical shaped mask is usually employed. In general, the longer focal length lenses have employed thinner overlays with masks having a reduced conical angle. The RF sputtering target is

85

substantially larger than that of the mask aperture so that molecular transfer occurs over wide angles. The pressure is controlled during the deposition procedure so that diffusion occurs producing a smooth surface topology. This effect is apparent in Figure 6.

The performance of two generalized Luneburg lenses utilized as an inverting beam expander is shown photographically in Figures 51, 52, 53 and 54. It has been designed for a 3X expansion ratio and provides an output aperture of 1 cm. The operation of the beam expander utilizing individual ray traces traversing the expander from left to right using 25 mW at 0.63μ is shown in Figure 51, Section (a). Rays traversing the individual lenses are clearly evident in some portions of the waveguide, while in other regions no scattering can be observed. Unfortunately this beam expander has a serious scattering defect in the substrate isolation layer near the focus (but not at the focus). The smaller expansion lens exhibits considerably more scattering than is typical, while in the latter it is more representative of Ta_2O_5 thin-film overlays. Some scattering is apparent from the waveguide in the region of the input. This is due to a prior contact of a prism coupler. Section (b) shows that this region is more aggravated by additional prism contacting in both the input and output regions. The output aperture with throughput intensity is apparent from scattered radiation at the edge of the silicon wafer reflected by black paper. Section (b) of Figure 51 utilizes an input beam nearly filling the expander lens aperture. The expander objective shows two Newton rings made apparent by interference of the scattered radiation. Some dark streaks are also apparent in this lens which arises from the substrate damage near the focal region.

Figure 52 illustrates the propagation of a single axial ray of the same X3 beam expander, while Figure 53 illustrates the trajectory of an offset ray through the same expander. Figures 52 and 53 have utilized a substantial increase of exposure to shift the range of Figure 51 by another order of magnitude so as to accentuate defects. In Figure 52, the scattering halo surrounding a single ray through the

86
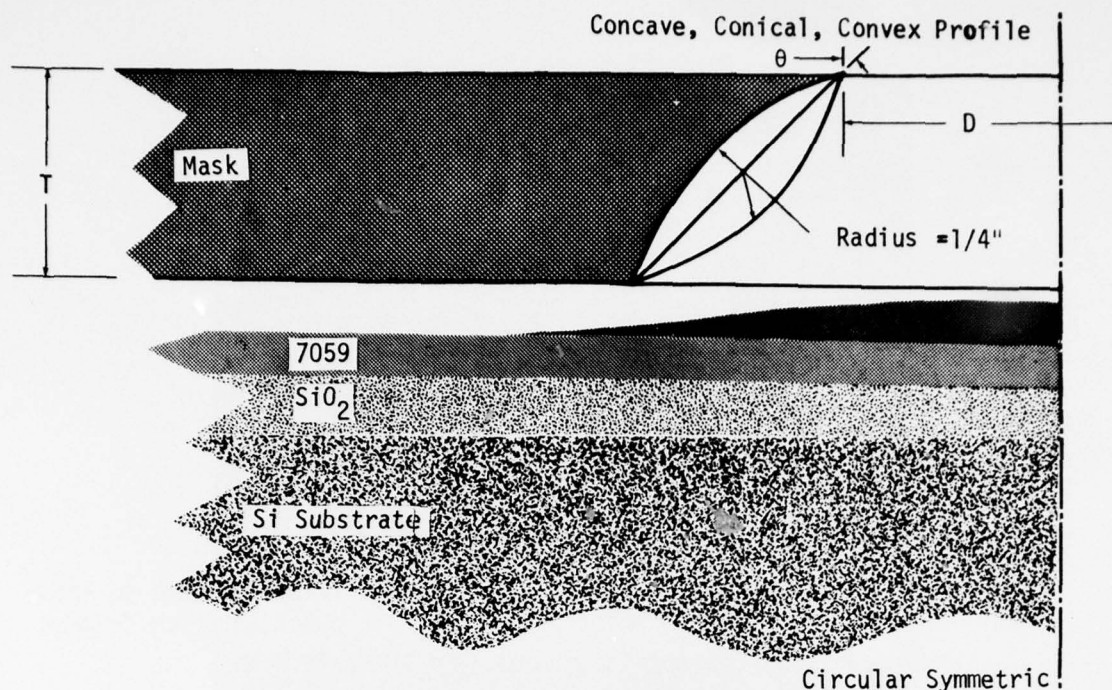
Figure 50. Cross Section of Various Deposition Mask Shapes Investigated to Control the Waveguide Luneburg Lens Radial Thickness Profile.

expander lens is apparent. The throughput power scatter from black paper exiting the silicon wafer is also apparent. This photograph shows that low-scatter loss 7059 waveguide is realizable.

Figure 53 shows the presence of mode conversion which occurs in the thicker expansion Luneburg lens and the lack of mode conversion in the thinner objective lens. Fractional mode conversion from TE_0 to TE_1 occurs at the expander lens entrance interface. The trajectory of these two modes separate in the expander lens, and the TE_1 mode is converted again back to the TE_0 mode at the exit interface where it propagates through the remainder of the system as another ray. The intervening waveguide will not support this second TE_1 mode. This mode conversion process does not occur in the objective lens because of its thinner cross section. Mode conversion presumably occurs in Figure 52, however cannot be observed because each of the rays traverse the same path. The intensity of the ray due to mode conversion is approximately -10 dB relative to the lowest order mode. This mode conversion can further be reduced by using an under-

87

Focus

(a)　　　　Luneburg Lenses　　　　Scattering Due to Prior
　　　　　　　　　　　　　　　　　Coupling Prism Contact

Input　　　　　　　　　　　　　　　　　　　　　Edge Emission

(b)　　Scattering Near Focus Due to Substrate Damage
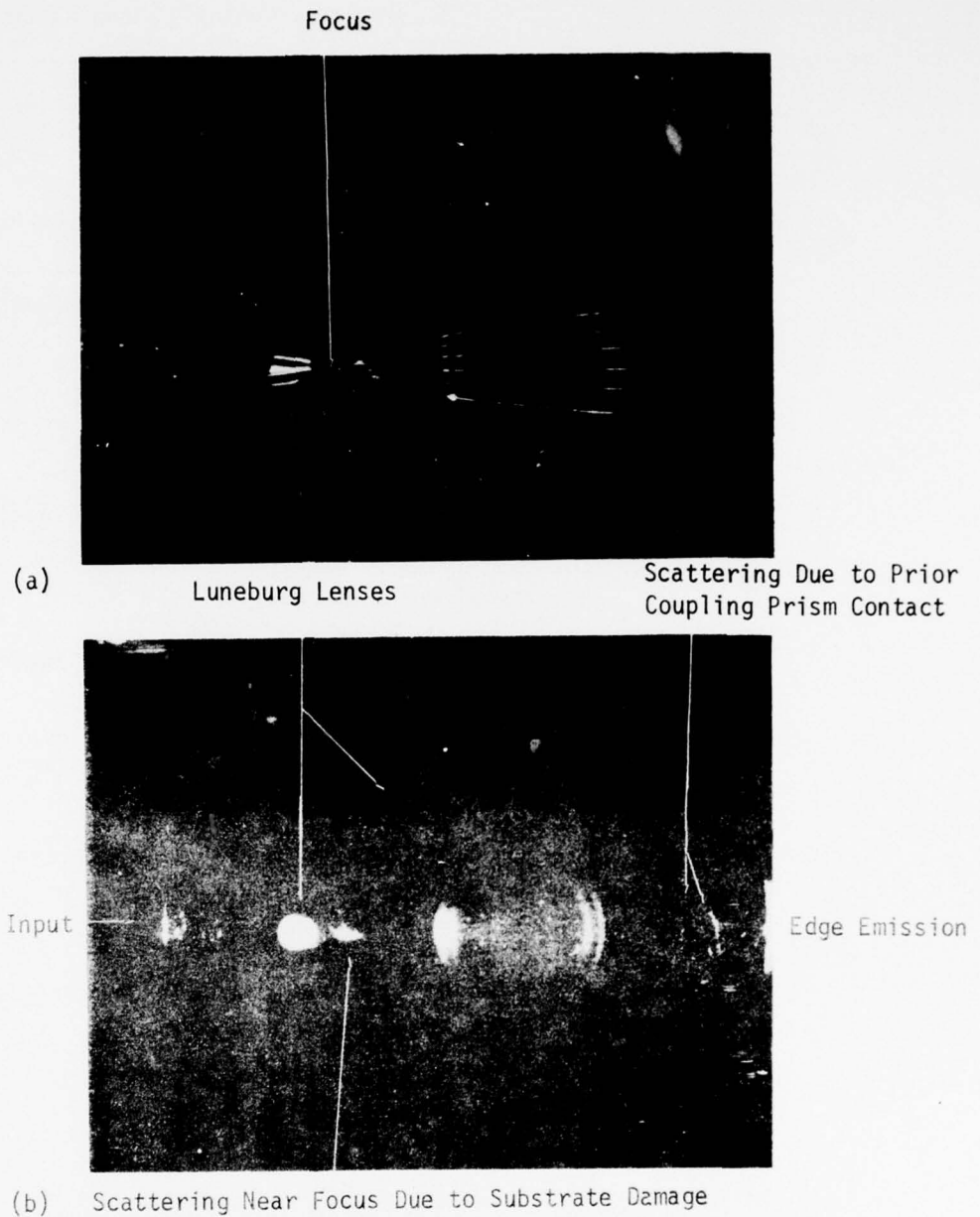
Figure　51.　Operation of Generalized Luneburg Lens Beam Expander (X3)
Using Ta_2O_5 on 7059 on Thermally-Grown SiO_2 on Si (a) Scattering
of Individual Ray Traces Through Lenses Using 6328 Å Radiation
Extending Over 1 cm Aperture (Output), (b) Scattering of Con-
tinuous Wide Aperture Beam Through Same Beam Expander Using
Uniform Illumination.
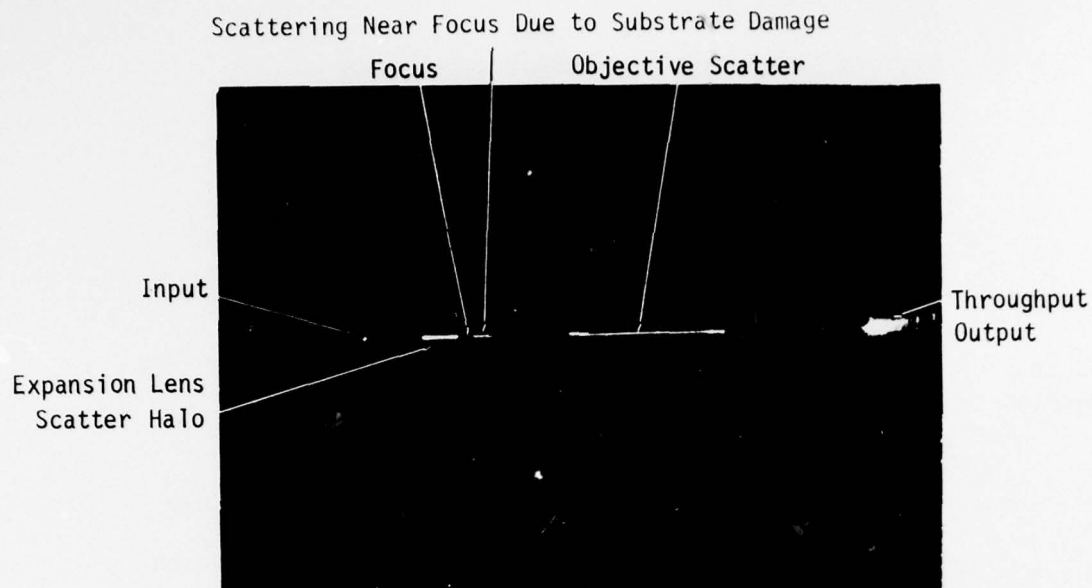
Figure 52. Axial Ray of Generalized Luneburg Lens Beam Expander
(X3) of Figure 51 Showing Halo Scatter Around Expansion
Lens, Scatter From Surface Defect, and Scatter of Objective
and Throughput Intensity Output.
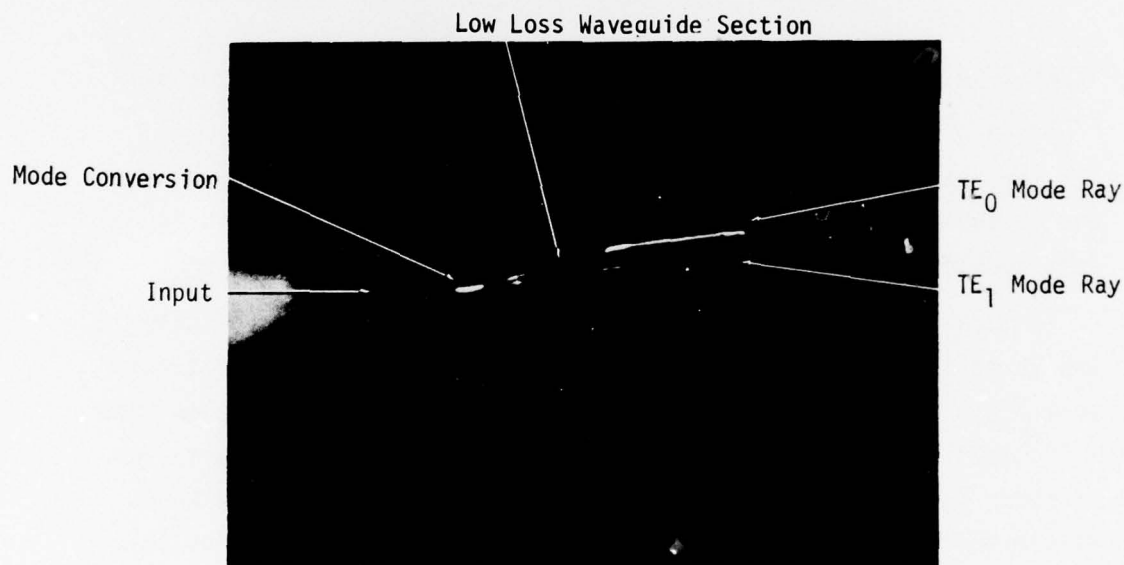
Figure 53. Operation of Generalized Luneburg Lens Beam Expander (X3)
Showing Scattering of a Single Ray Where Mode Conversion
Occurs in the First Lens Producing Two Refraction Angles
and Mode Conversion Occurs Again Showing Two Ray Traces
for the TE_0 Mode Through the Remainder of the Expander

89

Prism Coupler
Hypotenuse
Face

Si Wafer Edge

Output Beam
Intensity
Distribution
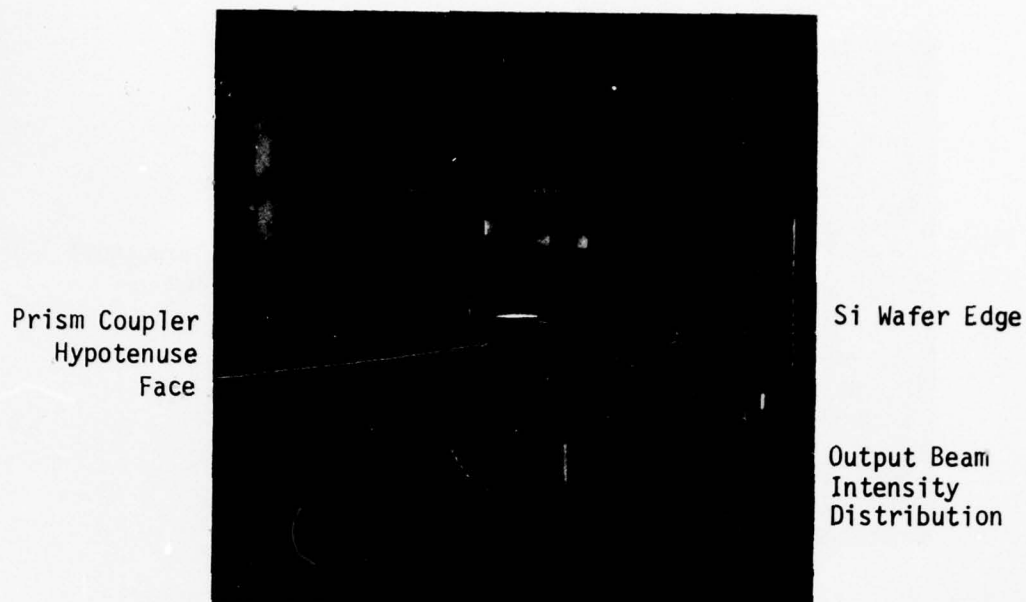
Figure 54.   Output Beam Intensity Distribution From Generalized
Luneburg Lens Beam Expander (X3) Shown in Figure 51

layer lens instead of the overlay configuration or can be eliminated
by using the symmetric interleave as illustrated in Figure 2.

The near-field, exit-field distribution from this X3 beam expan-
der is shown in Figure 54 by imaging the distribution in the prism
exit coupler.

A much larger expansion ratio is required for coupling of GaAs
lasers to the full aperture of the integrated optical Fourier trans-
form "chip" to obtain a useful time-bandwidth-product. The plan view
of another generalized Luneburg lens inverting expansion lens system
is shown in Figure 55 where the Newton ring indicates the thickness
of the objective lens. The expansion ratio is X90 for this design.
An enlargement of the expansion lens, also showing the Newton rings,
is shown in Figure 56. The diameter of this lens is 250μ and is
approximately four times thicker than the objective. The Newton
rings are not perfectly symmetrical, showing the effect of offset
during the deposition relative to the source target. This type of

90

Objective   Expander Lens
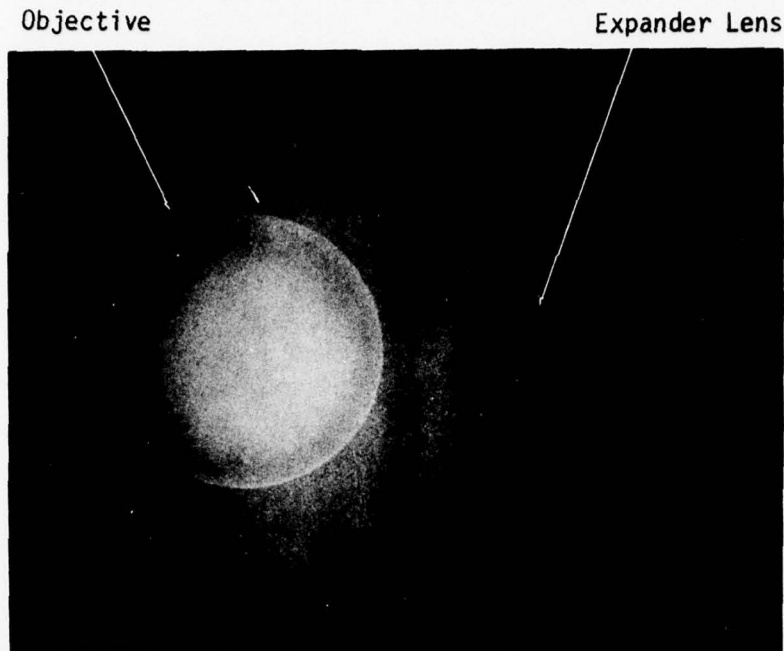
Figure 55. Macro Photograph of Luneburg Lens Beam Expansion System
            (Plan View) Showing Newton Ring of the Objective Thickness
            Profile. Expansion Ratio 90X.

asymmetry when used off axis can introduce an odd aberration, whereas,
on axis, will yield an even aberration.

The operation of the 90X beam expander used with the output
applied as individual rays on the objective producing beam compres-
sion is illustrated in Figures 57 and 58. These photographs have
been overexposed to bring out the individual ray traces through the
waveguide. Where scattering occurs, halos appear. In Figure 57
three rays have been employed which intersect with the expansion lens,
which is apparent and identified in the photograph of Figure 57. The
rays beyond the expansion lens rapidly become diffuse because the
exit aperture of each ray is less than 10µ, producing divergence by
diffraction. The angular size of this beam is evidenced by the
throughput radiation scattering from the edge of the Si wafer.
Figure 58 is identical to that of Figure 57 except that the two addi-
tional marginal rays do not intersect the expansion beam and thus
traverse the substrate and exit as indicated. These two rays do not

91

250μ Dia.
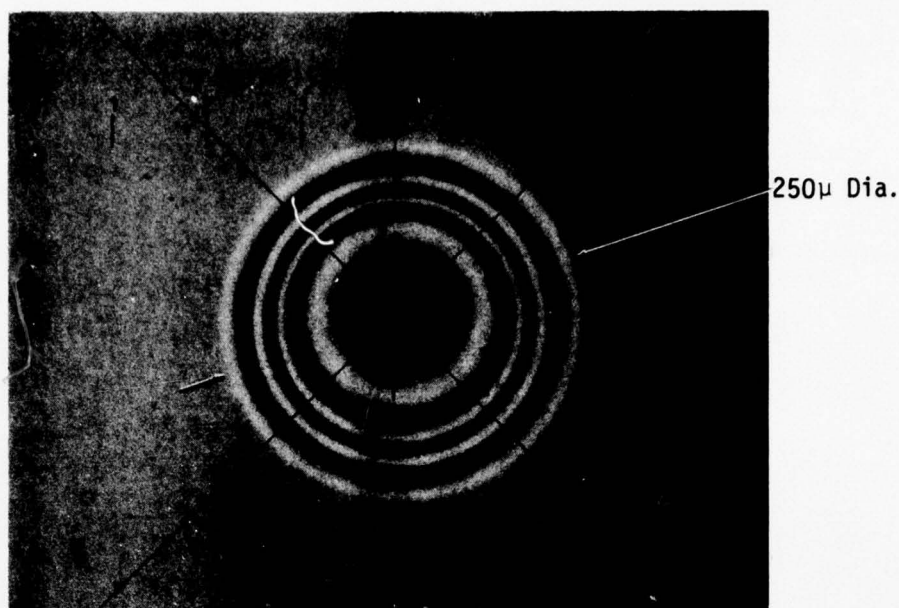
Figure 56.   Enlargement of the Expansion Luneburg Lens in Fig. 55
             Showing Newton Rings Depicting the Radial Thickness
             Profile (radial asymmetry due to off set during
             deposition).

intersect the expansion lens because of an error in the lens thickness profile causing spherical aberration for this outer zone.

The operation of the X90 generalized Luneburg beam expander with the input applied to the expansion lens traversing the system in an opposite direction to that of Figures 57 and 58 is shown in Figure 59. Again it has been necessary to overexpose the film to depict the ray trajectory through the expansion lens system. Scattering due to application of a prism coupler is evident in the output region. Throughput through the beam expansion has been obscured by a black screen showing the forward low angle scatter from the objective lens. The output collimation of the generalized Luneburg lens X90 beam expander is shown in Figure 60. The exit beam from the output prism coupler has been made visible by scanning white paper through the beam longitudinally. The collimated output beamwidth is 4mm. Several X90 beam expanders have been fabricated, demonstrating that the processing is sufficiently under control to obtain collimation for each unit. This is achieved by control of the deposition time.

92
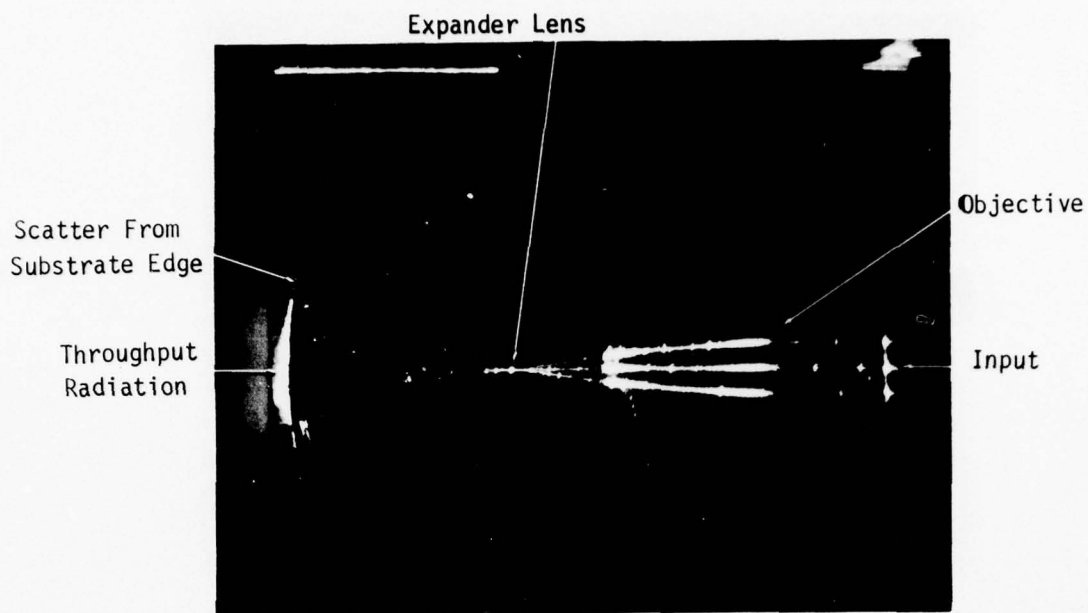
Figure 57. Individual Ray Traces Through Generalized Luneburg Lens
Beam Expander (X90) With Input Applied to Objective Pro-
ducing Convergence on Expander Lens Showing Throughput
Scattered From Edge of Substrate.
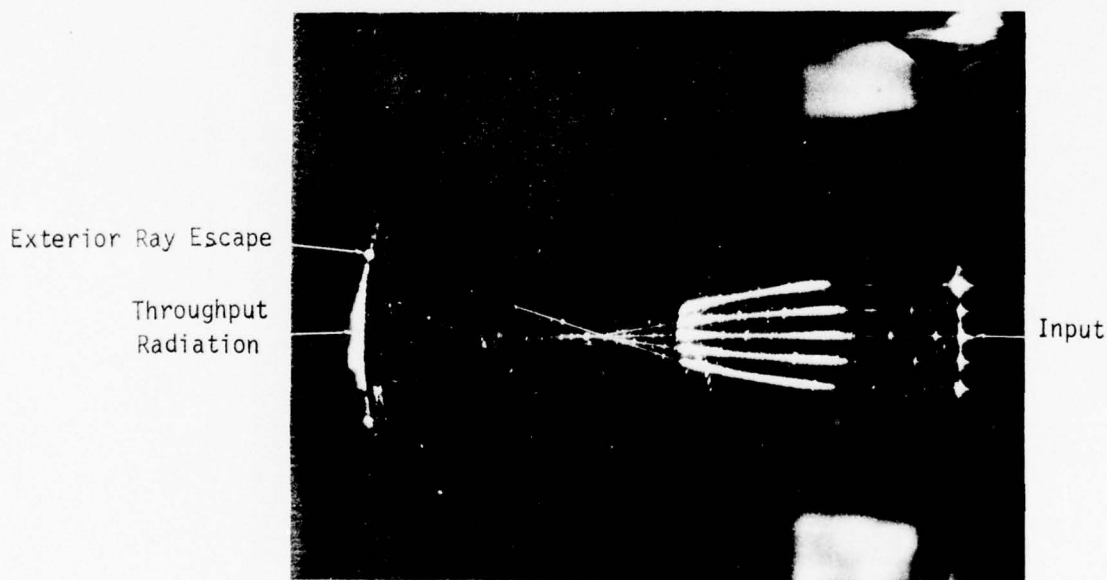
Figure 58. Individual Ray Traces Through Generalized Luneburg Lens
Beam Expander (X90) With Input Applied to Objective Pro-
ducing Convergence on Expander Lens Showing Throughput
Scattered From Edge of Substrate With Two Additional Ray
Traces Which Do Not Impinge Upon the Small Expansion Lens.

93

Output Scatter
on Black Screen
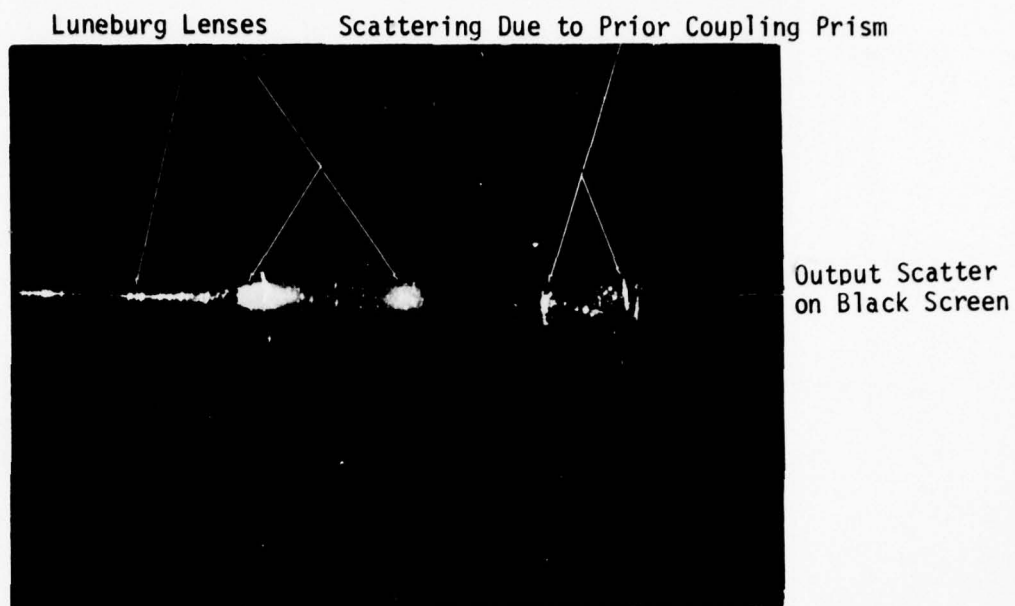
Figure 59. Operation of Generalized Luneburg Lens Beam Expander (X90)
Shown in Figure 55 Using Ta_2O_5 Lens Overlays on Thermally-
Grown SiO_2 on Si (Same as Figure 51).

4 mm
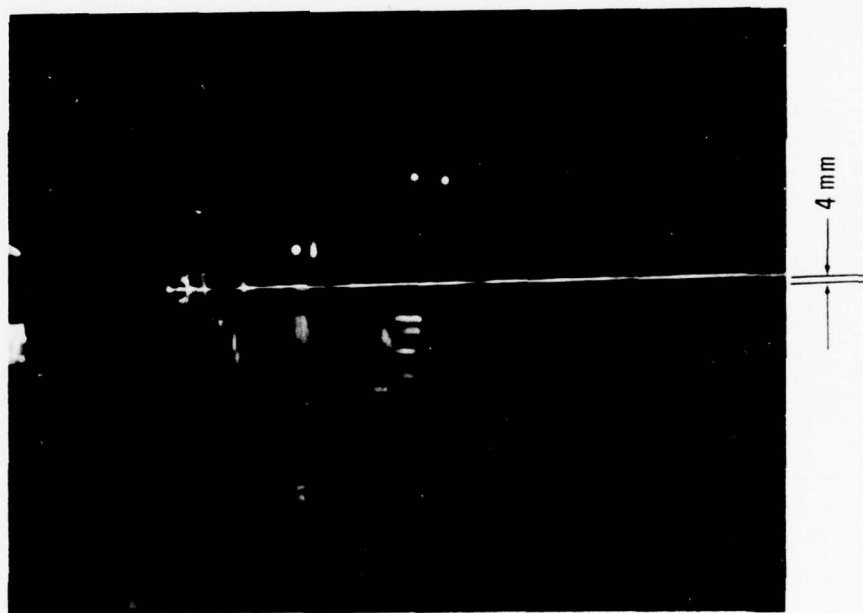
Figure 60. Generalized Luneburg Lens Beam Expander (X90) With Prism
Output Coupler Showing Output Beam Collimation.

94
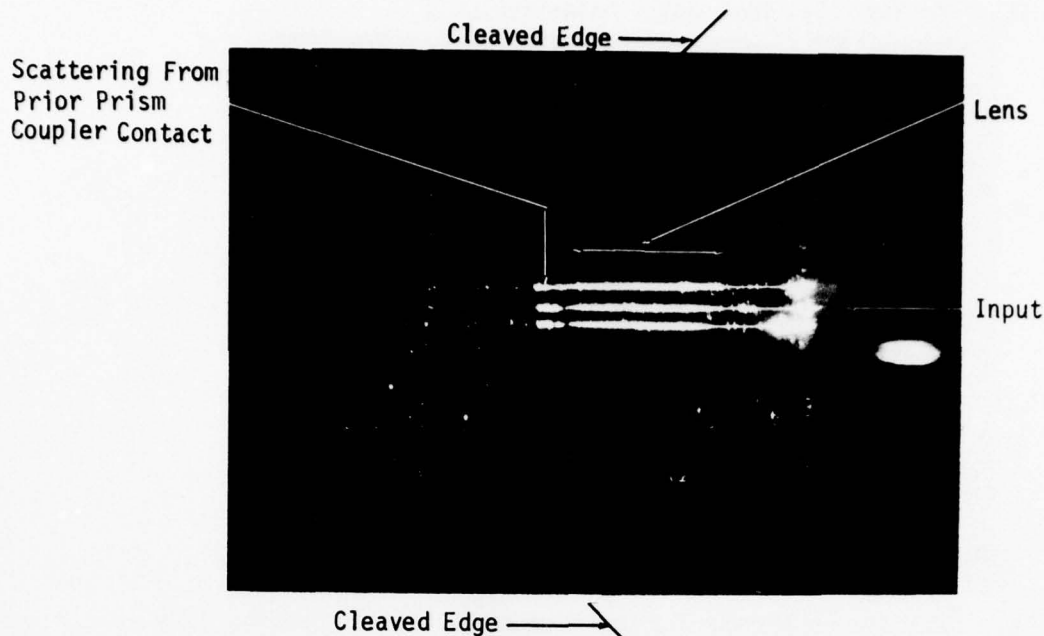
Figure 61. Ray Traces Through Generalized Luneburg Lens Having
Focal Length of 7.5 cm Using Cleaved Retroreflectors.

Generalized Luneburg lenses with comparatively long focal length
are another type of requirement. They have been demonstrated by
using retroreflectors. The operation of one example is shown in
Figure 61 using three ray traces through the system. Again the photo-
graph has been overexposed to partially depict rays traversing the
Corning 7059 waveguide. The focus is obscured by the light shield of
the input prism coupler. The exit lens interface has also been
obscured by scattering from a prior prism contact. Each of the
reflectors employ total internal reflectors using cleavage for their
formation. The focal length of the lens depicted in Figure 61 is
approximately 7.5 cm. Close inspection of the incident rays and exit
rays from the retroreflector shows that they are not parallel,
whereas the angle due to cleavage is exactly 90°. This nonparallel-
ism is due to a 3° offset from the {100 plane} in the Si substrate.

Another lens having a comparatively long focal length beyond that
of the substrate dimensions is depicted in Figure 62. This lens
shows the presence of a higher order mode and thus exhibits two foci.
Rays traversing the lens and exiting the lens are of the TE_0 mode.

95

TE$_0$ Mode Ray   TE$_1$ Mode Ray   Objective Lens

Scatter From
Prism Contact
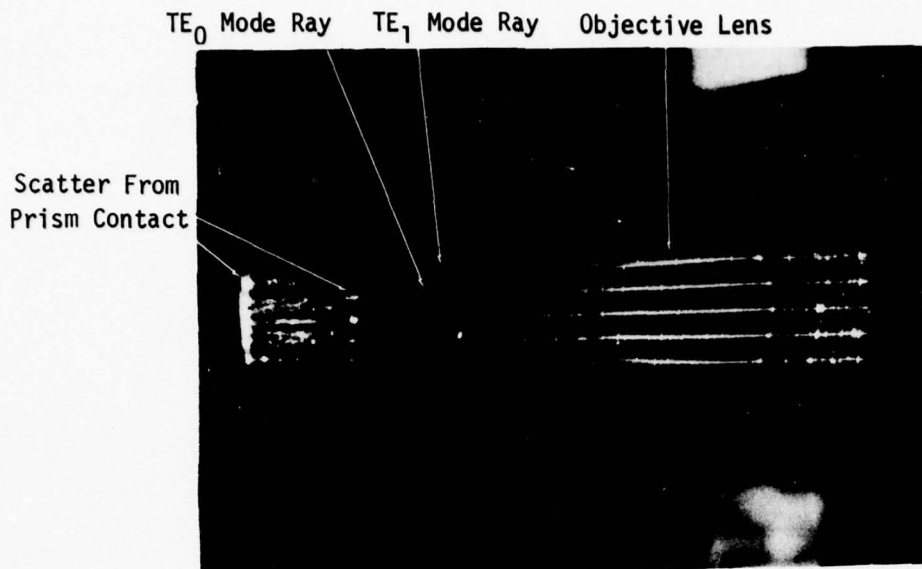
Figure 62.   Ray Traces Through Generalized Luneburg Lens Showing Halo
             Scatter in the Lens Region and Mode Conversion With Equal
             Power in TE$_0$ and TE$_1$ Modes Providing a Focal Length of
             3.4 cm and 10.1 cm, Respectively. (Selected Sample to Show Modes)

The power is divided between TE$_0$ and TE$_1$ modes approximately equally
at the lens entrance face. Mode conversion of the higher order
to the zero order occurs at the exit face. Suppression of mode con-
version is accomplished by introducing symmetry in the waveguide as
exemplified in Figure 2. Inspection of the radial refractive-index
profile, Figure 16, and the corresponding radial thin-film overlay
thickness profile, Figures 22, 45 and 47, show the relative thickness
and thickness gradient at the edge of Luneburg lenses as the focal
length is increased. Exploiting symmetry prevents the excitation of
TE$_1$ modes. The interface discontinuity will excite high order modes.
Control of the thickness will prevent propagation of TE$_2$ and higher
orders. In general the sharp transitions are not realized experimen-
tally (see Figure 42, AFAL TR-76-54). The photograph of Figure 62
also shows residual scratches due to prior contacting of prism
couplers.

Quantitative diffraction data for a series of generalized Luneburg lenses will follow comparing the measured diffraction pattern with the illumination function and with the mask shape employed to form the lens.* Figures 63 and 64 depict measured diffraction patterns for a generalized Luneburg lens having a focal length of 4.5cm using uniform illumination which will produce the $\text{sinc}^2 x$ function. The input beamwidth W has been varied in the range 7.5 to 1.0 for the sequence of Figures 63 and 64. The measured beamwidth in microns at the 5 dB point is indicated on each diffraction pattern with the calculated beamwidth enclosed in parenthesis for each of the input apertures. For the largest illumination width, W=7.5mm, the ratio of measured beamwidth to calculated beamwidth is 2.6, decreasing to 1.95 for W=5mm, 1.63 for W=4mm, 1.25 for W=3mm, 0.9 for W=2mm and 0.6 for W=1mm. Inspection of this sequence and the gradual reduction of near-in sidelobes shows that as the illumination aperture is reduced, the magnitude of the aberration is reduced. The measured results indicating that the diffraction pattern width is less than the calculated value should not be disturbing because it only indicates that the waveguide lens is in the far field of the input aperture iris and that the true illumination function is not uniform but is developing a distribution resembling the sinc x function. One may conclude that the lens is operating near the diffraction limit for an input aperture of 3mm.

Each of the diffraction patterns in the sequence shown in Figures 63 and 64 shows an asymmetry of the sidelobes which is due to leakage around the fiber probe employed to scan the diffraction pattern. Inspection of the diffraction patterns for W=5,4 and 3mm shows a consistent repetition of the sidelobes with increasing null depth as the aperture is decreased. This is due to a decreasing spherical aberration as the lens is stopped down. Reversal of this trend appears in the diffraction pattern for W=7.5mm which suggests a higher order even distortion of the quadratic phase error. These data suggest that the Luneburg lens thickness is excessive in the 3-5mm zone and that the thickness may be deficient in the zone beyond 5mm. This

* See page 108 for experimental method

97

Figure 63. Collage of Diffraction Patterns for the Same Generalized Luneburg Lens Where the Input Aperture Has Been Varied to Observe the Zonal Effects Upon the Diffraction Pattern. Lens Ta_2O_5-on-7059 on SiO_2/Si. The Focal Length = 4.5 cm. Uniform Illumination
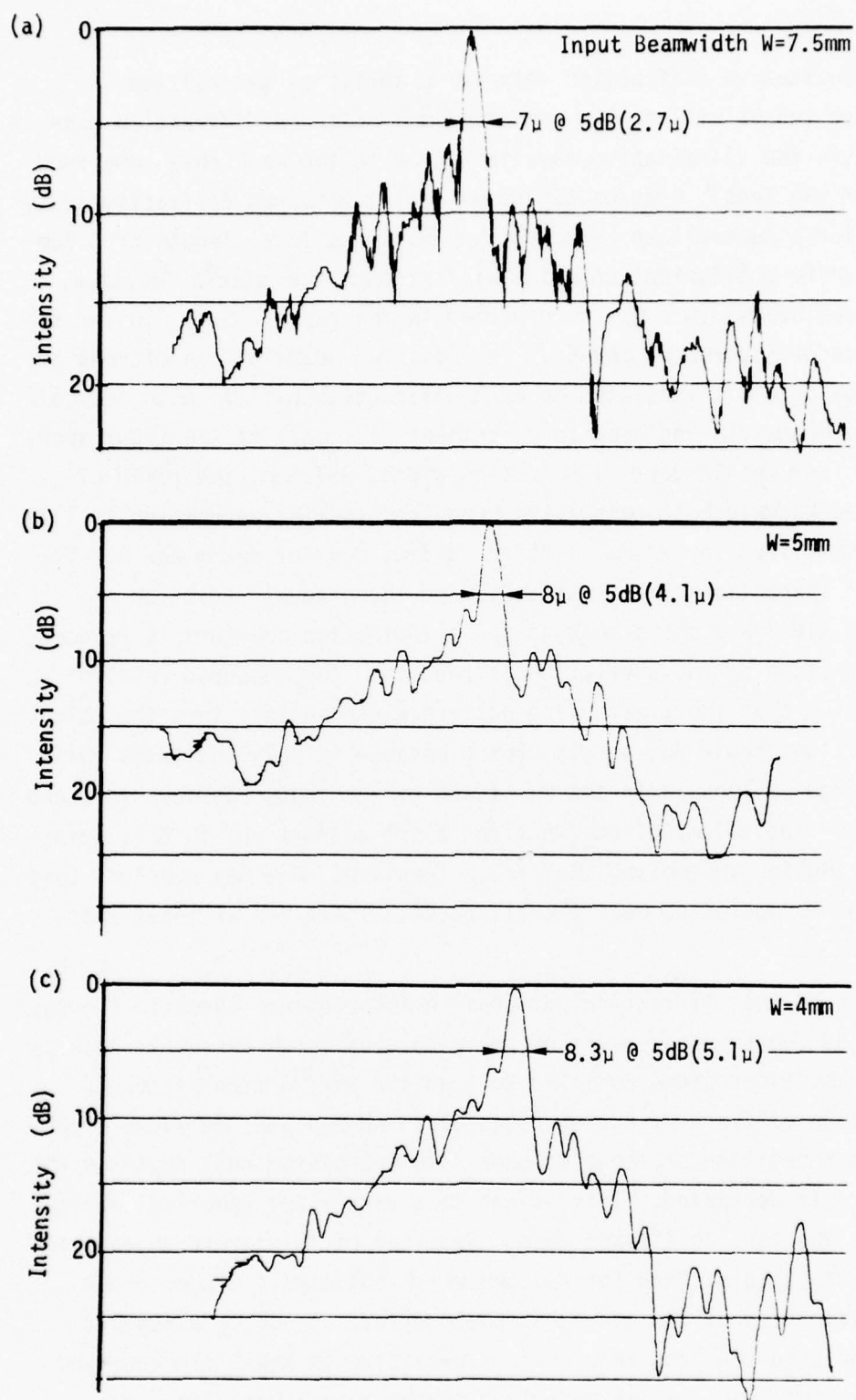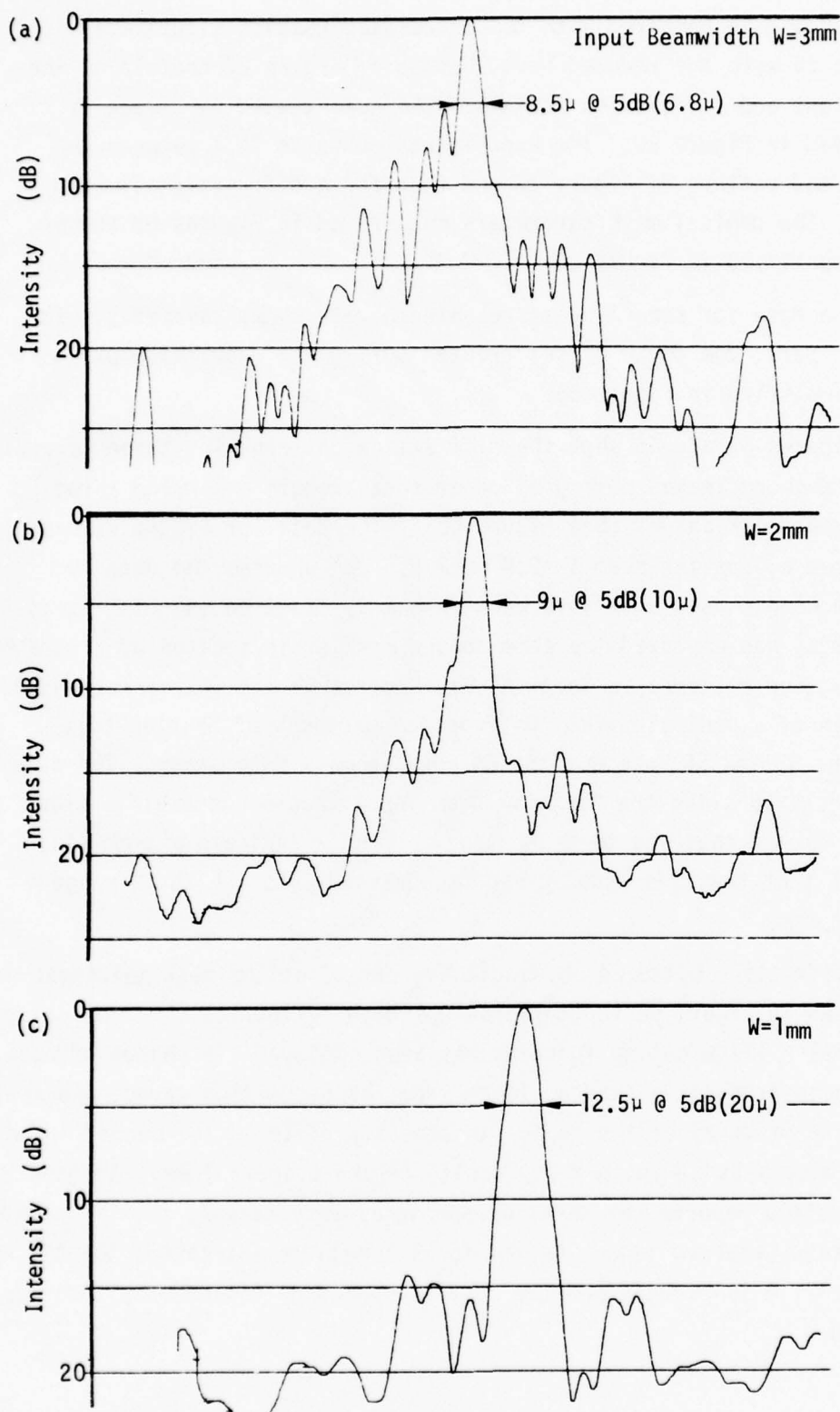
Mask: Conical $\Theta=30°$, T=3.8mm, D=19mm

98

(a) Input Beamwidth W=3mm

8.5μ @ 5dB(6.8μ)

Intensity (dB)

(b) W=2mm

9μ @ 5dB(10μ)

Intensity (dB)

(c) W=1mm

12.5μ @ 5dB(20μ)

Intensity (dB)

Mask:Conical Θ=30°, T=3.8mm, D=19mm

Figure 64. Continuation of Collage of Diffraction Patterns for the Same Generalized Luneburg Lens Where the Input Aperture Has Been Varied to Observe the Zonal Effects Upon the Diffraction Pattern. Lens Ta_2O_5-on-7059 on SiO_2/Si. The Focal Length = 4.5 cm.

99

data should be compared with the calculated results illustrated in Figure 25 with the reduced perturbation of Figure 27 containing the wavefront and diffraction pattern. The accentuated ray trace is depicted in Figure 25. The experimental results fall between the distorted pattern of Figure 27 and that for a diffraction-limited beam. The conical mask parameters enumerated in Figures 63 and 64 are identified in Figure 50.

The data for some lenses presented herein shows asymmetry. It is, in part, due to an offset created during the deposition process as exemplified in Figure 56.

Figures 65 and 66 show the diffraction patterns for three generalized Luneburg lenses having a longer focal length employing three different mask shapes (See Figure 50). The data for Figure 65 has utilized a Gaussian beam (W=2.4 mm @ 8.6 dB) whereas the data for Figure 66 has used a uniform beam (W=6 mm). Section (a) of Figures 65 and 66 has employed the same convex mask cross section of Figure 50. Diffraction patterns in Section (b), Figures 65 and 66, correspond to the use of a conical mask. Diffraction patterns of Section (c), Figures 65 and 66, are due to the concave mask edge shape. The data of Figure 65 using the Gaussian beam input should not exhibit side lobes except that due to truncation. It does indicate a promising result that the side lobes can be suppressed into the 25 dB range and beyond.

Diffraction patterns showing the gross effect of mask thickness are depicted in Figure 67 for three values with cylindrical and conical shapes. A Gaussian illumination function has been employed. A change of mask thickness produces a shadow effect from the deposition target and controls the rate of decay of the radial thickness profile in the manner in which these errors build up in the vicinity of the primary lobe. In general, the profile reported by Zernike[35] approaches very closely that required for a classic Luneburg lens. As the focal length is increased, the thickness of the film is reduced and the cone is opened up toward a cylinder and beyond.

100
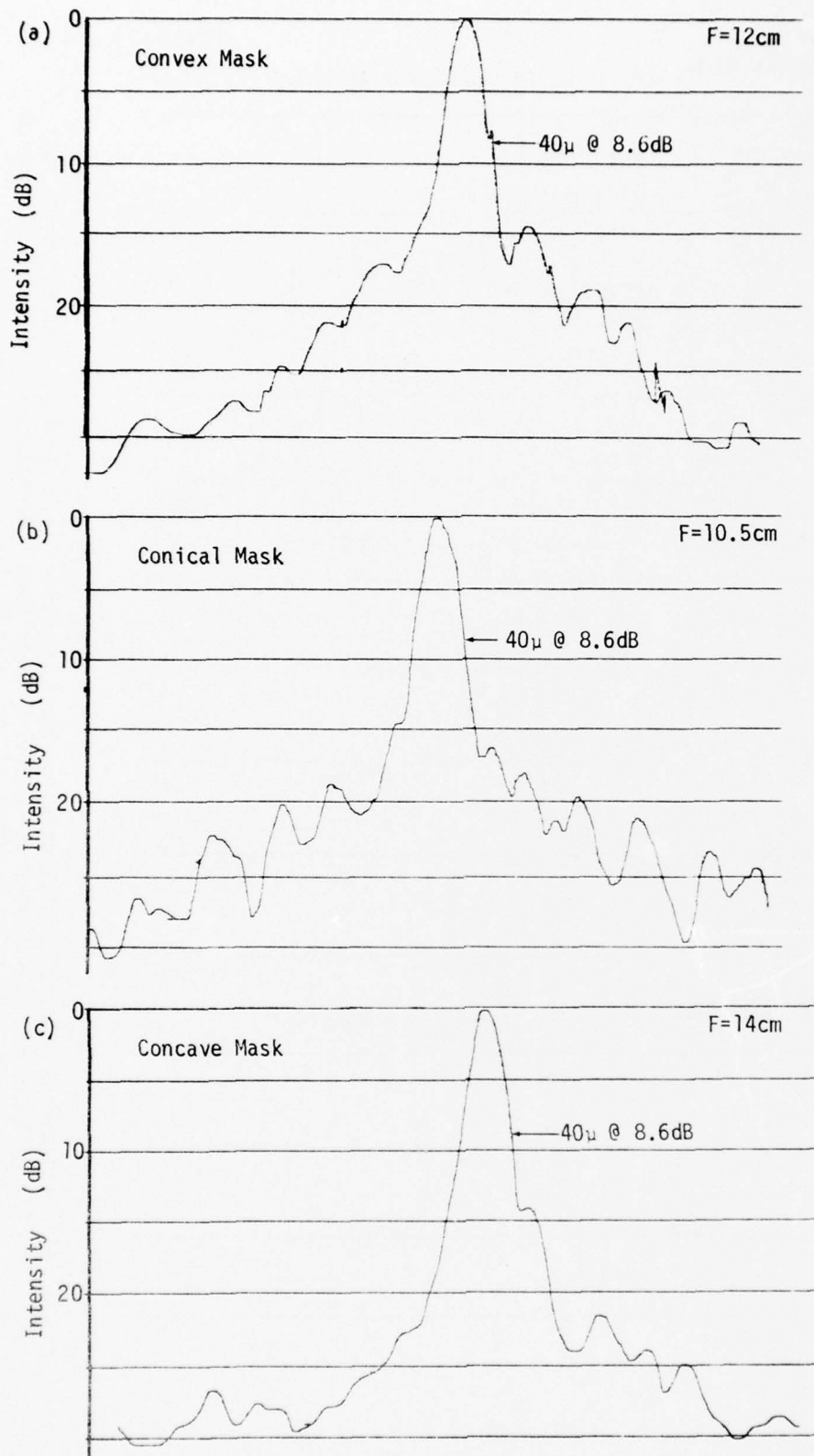
Figure 65. Collage of Diffraction Patterns for the Same Generalized Luneburg Lens Where the Mask Edge Shape Has Been Varied to Observe Effects Upon Diffraction Pattern. Lens Ta_2O_5-on-7059 on SiO_2/Si. Focal Length = ≈11 cm. Input Gaussian Beam Width 2.4mm @ 8.6dB

101
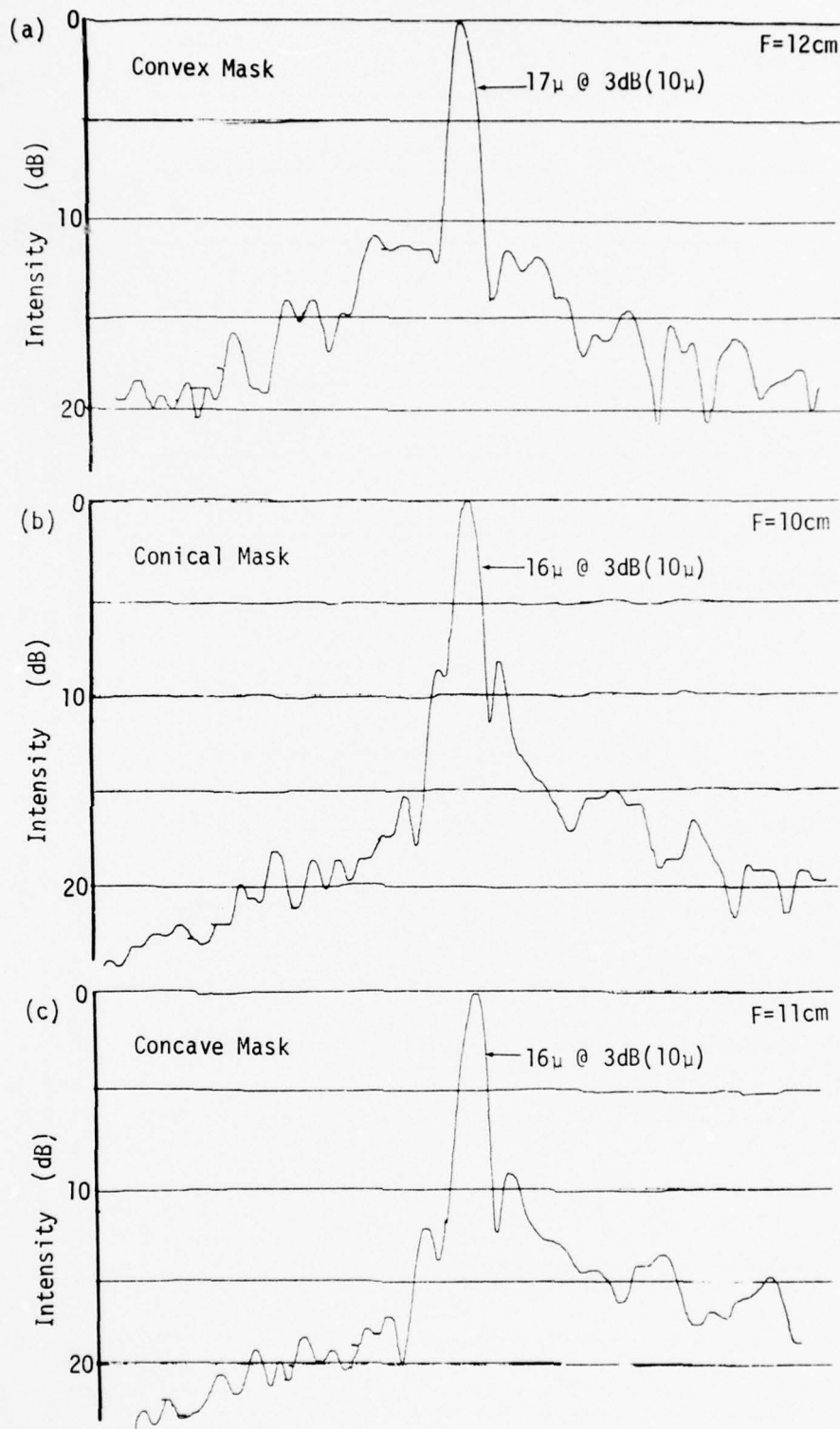
Figure 66. Collage of Diffraction Patterns for the Same Generalized Luneburg Lens Where the Mask Edge Shape Has Been Varied to Observe Effects Upon Diffraction Pattern. Lens Ta_2O_5-on-7059 on SiO_2/Si. Focal Length = ≈11 cm. Input Illumination Uniform W=6mm.

(a) T=1.3mm   Θ=45°   F=10cm

D=12.7mm

←30μ @ 8.6dB

Intensity (dB)

0

10

20

(b) T=2.5mm   Θ=0°   F=10cm

D=12.7mm

←30μ @ 8.6dB

Intensity (dB)

0

10

20

(c) T=3.8mm   Θ=0°   F=10cm

D=12.7mm

←30μ @ 8.6dB

Intensity

0

10

20
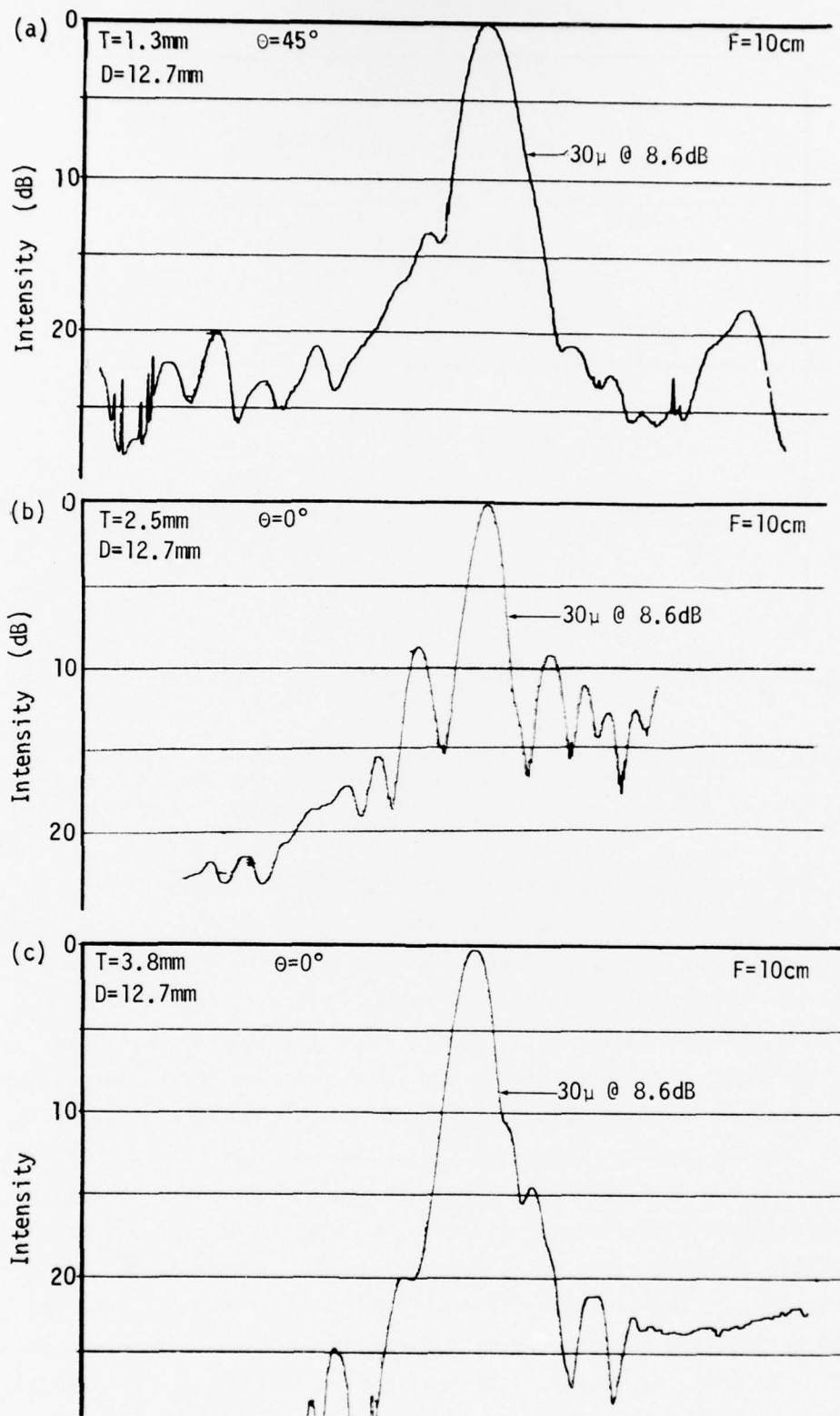
Figure 67. Collage of Diffraction Patterns for Generalized Luneburg Lens Where the Mask Thickness and Conical Edge Has Been Varied to Observe Effects Upon Diffraction Pattern. Lens Ta_2O_5-on-7059 on SiO_2/Si. Focal Length = 10 cm. Gaussian Beam Width 2.4 mm @ 8.5 dB.

103
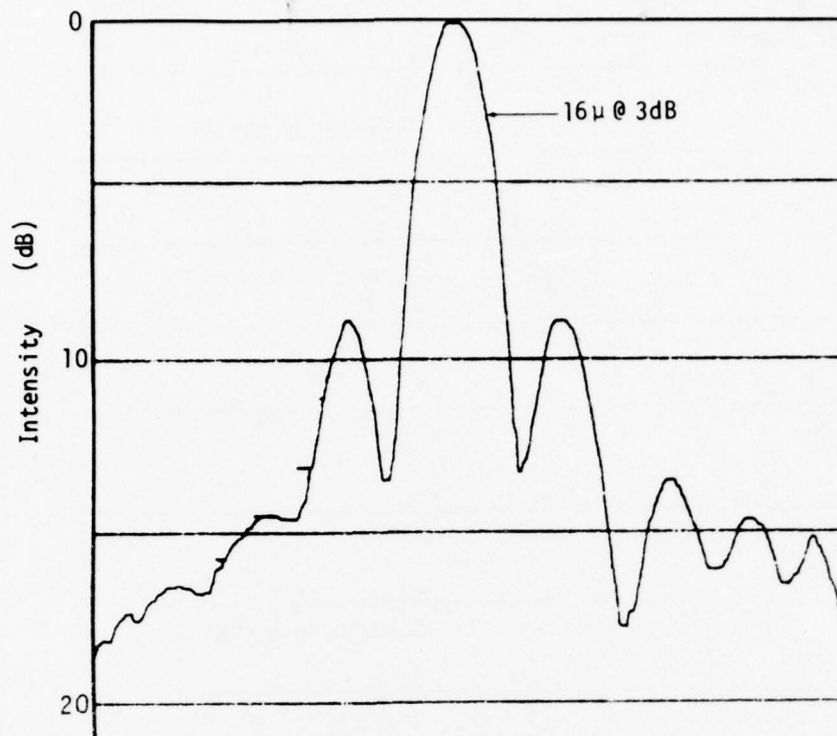
Figure 68. Generalized Luneburg Lens Diffraction Pattern (Same as Figure 66, Section (b), Except for the Use of Reimaging System), Focal Length F=10 cm, Uniform Illumination W=6 mm.

The generalized Luneburg lenses depicted in Figures 64, 65, 66 and 67 have comparatively long focal lengths, some of which extend beyond the substrate. For these lenses, an optical fiber probe has been employed to directly scan the diffraction pattern, rather than employing the re-imaging system described in the following section. The diffraction pattern, Figure 68, is the same as the pattern depicted in Figure 66, Section (b), except that it has been remeasured using a re-imaging system. The results depicted in Figure 68 were obtained using a Zeiss metallographic (long working distance) 40X objective. This refractive microscope objective is known to be near-diffraction limited. For this long focal length lens on a substrate of limited dimension, it was necessary to position the prism coupler near the lens so that the focal point is outside of the thin-film waveguide and prism coupling region. The measured beam width is approximately 1.6 greater than the calculated diffraction limited beam width using

104

a nearly uniform aperture illuminations 6 mm wide. The side lobe level is at 8 dB instead of the 13 dB for uniform illumination and is symmetrical. From this side lobe level and the null depth, it can be inferred that some spherical aberration is present and that the wavefront phase error is approximately $\pi/2$. Symmetry of the diffraction pattern indicates the lack of a cubic phase error (coma).

The diffraction pattern of a generalized Luneburg lens with a substantially larger numerical aperture is shown in Figure 69. The lens has employed a Ta_2O_5 overlay on BaO-rich 7059 waveguide on 7059. The lens f/number is 1.07, however, it is illuminated so as to operate with an f/number of 2.4 in Section (a) and 4.8 in Section (b). A large diameter Gaussian beam is employed with an iris as a source so that the smaller beam is approximately uniform, while the larger beam approximates the cosine. This diffraction pattern was measured using the re-imaging system described in the following section where the properties of the re-imaging lenses are illustrated. The measured beam width is 5 microns @ 3 dB for both diffraction patterns. The calculated beam width is 1.8 and 3 microns, whereas the ratio, measured to calculated beam widths, is 2.7 and 1.6, respectively.

The inferior performance measured in Figure 69, particularly the former (a), is in part due to several causes. First, the prism coupler introduces a significant spherical aberration and second, the measured results are the convolution of the thin-film lens performance and the re-imaging lens performance, which for this case, are comparable. Further, these results should be compared with the calculated diffraction patterns of Figure 24 or Figure 33 with a larger spherical aberration due to defocusing and its correction in Figure 34 by the slight shift of the focal position or its inverse phase distortion depicted in Figure 38 and its refocused diffraction pattern in Figure 39. These results show that small focused spots are realizable, however, improvements of thin-film lens performance and/or re-imaging lens performance, together with suppression of the spherical aberration introduced by the prism (using an aplanatic hypotenuse), is required to more nearly achieve diffraction limited performance.

105
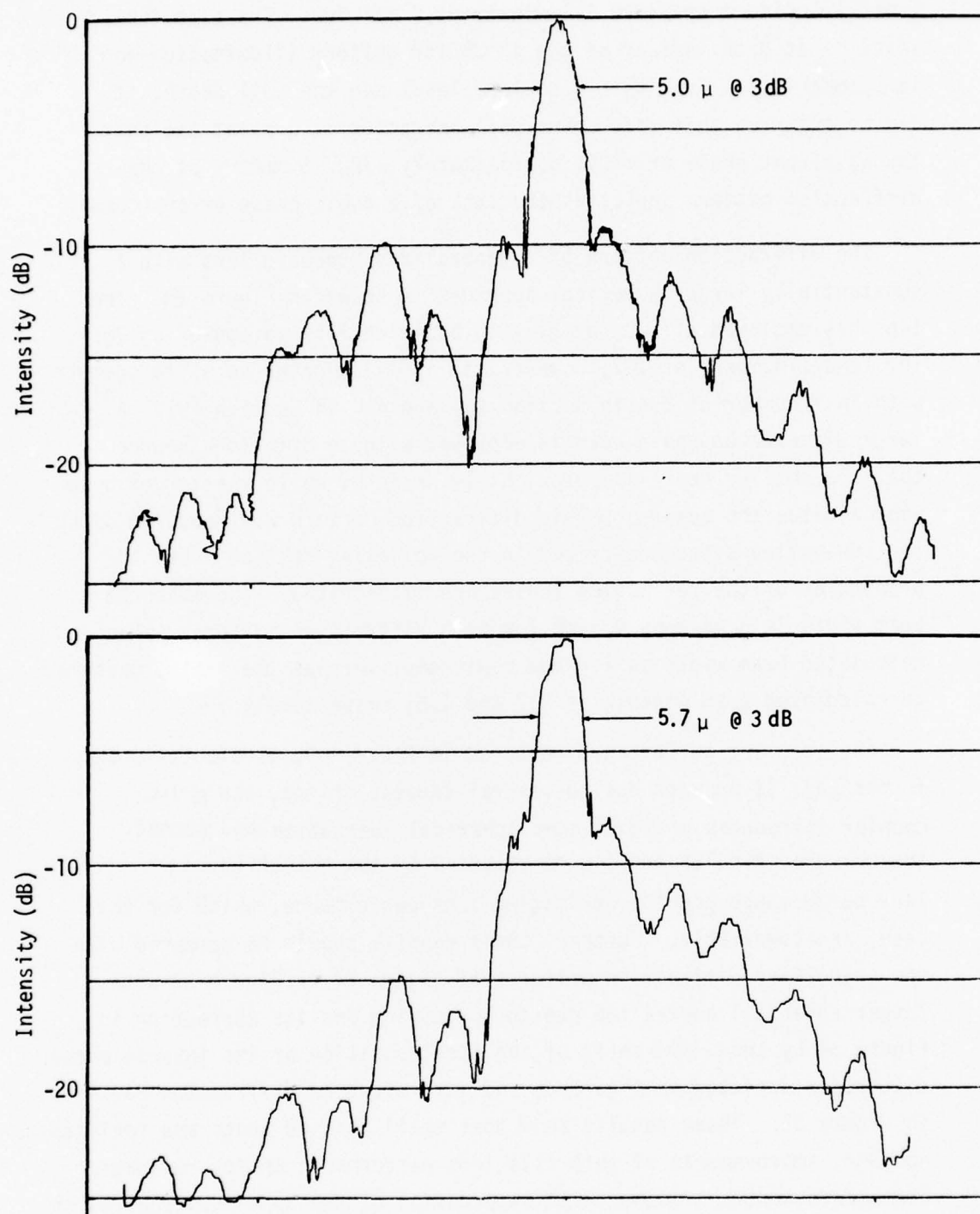
Figure 69. Generalized Luneburg Lens Diffraction Pattern, Ta_2O_5 Lens-on-BaO-rich 7059-on-7059, Lens Diameter 11.2^2 mm, Focal Length 12 mm, Using (a) Cosine Illuminated 5 mm Aperture and (b) 2.5 mm Irised Section of (a) Approximately Uniform).

106

The fact that the side lobe level and its decay on the left side of the diffraction pattern in Figure 69 is substantially different is due to the fact that the input beam, when extended in width, encompasses a visible scattering center. The fact that the wide lobe period and the primary lobe width are substantially identical in both patterns when the aperture is increased, strongly suggests that the measured diffraction pattern is dominated by the re-imaging lens performance, rather than being determined by the Luneburg lens performance. (See Figure 72).

107

5. Optical Waveguide Lens Characterization

The performance of conventional optical elements is determined by various procedures such as measurement of the diffraction pattern for an accurately known source or by measurement of modulation transfer function for periodic sources having variable period.[41,42] In each case, access to the image plane is required for probing of the field intensity in the image plane. For optical waveguide lenses, this technique is not practical because the lens is immersed in an ambient dielectric waveguide.

When the ambient dielectric waveguide exhibits uniform scattering it is possible to observe the field distribution spatially through the scattering mechanism. However, in general the lens and waveguide which exhibit sufficient scattering for this type of observation also represents an unsatisfactory lens for use in an optical Fourier transform.

The technique employed herein has utilized a re-imaging procedure which is illustrated in the schematic of Figure 70. Prism couplers are employed to launch beams within the thin-film waveguide, which traverse the lens under investigation utilizing another prism coupler to extract the field which is relayed and re-imaged with magnification where it is possible to probe the field distribution in this latter plane. An optical fiber probe has been employed with its entrance face metalized which contains a thin slit. The fiber probe is mechanically scanned in any of the three major axes providing a signal to drive a recorder, while the optical signal is detected, amplified and compressed to give a logarithmic scale for the recorder. All experimental diffraction patterns reproduced herein have been measured in this manner. The physical apparatus showing the laser source, collimation optics, waveguide assembly with prism couplers, re-imaging lens, mechanically scanned fiber probe and recorder are depicted in Figure 71.

108
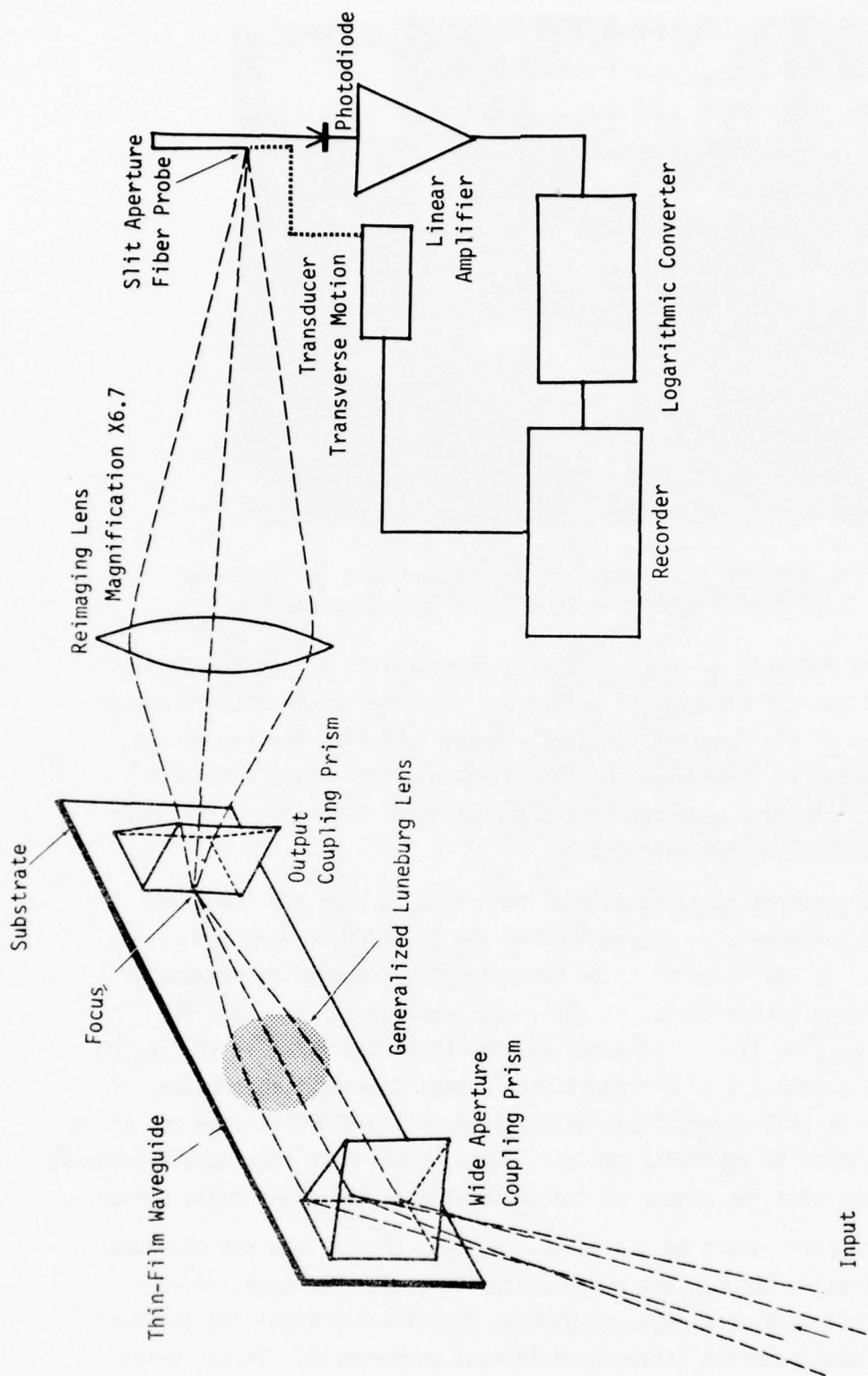
Figure 70. Schematic of Reimaging Technique to Characterize Thin Film Waveguide Lenses

109
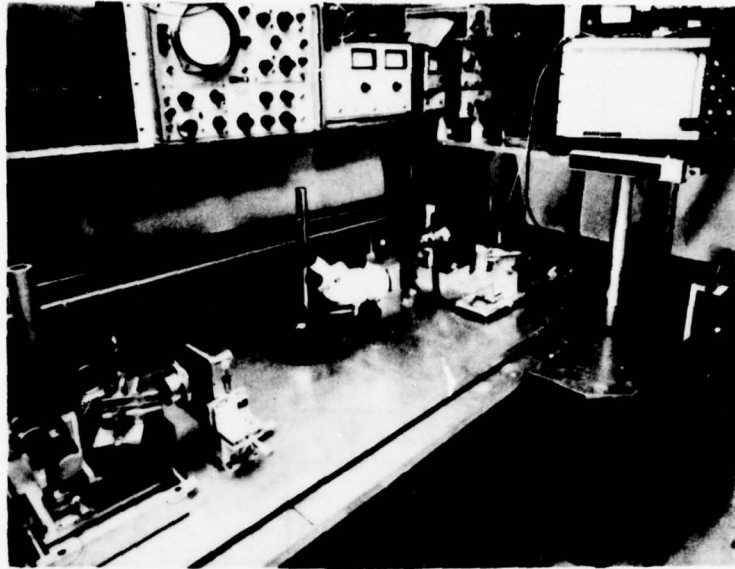
Figure 71. Photograph of Apparatus for Measurement of Thin-Film
Waveguide Lenses Using Fiber Probe of Re-imaging Beam

The measured re-image intensity distribution is the convolution
of all optical elements in series and thus the measured distribution
is that of the "poorest" optical element including the sum of all
aberrations. Therefore, characterization of thin-film waveguide
optical elements requires that the additional elements exhibit near
diffraction-limited performance.

Non-uniform coupling across the prisms in both the input and
output contribute to degradation of the observed diffraction pat-
terns. It was found that the prism couplers require an extremely
sharp edge without chips at the right angle corner and that the
faces must be flat. The prism coupler with flat faces in the region
of the convergent or divergent beam causes spherical aberration. To
eliminate this effect, some aplanatic prisms were fabricated and are to
be employed in the focal region. These prisms have spherical hypotenuse
surfaces with the center of radius located at the right angle corner.

The performance of the re-imaging lens enters into the observed
distribution through the convolution integral. Two types of re-
imaging lenses were employed without specifically acquiring the unit
which would exhibit diffraction-limited performance. These lenses
are (a) Spectra-Physics Model 333 Objective, focal length 86mm and

110

f-number 3.5, and (b) Wollensak Oscillo-Raptar, focal length 75mm and f-number 1.9. Using a 1μ diameter pinhole and 6328 Å radiation, the measured transverse field intensity distribution is shown in Figure 72 for several cross sections in a region of the focus. Cross sections before and after focal region are included. The re-imaged pinhole should yield theoretically diffraction patterns identical to that of Figures 23, 46, and 48, except for the scale factor due to magnification. The measured re-image diffraction patterns of the pinhole fall short of the theoretical diffraction pattern in several ways. The nulls between the first sidelobe and the primary lobe are partially filled in, and the level of the first sidelobe is slightly higher indicating the presence of spherical aberration in the re-imaging lens. The more rapid decay of sidelobes and nearly complete fill-in of nulls indicates the effect of scattering from within the relay lens elements. Further, it is difficult to determine the focus accurately without measuring numerous cross sections.

Inspection of the measured diffraction patterns through the depth of field will show how the relay lens can affect the observed diffraction pattern of a thin-film waveguide lens. It is evident that more precise measurements extending over a larger dynamic range with less scattering is required to more accurately characterize waveguide lenses which are required to achieve near diffraction-limited operation.

It is interesting to note the rate of side lobe decay in each of the relay lenses which must be due to internal scattering between the various lens elements. It will be necessary to reduce this effect substantially so as not to contribute to the observed side lobes and scattering in the thin-film lenses. At this juncture, the thin-film lens performance is comparable to that of the relay lenses so far as wide angle scattering is concerned.

111
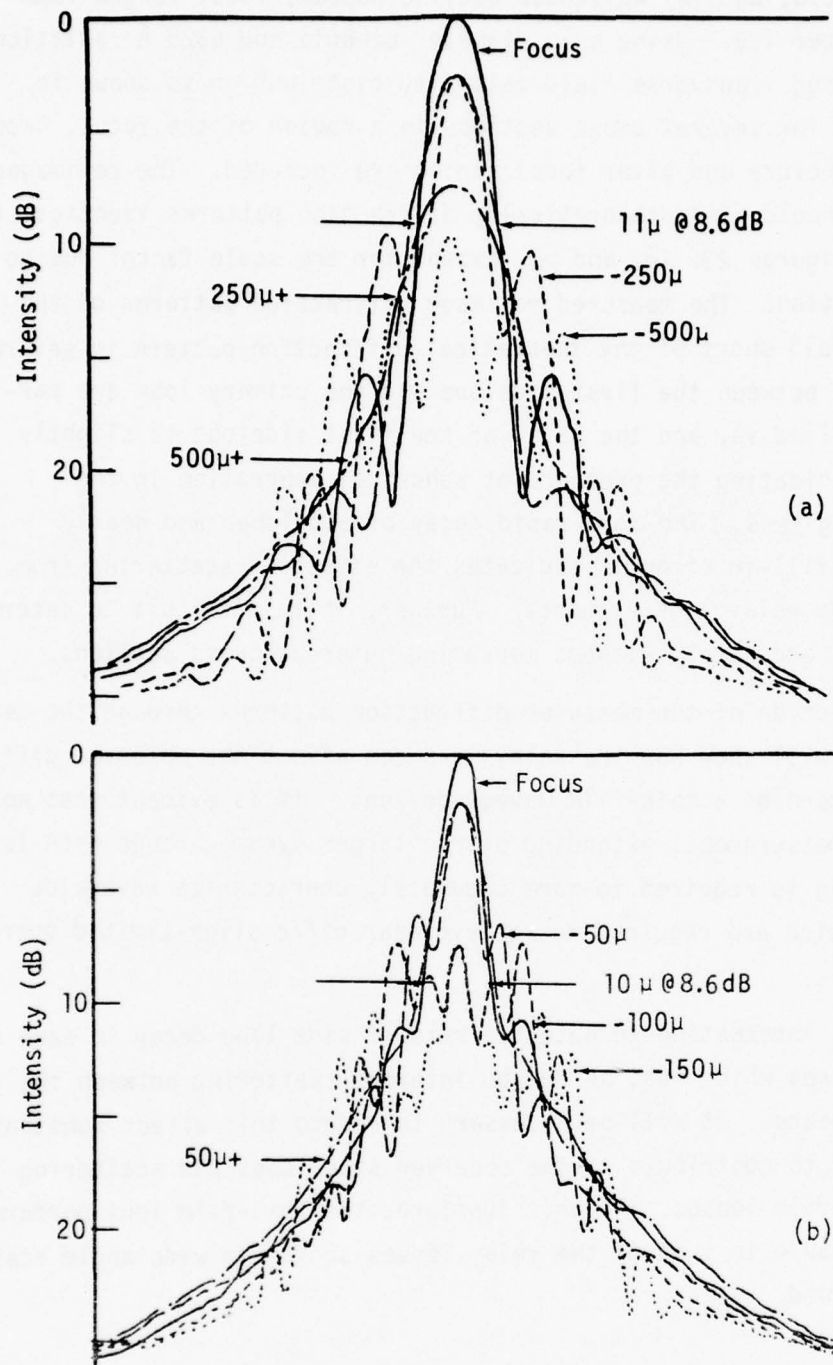
Figure 72   Measured Transverse Beam Intensity Profiles in the
Region of the Focus for Two Types of Reimaging Lenses
on Both Sides of the Focus Using a 1-Micron Diameter
Pin Hole and 6328 Å Radiation (a) Spectra-Physics
Model 333 Objective, FL=86 mm, f=3.5 and (b) Wollensak
Oscillo-Raptar FL=75 mm, f=1.9.

112

D. REFLECTORS FOR THIN-FILM WAVEGUIDE

An important consideration for the design of thin-film waveguide
optical systems is the requirement for reflectors so as to enable
folding of the optical system on a substrate of limited dimensions
and area. The reflector in the plane of the waveguide must function
efficiently and not give rise to the scattering or radiation losses.
An important consideration in the design of waveguide reflectors is
the angular range over which they function efficiently and the means
to achieve reflectivity at any angle of incidence. This section con-
siders reflectors formed by cleavage in single-crystal substrates
that extend through the waveguide thin films.

Dielectric waveguide reflectors which utilize sharp boundaries
are based upon the phenomena of total internal reflection, and there-
fore the angle of incidence is restricted. For 7059 waveguide the
angle of incidence must be greater than 39°. For lesser angles of
incidence it is necessary to metalize the boundary to obtain total
reflection. Aside from waveguide losses, the loss of reflectors
based upon total internal reflection or single metallic reflections
in the near infrared have proven to be insignificant, i.e., less than
0.3 dB.

The operation of a thin-film waveguide retro-reflector employing
total internal reflection is shown in Figure 73 where the substrate
has utilized thermally-grown SiO_2 on {100} Si surface. Silicon
nominally cleaves on the {110} face. The retro-reflector illustrated
in Figure 73 indicates a slight convergence of the return beam. This
is due to the fact that the Si wafer is offset from the {100} plane
by approximately 3°. The first reflective surface is perfect and the
scattered radiation indicates no loss upon reflection. The second
cleavage edge is imperfect, showing some wide-angle forward scatter-
ing. The reflected ray traverses a section of very low loss wave-
guide before intercepting scattering particles.   Figure 74 illustrates
the operation of a metallized cleaved reflector operating at near nor-
mal incidence. This reflector exhibits some wide angle scatter.

113
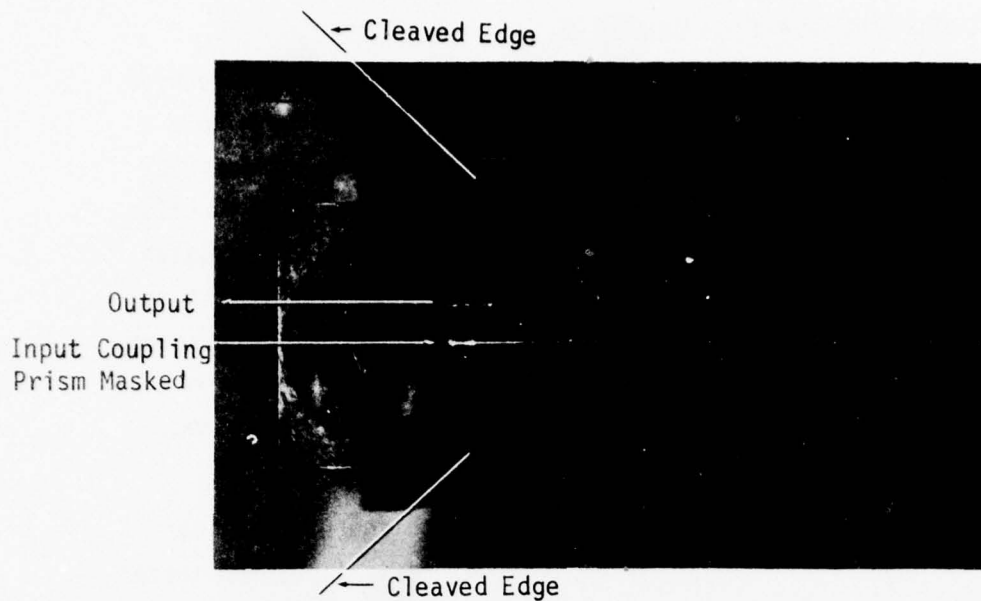
Figure 73. Thin-Film Waveguide Retro-reflector Using Total Internal Reflection Employing 7059 Waveguide on Thermally-Grown SiO$_2$ on {100} Si with Input Ray Incident on Near Perfect First Cleaved Edge and with Imperfect Reflector at Second Edge.
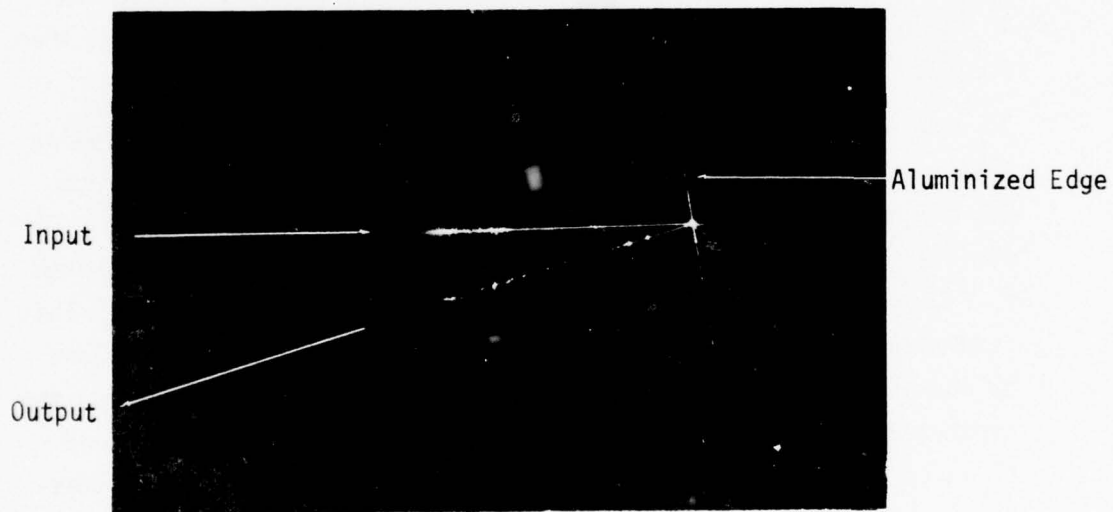
Figure 74. Thin-Film Waveguide Reflector Employing 7059 Waveguide on Thermally-Grown SiO$_2$ on Si Using {110} Cleaved Edge with Aluminization on Edge Only.

(a) {110} (b)

Silicon ——
Thermally-Grown SiO$_2$ ——
7059 Waveguide ——
Ta$_2$O$_5$ Lens Overlay ——
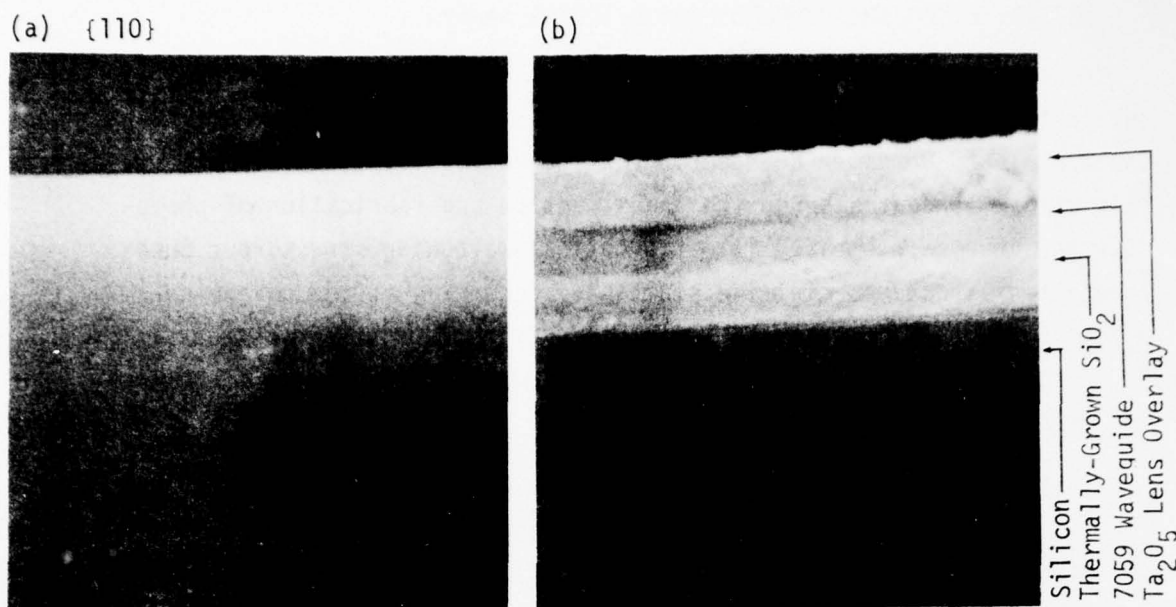
Figure 75.   Scanning Electron Micrograph of Cleaved Reflector Through
Ta$_2$O$_5$ Overlay Luneburg Lens on Corning 7059 Waveguide on
Thermally-Grown SiO$_2$ Isolation Layer on Si Substrate:
(a) Untouched {110} face, (b) Intentionally etched (HF) to
delineate each of the oxide layers.

The perfection of the cleaved reflector surface through the single
crystal substrate and the polycrystalline thin films is illustrated in
Figure 75.   Section (a) is the native cleaved surface.   Because the
various layers are not apparent, an etch has been intentionally em-
ployed to delineate the oxide layers.   The combined thickness of the
thermally-grown oxide and Corning 7059 waveguide is 1μ.

Reasonably perfect reflectors are obtained with lengths of several
centimeters with conventional metallographic techniques when both seg-
ments being cleaved are of comparable dimensions.   Near the edge of a
large diameter wafer (>10 cm), some evidence of imperfection is apparent
presumably due to the nature of the crystalline growth for the larger
diameters.

115

E. OPTICAL WAVEGUIDE COUPLED PHOTODETECTOR ARRAYS

A portion of this Optical Waveguide Lens II program was carried out in the Solid State Electronics Laboratory of the Department of Electrical and Computer Engineering at the University of Cincinnati. This effort concentrated on the investigation and fabrication of photo-detector arrays integrated into the optical waveguide structure. Such integrated structures minimize scattering occurring at the waveguide-detector coupling so that the limitations on resolution and dynamic range in integrated Fourier transform processing devices imposed by scattering are minimal.

In the course of the program, several photodetector arrays with carefully prepared tapers were fabricated at the University and delivered to Rockwell International for subsequent deposition of the waveguide and lens and which were subsequently delivered to the Air Force Avionics Laboratory. This program, in conjunction with another sponsored by the Air Force Office of Scientific Research, demonstrated the first inte-grated charge coupled device image array with an optical waveguide structure. Some results of these combined efforts are contained in the preprint and reprint, Appendices C and D, entitled, "Integrated Optical Waveguide and Charge Coupled Device Image Array" and "Linear Charge Coupled Device Detector Array for Imaging Light Propagating in an Inte-grated Thin-Film Optical Waveguide," respectively. The following sections expand upon the work reported in the appendices avoiding duplication and, therefore, should be read together:

1. Waveguide-Detector Coupling

Waveguide-detector coupling is an important consideration for appli-cations of the integrated structure to Fourier signal processing in that efficient coupling maximizes detector signal sensitivity and maximize adjacent channel signal rejection. The latter property is due to the fact that light which is not coupled from the waveguide into the detector can be scattered into adjacent channels. For the devices fabricated during this program (see Appendix C, Figure 2C and Appendix D, Figure 1D, for example), the SiO_2 layer isolating the optical waveguide from the silicon surface tapers to vanishing thickness in the detector region.

116

Light propagating in the optical waveguide is then multiply-refracted into the detector region.[15] As we note elsewhere in this report, minimizing the array element center-to-center spacing allows the resolution to be maximized. Such spacings are expected to be limited by lithography considerations. On the other hand, the photodiode length along the direction of light propagation needs to be sufficiently long so that nearly all the light incident is multiply-refracted into the silicon substrate. This length should not be long enough to require large aspect ratios which would disrupt normal device processing. We determined this length L_0 for the TE_0 mode and plotted this optimum value of detector length as a function of waveguide thickness d for a waveguide refractive index of n_g=1.61. This refractive index is characteristic of 7059 sputtered glass waveguides. The result of the calculation is shown in Figure 2D included in the Appendix for λ=.9 μm and .6 μm. The portions of the curves to the left of the dotted vertical lines are the regions in which only a single TE mode can exist. In the single mode regions, the optimum detector lengths would allow fabrication of efficient photodiodes with reasonable aspect ratios and with center-to-center spacings approaching photolithographic limits. However, for multimode waveguides, the corresponding optimum detector lengths become quite long. It is fortunate that, in many signal processing applications such as spectrum analysis, use of a single-mode waveguide is advantageous in view of other considerations. In Fourier optical processing utilizing optical waveguide lenses, the integrated waveguide-detector array described herein is utilized in focal plane imaging. If L_0 exceeds the depth of focus for such applications, then an array of channel waveguides with one passing directly over each photodiode would be required to preserve signal integrity.

2. Photodetector Array

The photodiode arrays fabricated in The University of Cincinnati Solid State Electronics Laboratory and delivered to Rockwell International for further processing are shown in Figure 76. Each {100} oriented wafer contained approximately 8 such arrays along a line located near the wafer edge. Over the remaining area of the wafer, a thick layer of thermally-grown SiO_2 was formed (1 μm) so as to provide sufficient isolation of the waveguide from the silicon substrate. An etched taper in the SiO_2 layer was formed

117
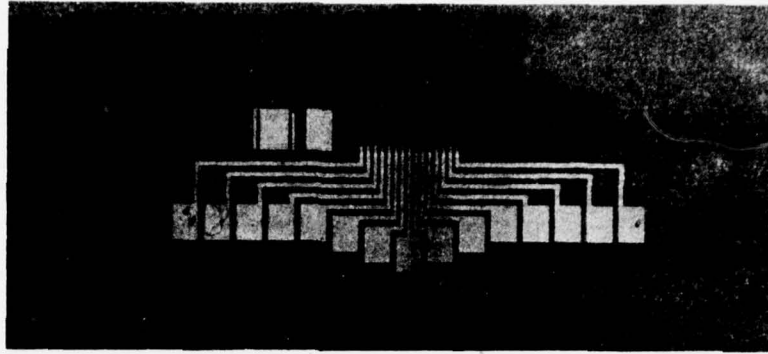
(a) Plan View of Waveguide-Coupled Photodetector Array with Lead Fan-Out
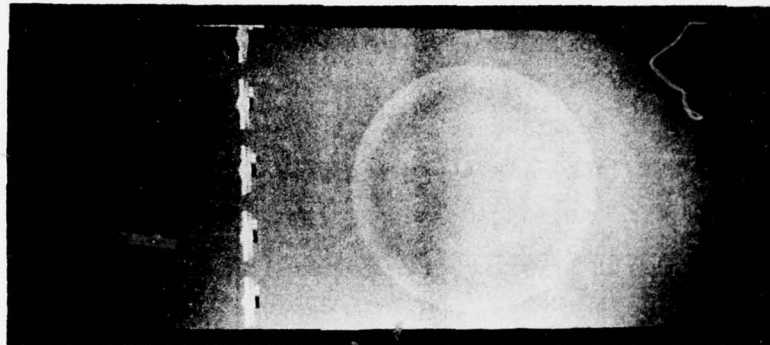
(b) Luneburg Lens with Waveguide-Coupled Photodetector Arrays
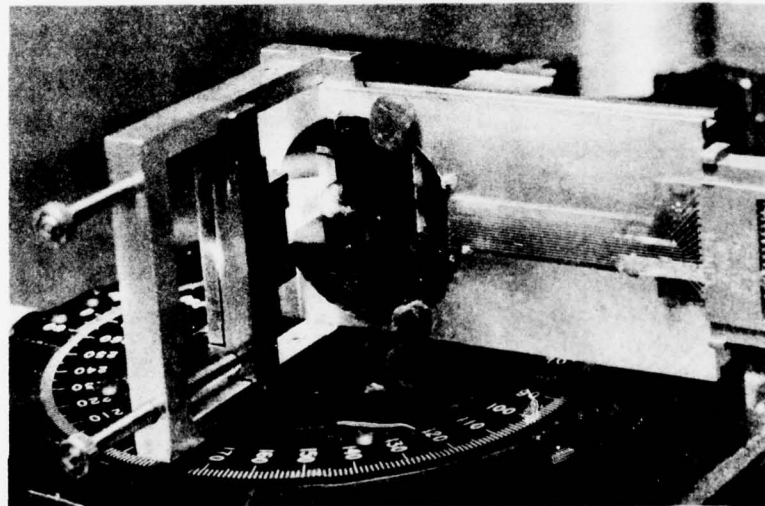
(c) Experimental Apparatus Employed to Demonstrate Operation of Luneburg
     Lens Focus on Detector Array (Scattering of Lens Apparent)

Figure 76.   Photographic Collage of Waveguide Coupled Photodetector
             Array Showing (a) Plan View of Array With Lead Fan-Out,
             (b) Array With Luneburg Lens, and (c) Apparatus Employed
             to Demonstrate Operation of Luneburg Lens Focused on
             Detector Array.

118

approaching the photodiode regions to provide a gradual transition from the thick layer of SiO_2 to a layer of vanishing thickness in the detector region. This taper was formed by undercutting in which the HF etching solution temperature and concentration were carefully controlled.

Each detector array contained 19 elements having a center-to-center spacing of 32 μm. Of the 32 μm, the device width is 25 μm along with 7 μm of isolation. Preferentially-etched V-grooves were formed utilizing KOH as the etchant between photodiodes to prevent leakage. The photo-diodes were characterized by a uniform breakdown voltage of 120 volts at 10 μa. We expect that the use of the V-groove isolation would allow arrays having devices of similar high quality to be fabricated having 1/2 of the above center-to-center spacing. The arrays were processed using n type substrates having a resistivity of 8 ohm-cm. The p diffusion of boron was performed utilizing a boron nitride source. Estimated concentration of the p regions is 10^{16} cm.$^{-3}$ In all, 5 mask steps were utilized in the fabri-cation process. The photographic collage of Figure 76 depicts the wave-guide coupled photodetector array in Section (a) with its lead fan-out contacts. The individual detector sections are apparent. The tapered SiO_2 transition region coupling the waveguide to the detector is evi-denced by Newton fringes. The macroscopic view in Section (b) indicates the presence of a thin-film Luneburg lens positioned to focus the beam on the central detector array. Section (c) of Figure 76 indicates ap-paratus for coupling of radiation into the waveguide optic section show-ing the scattered transmission through the lens section which focuses the radiation onto one photodetector array with leads attached to ex-tract the signal.

3. Integrated Waveguide-Coupled Photodetector Arrays with Charge Coupled Readout

The integrated waveguide-charge coupled device detector array devices have the structure shown in Figure 77. These detector arrays consist of an array of photodiodes formed in n-type silicon connected in parallel by means of a series of gates to a CCD shift register. The charge transfer portion of the device utilizes a two-phase, overlapping-gate structure consisting of one level of polysilicon electrodes insulated by an additional layer of SiO_2 from a second level of overlapping aluminum electrodes.[43] One CCD unit cell corresponds to each photodiode. Channel isolation is main-tained through the series of gates by the presence of channel stopping n+

119

(a)

(b)

(c)
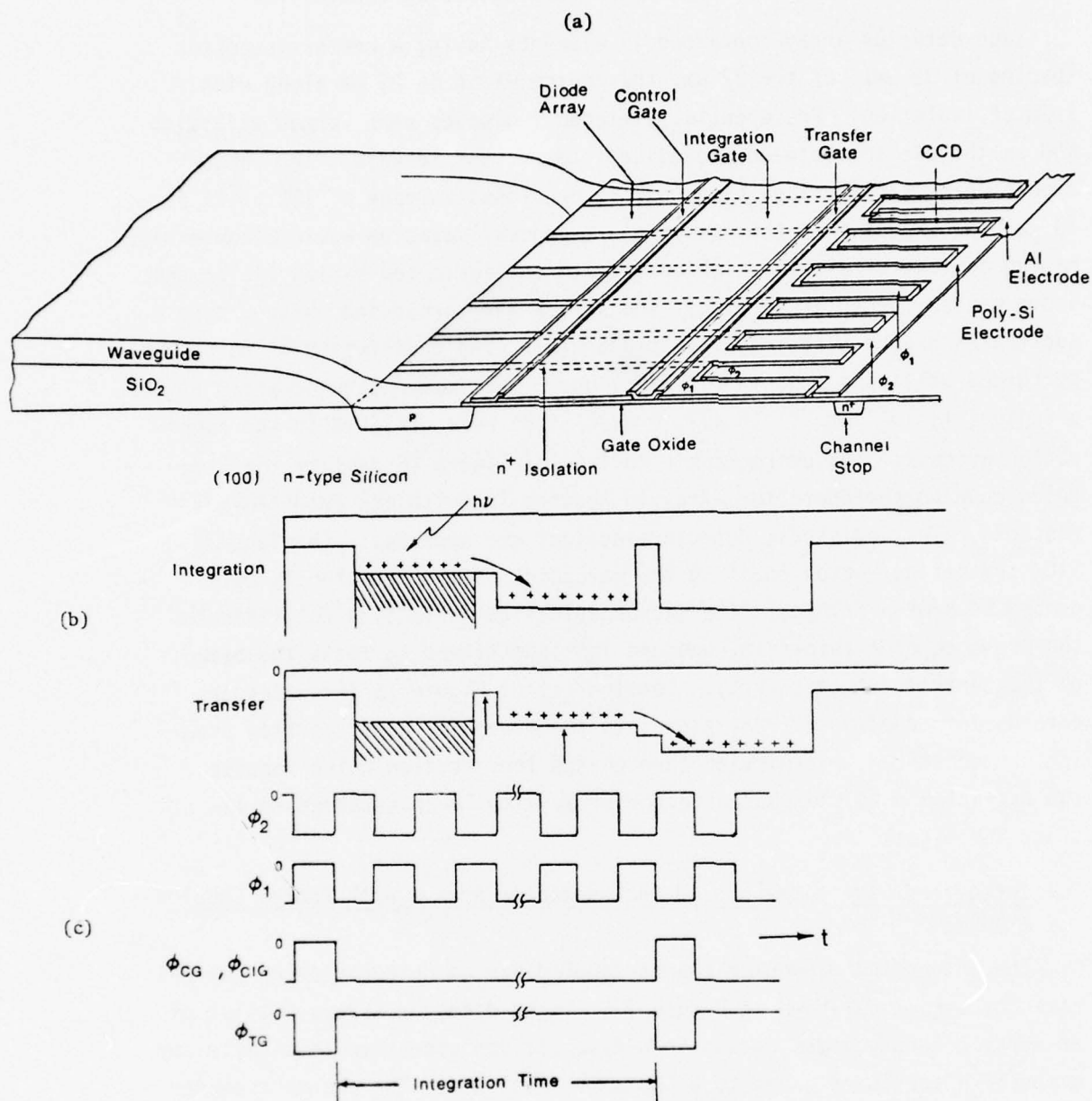
Figure 77. (a) Device Configuration of the Integrated Optical Waveguide-CCD Detector Array

(b) Surface Potential Profile During Integration and Transfer Cycles

(c) Electrode Waveforms for the Control Gate (CG), the Charge Integration Gate (CIG), the Transfer Gate (TG), and the Phase 1 and Phase 2 Gates (ϕ_1 and ϕ_2)

120

regions. The detector array integrates the optical signal incident on the array of photodiodes as the potentials of the control and integration gates are adjusted, as indicated in Figure 77, so that charge excited by incident light collects underneath the integration gate. At the end of the integration period T, the transfer gate is turned on so that the collected charge is transferred into the shift register. This charge transfer occurs simultaneously for each array element and in a time less than 1/2 of the CCD clock period. Once this charge has transferred into the shift register, the transfer gate is turned off and the charge is shifted along the register to the end where a serial, discrete-time signal emerges representing the spatial light distribution.

The electronic drive circuitry for the CCD device of Figure 77 is shown in Figure 78. The two-phase clock generator is shown in Figure 78-a. The device was normally operated with overlapping pulses in the 100Khz frequency range. The frequency was determined by $(R_2+R_3)C_2$, while the overlap is determined by R_1C_1. The two-phase clock generator is formed from a dual monostable multivibrator (MC14528) operating in a free-running oscillator mode. The overlap of the two clock waveforms is obtained by utilizing two D-type flip-flops (CD4013A) in conjunction with two NAND gates (CD4011A). Two noninverting buffer amplifier stages (CD4050) are also included. The presence of the variable resistors at the ϕ_1 and ϕ_2 terminals allow independent adjustment of the DC levels. The circuitry in Figure 78-b is used to generate the charge integration gate (CIG) electrical waveform and the transfer gate (TG) electrical waveform. The phase 1 clock voltage ϕ_1 is applied to two 7-stage binary counters (CD4024AE) in series which count the clock pulses. A D-type flip-flop (CD4013A) in conjunction with a NAND gate (CD4011A) is used along with the counter to generate a clock pulse after a specified number of clock cycles. This pulse then passes through an inverting buffer amplifier (CD4049A) to produce the transfer gate electrical waveform and through an additional inverting buffer amplifier to produce the integration gate electrical waveform. The circuitry in Figure 78-c uses two single monostable multivibrators (CD4047) to generate a train of several low-duty cycle rectangular pulses for measurement of CCD transfer inefficiency. These pulses are separated by a clock period and are injected into the CCD serial input gate (IG). The train of several pulses is followed by a long period in which no pulses are generated. This pattern is then repeated periodically. Details of the experimental determination of transfer inefficiency are given in Appendix C.

121
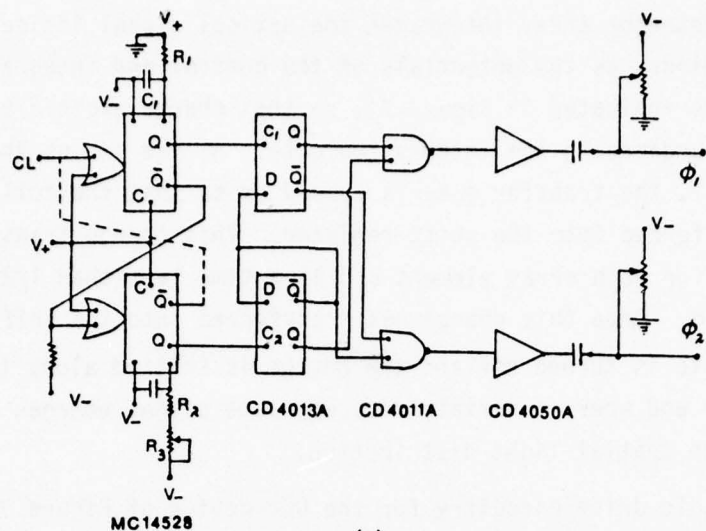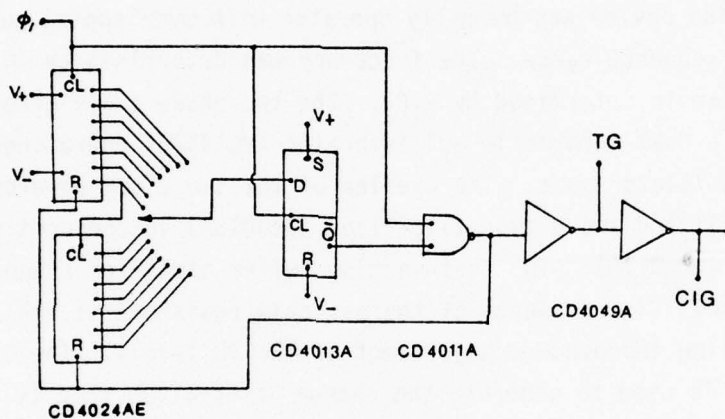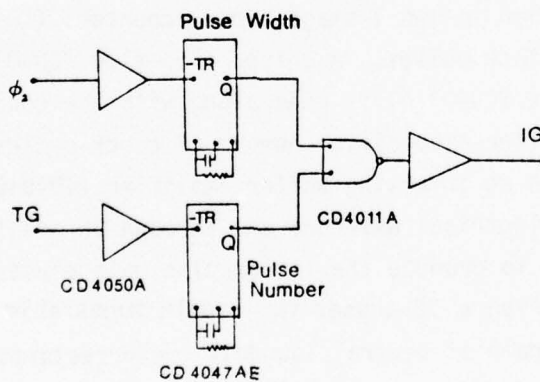
Figure 78. (a) Circuitry for Generating Two-Phase Clock Voltages (ϕ_1 and ϕ_2)
(b) Circuitry for Generating the Transfer Gate (TG) and Charge Integration Gate (CIG) Electrode Waveforms
(c) Circuitry for Generating Serial Input Gate (IG) Signal for CCD Charge Transfer Efficiency Measurement

122

III. REVIEW

A. CONCLUSIONS

The thin-film waveguide positive inhomogeneous refractor identified as the generalized Luneburg lens has been investigated, calculating the performance and demonstrating its operation with quantitative measurement of its diffraction patterns, together with its use as a beam expander and its use with reflectors. The detailed considerations have emphasized factors of interest for application to an integrated optical Fourier transform "chip" that may be employed as a real time microwave spectrum analyzer. Consideration of the reflector has been included as a means to fold the optical axis so as to employ a minimum substrate area. An unusually large expansion ratio has been demonstrated for application to the coupling of a GaAs laser to the full aperture required of a Fourier transform lens. The effort has included the demonstration of waveguide coupled photodetector arrays for application in the spatial frequency plane of the transform lens. The photodetector array has also been demonstrated with a charge coupled read out mechanization. This latter waveguide coupled photodetector array and CCD effort has been performed by the Department of Electrical and Computer Engineering at the University of Cincinnati.

The approach has emphasized the application of Ta_2O_5 as the high index lens film used together with Corning 7059 as a waveguide, all of which are deposited upon thermally-grown SiO_2 as an isolation layer on a silicon substrate. This structure permits the integration of the optical components with their electronic counterpart on a single substrate. The problem of scattering and its effect upon the dynamic range and the resolution of the Fourier transform has received consideration which, in part, led to the choice of this preferred material-structure because the thermally-grown oxide has yielded the smoothest low scattering surface thus far identified upon which thin-film waveguide lenses and other associated integrated optical components can be deposited.

A numerical procedure has been developed to compute the performance of thin-film waveguide generalized Luneburg lenses and lens systems. Starting from the waveguide lens thickness profile determining the ray traces, the ray trace through the inhomogeneous lens is determined together with the ray intercept in the image plane. With this data, the wavefront phase error is determined and the resulting intensity diffraction pattern is calculated. The procedure allows the introduction of various types of waveguide thickness profile errors to be introduced and the calculation of the effect upon the diffraction pattern. Numerous examples have been included. Some of these computer results correlate with experimental observations.

Luneburg lenses having F/D extending from 0.5 to 10 have been fabricated. Some representative diffraction patterns characterizing their performance have been included. Various shapes of deposition masks have been employed to control the radial lens thickness profile. Some representative data showing these effects upon the diffraction pattern has been included. Depending upon the aperture employed, the performance of these lenses approach diffraction-limited operation in varying degrees ranging from 2.5 with data at 1.6 and extending down to near unity. Measured diffraction spot widths approaching 5 microns has been achieved. The measured results, utilizing a re-imaging technique, have shown that this performance is comparable to that of the re-imaging lenses. The presence of the prism coupler normally introduces spherical aberration into the measured results which can, however, be eliminated.

Several beam expanders have been demonstrated showing that the lens mask positioning can yield a collimated beam reproducibly. Cleavage through the substrate and overlaying films can produce an interface of sufficient perfection to implement total internal reflectors.

Waveguide coupling to photodetector arrays has been demonstrated. The fabrication of lenses, which focus on these detectors accurately, has been reproducibly demonstrated.

In general, the focal length of Luneburg lenses is adjusted by the lens radius and shaping of the lens conical mask together with control of the lens thickness. Minor adjustments of the focal length by control of the thickness have been demonstrated by way of the numerical analysis and by way of scaled experiments.

Substantial further improvement of these lenses should be possible, providing for their use with larger numerical apertures by matching of the radial thin-film thickness profile more exactly to the required computed thickness profile. Further effort reducing the scattering of both the lens films and waveguide films is required. Inversion of the deposition process and an improved level of cleanliness is essential. Some results attained thus far are equal to or exceed any other films reported thus far. Reproducibility of these results is required over a larger substrate area. Scattering of the lens film must be reduced. Suppression of mode conversion must be incorporated. Means to satisfy both of these requirements are suggested herein. The beam expansion lens system will eventually require a spatial filter to improve the transverse mode purity.

Results, thus far, based upon the use of thin-film Luneburg lenses on a thermally-oxidized silicon substrate, provide one attractive approach to the implementation of an integrated optical Fourier transform "chip". This approach uses well known established manufacturing processes and thus the chip can be implemented economically and integrated with its associated electronics.

B. ACKNOWLEDGEMENTS

125

APPENDIX A

AN INTEGRATED OPTICAL APPROACH TO THE FOURIER TRANSFORM

D. B. Anderson, J. T. Boyd, M. C. Hamilton,
and R. R. August

Abstract - A wideband, real-time, spectrum analyzer is examined as a viable integrated optical circuit for processing electronic signals. The spectrum analyzer includes a Luneburg beam expansion lens system, a surface elasto-optic Bragg spatial modulator, reflectors, a Luneburg Fourier transform lens, and a waveguide coupled photodetector array; all formed on thermally-grown SiO_2 on Si as the substrate. A distributed-feedback (GaAl)As laser with hybrid coupling is included as the carrier for the optical Fourier transform. The developmental status of this integrated optical spectrum analyzer and its essential *design* considerations are delineated.

D. B. Anderson and R. R. August are with the Electronics Research Division, Rockwell International Corporation, Anaheim, California 92803.

J. T. Boyd, a consultant for Rockwell International, is with the Electrical and Computer Engineering Department of the University of Cincinnati, Cincinnati, Ohio 45221.

M. C. Hamilton is with the Air Force Avionics Laboratory, Wright-Patterson Air Force Base, Dayton, Ohio 45434.

127

I.   INTRODUCTION

Coherent optical information processing employs diffraction phenomena as manifested by the optical Fourier transform. It is admirably suited to execute linear analog operations such as matrix products, transforms and related convolution or correlation integrations. Its development over a score of years has been motivated by the potential for large information handling capacity [1,2]. This is achieved by data manipulation in a two-dimensional image format processed in a parallel organization in contrast to one-dimensional electronic signal processing which often employs a serial organization.

Current equipment for optical information processing with large time-bandwidth-products is expensive and bulky. Some of the large information handling capacity is compromised at the input or output interfaces when real-time operation is required. It requires precision related to the optical wavelength which, in turn, requires a mechanical structure with sufficient mass to obtain the necessary rigidity. Thus far, miniaturization has not had a significant impact.

Application of an integrated optics format to the Fourier transform provides the potential for a significant reduction in size and weight. Use of a single substrate and planar lithographic processes provides for rigid optical alignment. Planar batch fabrication processing can lead to a substantial reduction of cost. However, optical signal processing in an integrated optics format is limited to a single transverse dimension. For applications involving signals as a function of time, such as RF spectral analysis [3,4], this one-dimensional characteristic is of no consequence. However, an integrated optical approach to spectral analysis

128

must compete with alternative technologies on the basis of cost and performance. Some of these alternatives include: a bank of narrow band filters, digital transistor logic organized for the "fast" Fourier transform, and the chirp-Z algorithm implemented with either charge-coupled [5] or surface elastic wave [6] devices. Real-time operation with wide bandwidth approaching 1 GHz obtained on a single "chip" is expected to be the primary attributes of an integrated optical approach to an RF spectrum analyzer.

Some of the theory related to the spectrum analyzer is developed herein, together with an exposition of design considerations as related to the whole "chip". Companion papers [7,8] delineating specific considerations for the optical waveguide lenses and the waveguide coupled detector array are included in this special issue.

II.   THEORY OF OPERATION

The optical Fourier transform configuration considered herein is illustrated in Fig. 1. It requires a coherent source (single transverse and longitudinal mode) and an optical lens system to expand the beam with a prescribed aperture distribution and width. The transform configuration also employs a spatial modulator which Bragg diffracts the optical radiation in linear proportion to the applied signal frequency and amplitude. This diffracted radiation is collected by the Fourier transform lens and emerges as a transverse spatial distribution which is detected in the focal plane. Because the detectors respond to the intensity spatial distribution in the transform plane, the resulting electrical signal is a Wiener spectrum of the input signal.

129

An integrated optical circuit layout to implement the RF spectrum analyzer on a single substrate is depicted in Fig. 2 as representing the schematic of Fig. 1. It includes a Luneburg beam expansion lens system, a surface elasto-optic Bragg diffraction modulator, reflectors, a Luneburg Fourier transform lens, and a waveguide-coupled photodetector array; all arranged as thin-film waveguides on thermally-grown SiO_2 on a common Si substrate. A distributed-feedback (GaAl)As laser with hybrid coupling to the waveguide is included to provide the optical carrier. The optical axis could obviously be folded into other configurations.

Considering the optical geometry shown in Fig. 1 as a planar waveguide, the field amplitude $E(y_2)$ in the transform plane is related to the field amplitude in the input plane $E(y_0)$ according to [9]

$$E(y_2) = b \int_{-\infty}^{\infty} E(y_0) e^{i \frac{kN_e(m)y_2}{F} y_0} \, dy_0 \, , \qquad (1)$$

where y is in the waveguide surface perpendicular to the axis of wave propagation (z axis) and the x axis is normal to the waveguide surface. The x dependence of the field contains the form of the waveguide modes and will be suppressed here for conciseness, however, its effect on Bragg diffraction has been incorporated [10]. In (1) F is the lens focal length, $N_e(m)$ is the thin-film waveguide mode effective refractive index, $k = 2\pi/\lambda$ where λ is the optical wavelength, and b is a constant of proportionality. For a uniform plane wave over the input aperture D, the spatial output has the familiar form:

130

$$E_o^m(y_2) = bD \ Sinc\left(\frac{kN_e(m) \ Dy_2}{2F}\right) \quad , \tag{2}$$

where sinc x= sinx/x. The half-width between nulls of this diffraction pattern is

$$\Delta y_2 = \frac{\lambda f}{N_e(m)D} \tag{3}$$

which represents the smallest resolvable interval in the Fourier transform plane.

The optical axis in Fig. 1 and the surface elastic wave propagation axis are oriented so as to satisfy the Bragg condition at the signal center frequency. The z axis in Fig. 1 is thus at an angle $2\theta_B$ with respect to the optical axis of the incident wave where θ_B is the Bragg angle defined as

$$Sin\theta_B = \frac{\lambda f_{so}}{2N_e(m)v_r} \quad , \tag{4}$$

where f_{so} is the signal center frequency and v_r is the Rayleigh wave velocity. The interaction of the incident optical wave and the surface elastic wave has been treated elsewhere [10-13]. For operation of the spectrum analyzer, it is necessary to closely approximate the surface elastic wave as consisting of uniformly-weighted plane wave components within a diffraction angle $\delta\phi$ and no components beyond $\delta\phi$ where $\delta\phi$ is assumed sufficiently large so that the elasto-optic bandwidth is limited

131

by the transducer bandwidth [10]. Such a close approximation is possible through the use of tilted transducer arrays [14,15]. It is reasonable to assume the beam spread of the input optical wave is much less than $\delta\phi$. For this case, the optical beam spread will not be significantly altered by the elasto-optic interaction [16,18]. We further restrict our attention to the Bragg regime so as to eliminate the possibility of ambiguities caused by multiple scattering. Furthermore, as noted by Giallorenzi and Milton [16], second-order multiple scattering is avoided if $k_{s\ max} < 2\ k_{s\ min}$, where $k_{s\ min}$ and $k_{s\ max}$ are the minimum and maximum values of elastic wave propagation constant k_s over the range of the signal band.

Operation of the spectrum analyzer requires a linear relationship between the diffracted field amplitude and the signal amplitude spectrum, which is achieved by limiting the surface elastic wave intensity so that the input optical intensity is not significantly depleted. Cumulative and thus efficient energy transfer from the signal input to the diffracted optical beam only occurs when momentum conservation is satisfied [19]. Restricting our attention to only the surface elastic wave angular component which satisfies momentum conservation, the transverse electric field distribution in the Fourier transform plane $E(y_2)$ is given as.

$$E(y_2) = ab \int_{-\infty}^{\infty}\int_{-\infty}^{\infty} G(f_s)\ w(y_0) e^{-i\frac{2\pi}{v_r}(f_s - f_{so})\cos\theta_B y_0}$$

$$e^{i\frac{kN_e(m)y_2}{F}y_0}\ dy_0\ df_s .$$

(5)

132

In (5) f_s is signal frequency, $G(f_s)$ is the Fourier transform of the input signal $g(t)$, y_0 and y_2 are transverse spatial coordinates as indicated in Fig. 1, a is a collection of constants including the elasto-optic diffraction efficiency and $w(y_0)$ is a window function defined such that

$$w(y_0) \begin{cases} \neq 0, & |y_0| < D/2 \\ = 0, & |y_0| > D/2 \end{cases} \tag{6}$$

We have chosen to evaluate the transform over the infinite interval and include the effect of a finite beam by means of the window function [20]. Carrying out the integration in (5) yields

$$E(y_2) = a \int_{-\infty}^{\infty} G(f_s) W \left[y_2 - \frac{\lambda f \cos\theta_B}{N_e(m) v_r} (f_s - f_{so}) \right] df_s , \tag{7}$$

where $W(y_2)$ is the Fourier transform of the window function.
The expression (7) for the transverse field distribution in the transform plane is the usual result of performing a truncated Fourier transform in that it is a convolution of the Fourier transform of the input signal and the Fourier transform of the window function. In the limit of no truncation and uniform weighting $W(y_2)$ approaches a delta function so that (7) reduces to

$$E(y_2) = \frac{ab v_r}{\cos\theta_B} G \left(f_{so} + \frac{v_r N_e(m)}{\lambda f \cos\theta_B} y_2 \right) . \tag{8}$$

133

For no truncation the field $E(y_2)$ is thus a direct mapping of the Fourier transform of the input signal along the y_2 axis with scale factor $(\lambda f \cos \theta_B)/N_e(m)v_r$. In the case of finite truncation, the convolution (7) will yield an accurate mapping of the Fourier transform of the input signal if the spectral width of $W(y_2)$, given by (3) for an optical plane wave over the aperture D, is much less than the input signal spectral width, i.e.,

$$\frac{D\cos\theta_B}{v_r} \Delta f_s \gg 1. \tag{9}$$

For case of interest, θ_B is of the order of a few degrees, $\cos\theta_B \approx 1$ and (9) reduces to

$$T \Delta f_s \gg 1 \tag{10}$$

where $T = D/v_r$ is the transit time of the surface elastic wave across the optical aperture. Thus, the condition for negligible effects due to truncation leads to the requirement that the time-bandwidth-product be much greater than unity. Although the convolution (7) of the signal transform with the transform of the window function provides a spectral estimate of $G(f_s)$, an improved estimate can be achieved by weighting the signal window [20]. A uniform weighting function produces the sinc x distribution for $W(f_s)$ which leads to a spectrum analyzer with finite adjacent-channel response for a continuous single electronic signal input. A tapered weighting function, however, will suppress the sidelobe of the sinc x

134

function and Gaussian weighting will eliminate the sidelobes.

III.   SPECTRUM ANALYZER DESIGN CONSIDERATIONS

To examine the frequency resolution, consider an electronic signal frequency f_s departure from the signal center frequency by an amount δf_s. The corresponding diffracted wave component departs from the z axis by an angle $\delta\theta$, where

$$\delta\theta = \frac{\lambda}{N_e(m)v_r}\ \delta f_s \ .$$

(11)

For a wave propagating at this angle with respect to the z axis and having constant amplitude within the aperture width D, the resulting diffraction pattern in the transform plane is given by (2) except for a displacement δy_2 of the position of the maximum, where

$$\delta y_2 = f\delta\theta$$

$$= \frac{f\ \lambda}{N_e(m)v_r}\ \delta f_s \ .$$

(12)

Using the Rayleigh criteria for resolution, the minimum frequency difference which can be resolved occurs when $\delta y_2 = \Delta y_2$, i.e.,

$$\delta f_{s\ min} = \frac{v_r}{D} = 1/T \qquad \text{Uniform Weighting}$$

(13)

$$= 1.41/T \quad \text{Truncated Gaussian Weighting}$$

135

where the truncation width is at the 1/e value [21]. If Δf_s is the electrical signal bandwidth, then the number of resolvable frequency intervals N is given as

$$N = \frac{\Delta f_s}{\delta f_{s\ min}} = \Delta f_s T \quad , \tag{14}$$

Thus, as in other transform techniques, the number of resolvable frequency intervals is the appropriate time-bandwidth-product.

Assuming an optical waveguide structure having a Rayleigh velocity $v_r = 4.2$ km/s, the time-bandwidth-product of a spectral analyzer using (14) is depicted in Fig. 3 for several values of transform aperture. Thus, for a lens aperture of 1.5 cm and a surface elastic wave transducer bandwidth of 280 MHz yields a time-bandwidth-product of 1000.

For an optical wavelength of 0.9 μm and an optical waveguide effective refractive index of 1.6, the relationship of temporal frequency resolution corresponding to the spatial interval in the transform lens output frequency plane is depicted in Fig. 4, using (13). The limits imposed by diffraction are also included in the figure for a lens aperture of 1 and 2 cm as a frequency band determined by the exact weighting function utilized. The spectrum analyzer frequency resolution for several Fourier transform lens focal lengths is thus related to the photo-detector array element spacing depicted in Fig. 4. Thus, if the minimum detector period is 6 μm, due to photolithographic limits for the detectors and the required frequency resolution is 0.5 MHz, the required lens focal length becomes greater than 8.9 cm, which may be obtained with a lens

diameter of 1 cm with a uniform weighting function. However, with
a truncated Gaussian, either a longer focal length or a reduced detector
period must be employed. If, on the other hand, the focal length is
reduced to 1 cm for the same temporal frequency resolution, the litho-
graphy requirements are increased; that is, the lithography art employed
must achieve a detector spacing of 0.7 μm. This latter dimension is
currently considered impractical for a photodetector array. It is possible
to define an array of rectangular image line waveguides with this center-
to-center dimension, however, and use a waveguide fan-out array for
coupling between the focal plane and a detector array with a larger period.
This tradeoff between detector array lithographic resolution is dependent
upon the focal length employed and the ability to fold the optical axis
across the available spectrum analyzer substrate area, as indicated by
the example in Fig. 2.

In the preceding analysis we assumed an idealized plane wave optical
input. In practice the input optical wave would have both a finite beam
spread and a finite frequency linewidth. If we consider an input beam
spread Δ, then Bragg diffraction of the various input wave angular com-
ponents will occur for different surface elastic wave angular components
corresponding to a constant frequency f_s. Such behavior could lead to a
compromise in frequency resolution of the spectrum analyzer unless

$$\Delta \leq \delta\theta_{min} \; , \tag{15}$$

where $\delta\theta_{min}$ is the diffracted wave angular change corresponding to the

137

minimum resolvable frequency $\delta f_{s\ min}$. Using (13) and (11) in (15), the input optical beam spread will not compromise frequency resolution if

$$\Delta \leq \frac{\lambda}{N_e(m)v_r}\ \delta f_{s\ min}$$

$$\leq \frac{\lambda}{N_e(m)D} \qquad . \tag{16}$$

Thus, the input optical wave must be near diffraction-limited so as to not degrade the temporal frequency resolution (13). This defines the requirement on the beam expansion collimation and transform lens focal length tolerances.

Now considering the effect of the optical wave finite frequency linewidth, the magnitude of k_i and k_d will change so that phase-matched deflection will occur at different angles for a constant signal frequency. A change in input laser frequency $\Delta\omega_i$ will cause a change in the output diffracted angle $\Delta\theta$ that can be expressed as

$$\Delta\theta = 2\ \frac{\Delta\omega_i}{\omega_i}\ \sin\theta_B \quad . \tag{17}$$

Spectrum analyzer frequency resolution will not be compromised as long as the above angular change is less than $\delta\theta_{min}$, i.e.,

$$\frac{\Delta\omega_i}{\omega_i} = \frac{\Delta\lambda}{\lambda} = \frac{\lambda}{2\ N_e(m)D\sin\theta_B} = \frac{\delta f_{s\ min}}{f_{so}} \quad , \tag{18}$$

138

where $\Delta\lambda$ is the linewidth in terms of wavelength. For λ = .9 μm, $N_e(m)$ = 1.6, D = 1.0 cm, and θ_B = 5° we find $\Delta\lambda$ = 2.5 $\overset{o}{A}$. Distributed-feedback (DFB) or distributed Bragg reflection (DBR) GaAs semiconductor lasers and gaseous lasers do exhibit lesser linewidth. The condition (18) and (16) which place stringent requirements on laser frequency linewidth and angular spread correspond to diffraction limited operation. If the spectrum analyzer resolution is instead limited by detector element center-to-center spacing, then the above conditions may be reduced to the point where

$$\Delta \; < \; \ell/f \tag{19a}$$

$$\frac{\Delta\omega_i}{\omega_i} \; = \; \frac{\Delta\lambda}{\lambda} \; < \; \frac{\ell}{2f\sin\theta_B} \quad . \tag{19b}$$

In (19) ℓ corresponds to the detector array element center-to-center spacing. Thus, for ℓ = 25 μm and f = 5 cm, the maximum values of $\Delta\lambda$ and Δ which do not compromise resolution are increased from the previous example to 22.5 $\overset{o}{A}$ and .5 milliradians, respectively. The laser source emission wavelength must also be stable to preserve calibration of the spectrum analyzer. The emission wavelength of (GaAl)As DFB and DBR injection lasers is stabilized by the internal grating.

The performance of the integrated optical spectrum analyzer will be compromised by Rayleigh and/or Mie scattering originating in both the waveguide and lens regions. Scattering will adversely affect both frequency resolution and the dynamic range. Scattering will have a

139

greater effect on the dynamic range, the degree of which remains to be determined experimentally. The degree of Rayleigh and Mie scattering is largely dependent upon materials and processing. The effects of scattering are also position dependent along the optical axis. Analysis of the scattering process has shown that, as long as the scattering loss is not more than 1 dB/cm, frequency resolution will not be adversely affected [22].

IV.   SPECTRUM ANALYZER IMPLEMENTATION

One form of an integrated optical spectrum analyzer is illustrated in Fig. 2 where, with the exception of the laser source, all of the components are combined on a single substrate. The surface of thermally-grown SiO_2 is particularly useful because it has a low refractive index and can yield an extremely smooth surface. Corning 7059 is a typical low-loss, thin-film material applicable for use with the thermally-grown SiO_2 as an isolation layer on Si as a substrate. Fig. 5 depicts the calculated waveguide absorption for Corning 7059 of several thicknesses as a function of the thermally-grown SiO_2 isolation layer thickness due to the waveguide evanescent field penetration into the silicon substrate [23]. Use of silicon as a substrate has a further advantage that a detector array and the associated signal processing electronic circuit can be integrated into the same substrate [24].

The thin-film waveguide lenses shown are of the general Luneburg class [25,26,7]. These lenses are circular symmetrical and employ a gradual radial refractive index profile which minimizes interface scattering. Fabrication is simple and reproducible [25]. When properly designed, they

140

are free of the spherical aberration, coma, however, obviously exhibit circular field curvature. Fig. 6 illustrates a plan view of two Luneburg lenses for use as a beam expander. An overlay of Ta_2O_5 on 7059 waveguide on a 7440 substrate has been employed. The Newton rings in section (a) of the figure indicates the profile. Sections (b) and (c) indicate separate ray traces through both lenses and around the circumference of the larger lens, respectively. Their f-number is F/D = 0.5. Keeping a constant radius and altering the radial refractive index profile allows the focal length to be increased.

Reflectors are necessary to fold the spectrum analyzer optical axis so as to be contained within the available substrate area. One successful technique to form reflectors for Corning 7059 waveguide on thermally-grown SiO_2-on-Si is by cleavage of the substrate along a {110} face when normal to the waveguide surface. Fig. 7 illustrates the operation of a retro-reflector employing the above materials. Comparison of the scattering loss between Figs. 7 and 6 dramatically demonstrates the merits of waveguide formed on thermally-grown SiO_2.

The surface elasto-optic spatial modulator requires a piezoelectric to launch Rayleigh waves. Zinc oxide has been successfully deposited by RF sputtering [27] for various elastic wave devices [28,29] and has been employed to launch Rayleigh waves to demonstrate the surface elasto-optic interaction on SiO_2 [30] and on GaAs [31]. Optimum piezoelectric coupling is obtained by placing the interdigital transducer array between the ZnO and the waveguide with its substrate [32].

The diffraction efficiency of several surface Bragg-type, elasto-optic interactions is depicted in Fig. 8 [33,10] as a function of the

141

applied power in the elastic form. These experiments indicate the range
where linearity occurs. In the range where high diffraction efficiency
occurs, a large signal analysis is required which will show a deviation
from the true transform. Use of the linear region permits a greater
flexibility in the choice of waveguide material because a high photo-
elastic constant is not essential. This condition also relaxes the
requirement for minimum electrical to elastic conversion efficiency,
thus permitting the achievement of a wider band transducer design. One
important parameter influencing the spectrum analyzer design and time-
bandwidth-product is the elastic wave velocity of the multiple layered
structure in the elasto-optic interaction region. Penunuri [34] has
calculated the velocity for Rayleigh and Love waves for the thermally-
grown SiO_2 on Si structure as a function of the frequency-overlay-film-
thickness product which is depicted in Fig. 9. The thickness film product
has units of velocity and for the regime of interest, yields a Rayleigh
velocity range of 4.0-4.5 km/sec. Propagation losses of this waveguide-
isolation-layer-substrate structure remain to be determined. Excessive
losses will alter the aperture weighting function and limit the useful
aperture. However, the available data derived from similar delay lines
suggests that these losses will not be serious. Wideband elasto-optic
interactions have been demonstrated using a multiple array of interdigital
transducers stagger-tuned and tilted to satisfy the Bragg condition.
An elasto-optic bandwidth of 358 MHz has been demonstrated using diffused
waveguide on y-cut $LiNbO_3$. Following the design principle of Tsai [14],
we have calculated the expected performance of a four element design

142

depicted in Fig. 10. The calculated electronic-elastic conversion loss of a four transducer stagger-tuned and tilted array on thermally-grown SiO_2 with a ZnO overlay is indicated. The material constants used in the calculation were extrapolated from the results of Hickernell [29]. A series inductor for each of the transducers connected in parallel is assumed. If performance equivalent to that depicted in Fig. 8 is achieved, a diffraction efficiency of 4% is estimated with an input electrical power of 100 mW at an optical wavelength of 0.9 μm. This diffraction efficiency is near the upper limit allowed for a spectrum analyzer.

The combination of a thin-film Luneburg lens deposited on a substrate containing an integrated waveguide-detector array is shown in Fig. 11. The lens has F = 1.2 cm and D = 1.1 cm. The waveguide is coupled to the photodetector junction by removing the thermally-grown SiO_2 isolation layer. Radiation from the waveguide couples to the detectors through the evanescent field using a taper in the SiO_2 transition region [24]. The photodetectors in the array are isolated by preferentially-etched grooves. In an integrated optical spectrum analyzer it may be desirable to provide a serial readout of the signal power density spectrum contained in the photodetector array to minimize the interconnection problem with a multiplicity of detectors. Serial readout can be easily accomplished by coupling to a charge-coupled device [8].

A coherent source is required as the optical carrier for the spectrum analyzer. A gas laser coupled via a prism or grating coupler is one solution; however, a semiconductor laser directly coupled to the thin-film waveguide is more commensurate with the integrated optical approach. However, its emission must be stable in the lowest order mode and must have

143

the requisite narrow linewidth. The distributed-feedback (GaAl)As laser appears to fulfill the requirements. The hybrid coupling provides for independent evaluation, optimization and satisfaction of the heat sink requirements for continuous wave operation. The parallel end-butt coupling technique [35] appears to be an effective solution but requires an elaborate alignment. An alternate approach, more amenable, is a traveling evanescent side wall coupler. In such a coupler, a cleaved side wall parallel to the laser stripe axis and perpendicular to the junction exposes the laser field to the optical waveguide. Efficient evanescent wave coupling can then occur where the grating is formed on the thin-film waveguide contact surface [36]. This evanescent field side wall coupler excites the polarization crossed to that of the parallel end-butt technique.

A Fabry-Perot type GaAs electron injection laser has been employed to demonstrate side wall coupling to a $Ga_{.3}Al_{.7}As$ thin-film waveguide epitaxially grown on Al_2O_3 substrate. Fig. 12(a) is a macrophotograph of the laser chip mounted between the heat sink and pressed against the waveguide surface, while Fig. 12(b) depicts the infrared emission from the termination of the waveguide and some scattering along the waveguide. This coupling arrangement has the advantage that the laser may be positioned and aligned with respect to the spatial filter and optical axis of the spectrum analyzer configuration shown in Fig. 5.

144

V. CONCLUSIONS

From the analysis and experimental results thus far obtained, it is concluded that a wideband, real-time spectrum analyzer is a viable application of the integrated optics technology when based upon the thermally-grown oxide on silicon substrate. Such a spectrum analyzer can function in a time-frequency regime which is not readily available through alternative technologies. Further experimental development is essential to verify this conclusion. Use of silicon provides the potential for integration with associated interface electronics. Use of the integrated optics format for signal spectrum analysis requires the use of a stable laser with narrow linewidth for the optical carrier, which can be best fulfilled by a distributed-feedback (GaAl)As laser.

REFERENCES

1. J. T. Tippett, D. A. Berkowitz, L. C. Clapp, C. J. Koester and A. Vanderburgh, Editors, Optical and Electro-Optical Information Processing, MIT Press 1965.

2. K. Preston, Jr., Coherent Optical Computers, McGraw-Hill 1972.

3. M. C. Hamilton and D. A. Wille, "Acousto-optic Diffraction in Optical Waveguides," Digest of Technical Papers, Topical Meeting on Integrated Optics, New Orleans, Louisiana, January 21-24, 1974.

4. M. C. Hamilton, D. A. Wille, and W. J. Miceli, "An Integrated Optical RF Spectrum Analyzer," IEEE 1976 Ultrasonic Symposium Proceedings, Annapolis, Maryland.

5. R. W. Broderson, C. R. Hewes, and D. D. Buss, "A 500-State CCD Transversal Filter for Spectral Analysis," IEEE Trans. Electron. Dev., Vol. ED-23, pp 143-151, 1976.

6. J. D. Maines and E. G. S. Paige, "Surface-Acoustic-Wave Devices for Signal Processing Applications," Proc. IEEE, Vol. 64, pp 639-652, 1976.

7. D. B. Anderson, R. L. Davis, J. T. Boyd, and R. R. August, "Comparison of Optical Waveguide Lens Technologies," This issue.

8. J. T. Boyd and C. L. Chen, "Integrated Optical Waveguide and Charge-Coupled Device Image Array," This issue.

9. J. W. Goodman, Introduction to Fourier Optics, McGraw-Hill 1968.

10. E. G. H. Lean, J. M. White, and C. D. W. Wilkinson, "Thin-Film Acousto-optic Devices," Proc. IEEE, Vol. 64, pp 779-788, 1976.

11. E. G. H. Lean, "Interaction of Light and Acoustic Surface Waves," in Progress in Optics, E. Wolf, Ed., Vol. 11, pp 123-166, North Holland, 1973.

12. N. Uchida and N. Niizeki, "Acousto-optic Deflection Materials and Techniques," Proc. IEEE, Vol. 61, pp 1073-1092, 1973.

13. Y. Omachi, "Acousto-optical Light Diffraction in Thin Films," J. Appl. Phys., Vol. 44, pp 3928-3933, 1973.

146

14. C. S. Tsai, M. A. Alkaider, L. T. Nguyen, and B. Kim, "Wideband Guided-Wave Acousto-optic Bragg Diffraction and Devices Using Multiple Tilted Surface Acoustic Waves," Proc. IEEE, Vol. 64, pp 318-328, 1976.

15. B. Kim and C. S. Tsai, "High-Performance Guided-Wave Acousto-optic Scanning Devices Using Multiple Surface Acoustic Waves," Proc. IEEE, Vol. 64, pp 788-793, 1976.

16. T. G. Giallorenzi and A. F. Milton, "Light Deflection in Multimode Waveguides Using the Acousto-optic Interaction," J. Appl. Phys., Vol. 45, pp 1762-1774, 1974.

17. R. V. Schmidt, "Acousto-optic Interactions Between Guided Optical Waves and Acoustic Surface Wave," IEEE Trans. Son. and Ultrason., Vol. SU-23, pp 22-32, 1976.

18. E. I. Gordon, "A Review of Acousto-optical Deflection and Modulation Devices," Proc. IEEE, Vol. 54, pp 1391-1401, 1966.

19. W. S. C. Chang, "Acousto-optical Deflection in Thin Films," IEEE J. Quant. Electron., Vol. QE-7, pp 167-170, 1971.

20. M. Schwartz and L. Shaw, Signal Processing: Discrete Spectral Analysis, Detection and Estimation, McGraw-Hill, 1975.

21. L. D. Dickson, "Characteristics of a Propagating Gaussian Beam," Appl. Opt., Vol. 9, pp 1854-1861, 1970.

22. J. T. Boyd, "Effect of Scattering on Thin-Film Waveguides and Waveguide Lenses as Applied to Optical Fourier Transform Processing," Appendix A in Technical Report AFAL-TR-76-54, Air Force Avionics Laboratory, 1976, and to be published.

23. C. L. Chen, "Thin Film Optical Waveguide and Integrated Photodetector," MS Thesis, Department of EE, Univ. of Cincinnati, 1975.

24. J. T. Boyd and C. L. Chen, "Integrated Optical Silicon Photodiode Array," Appl. Opt., Vol. 15, pp 1389-1393, 1976.

25. F. Zernike, "Luneburg Lens for Optical Waveguide Use," Optics Commun., Vol. 12, pp 379-381, 1974.

26. S. P. Morgan, "General Solution of the Luneburg Lens Problem,"
    J. Appl. Phys. Vol. 29, pp 1358-1369, 1958.

27. F. S. Hickernell, "Zinc-Oxide Thin-Film Surface-Wave Transducers,"
    Proc. IEEE Vol. 64, pp 631-635, 1976.

28. F. S. Hickernell, "The Acoustic Properties of Oxide Films and Their
    Application to Acoustic Surface Wave Devices," J. Sol. St. Chem. Vol. 12,
    pp 225-231, 1975.

29. F. S. Hickernell, "DC Triode Sputtered Zinc Oxide Surface Elastic Wave
    Transducers," J. Appl. Phys. Vol. 44, pp 1061-1071, 1973.

30. N. Chubachi, J. Kushibiki, and Y. Kikuchi, "Monolithically Integrated
    Bragg Deflector for an Optical Guided Wave Made of Zinc-Oxide Film,"
    Elec. Lett. Vol. 9, pp 193-194, 1973.

31. K. W. Loh, W. S. C. Chang, W. R. Smith, and T. Grudkowski, "Bragg
    Coupling Efficiency for Guided Acoustooptic Interaction in GaAs," Appl.
    Opt. Vol. 15, pp 156-166, 1976.

32. G. S. Kino and R. S. Wagers, "Theory of Interdigital Couplers on
    Nonpiezoelectric Substrates," J. Appl. Phys. Vol. 44, pp 1480-1488,
    1973.

33. D. A. Wille and M. C. Hamilton, "Acousto-Optic Deflection in Ta_2O_5
    Waveguides," Appl. Phys. Lett. Vol. 24, pp 159-161, 1974.

34. D. Penunuri, "Some Theoretical Aspects of Surface Acoustic Wave Propa-
    gation," PhD Thesis, Electrical Engineering Department, University of
    Southern California, 1976.

35. R. G. Hunsperger and A. Lee, "Parallel End-Butt Coupling of GaAs Laser
    Diode and a Thin-Film Waveguide," Technical Digest of the Topical
    Meeting on Integrated Optics, Salt Lake City, Utah, 1976.

36. J. T. Boyd and C. S. Kuo, "Composite Prism-Grating Coupler for
    Coupling Light into High Refractive Index Thin-Film Waveguides," Appl.
    Opt. Vol. 15, pp 1681-1683, 1976.
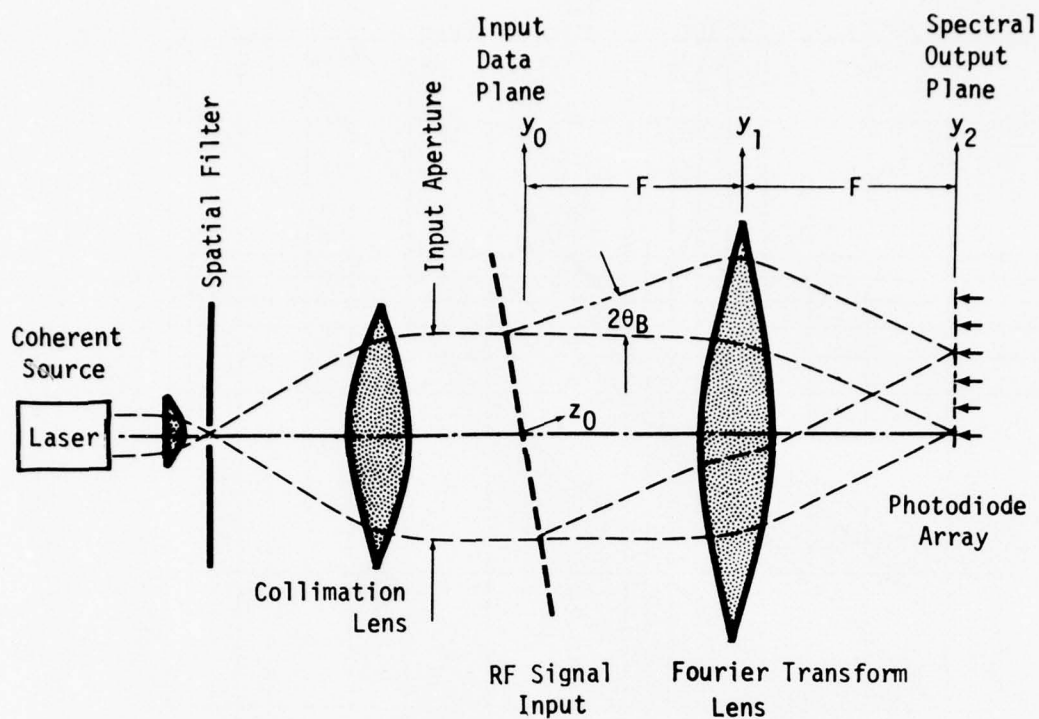
Figure 1A. Coherent Optical Fourier Transform Spectrum Analyzer
Schematic
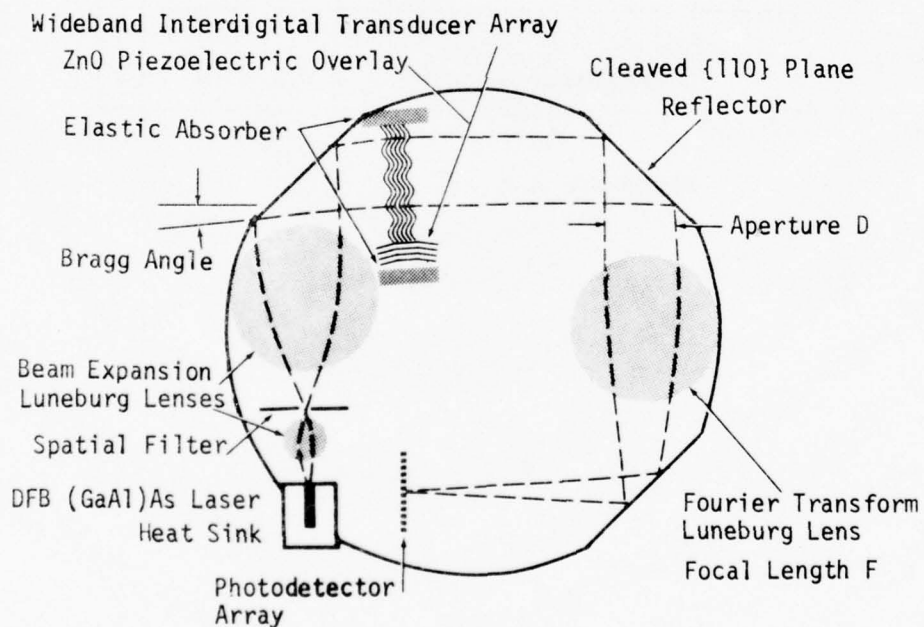
Figure 2A. Integrated Optical Fourier Transform "Chip" Layout for
F/D 6 and 7.6 cm Dia. Structure includes Corning 7059
waveguide film on thermally-grown SiO_2 isolation layer
on {100} Si substrate with overlays of Ta_2O_5, ZnO, and
Al.

149
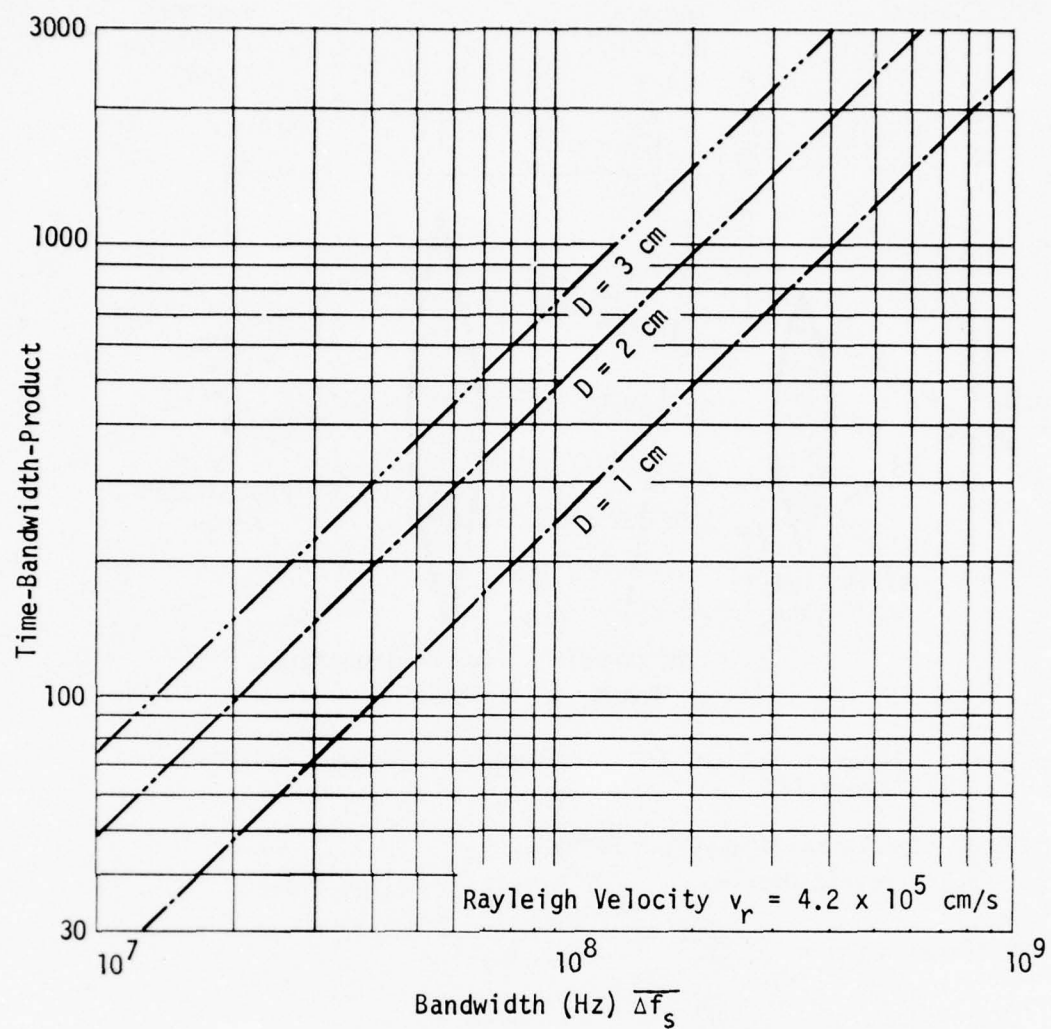
Figure 3A.   Spectrum Analyzer Time-Bandwidth-Product.
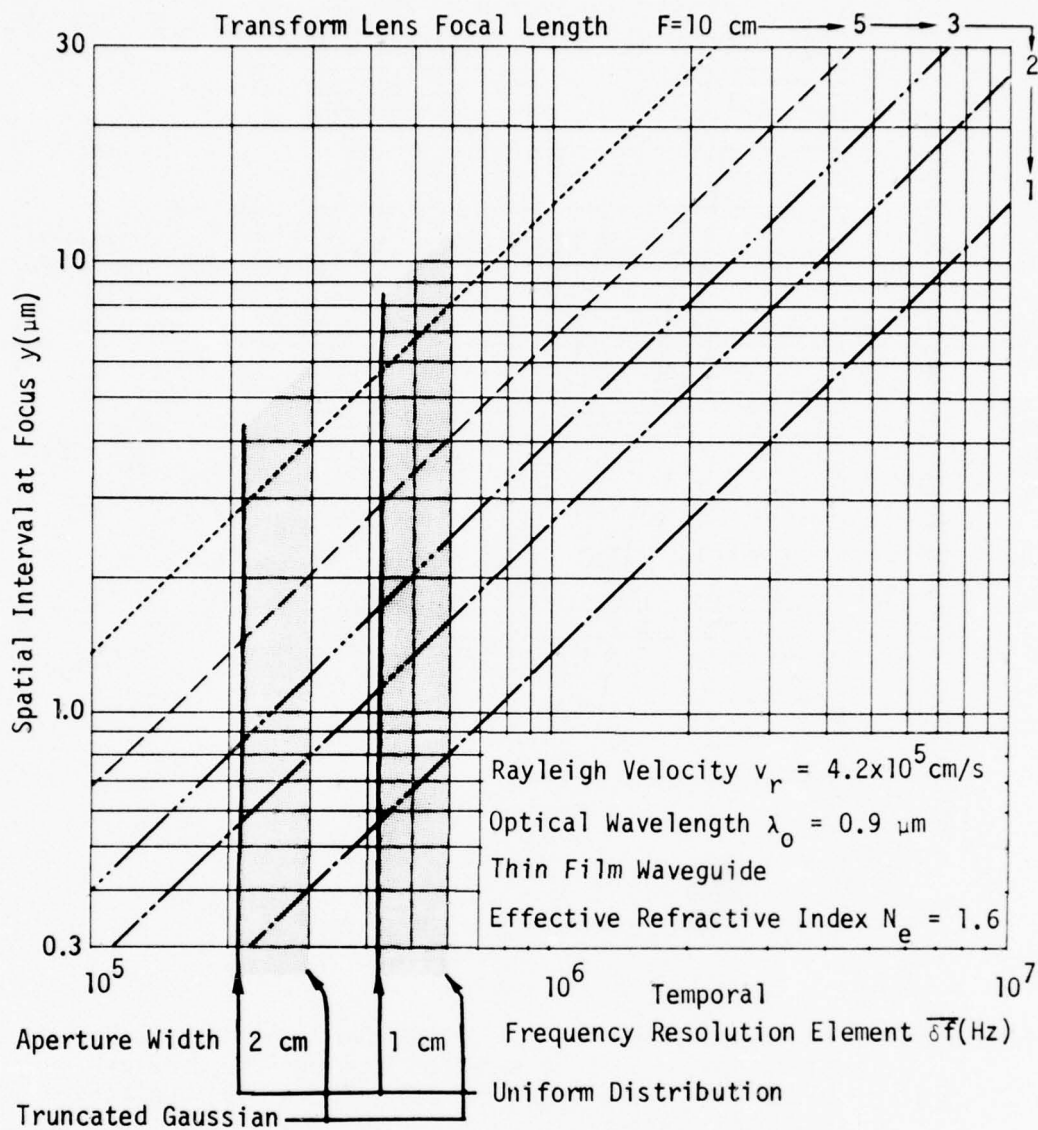
Figure 4A.   Optical Fourier Transform Spatial-Temporal Resolution
Limited by Either Detector Period or Aperture Diffraction
where Aperture Distribution Ranges from Uniform to Trun-
cated Gaussian.

151
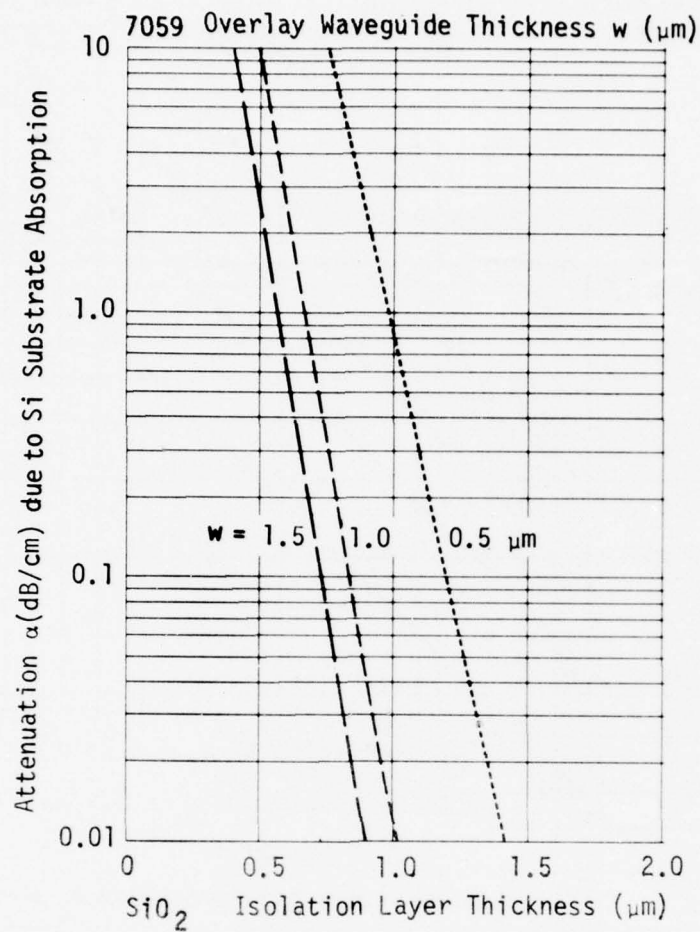
Figure 5A. Thin-Film Waveguide Attenuation due to Evanescent Field
Absorption in Si Substrate for Corning 7059 Overlay
Waveguide Thickness and Thermally-Grown SiO_2 Isolation
Layer Thickness [23].

152

(a)

(b)

(c)
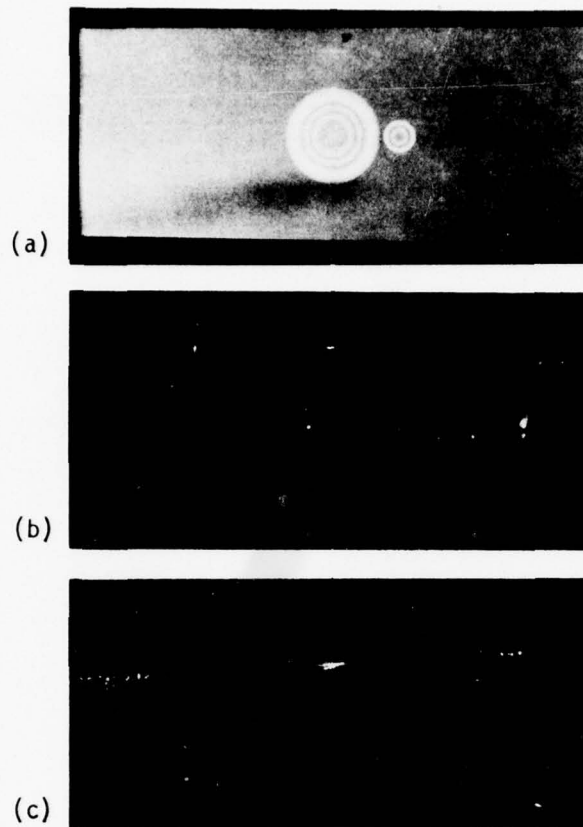
Figure 6A. Thin-Film Luneburg Lenses Using Ta_2O_5 on Corning 7059-on-7440 Glass: (a) plan view of beam expansion system showing Newton rings indicating the radial tapered thickness profile, (b) scattering of ray traces through beam expansion system using 6328 Å radiation, and (c) circumferential ray trace around Luneburg lens.

Cleaved Edge

Input
Output
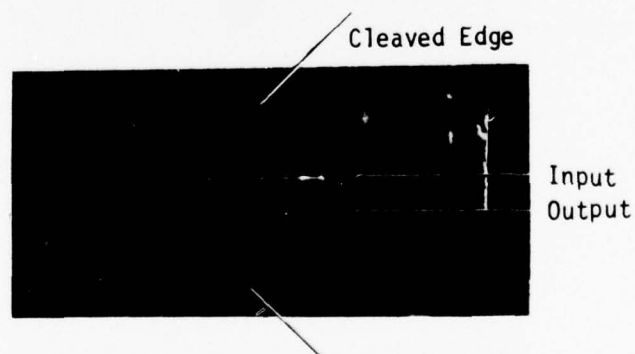
Figure 7A. Cleaved Retroreflector Employing Corning 7059 Waveguide on Thermally-Grown SiO_2-on-Si.

153
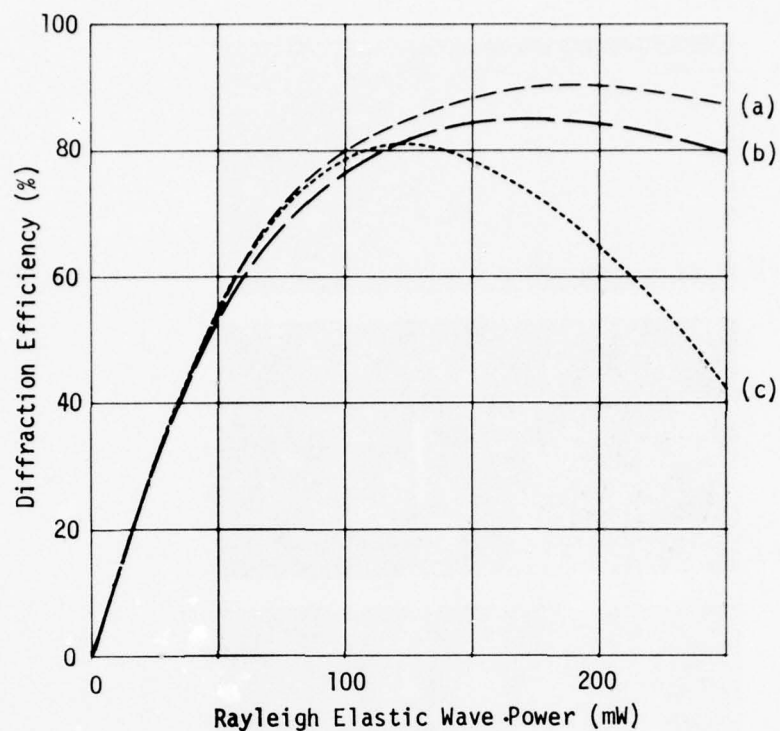
Figure 8A.   Surface Elasto-Optic Bragg-Type Diffraction Efficiency for
Waveguide Structures: (a) Ta_2O_5-on-Si[3], (b) Nb_2O_5-on-
$LiNbO_3$, and (c) Ti or Ni-indiffused-$LiNbO_3$ [10], for TM
modes at 290 MHz.
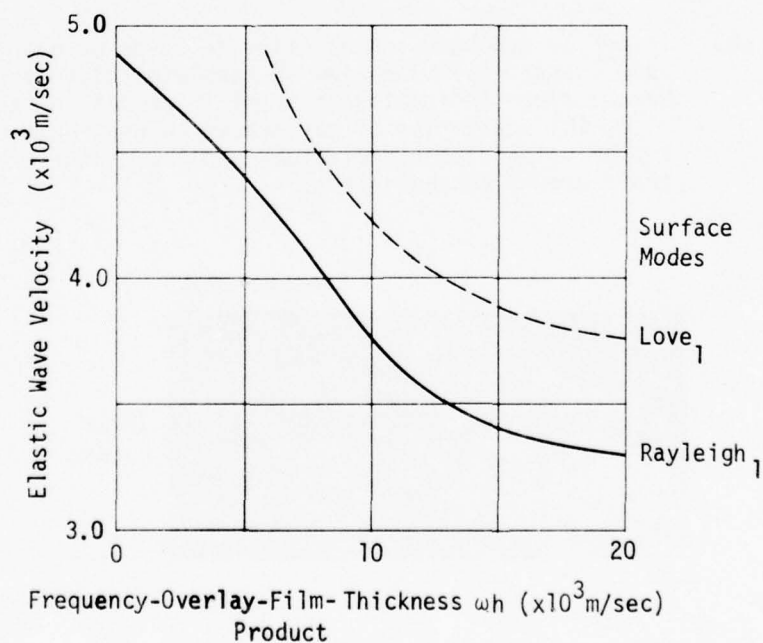
Figure 9A.   Calculated Surface Elastic Wave Velocity Dispersion for
Thermally-Grown SiO_2 Overlay on Si Substrate {001} Cut,
[100] Propagation, [33].

154
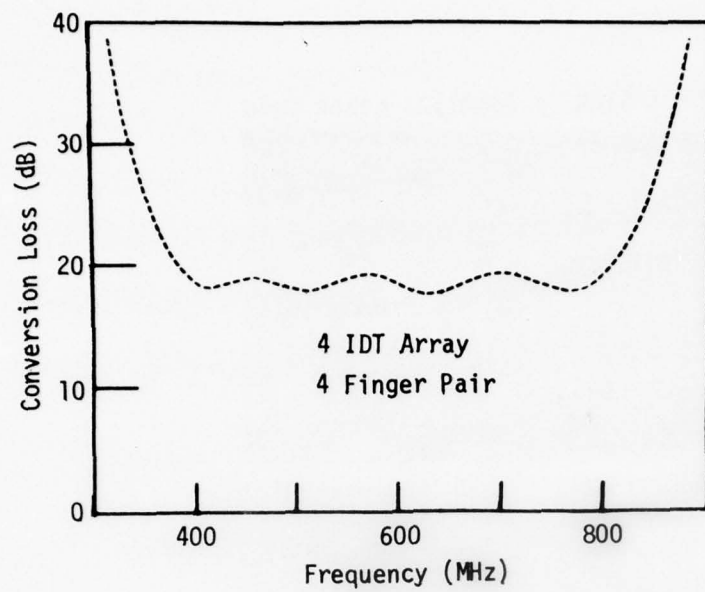
Figure 10A.   Calculated Electronic-Elastic Conversion Loss for Two Wide-band, Bragg-Type Interdigital Transducer Arrays after Tsai [14].
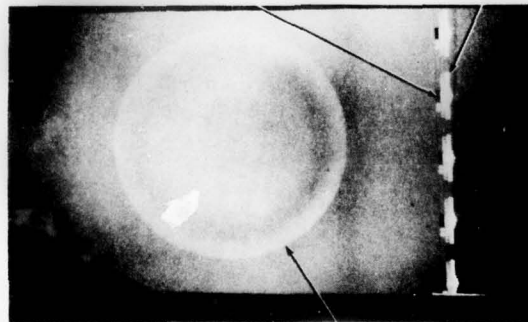
Figure 11A.   A Luneburg Lens Integrated with a Linear Array of Photo-detectors Arranged in Groups.

155

Laser Heat Sink   (GaAl)As Laser Chip

(a)

Al$_2$O$_3$ Substrate   Output Waveguide

(b)

(GaAl)As Laser Emission
From Side Wall Coupler
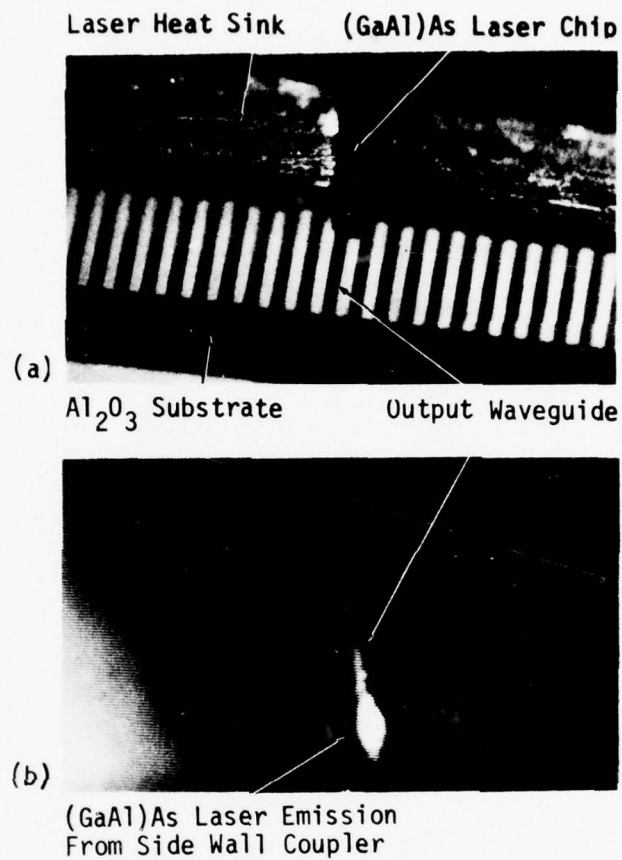
Figure 12A.   Hybrid Coupling of (GaAl)As Laser to Ga$_3$Al$_7$As Waveguide
Via the Laser Fabry-Perot Side Wall Evanescent Field.

156

APPENDIX B

COMPARISON OF OPTICAL WAVEGUIDE LENS TECHNOLOGIES

D. B. Anderson, R. L. Davis, J. T. Boyd,
and R. R. August

Abstract -- Various materials, lens structures, and processes are examined
relative to the lens requirements of an RF spectrum analyzer implemented
through the use of an integrated optics format. Factors which distinguish
optical waveguide lenses and reflectors from conventional imaging lens
systems are enumerated. It is concluded that a thin-film Luneburg lens is
the most viable planar approach based upon the use of oxides and, when
high refractive index materials must be employed, the spherical depressed
geodesic becomes a feasible alternate.

D. B. Anderson, R. L. Davis, and R. R. August are with the Electronics
Research Division, Rockwell International Corporation, Anaheim, CA 92803.

J. T. Boyd, a consultant for Rockwell International, is with the
Electrical and Computer Engineering Department of the University of
Cincinnati, Cincinnati, OH 45221.

I.   INTRODUCTION

The application of an integrated optics approach to the Fourier trans-
form signal processing function is being developed with the expectation of
realizing a wideband, real-time, compact, economical spectrum analyzer as a
functional component [1,2]. Coherent optical signal processing [3] require
refractors and reflectors with near diffraction-limited performance which a
compatible with planar technology. For compactness and wavelength stabilit
a distributed-feedback electron injection laser is preferred, which dictate
the use of the near infrared. Economics, alignment stability, and small
size compels the use of a single substrate which requires lenses of compara
tively small f-number and reflectors for folding of the optical axis so as
be contained within the available substrate area. An optical spectrum
analyzer also includes a photodetector array, a signal input spatial modula
tor and associated electronics. These elements can best be "integrated"
with the optical lenses on a silicon substrate using the thermally-grown
oxide for optical waveguide isolation.

The optical waveguide lens bibliography [4-10] is infinitesimal when c
pared with that of conventional optical lenses and their microwave counter-
parts. Lenses which conform to an integrated optics format exhibit various
different degrees of freedom which are not available to conventional optica
lens designers but are similar to waveguide structures exploited in the
microwave antenna art [11,12]. Therefore, this paper will delineate the
distinguishing differences and will treat materials and process considera-
tions and their relative compatibility with thin-film waveguide lens struc-
tures.

158

II. OPTICAL WAVEGUIDE LENSES CONSIDERATIONS

For an integrated optical spectrum analyzer, several additional considerations dictate a preference for the near infrared aside from the characteristics of GaAs lasers. The presence of Rayleigh scattering in thin-film optical waveguides and lenses directly limits the Fourier transform dynamic range. The effective refractive index of optical waveguides is in part controlled by the waveguide thin-film thickness. Rayleigh scattering is reduced and waveguide tolerances are relaxed by use of the longer wavelength red.

In the near infrared, a wide variety of waveguide material-structures have been demonstrated which exhibit comparatively low loss [13,14]. They include: (1) large band-gap III-V and II-VI semiconductors which exhibit large refractive indices; (2) a family of oxides of intermediate refractive index; (3) a family of glasses of lower refractive index; and (4) a family of organics having a refractive index slightly greater than glass substrates. Various techniques to prepare thin-film waveguides include: (1) homo- and hetero-epitaxy, (2) RF-DC sputtering, (3) evaporation, (4) ion in- or out-diffusion, (5) ion exchange, (6) ion implantation, and (7) nuclear bombardment. The first three of these processes can lead to relatively large, sharp refractive index discontinuities at the waveguide substrate interface as determined by material composition, while the latter processes result in relatively weak or diffused discontinuities at the interface.

The losses exhibited by thin-film waveguides in the red and near infrared are largely due either to the absorption "tail" of the electron band-gap or to the scattering from inhomogeneous depositions and surface roughness. In most oxide thin films, the latter is currently the dominant loss.

The method of thin-film deposition, the state of the substrate, its tempera-
ture, and the stoichiometry of the deposition have a dramatic control of the
losses. The substrate surface roughness is of equal importance. For most
of the thin-film lenses and waveguides reported herein, Ta_2O_5 [15] is
employed as an overlay or underlayer film for lenses, and Corning 7059 glass
[16] is employed as the planar ambient dielectric waveguide. A variety of
glasses and substrate polishing techniques have been investigated with the
conclusion that thermally-grown SiO_2 on Si yields the smoothest low-scattering
substrate surface. Other surface preparation techniques investigated include
rouge, super (wet), fire, and the chemo-mechanical process [14].

An additional scattering loss occurs in waveguides bounded in both trans-
verse dimensions, or in reflectors with one transverse dimension, or at a
waveguide-lens boundary, due to the edge roughness. This edge roughness
arises from the lithographic mask and the method of etch, such as preferential
chemical or ion etch. The most satisfactory means to define a waveguide-lens
interface employs a graded gaseous diffusion around a lens mask during deposi-
tion. The waveguide thickness is thus tapered, however, care is required to
prevent coupling into the substrate [5,17,18] or into higher order modes.

The optical waveguide material-structure selection is conditioned by the
requirements for wave binding to a guide ($n_{waveguide} > n_{substrate}$) and for
minimization of losses. The optical power (convergence and divergence) of a
lens system is, in part, determined by the refractive index differences em-
ployed between the lens and the refractive index in which the system is embedded.
A lens system design, in general, requires the use of the largest practical
range of refractive indices to minimize length. The use of materials where

160

the thin-film waveguide effective refractive index is only slightly greater than the substrate severely limits the numerical aperture. It is possible to circumvent this condition by the use of geodesic lenses which employ a nonplanar contour to control the lens optical thickness.

Conventional optical refractors employ two dimensions with spheric, aspheric, and cylindric surfaces and are usually immersed in free space having a refractive index of unity. The total range of refractive indices of materials in the red and near infrared extends between 1.3 and 3.6 whereas the more typical values are between 1.4 and 1.8. Positive lens elements are produced by convex surfaces and negative lenses are produced by concave surfaces. On the other hand, optical waveguide lens elements are always immersed in another dielectric which may have an effective refractive index greater than or less than the optical element (except geodesic). The maximum/minimum ratios of refractive indices for waveguide lens elements extend from approximately 2.5 to 0.4 whereas the typical range is contained within the ratio 1.4 to 0.7. Because the refractive index ratio may be less than unity, it is also possible to create positive waveguide lens elements using convex interfaces and negative waveguide lenses with concave interfaces.

Because the effective refractive index is also related to the film thickness, it is possible to create inhomogeneous refractors using homogeneous materials [4]. Thin-film waveguide refractors may be formed by (1) the insertion of another dielectric in the lens region, (2) the addition of another higher index film as either an overlay or underlay of the waveguide in the lens region, or (3) as changes of waveguide thickness. Changes of

161

the waveguide effective refractive index can be implemented as a partial
undercut in the lens region or an overlay exterior to the lens region
forming a part of the waveguide, or an undercut of the waveguide film external
to the lens. Except for the materials and film thicknesses, each of these
processes is distinguished by the order of deposition and/or ion etch
through waveguide-lens masks. The wavelength dependence on thickness intro-
duces a chromatic aberration which is greater than that inherent in the bulk
material. When the waveguide thickness is sufficient to support additional modes,
and when the waveguide-lens interfaces introduce mode conversion, the prop-
erties of a lens system will be multi-valued.

An example of homogeneous refractors used to form a non-inverting tele-
photo lens system is illustrated in the photograph collage of Fig. 1. The
plan view of the negative element showing the thickness profile via Newton
rings is depicted in Fig. 1(a). Both the positive and negative refractors
employ Ta_2O_5 as an overlay on the Corning 7059 waveguide. Individual rays
and wide-beam transmission of 6328 Å radiation through the lens system is
evident in Sections (b) and (c), respectively. The telephoto ratio is 1/2 and
a 1 cm aperture has been employed. Visibility of this propagation from the
side is indicative of excessive Mie scattering. Further, the waveguide-lens
interface scattering is also clearly evident and, thus, this lens system per-
formance is not acceptable for use in the optical spectrum analyzer.

III. PLANAR LUNEBURG LENS

The inhomogeneous planar circular refractor, due to Luneburg [19], has
been investigated as an alternative. Interest in the Luneburg lens
[11,12,19,20] arises because it is free of all aberrations except curva-
ture of field and because of the simplicity of its fabrication as a thin-film

162

waveguide structure [6]. Fig. 2(a) illustrates the cross-section of a planar waveguide Luneburg lens with a higher index underlayer between the uniform thin-film waveguide and the substrate. The ray trajectory through the lens is depicted in Fig. 2(b). A Luneburg lens is a circular symmetric refractive structure which will form perfect geometric images of two given concentric circles on each other [20]. If one of the circles is of infinite radius, the lens will focus a collimated beam from any direction exactly to a point on the opposite focal edge. The lens is circular symmetric providing a 2π field of view and employs a radial refractive index profile. This circular symmetric feature is of particular interest in integrated optics where the substrate area is limited because folding of the optical axis may use the lens for several purposes. The waveguide Luneburg lens has a further advantage, that all refractive index variations are continuous, smooth and slow functions with respect to the optical wavelength. Scattering and mode conversion are, therefore, less than in other type waveguide lenses.

Classical Luneburg lenses focus on the opposite edge yielding an f-number of 0.5, which is inconvenient for an integrated optical spectrum analyzer [2] because of the high resolution lithography required to resolve and detect radiation in the focal region. A generalized Luneburg lens having a focal point beyond the lens edge for a plane wave input, overcomes the above disadvantage of the classical Luneburg lens. The geometry for this generalized lens is illustrated in Fig. 2(b).

By following a procedure based on Fermat's principle and similar to that used by Brown [12] in deriving the index profile corresponding to the classical Luneburg lens, we have determined the constraint on index variation

163

n(r) required to focus a beam of parallel rays at a point a distance r_1 from the center of the circular lens region to be

$$n(r,m) = n_e(m) \ \exp \ \frac{\sqrt{n_e(m)^2 r_0^2 - r^2 n^2(r)}}{\pi n_e(m) r_1} \ . \tag{1}$$

In the above equation, r is the radial coordinate from the lens center along the waveguide surface, r_0 is the radius of the lens region, and $n_e(m)$ is the effective refractive index for the waveguide mode (m) of interest. Note that the above equation is not solved for n(r,m), but n(r,m) is readily determined from Eq. (1) numerically as a function of r_1. The derivation of the constraint on the refractive index profile (1) involves an approximation which is reasonable for $F/D = F/2r_0 > 1.3$. Fig. 3 depicts the normalized effective refractive index profile as a function of the normalized lens radius for several f-numbers. It indicates that the transverse profile becomes more uniform having a lower refractive index over a larger central region of the lens as the focal length is increased.

Fig. 4 depicts the minimum required effective refractive index at the center of the Luneburg lens relative to its waveguide ambient refractive index as the lens focal length is increased. For the classic Luneburg lens $n(0,0) = \sqrt{2}$, a high index layer like Ta_2O_5 or Nb_2O_5 on 7059 [6] is required for $F/D = 0.5$. Luneburg lenses have been realized using an "all" 7059 thin film when $F/D \gtrsim 6$. The photographic collage of Fig. 5 illustrates a Luneburg lens refractive index profile via Newton rings (a) and the operation of a lens via the scattered rays (b,c), and when illuminated by a 1 cm wide beam (d). The photographs of Fig. 5 (b and c) include reflections from the substrate back surface in the region of the Luneburg lens. The structure employed consists of Ta_2O_5 (2.2) lens overlay on 7059 (1.59) waveguide on a

7440 substrate. The lens, f-number=1.5, is obtained by use of a conical hole in a thick mask similar to that used by Zernike [6]. This cone base diameter is 1.14 cm, the cone half angle is 15°, and the mask thickness is 2.54 mm. Scattered radiation in Fig. 5 is a substantial reduction of that appearing in Fig. 1.

A comparison of Luneburg lens profiles is illustrated in Fig. 6 as a function of the normalized radius. The experimentally determined lens thickness using the Newton rings and by Tally-Surf is shown in Fig. 6 as a solid line (a). The curve marked (b) shows the calculated refractive index profile for ideal Luneburg lens. Curve (c) is the calculated refractive index profile using the experimentally determined thickness profile where the waveguide thickness is 0.6 μm. It is obvious that the measured and calculated profiles are reasonably matched in the center region with a substantial deviation around the outer annulus. The transmission of individual rays through the Luneburg lens of Fig. 5(a) and profiles of Fig. 6 is shown in Fig. 5(b) and (d) when the lens has been stopped down to an f-number of 2. When the aperture is increased to an f-number of 1.6, aberrations appear at the focus in Fig. 6(c) which correspond to the exterior rays traversing the outer edge of the lens where the experimentally determined refractive index profile does not adequately match the required ideal profile. Reshaping of the mask to form the lens is required to more closely approach the ideal profile for the larger numerical aperture.

IV. GEODESIC LENS

All the lenses considered thus far have employed a change of effective refractive index by altering the thin-film composition and thickness to alter the wavefront in the guide, whereas, it is also possible to employ curved surface topology which alters the propagation length because rays

165

will propagate along geodesics of the surface according to Fermat's principle. Geodesic lenses are of particular interest when the waveguide refractive index is slightly greater than the substrate as occurs for in- and out-diffused $LiNbO_3$ [21], ion exchange in glass [22], and for (GaAl)As heteroepitaxial structures.

Nonplanar surfaces are usually not considered to conform to integrated optical format; however, simple spherical depressions in the substrate are easily fabricated by the ophthalmic optical industry for bifocals. These structures are considered herein because they provide the means to realize an effective refractive index beyond that available from useful materials.

Righini, et al, [7] and Toraldo di Francia [23] have fabricated a variety of geodesic lenses drawing from earlier work on microwave scanning antennas. Spiller and Harper [8] have pointed out that the aberrations of the spherical depression geodesic lens are opposite in sign to those of the refractive lens, and thus may be combined for its suppression. Verber, et al, [9] using ion exchange glass waveguide, have demonstrated uncorrected geodesic lenses. Rinehart [24] has considered a nonspherical surface of revolution as a means to achieve the Luneburg lens in the microwave regime, while Wood and Vahey [10] have considered oblate spheroids. It should be noted that the spherical depression geodesic lens is also functional for surface elastic waves exhibiting identical geometric properties [25]. The cross section of a spheric depressed geodesic lens is illustrated in Fig. 7 with the ray trace through the plan view. The paraxial focal length of a spheric geodesic lens [25] is given by

$$F = \frac{R_c}{2(1-\cos\theta)} \qquad (2)$$

166

where R_c is the radius of the depressed surface at the intersection with the plane and θ is the half-angle of the chord. The geodesic lens f-number as a function of the angular sector of the spherical depression (2) is depicted in Fig. 8.

Several problems are associated with the geodesic lens. First, care is required to fabricate a sharp edge without chipping which creates wide-angle scattering at the intersection of the plane and sphere. This edge must be rounded to minimize scattering, radiation loss at the transition, and mode conversion. A method is required to uniformly produce a small radius reproducibly. Once the substrate is suitably prepared, a thin film must be formed on the surface to act as a waveguide, the thickness of which must be uniform over all surfaces to avoid unwanted refraction. Waveguides formed by diffusive processes satisfy this requirement [9]. For the large polar angles needed to achieve fast lenses, deposition of uniform film thickness over all the curved surfaces is difficult. It is possible to deposit a radially symmetric film to correct spherical aberration [8].

The performance of a quasi- Rinehart-Luneburg geodesic lens (non-spherical) is illustrated in Fig. 9 for the near tangential ray. A reflection from the substrate back surface of this ray is also evident. The concave geodesic lens (chord diameter 3.8 mm) employed a Corning 7059 thin-film RF-sputtered deposit on the 7440 substrate. A "super" polished finish was employed for both the planar and spherical surfaces. Rays traversing the planar substrate exhibit scattering loss of approximately 1 dB/cm, whereas, in the region of the transition and depression, considerably more loss occurs. Another problem with geodesic lens fabrication is the accurate control of the chord diameter and the accurate placement of the lens with respect to other optical elements, such as required for beam expansion.

167

V. EXPERIMENTAL WAVEGUIDE LENS DIFFRACTION PATTERNS

The performance of optical waveguide lenses as determined by measurement of the diffraction pattern is encumbered by the ambient waveguide film and the intervening coupling to the free space diffracted beam. The technique we have employed utilizes wide aperture prism input and output couplers with the waveguide lens to be evaluated located between the couplers. Re-imaging with magnification is employed in the output beam with a fiber-coupled detector for scanning of the output intensity distribution. No correction for spherical aberration of the prism employed at the lens focus couplers has been introduced.

The diffraction patterns of a thin-film waveguide Luneburg lens (a) and an uncorrected spherical depression geodesic lens (b) are illustrated in Fig. 10 using a logarithmic intensity scale and a linear transverse scale reduced by the re-imaging magnification. The Luneburg lens employed Ta_2O_5 on a barium-rich RF-sputtered 7059 waveguide on a 7059 substrate. The lens diameter is 11.2 mm and the focal length is 12 mm. The input beam was collimated and aperture-limited to produce a uniform distribution with a 5 mm beamwidth. The resulting diffraction pattern in Fig. 10(a) exhibits a comparatively well-formed sinc x function. The measured beamwidth referred to the focus is 5 μm at the 3 dB point. The first sidelobe level should be 13 dB down, whereas, the observed sidelobes are approximately 10 dB down. The presence of nearly-symmetrical sidelobes elevated by 3 dB with reasonably defined nulls between the sidelobes is indicative of a quadratic phase error of approximately $\pi/2$ at the edge of aperture. The symmetry and null depth suggests the absence of a cubic phase error. The lack of a systematic side-lobe decay on the left-hand side of the diffraction pattern is attributed to

168

a visible scatterer. The quadratic phase error (spherical aberration) could arise from the input coupling prism, or output coupling prism surface or contact figure, or the lack of correction for the prism thickness in the focal region or in the re-imaging system. The recorded data of Fig. 10 is the convolution of the optical waveguide lens, re-imaging lens and intervening coupling prisms. Detailed analysis to identify the major phase-front error contributor remains.

The performance of an uncorrected spherical depression geodesic lens using an RF-sputtered 7059 waveguide on a 7440 substrate is illustrated in Fig. 10(b). The lens diameter is 14.4 mm and its focal length is 28 mm. A Gaussian beam without truncation was employed for the input where its width was 2 mm at the $1/e^2$ point. The measured output beamwidth at the lens focus is 11 μm at the -8.6 dB point. This diffraction pattern is not well-ordered, that is, the sidelobes are not regular and do not exhibit a systematic decay which indicates that aberrations are dominant, which is to be expected because the lens is spherical and has not been corrected.

The presence of appreciable energy in the sidelobes and their slow decay to a residual level due to scattering becomes a serious compromise for an integrated optical spectrum analyzer, affecting both resolution and dynamic range. These diffraction results and the experience developed during an effort to reduce scattering has led to the use of a more promising waveguide material-structure. This structure employs Corning 7059 waveguide and Ta_2O_5 as an underlayer lens, all deposited on a thermally-grown SiO_2 isolation layer on an Si substrate. The thermally-grown SiO_2 isolation layer with sufficient thickness ($\sim 1 \leq 2$ μm) should approach the characteristics of low loss fibers because the material evolves from the same process, however, an excessive film growth or use of other processes yields an imperfect surface

giving rise to excessive scattering. Further, the use of 7059 over the Ta_2O_5 suppresses the scattering of Ta_2O_5 in the thin sections at the transition into the lens. As with the processing for low loss fibers, extreme purity and cleanliness is required during the processing. One problem not yet addressed is the requirement for a superstrate to isolate the integrated optical circuit from its external environment - presumably, an organic deposited from solution will evolve. The measured diffraction patterns depicted in Fig. 10 show that considerable effort remains to achieve near diffraction-limited operation, as required for an integrated optical spectrum analyzer [2]. A more accurate match of the Luneburg lens thickness profile to the required effective refractive index profile remains to be developed by shaping of the mask, the ion source and the deposition conditions.

The measured transverse distribution of propagation of a Gaussian beam is illustrated in Fig. 11 for an ultra-low loss 5 cm section of Corning 7059 waveguide RF-sputtered upon thermally grown SiO_2 on Si. The beam profile, prior to entry into the input coupling prism, is illustrated in Fig. 11(a) without use of a re-imaging system. The beam profile, after traversing the waveguide and prism couplers, is depicted in Fig. 11(b). With exception of the recorded noise, this diffraction pattern is a reasonable facsimile of the input beam profile. It shows that the spurious responses are more than 25 dB down.

VI. REFLECTORS

Another important consideration in the design of thin-film waveguide optical systems is the requirement for straight and curved reflectors. They must function efficiently and not give rise to scattering or radiation loss. A straight-line, tapered edge provides one effective solution for reflectors;

170

however, it is restricted to the angular range of total internal reflection. The minimum critical angle of incidence is

$$\alpha_{c\ min} = \sin^{-1} \frac{n_s}{n_w} \tag{3}$$

where n_s is the refractive index of the substrate and n_w is the refractive index of the waveguide material. For waveguides having refractive index slightly greater than the substrate, this tapered edge approach restricts its use to near-grazing incidence. Again, care must be exercised to avoid the tapered edge acting as a coupler into the substrate [17,18].

An alternative approach employed successfully depends upon the use of thermally-grown SiO_2 on Si as a single crystal substrate. It is possible to reproducibly cleave through the substrate, isolation layer and waveguide thin-film producing crystallographically perfect facets on the {110} face. When the silicon is oriented so that the waveguide plane is orthogonal to the cleaved plane, Eq. 3 may be used where n_s=1 which leads to a much wider range of total internal reflection. The cleaved surface may be metallized permitting efficient reflection at normal incidence. The operation of a metallized cleaved reflector is illustrated in Fig. 12 using 7059 waveguide on thermally-grown SiO_2 on Si as a substrate. The reflection loss is insignificant. The difference of ray trace intensity is due to less scattering. Observed losses in this waveguide on thermally-grown SiO_2 on Si approached 0.1 dB/cm.

Curved reflectors cannot be produced by cleavage. Attempts at polishing to produce curved orthogonal edges consistently led to microscopic chips and wide-angle scatter. Large curvature reflectors formed by rounding of the substrate edge to fold the optical path from one side of the substrate to another, can be employed as a step toward conflection systems [19]. Because tapered

171

edges are restricted to near-grazing incidence, curved reflectors must follow design procedure for deep conics [26].

VII. CONCLUSIONS

A variety of thin-film waveguide optical elements have been investigated with expectation that they may be employed in a Fourier transform signal processing function. Near diffraction-limited performance is required of these refractors and reflectors. It is concluded that a thin-film Luneburg lens is the most viable planar approach based upon the use of oxides, and when high-refractive index substrate materials must be employed the spherical depressed geodesic becomes a feasible alternative.

One problem identified is the presence of Rayleigh and Mie scattering which limits the dynamic range of the Fourier transform. Currently, thermally-grown SiO_2 on Si yields the smoothest low-scattering isolation layer and substrate for deposition of waveguides, lenses, and cleaved reflectors, useful in the near infrared.

REFERENCES

1. M. C. Hamilton, D. A. Wille, and W. J. Miceli, "An Integrated Optical RF Spectrum Analyzer," IEEE 1976 Ultrasonic Symposium Proceedings, Annapolis, Maryland.

2. D. B. Anderson, J. T. Boyd, M. C. Hamilton, "An Integrated Optical Approach to the Fourier Transform," this issue.

3. K. Preston, Jr., Coherent Optical Computers, McGraw-Hill 1972.

4. R. Shubert and J. H. Harris, "Optical Guided-Wave Focusing and Diffraction," J. Opt. Soc. Am., Vol. 61, pp 154-161, 1971.

5. R. Ulrich and R. J. Martin, "Geometrical Optics in Thin Film Light Guides," Appl. Opt., Vol. 10, pp 2077-2085, 1971.

6. F. Zernike, "Luneburg Lens for Optical Waveguide Use," Opt. Communications, Vol. 12, pp 379-381, 1974.

7. G. C. Righini, V. Russo, S. Sottini, and G. Toraldo di Francia, "Geodesic Lenses for Guided Optical Waves," Appl. Opt., Vol. 12, pp 1477-1481, 1973.

8. E. Spiller and J. S. Harper, "High Resolution Lenses for Optical Waveguides," Appl. Opt., Vol. 13, pp 2105-2108, 1974.

9. C. M. Verber, D. W. Vahey, and V. E. Wood, "Focal Properties of Geodesic Waveguide Lenses," Appl. Phys. Lett., Vol. 28, pp 514-516, 1976.

10. V. E. Wood and D. W. Vahey, "Aspherical Axially Symmetric Geodesic Lenses for Integrated Optics," 1976 Annual Meeting of the Optical Society of America, Tucson, Arizona.

11. R. C. Johnson, "Optical Scanners," R. C. Hansen, Editor, Microwave Scanning Antennas, Vol. 1, pp 213-261, Academic Press 1964.

12. J. Brown, "Lens Antennas," R. E. Collin and F. J. Zucker, Editors, Antenna Theory Part 2, pp 104-150, McGraw-Hill 1969.

13. W. S. C. Chang, M. W. Muller and F. J. Rosenbaum, "Integrated Optics," M. Ross, Editor, Laser Applications, Vol. 2, Academic Press, 1974.

14. T. Tamir, Editor, Integrated Optics, Springer-Verlag, 1975.

15. D. H. Hensler, J. D. Cuthbert, R. J. Martin, and P. K. Tien, "Optical Propagation in Sheet and Pattern Generated Films of Ta_2O_5," Appl. Opt., Vol. 10, pp 1037-1042, 1971.

16. J. E. Goell, "Barium Silicate Films for Integrated Optical Circuits," Appl. Opt., Vol. 12, pp 737-742, 1973.

17. P. K. Tien, R. J. Martin, and G. Smolinsky, "Formation of Light-Guiding Interconnections in an Integrated Optical Circuit by Composite Tapered-Film Coupling," Appl. Opt., Vol. 12, pp 1909-1916, 1973.

18. P. K. Tien, G. Smolinsky, and R. J. Martin, "Radiation Fields of a Tapered Film and a Novel Film-to-Fiber Coupler," IEEE Trans., Microwave Theory Tech., Vol. MTT-23, pp 79-85, 1975.

19. R. K. Luneburg, Mathematical Theory of Optics, University of California Press, 1974, Reprint of mimeographed notes, Brown University Press, 1944.

20. S. P. Morgan, "General Solution of the Luneburg Lens Problem," J. Appl. Phys., Vol. 29, pp 1358-1369, 1958.

21. I. P. Kaminow and J. R. Carruthers, "Optical Waveguiding Layers in $LiNbO_3$ and $LiTaO_3$," Appl. Phys. Lett., Vol. 22, pp 326, 1973.

22. T. G. Giallorenzi, E. J. West, R. Kirk, R. Ginther, and R. A. Andrews, "Optical Waveguides Formed by Thermal Migration of Ions in Glass," Appl. Opt., Vol. 12, pp 1240, 1973.

23. G. Toraldo di Francia, "A Family of Perfect Configuration Lenses of Revolution," Opt. Acta, Vol. 1, pp 157-163, 1955.

24. R. F. Rinehart, "A Solution of the Rapid Scanning Problem for Radar Antennae," J. Appl. Phys., Vol. 19, pp 860-862, 1948.

25. T. Van Duzer, "Lenses and Graded Films for Focusing and Guiding Acoustic Surface Waves," Proc. IEEE, Vol. 58, pp 1230-1237, 1970.

26. H. P. Brueggemann, "Deep Conic Cassegrains," Chapter VIII, Conic Mirrors, Focal Press Limited, 1968.

174
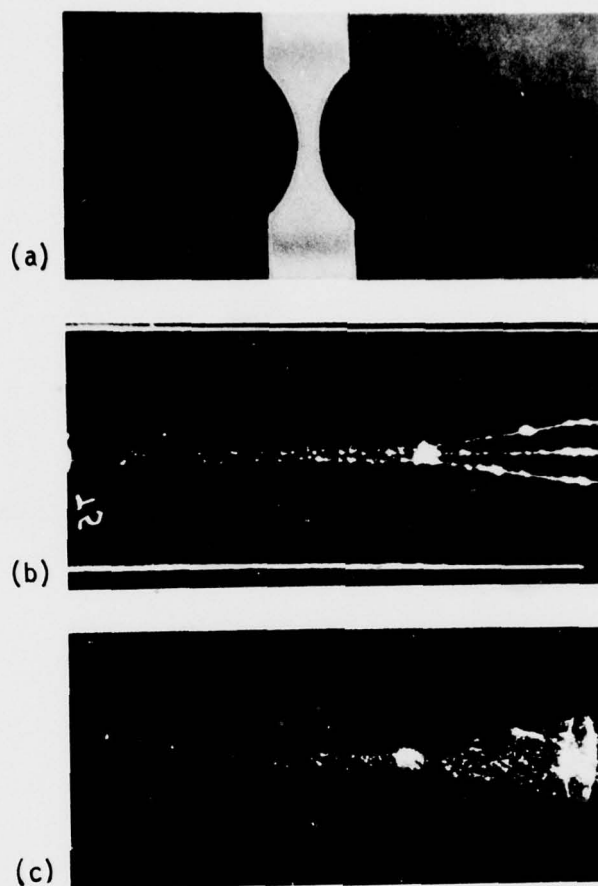
Figure 1B.   Homogeneous Thin-Film Waveguide Refractors Using Ta_2O_5 on Corning 7059 on 7440 Glass: (a) a plan view of negative refractors showing Newton rings indicating tapered edges, (b) scattering of ray traces through telephoto lens system using 6328 Å radiation, and (c) same as (b) except using 1 cm wide input beam.

175
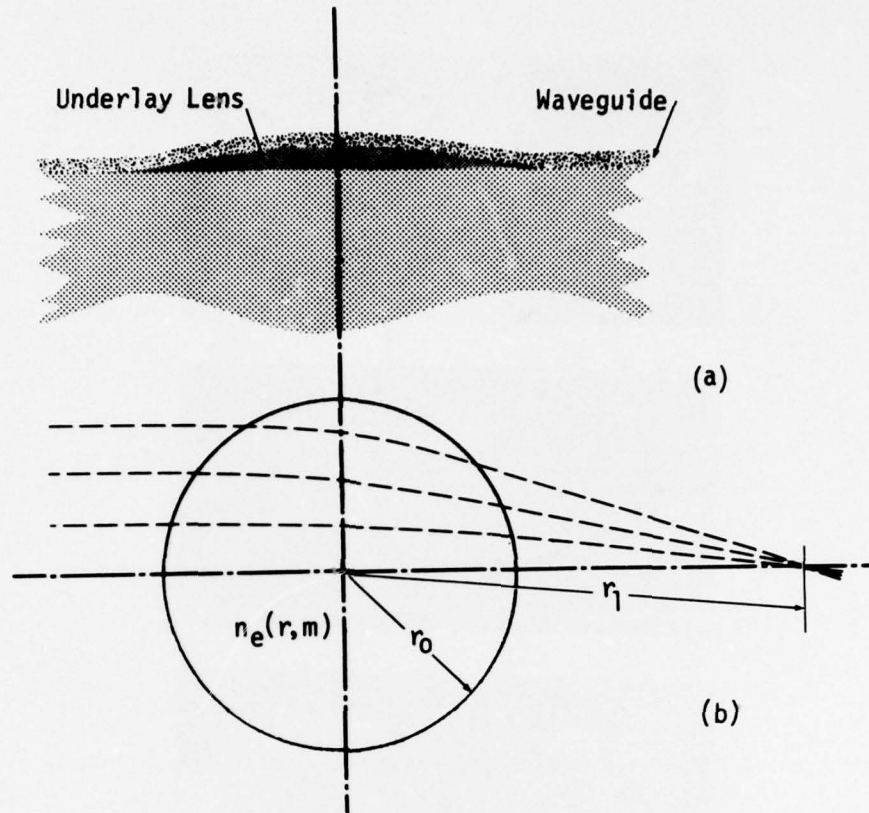
Figure 2B.   Thin-Film Waveguide Luneburg Lens: (a) cross-section using high index underlayer with continuous waveguide, and (b) ray traces through generalized Luneburg lens.

176
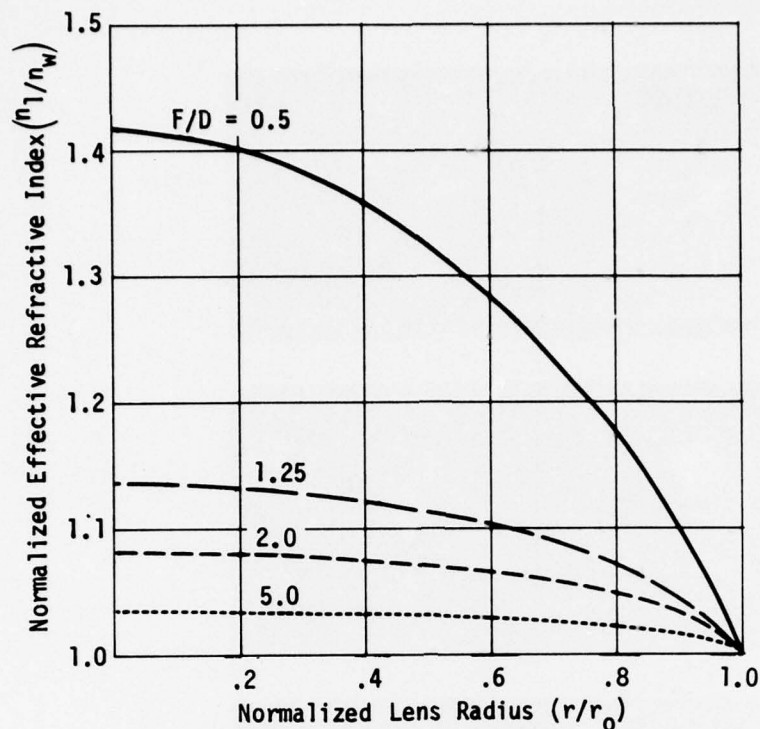
Figure 3B.   Normalized Radial Effective Refractive Index Profile as a
             Ratio ($n_{lens}/n_{waveguide}$) for Several Values of f-number
             (F/D).
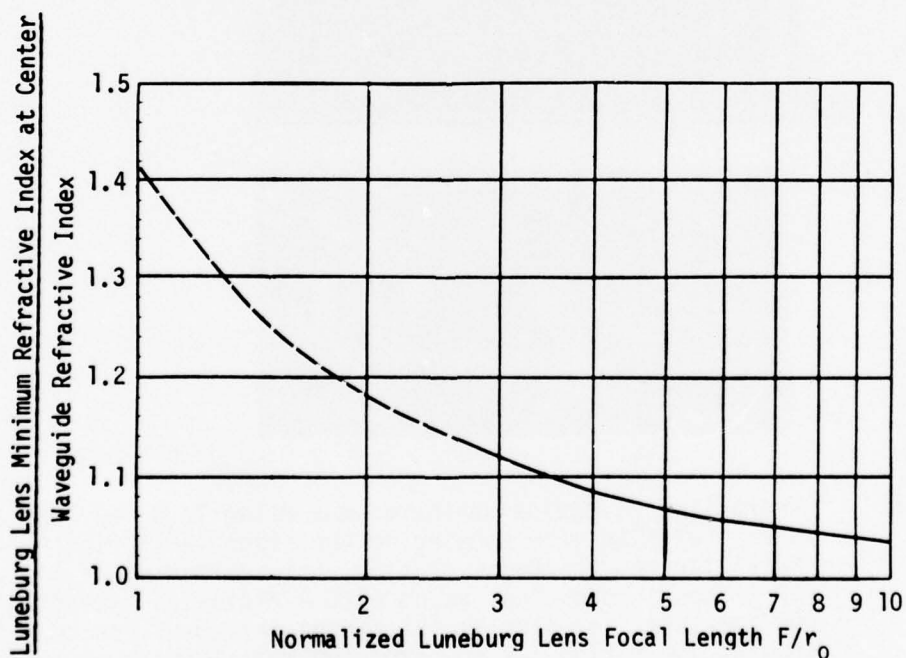
Figure 4B.   Thin-Film Waveguide Luneburg Lens Design Requirement (the
             minimum ratio of refractive indices at center per perimeter
             versus normalized focal length (F/r_0).

177
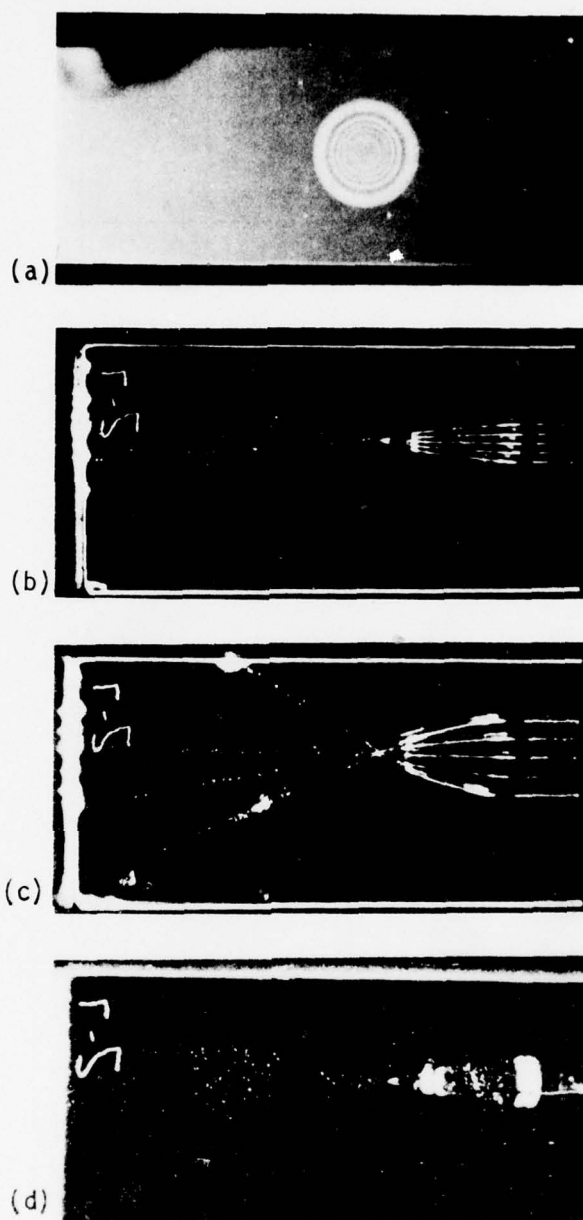
Figure 5B.   Generalized Waveguide Luneburg Lens Using Ta_2O_5 on 7059 on 7440: (a) plan view showing Newton rings indicating the radial tapered thickness profile, (b) scattering of individual ray traces through lens using 6328 Å radiation extending over 5mm aperture, (c) same as (b) except increased aperture is showing aberration due to incorrect radial thickness profile, and (d) same as (b) except using continuous 5mm wide beam.

178
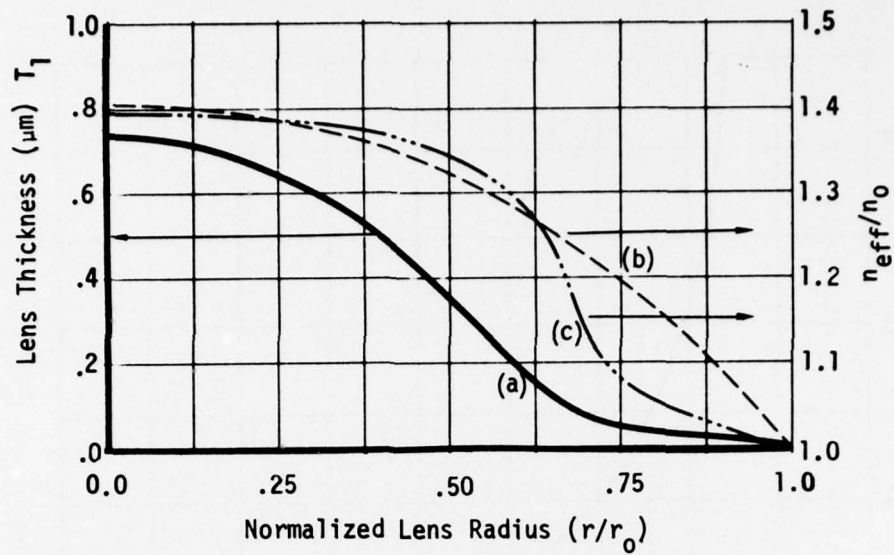
Figure 6B. Waveguide Luneburg Lens Radial Profiles: (a) radial lens thickness profile derived from Newton rings depicted in Fig. 5B, (b) ideal effective refractive index profile, and (c) calculated effective refractive index profile using data of (a).
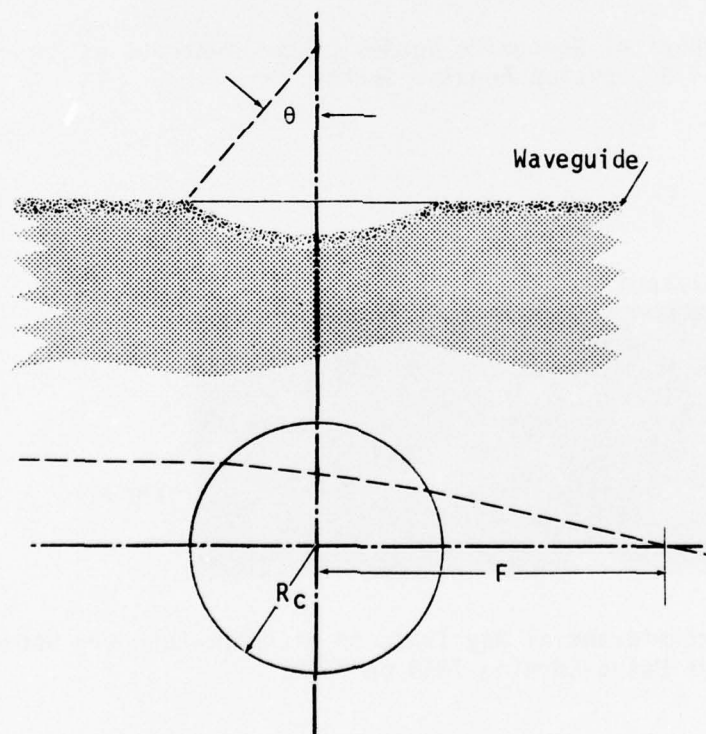
Figure 7B. A Thin-Film Waveguide Geodesic Lens: (a) cross-section, and (b) projected ray trace through geodesic lens.
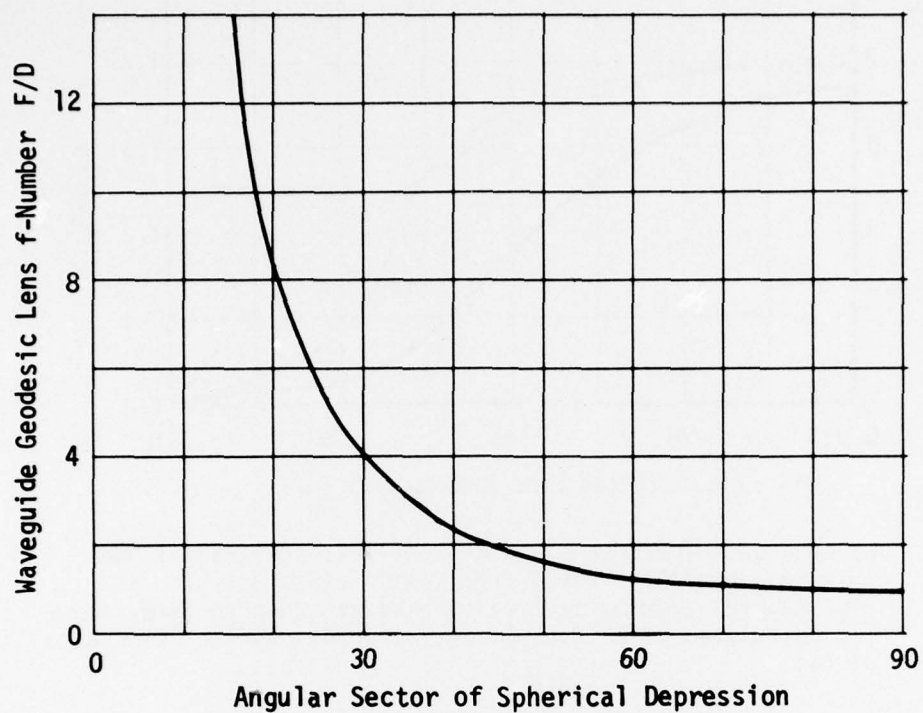
Figure 8B.   Spherical Waveguide Geodesic Lens f-number as a Function of the Depression Angular Sector.
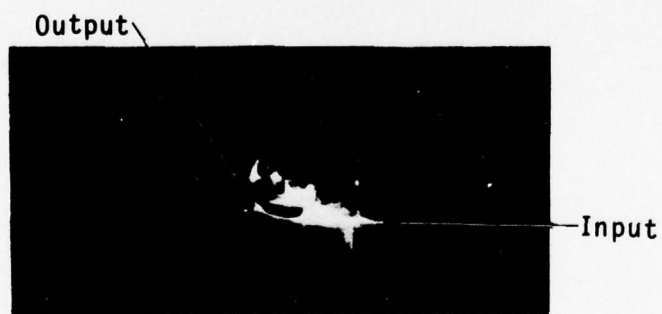
Figure 9B.   Circumferential Ray Trace of Rinehart-Luneburg Geodesic Lens Using Corning 7059 on 7440.

180
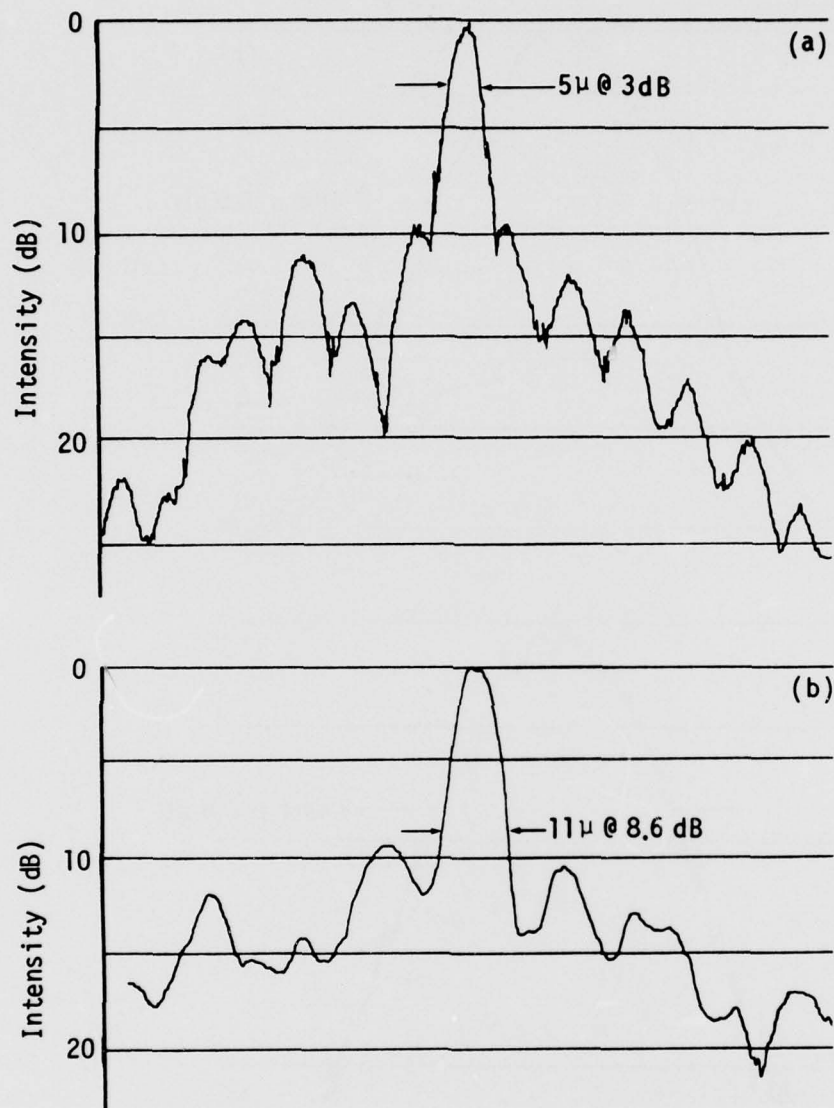
Figure 10B. Experimentally Measured Waveguide Lens Diffraction Patterns: (a) planar thin-film Luneburg lens using Ta_2O_5 on BaO-rich 7059 on 7059 and a uniform illuminated aperture of 5 mm, F=12 mm, and (b) spherical depression waveguide geodesic lens using 7059 on 7440 using 7 mm Gaussian input beam depicted in Fig. 11B, F=20 mm.
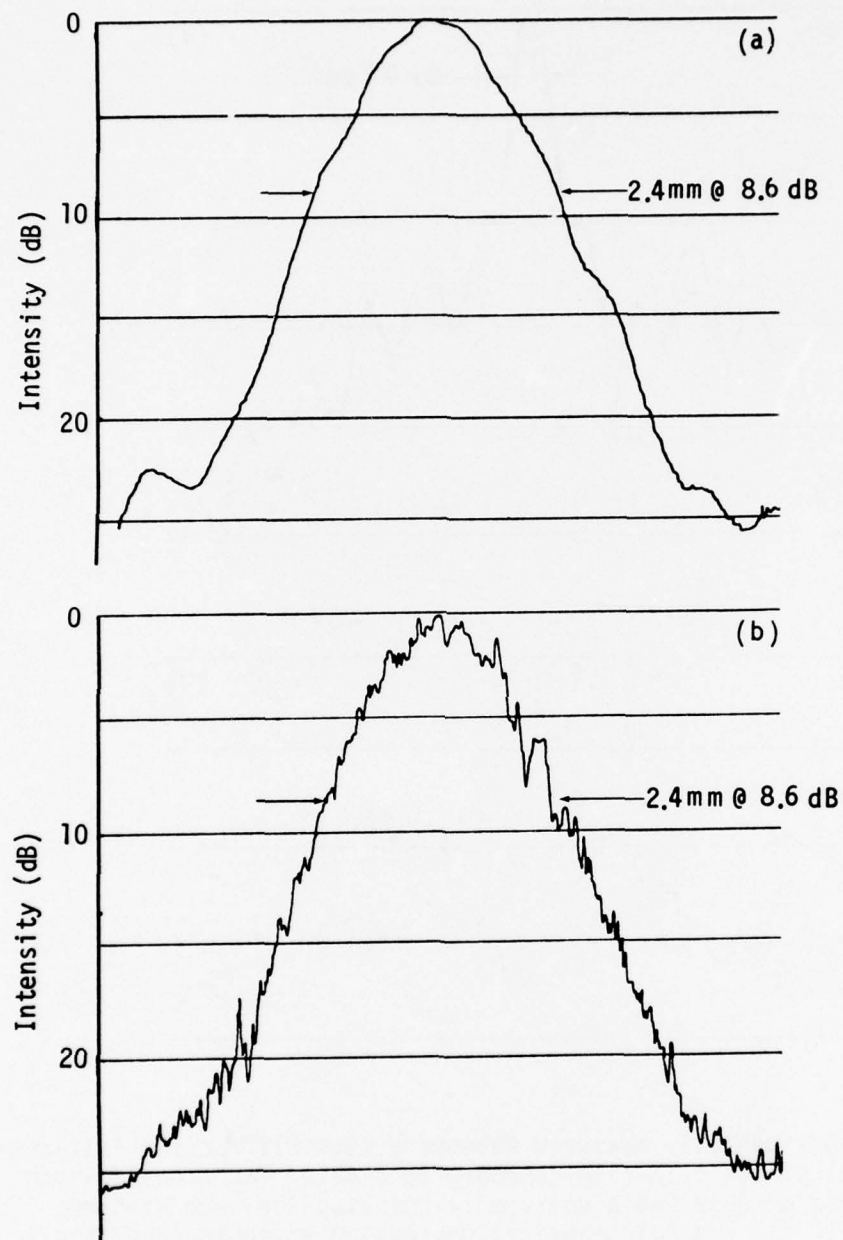
Figure 11B.   Waveguide Scattering Using 7059 Waveguide on Thermally-Grown SiO$_2$ on Si: (a) Gaussian input beam profile, and (b) measured output beam profile after propagating through BK-7 input/ output coupling prisms and 5 cm of 7059 waveguide.

182
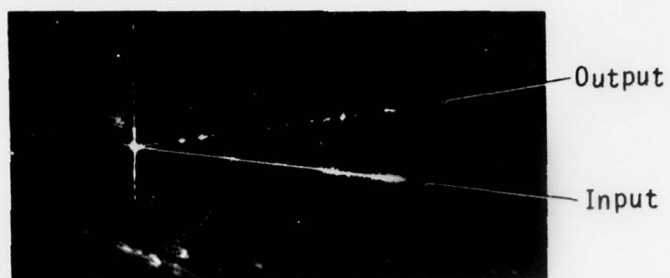
Figure 12B. Thin-Film Waveguide Reflector Using Cleaved Metallized Edge (Al) of 7059 Waveguide on Thermally-Grown SiO_2 on Si.

APPENDIX C

INTEGRATED OPTICAL WAVEGUIDE AND

CHARGE COUPLED DEVICE IMAGE ARRAY *

J.T. Boyd and C.L. Chen
Solid State Electronics Laboratory
Department of Electrical and Computer Engineering
University of Cincinnati
Cincinnati, Ohio   45221
(513) 475-4461

Abstract

The device structure and experimental operation of an integrated optical waveguide and charge coupled device (CCD) detector array are considered. The use of silicon as a substrate allows direct fabrication of the CCD detector array and a thermally oxidized layer of SiO_2 forms an effective substrate for waveguide deposition. The detector array is composed of a two-phase, overlapping-gate CCD with first level polycrystalline silicon electrodes and second level aluminum electrodes connected in parallel by means of a series of gates to an array of photodiodes. In the photodiode region the SiO_2 layer is tapered to a termination so that with minimal scatter, light is multiply-refracted into the detector region. The center-to-center detector element spacing of the device fabricated and successfully operated is 32 μm. Optimum detector length is considered as a function of waveguide thickness. The integrated waveguide-CCD array is expected to become an integral part of various signal processing devices.

185

I. INTRODUCTION

An integrated optical waveguide and charge-coupled device (CCD) linear
imaging array have been fabricated and successfully operated. Such an
integrated device is expected to find many applications in integrated
optical signal processing device structures. Optical signal processing
using an integrated optical format combines the advantages of parallel
processing with those present in an efficient, compact, and economical
device. Parallel processing occurs when information is imparted to the
transverse spatial distribution of an optical wave. Appropriate modulation
and processing techniques include highly-efficient and wide band
acoustooptic deflection,[1-4] electrooptic deflection,[5,6] and one-dimensional
spatial Fourier transformation performed by an optical waveguide lens.[7]
For example, integrated optical acoustooptic deflection, optical waveguide
lenses, and an integrated waveguide-detector such as described herein, can
be used to perform wide band spectrum analysis of electronic signals.[8] In
this and general integrated optical signal device configurations information
carried by the light wave can be converted to electrical signals by means
of a detector array. With the presence of a CCD in the detector array,
transformation of the electrical signal from a parallel format into a
serial format occurs in a natural and simple way. Information capacity of
integrated optical signal processing devices will be limited by beam
diffraction or array resolution and detector dynamic range. As the presence
of optical scattering will reduce this capacity, integration of the array
into the optical waveguide, and thereby minimizing scattering occuring in

186

waveguide-detector coupling, will allow superior performance as compared with the use of an external detector array.

The integrated waveguide-CCD detector array may find additional applications based on its inherent property of parallel entry of signal information into a CCD shift register. Optical injection of parallel signals into CCDs offers significant advantages over electrical injection techniques, in that for the latter sophisticated stabilized charge injection circuits are required for each entry tap.[9] Furthermore, capacitive coupling limits both the proximity of adjacent taps and the maximum usable signal frequency for parallel electrical injection. Parallel optical signal injection using bulk optical waves along with a mask to implement a fixed tap weight transversal filter has previously been demonstrated.[10] We anticipate that the use of integrated optical channel waveguide-detector structures would yield a device with greatly increased channel density and channel isolation. Parallel integrated optical signal injection into CCDs may also find application in multi-plexing, programmable filtering, and memory devices.

The integrated waveguide-CCD detectors use silicon as a substrate. Besides allowing fabrication of a sophisticated detector array providing serial signal output, use of silicon allows fabrication of a variety of electronic circuitry on the same substrate. Furthermore, surface elastic waves can be excited efficiently on silicon using a ZnO film in the transducer region.[11] The thermally-oxidized SiO_2 layer, not being a deposited film, presents a very smooth, low refractive index surface for waveguide deposition. As the SiO_2/Si surface is well-suited for the

187

formation of channel waveguides by preferential etching,[12] an array of channel waveguides with each waveguide coupled to an array element could provide increased spatial resolution and reduce the effects of optical scattering and spatial sampling.

II. DEVICE STRUCTURE

The integrated optical waveguide and CCD linear image array are formed using a silicon substrate. Use of silicon allows the CCD detector array to be formed using the established processes of silicon device fabrication technology. The optical waveguide is formed on a layer of SiO_2 thermally-grown on the silicon surface. This layer is sufficiently thick (typically 1 μm.) so that evanescent coupling of light from the waveguide to silicon is negligible, except in the detector region.[13] In the detector region, the SiO_2 layer tapers to zero thickness so that light in the waveguide is multiply-refracted into the silicon substrate. A taper which minimizes optical scatter is formed by allowing a carefully controlled amount of undercutting to occur during etching in device processing.[14] A profile of the integrated waveguide - CCD detector structure is shown in Figure 1.

The basis of CCDs is the metal-oxide-silicon (MOS) capacitor. In Figure 1 electrodes are formed from both aluminum (Al) and conducting polycrystalline silicon (polysilicon). Potential wells for minority charge are formed at or near the silicon surface under the electrodes of such capacitors upon application of an appropriate voltage. Charge representing a signal level can be stored in such a well for short periods of time. Charge transfer occurs by creating a deeper well beneath an adjacent capacitor by applying a larger voltage. By alternating capacitor voltages in either a two, three, or four phase manner, unidirectional charge transfer along an array of MOS capacitors can be effected.[15] A p-n junction is located at each end of the capacitor array for serial injection and collection of signal charge.

188

The detector array in Figure 1 consists of an array of photodiodes formed in n-type silicon connected in parallel by means of a series of gates to a CCD shift register.[16,17] One CCD unit cell corresponds to each photodiode. Channel isolation is maintained through the series of gates by the presence of channel stopping n+ regions. The detector array integrates the optical signal incident on the array of photodiodes as the potentials of the control and integration gates are adjusted so that charge excited by incident light collects underneath the integration gate. At the end of the integration period T, the transfer gate is turned on so that the collected charge is transferred into the shift register. This charge transfer occurs simultaneously for each array element. This parallel transfer of charge occurs in a time less than 1/2 of the CCD clock period so that the CCD is essentially stationary. Once this charge has transferred into the shift register, the transfer gate is turned off and the charge is shifted along the register to the end where a serial, discrete-time signal emerges representing the spatial light distribution. As soon as the transfer gate is turned off, the photosensors begin integrating charge and the cycle is repeated. The integration time is thus given as

$$T = N/f_c \, , \tag{1}$$

where N is the number of CCD cells equal to the number of array elements and f_c is the CCD clock frequency. Because charge integration can occur while CCD readout takes place, sensing takes place essentially 100% of the time for reasonable values of N.[18]

189

The CCD shift register portion of the device is a two-phase, overlapping-gate structure consisting of one level of polysilicon electrodes insulated by an additional layer of SiO_2 from a second level of overlapping aluminum electrodes.[19] Use of such an overlapping gate structure is superior to a single-level electrode in that such devices are characterized by greater stability and a higher charge transfer efficiency or, equivalently, a lower transfer inefficiency.[20] Dispersion of signal information is thus minimized.

For many applications of the integrated waveguide - CCD detector array, minimizing the array element center-to-center spacing allows the information handling capability to be maximized.[8] Such spacings will generally be limited by lithography considerations. Large aspects ratios of the rectangular photodiode region are generally undesirable. The question thus arises as to whether the extent of the photodiode in the direction of light propagation L can be chosen sufficiently large so that nearly all light incident can be multiply refracted into the detector region. To examine this question, we consider the decay of light intensity along the photodiode surface in the direction of light propagation I(z), given as[13]

$$I(z) = I_0 e^{-\alpha_e z} \qquad . \qquad (2)$$

In (2) α_e is an effective decay constant accounting for light coupled into the photodiode region given as

$$\alpha_e = \frac{1-R}{d \tan \theta} \quad , \qquad (3)$$

where d is the waveguide thickness and θ is the waveguide mode characteristic angle with respect the waveguide surface normal. For the case of

multiple refractive coupling (zero thickness SiO_2 layer in the photodiode region) R in (3) is the appropriate Fresnel reflection coefficient at the waveguide-silicon interface for the mode characteristic angle and polarization in question.[21] We will restrict our present discussion to the TE_o mode. For a thin SiO_2 layer in the photodiode region evanescent wave coupling will occur causing the field in the waveguide to decay according to (2) and (3), but with R interpreted more generally as a composite reflection coefficient. As evanescent coupling is weaker than multiple refractive coupling, multiple refraction is preferred as it allows minimization of the photodiode length L required for efficient coupling. An analysis of photodiode quantum efficiency for the type of waveguide coupling described herein has shown that for a variety of situations the quantum efficiency increases with $\alpha_e L$ until $\alpha_e L \sim 3$.[14] Since further increase of $\alpha_e L$ causes no significant increase in quantum efficiency, an optimum value of detector length L_o can be defined as

$$L_o = 3/\alpha_e. \tag{4}$$

The magnitude of the device quantum efficiency for detector lengths greater than (4) saturates at a value determined by the silicon absorption coefficient at the wavelength of interest, depletion region depth, carrier diffusion lengths, and depth of the surface recombination region.

We have calculated the optimum detector length L_o for the TE_o mode as a function of waveguide thickness d for a waveguide refractive index of n_g = 1.61. This refractive index is characteristic of the KPR photoresist waveguides used in the experiments described herein, as well as characteristic of 7059 sputtered glass waveguides. The result of the

191

calculation is shown in Figure 2 for $\lambda=.9$ μm and $.6$ μm. The portions of the curves to the left of the dotted vertical lines are the regions in which only a single TE mode can exist. In the single mode regions the optimum detector lengths would allow fabrication of efficient photodiodes with reasonable aspect ratios and with center-to-center spacings approaching photo-lithographic limits. However, for multimode waveguides the corresponding optimum detector lengths become quite long. It is fortunate that in many signal processing applications use of a single-mode waveguide is advantageous in view of other considerations.[8] In Fourier optical processing utilizing optical waveguide lenses the integrated waveguide-detector array described herein would find application in focal plane imaging. If L_o exceeds the depth of focus for such applications, then an array of channel waveguides, one passing directly over each photodiode would be required to preserve signal integrity.

Utilization of the integrated waveguide-detector arrays is limited by a maximum input optical power density S_{max} incident on each photodiode before dispersion of the discrete time signal emerging from the CCD occurs. The optically-induced charge must remain less than the maximum signal charge handling capability of the CCD Q_{max}, given approximately as

$$Q_{max} = C_{ox}A\Delta V, \qquad (5)$$

where C_{ox} is the oxide capacitance per unit area, A is the area of each polysilicon electrode, and ΔV is the difference between the maximum and minimum values of CCD clock voltage. The presence of ΔV in (5) results from assuming two phase clock operation with pulse overlap. The maximum incident optical power density S_{max} is then just that value causing optically

192

induced charge in T seconds to be equal to Q_{max}, i.e.

$$S_{max} = \frac{h\nu C_{ox} A\Delta V}{e\eta sdT} \qquad (6)$$

where $h\nu$ is incident photon energy, η is the device quantum efficiency, e is electron charge, and s is the width of the detector along the surface perpendicular to the direction of light propagation. For the actual fabricated device described in the next section $C_{ox} = 2.95 \times 10^{-8}$ F/cm^2, $A = 1.56 \times 10^{-5}$ cm^2, $s = 25$ μm, and $L > L_0$ for $d = 1$ μm. Assuming typical or reasonable values of $\eta = .1$, $\Delta V = 10$ volts, $T = 10^{-5}$ sec., and $\lambda = .9$ μm, we find from (6) that $S_{max} = 25$ W/cm^2. This power density corresponds to a power of .25 mW for a 1 mm. diameter laser beam propatating in a 1 μm thick optical thin-film waveguide.

III. DEVICE OPERATION

The integrated waveguide-CCD detector array was fabricated using n type silicon having resistivity of 8 ohm-cm. and 100 orientation. The detector portion of the resulting device is shown in Figure 3. The presence of the photodiodes provides an electrode-free surface region for coupling light from the waveguide to the detector region by multiple refraction. This device contains 19 array elements with the photodiodes measuring 25 μm x 115 μm with 7 μm of isolation between adjacent elements. In view of Figure 2, the photodiode length of 115 μm is quite sufficient for effective coupling for the KPR photoresist waveguide employed in our experiments. However, this length would be somewhat long if we were to attempt to reduce the center-to-center spacing to the photolithographic limit. The two-phase overlapping gate CCD has a conventional charge collection diode for signal output and a charge injection diode for serial input. The latter allows for electronic evaluation of the CCD and for serial injection of bias charge.

193

A number of devices such as that shown in Figure 3 were fabricated on a single silicon wafer. After initial probe testing the wafer was segmented and individual arrays were mounted and bonded in dual-in-line packages. The packages employed were specifically altered so they accomodate a sufficiently large piece of silicon that would allow space for prism coupling of light into the waveguide and for waveguide propagation. Once packaged the devices could then be inserted in a socket attached to a standard prism coupling optical mount. A macroscopic view of HeNe laser light coupled into the optical waveguide is shown in Figure 4-a. The bright area on the left is a top view of the prism illuminated by scattered light, while the dark area in the center is the clamp pressing the prism against the surface. The streak of scattered light is approximately 125 μm wide and corresponds to the light beam which had been externally focused propagating until it reaches the detector region. Bonding wire leading from bonding pads on silicon to connections on the package is illuminated by scattered light. The detector array is located between the termination of the streak of light and the bonding pads. Because the magnification in Figure 4-a is considerably less than that in Figure 3, details of the CCD detector array are not resolvable. Note that there is no visible indication of excess scatter occuring in waveguide-detector coupling. Figure 4-b is an oscilloscope trace of the signal emerging from the CCD corresponding to the laser excitation in Figure 4-a. Differential amplification of the signal was used to eliminate some of the pickup from the clock pulses.

The device was operated with a two-phase clock producing overlapping pulses in the 100 KHz frequency range. Counter circuitry synchronized to the clock was used to control pulsing of the transfer gate so that this gate was turned on only after charge in the CCD shift register had been completely shifted out. Counter circuitry was also employed to provide a suitable

194

electronic input for electronic evaluation of charge transfer efficiency. Charge transfer efficiency can be evaluated by serially injecting several low duty-cycle rectangular pulses with each separated by one clock period.[20] By carefully noting the degradation of the leading and trailing edges of the pulse train, information regarding transfer efficiency can be inferred. For the devices fabricated we determined a transfer efficiency of .993 per double transfer. Although this value is adequate for performance of our 19 stage device, higher values can be obtained. Good charge transfer efficiency requires very sharp lateral potential barriers.[15] Although the purpose of the channel stop diffused regions is to provide such barriers, the device processing sequence we employed involved a high temperature thick gate oxide growth step after the channel stop diffusion. Further diffusion thus would occur during the oxide growth, resulting in more gradual lateral barriers. Evidence that this was indeed occuring was obtained from the transfer efficiency measurements in that larger values of bias charge than usual were required to eliminate fixed transfer loss.[20] The problem can be overcome by using ion implantation for channel stop doping and altering the processing sequence.

IV. SUMMARY

Successful fabrication and operation of a linear CCD image array integrated into an optical waveguide structure have been described. The integrated device is fabricated using silicon with a thick layer of thermally-oxidized SiO_2 serving as the waveguide substrate. Data have been presented with regard to the optimum array element size required for the light wave to be efficiently coupled into the detector region. Minimal excessive scattering in the region where coupling of light from the waveguide to the detector occurs was observed. The integrated structure that has been described herein is expected to serve as a basic element in integrated optical signal processing devices and to provide a method for parallel entry of information into CCDs. In any such applications the use of silicon allows for integration of additional electronic circuitry and devices with the integrated waveguide-CCD detector array.

REFERENCES

1. L. Kuhn, M. L. Dakss, P. F. Heidrich, and B. A. Scott, "Deflection of an Optical Guided Wave by a Surface Acoustic Wave," Appl. Phys. Lett. Vol. 17, pp. 265-267, 1970.

2. C. S. Tsai, M. A. Alhaider, L. T. Nguyen, and B. Kim, "Wideband Guided-Wave Acoustooptic Bragg Diffraction and Devices Using Multiple Tilted Surface Acoustic Waves," Proc. IEEE, Vol. 64, pp 318-328, 1976.

3. B. Kim and C. S. Tsai, "High-Performance Guided-Wave Acoustooptic Scanning Devices Using Multiple Surface Acoustic Waves," Proc. IEEE, Vol. 64, pp 788-793, 1976.

4. E. G. H. Lean, J. M. White, and C. D. W. Wilkinson, "Thin-Film Acoustooptic Devices," Proc. IEEE, Vol. 64, pp 779-788, 1976.

5. D. P. Giarusso and J. H. Harris, "Electrooptic Modulation in a Thin Film Waveguide", Appl. Opt. Vol. 10, pp 2786-2788, 1971.

6. C. S. Tsai and P. Saunier, "Ultrafast Guided - Light Beam Deflection/ Switching and Modulation Using Simulated Electro-optic Prism Structures in $LiNbO_3$ Waveguides," Appl. Phys. Lett. Vol. 27, pp 248-250, 1975.

7. R. Shubert and J. H. Harris, "Optical Guided Wave Focusing and Diffraction," J. Opt. Soc. Amer., Vol. 61, pp 154-161, 1971.

8. D. B. Anderson, J. T. Boyd, M. C. Hamilton, and R. R. August, "Integrated Optics Approach to the Fourier Transform," to be published.

9. M. H. White, I. A. Mack, F. J. Kub, D. R. Lampe, and J. L. Fagan, "An Analog CCD Transversal Filter with Floating Clock Electrode Sensor and Variable Tap Gains," Dig. of Tech. Papers, IEEE International Solid State Circuits Conference, Philadelphia, Pa., 1976.

10. M. A. Copeland, D. Roy, J. D. E. Beynon, and F. Y. K. Dea, "An Optical CCD Convolver," IEEE Trans Electr. Dev. Vol. ED-23, pp 152-155, 1976.

11. F. S. Hickernell, "Zinc Oxide Thin-Film Surface Wave Transducers," Proc. IEEE, Vol. 64, pp 631-635, 1976.

12. W. T. Tsang, C. C. Tseng, and S. Wang, "Optical Waveguides Fabricated by Preferential Etching," Appl. Opt. Vol. 14, pp 1200-1206, 1975.

13. P. K. Tien, and R. Ulrich, "Theory of Prism—Film Coupler and Thin Film Light Guides," J. Opt. Soc. Am. Vol. 60, pp 1325-1337, 1970.

14. J. T. Boyd and C. L. Chen, "Integrated Optical Silicon Photodiode Array," Appl. Opt. Vol. 15, pp 1389-1393, 1976.

15. C. H. Sequin and M. F. Tompsett, Charge Transfer Devices, Academic Press, 1975.

16. D. F. Barbe, "Imaging Devices Using the Charge Coupled Concept," Proc. IEEE Vol. 63, pp 38-67, 1975.

17. A. J. Steckl, R. D. Nelso.1, B. T. French, R. A. Gudmundsen, and D. Schechter, "Application of Charge Coupled Devices to Infrared Detection and Imaging," Proc. IEEE Vol. 63, pp 67-74, 1975.

18. M. F. Tompsett, G. F. Amelio, W. J. Bertram, R. R. Backley, W. J. McNamara, J. C. Mikkelsen, and D. A. Sealer, "Charge Coupled Imaging Devices: Experimental Results," IEEE Trans. Electr. Dev. Vol. ED-18, pp 992-996, 1971.

19. W. F. Kosonocky and J. E. Carnes, "Two Phase Charge-Coupled Devices with Overlapping Polysilicon and Aluminum Gates," RCA Rev. Vol. 34, pp 164-202, 1973.

20. R. W. Brodersen, D. D. Buss, and A. F. Tasch, "Experimental Characterization of Transfer Efficiency in Charge-Coupled Devices," IEEE Trans. Electr. Dev. Vol. ED-22, pp 40-46, 1975.

21. M. Born and E. Wolfe, Principles of Optics, Second Edition, Pergamon Press, 1964.
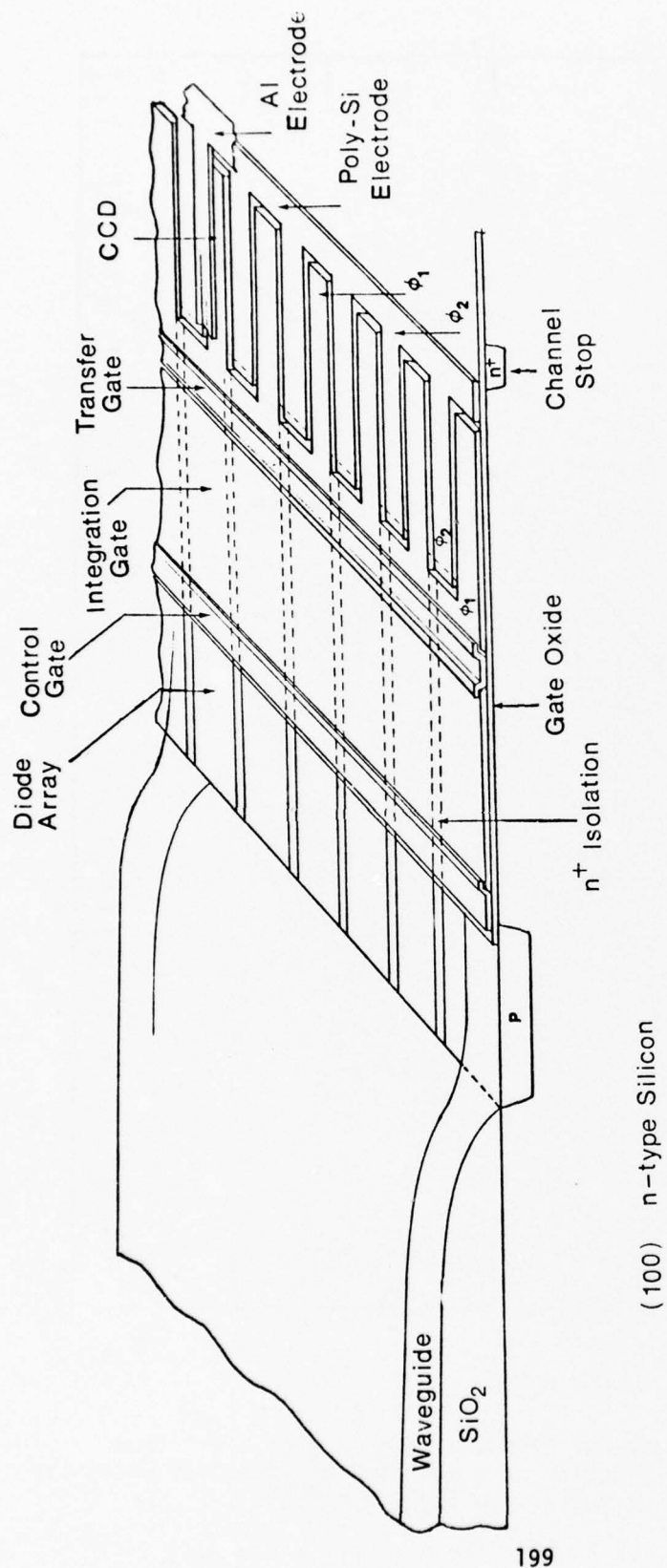
Figure 1C. Integrated Optical Waveguide and CCD Detector Array.

199

Figure 2C.   Detector Length for Efficient Coupling of Light from
             Waveguide to Detector as a Function of Waveguide Thickness
             for a Waveguide Refractive Index n = 1.61.

200

todiode
ay

ysilicon
egration gate

phase

ctrodes

Aluminum
Transfer Gates

Figure 3C.   Linear Photodiode Imaging Array Coupled to a Two-Phase,
Overlapping Gate CCD.

201
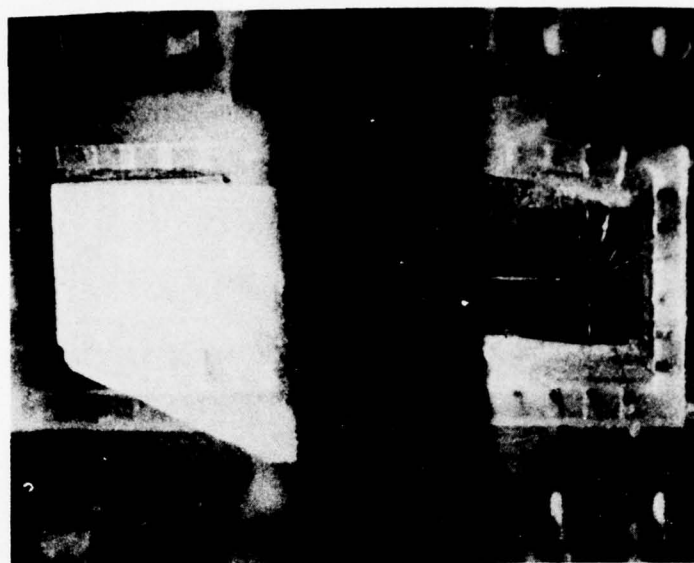
(a)

(b)

Figure 4C. (a) Light Propagating in an Optical Waveguide from the Prism Coupler to the Integrated CCD Detector Array.

(b) CCD Output Signal Corresponding to Illumination Shown in (a).

202

APPENDIX D

LINEAR CHARGE COUPLED DEVICE DETECTOR ARRAY FOR IMAGING
LIGHT PROPAGATING IN AN INTEGRATED THIN-FILM OPTICAL WAVEGUIDE*

C.L. Chen and J.T. Boyd
Solid State Electronics Laboratory
Department of Electrical and Computer Engineering
University of Cincinnati
Cincinnati, Ohio 45221
(513) 475-4461

ABSTRACT

We will discuss device design, fabrication, and operation of a linear charge coupled device (CCD) detector array integrated with a thin-film optical waveguide and applications of this structure to integrated optical signal processing and fiber optical communications. A two-phase, overlapping-gate CCD is connected in parallel by means of a series of gates to an array of photodiodes. The photodiode provides an electrode-free surface region so that a highly-efficient waveguide-detector coupling technique can be implemented. A thermally-oxidized layer of SiO_2 forms an effective substrate for the optical waveguide.

I. INTRODUCTION

A CCD linear imaging array integrated with an optical waveguide structure has been fabricated and successfully operated. In this integrated device guided optical waves propagate along the wafer surface entering the imaging device laterally as opposed to from the top or bottom of the device as in conventional imaging devices. Light can be confined in a thin-film in the transverse dimension perpendicular to the film surface by having a film thickness on the order of the optical wavelength and a refractive index greater than that of the substrate. As a thick layer of SiO_2 having refractive index n = 1.46 serves as the effective substrate for the thin-film waveguide, a wide variety of thin films having a larger refractive index can be utilized to form optical waveguides. If the film is uniform along the direction parallel to the axis of the detector array, a slab waveguide exists and the function of the CCD linear detector array is to image light in this transverse direction. This light variation could be the result of parallel optical signal processing performed at another location in the optical waveguide. Alternately, a number of parallel channel waveguides could be defined photolithographically with each channel waveguide coupling to a single array element. Although both types of structures are expected to find applications in signal processing and optical communications, the present discussion will generally be confined to the slab waveguide structure.

II. DEVICE STRUCTURE AND OPERATION

The integrated optical waveguide and CCD linear image array are formed on a common silicon substrate with the optical waveguide being formed on a layer of SiO_2. This layer is sufficiently thick (typically 1 μm.) so that evanescent coupling of light from the waveguide to silicon is negligible, except in the detector region. In the detector region, the SiO_2 layer tapers to zero thickness so that light in the waveguide is coupled into the silicon substrate.[1] A taper which minimizes optical scatter is formed by allowing a carefully controlled amount of undercutting to occur during etching in device processing. A profile of the integrated waveguide - CCD detector structure is shown in Figure 1. Note in Figure 1 that the waveguide is continuous along the diode region instead of directed and terminated onto this region. Such a configuration causes the light reflected from the waveguide-silicon interface to be totally-internally reflected from the waveguide surface and incident again on the waveguide-silicon interface. Since the waveguide continues along the detector region, this process repeats itself many times. The resulting multiple refraction of light into the detector minimizes detector loss due to reflection.

The detector array in Figure 1 consists of an array of photodiodes formed in n-type silicon connected in parallel by means of a series of gates to a CCD shift register. The charge transfer portion of the device utilizes a two-phase, overlapping-gate structure consisting of one level of poly-silicon electrodes insulated by an additional layer of SiO_2 from a second level of overlapping aluminum electrodes.[2] One CCD unit cell corresponds to each photodiode. Channel isolation is maintained through the series of gates by the presence of channel stopping n+ regions. The detector array integrates the optical signal incident on the array of photodiodes as the potentials of the control and integration gates are adjusted so that charge excited by incident light collects underneath the integration gate. At the end of the integration period T, the transfer gate is turned on so that the collected charge is transferred into the shift register. This charge transfer occurs simultaneously for each array element and in a time less than 1/2 of the CCD clock period. Once this charge has transferred into the shift register, the transfer gate is turned off and the charge is shifted along the register to the end where a serial, discrete-time signal emerges representing the spatial light distribution. As soon as the transfer gate is turned off, the photosensors begin integrating

Figure 1. Integrated optical waveguide and CCD detector array.

charge and the cycle is repeated. The integration time is thus N times the lock period where N is the number of CCD cells equal to the number of array elements. Because charge integration can occur while CCD readout takes place, sensing takes place essentially 100% of the time.[3] For many applications of the integrated waveguide - CCD detector array, minimizing the array element center-to-center spacing allows the information handling capability to be maximized.[4] Such spacings will generally be limited by lithography considerations. Large aspects ratios of the rectangular photodiode region are generally undesirable. The question thus arises as to whether the extent of the photodiode in the direction of light propagation L can be chosen sufficiently large so that nearly all light incident can be multiply refracted into the detector region. To examine this question, we consider the decay of light intensity along the photodiode surface in the direction of light propagation I(z), given as

$$I(z) = I_0 e^{-\alpha_e z} \qquad (1)$$

In (1) α_e is an effective decay constant accounting for light coupled into the photodiode region given as

$$\alpha_e = \frac{1-R}{d \tan \theta}, \qquad (2)$$

where d is the waveguide thickness and θ is the waveguide mode characteristic angle with respect the waveguide surface normal. R in (2) is the appropriate Fresnel reflection coefficient at the waveguide-silicon interface for the mode characteristic angle and polarization in question.[6] We will restrict our present discussion to the TE_0 mode. For a thin SiO_2 layer in the photodiode region evanescent wave coupling will occur causing the field in the waveguide to decay according to (1) and (2), but with R interpreted more generally as a composite reflection coefficient. As evanescent coupling is weaker than multiple re-

fractive coupling, multiple refraction is preferred as it allows minimization of the photodiode length L required for efficient coupling. An analysis of photodiode quantum efficiency for the type of waveguide coupling described herein has shown that for a variety of situations the quantum efficiency increases with $\alpha_e L$ until $\alpha_e L \sim 3$.[1] Since further increase of $\alpha_e L$ causes no significant increase in quantum efficiency, an optimum value of detector length L_0 can be defined as

$$L_0 = 3/\alpha_e. \qquad (3)$$

The magnitude of the device quantum efficiency for detector lengths greater than (3) saturates at a value determined by the silicon absorption coefficient at the wavelength of interest, depletion region depth, carrier diffusion lengths, and depth of the surface recombination region.

We have calculated the optimum detector length L_0 for the TE_0 mode as a function of waveguide thickness d for a waveguide refractive index of $n_g = 1.61$. This refractive index is characteristic of the KPR photoresist waveguides used in the experiments described herein, as well as characteristic of 7059 sputtered glass waveguides. The result of the calculation is shown in Figure 2 for $\lambda = .9$ µm and .6 µm. The portions of the curves to the left of the dotted vertical lines are the regions in which only a single TE mode can exist. In the single mode regions the optimum detector lengths would allow fabrication of efficient photodiodes with reasonable aspect ratios and with center-to-center spacings approaching photolithographic limits. However, for multimode waveguides the corresponding optimum detector lengths become quite long. It is fortunate that in many signal processing applications use of a single-mode waveguide is advantageous in view of other considerations.[4] In Fourier optical processing utilizing optical waveguide lenses the integrated waveguide-detector array described herein would find application in focal imaging. If L_0 exceeds
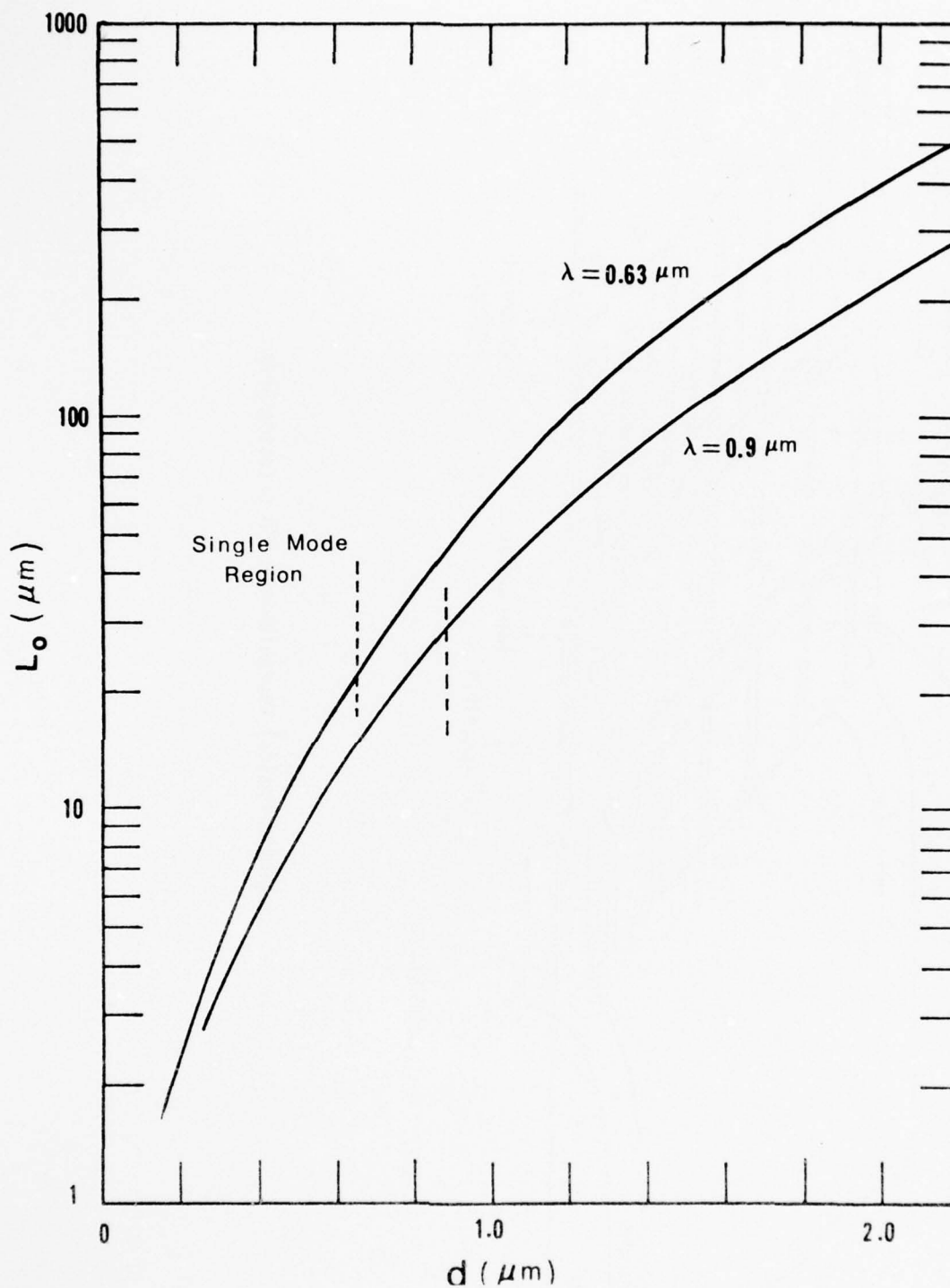
204
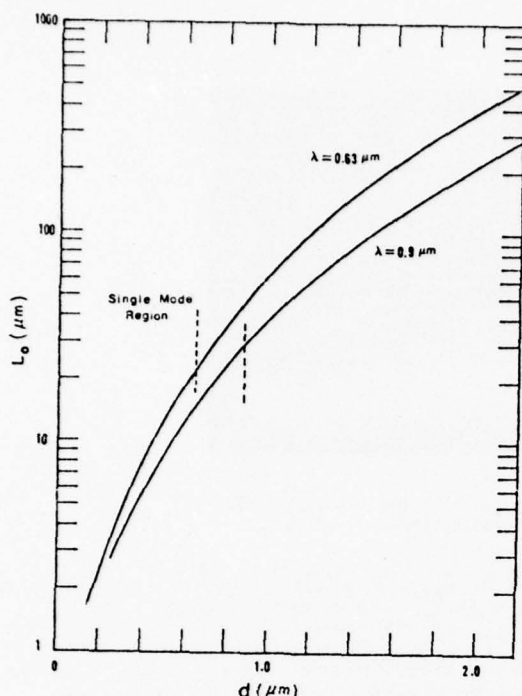
Figure 2. Detector length for efficient coupling of light from waveguide to detector as a function of waveguide thickness for a waveguide refractive index n = 1.61.
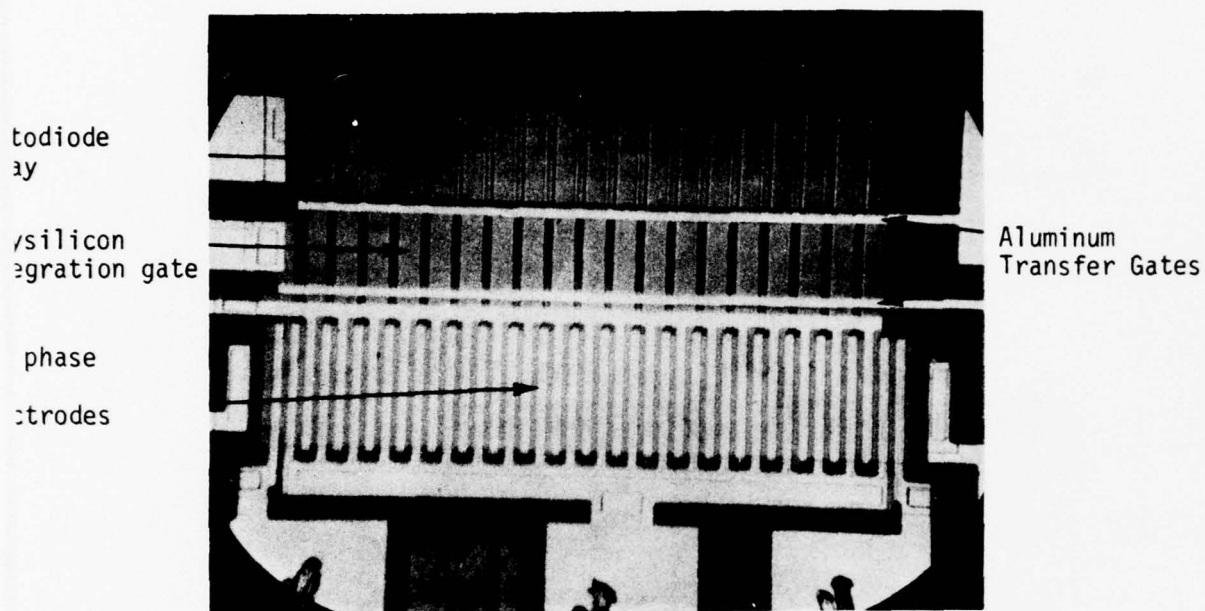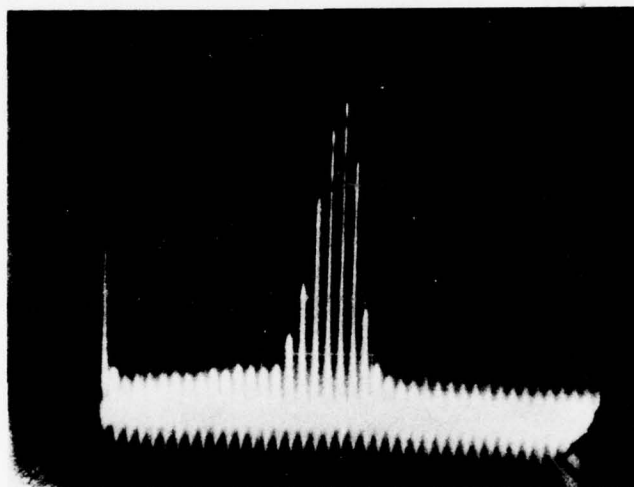

Figure 3. Linear photodiode imaging array coupled to a two phase, overlapping gate CCD.

the depth of focus for such applications, then an array of channel waveguides, one passing directly over each photodiode would be required to preserve signal integrity.

The integrated waveguide-CCD detector array configuration shown in Figure 1 was fabricated using n type silicon having resistivity of 8 ohm-cm. and 100 orientation. The detector portion of the resulting device is shown in Figure 3. This device contains 19 array elements with the photodiodes measuring 25 μm x 115 μm with 7 μm of isolation between adjacent elements. In view of Figure 2, the photodiode length of 115 μm is quite sufficient for effective coupling for the KPR photoresist waveguide employed in our experiments. However, this length would be somewhat long if we were to attempt to reduce the center-to-center spacing to the photolithographic limit. The two-phase overlapping gate CCD has a conventional charge collection diode for signal output and a charge injection diode for serial input. The latter allows for electronic evaluation of the CCD and for serial injection of bias charge.

After initial probe testing of fabricated devices, individual arrays were mounted and bonded in dual-in-line packages. The packages employed were specifically altered so they could accomodate a sufficiently large piece of silicon that would allow space for prism coupling of light into the waveguide and for waveguide propagation. Once packaged the devices could then be inserted in a

socket attached to a standard prism coupling optical mount. A macroscopic view of HeNe laser light coupled into the optical waveguide through a prism coupler[5] is shown in Figure 4-a. The bright area on the left is a top view of the prism illuminated by scattered light, while the dark area in the center is a clamp pressing the prism against the surface. The streak of scattered light is approximately 125 μm wide and corresponds to the light beam which had been externally focused propagating until it reaches the detector region. Bonding wire leading from bonding pads on silicon to connections on the package is illuminated by scattered light. The detector array is located between the termination of the streak of light and the bonding pads. Because the magnification in Figure 4-a is considerably less than that in Figure 3, details of the CCD detector array are not resolvable. Note that there is no visible indication of excess scatter occuring in waveguide-detector coupling. Figure 4-b is an oscilloscope trace of the signal emerging from the CCD corresponding to the laser excitation in Figure 4-a. Differential amplification of the signal was used to eliminate some of the pickup from the clock pulses.

The device was operated with a two-phase clock producing overlapping pulses in the 100 KHz frequency range. Counter circuitry synchronized to the clock was used to control pulsing of the transfer gate so that this gate was turned on only after charge in the CCD shift register had been completely shifted out. Counter circuitry was also employed to provide a suitable electronic input for electronic evaluation of charge transfer efficiency. Charge transfer efficiency can be evaluated by serially injecting several low duty-cycle rectangular pulses with each separated by one clock period.[7] By carefully noting the degradation of the leading and trailing edges of the pulse train, information regarding transfer efficiency can be inferred. For the devices fabricated we determined a transfer efficiency of .993 per double transfer. Although this value is adequate for performance of our 19 stage device, higher values can be obtained. Good charge transfer efficiency requires very sharp lateral potential barriers.[8] Although the purpose of the channel stop diffused regions is to provide such

205
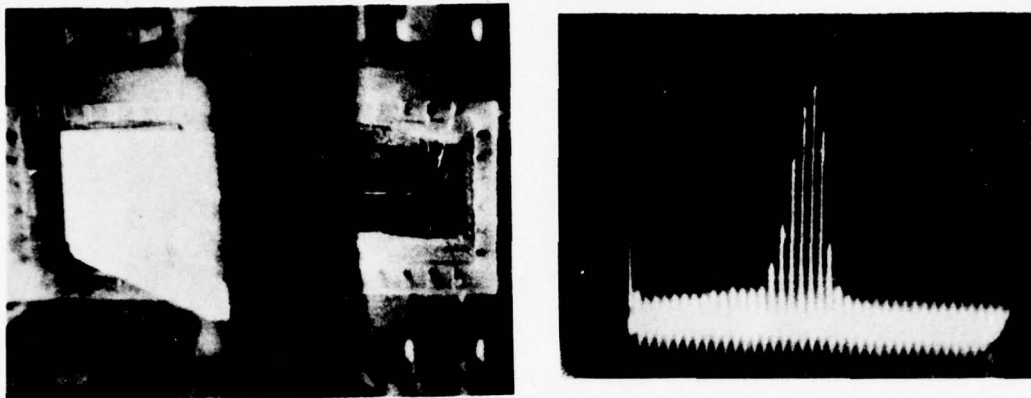
Figure 4. (a) Light propagating in an optical waveguide from the prism coupler to the integrated CCD detector array. (b) CCD output signal corresponding to illumination shown in (a).

n+ barriers, the device processing sequence we employed involved a high temperature thick gate oxide growth step after the channel stop diffusion. Further diffusion thus would occur during the oxide growth, resulting in more gradual lateral barriers. Evidence that this was indeed occuring was obtained from the transfer efficiency measurements in that larger values of bias charge than usual were required to eliminate fixed transfer loss.[7] The problem can be overcome by using ion implantation for channel stop doping and altering the processing sequence.

III. APPLICATIONS

The integrated optical waveguide and charge-coupled device (CCD) linear imaging array structure is expected to find many applications in integrated optical signal processing device structures.

Optical signal processing using an integrated optical format combines the advantages of parallel processing with those present in an efficient, compact, and economical device. Parallel processing occurs when information is imparted to the transverse spatial distribution of an optical wave. Appropriate modulation and processing techniques include highly-efficient and wide band acoustooptic deflection,[9] electrooptic deflection,[10] and one-dimensional spatial Fourier transformation performed by an optical waveguide lens.[11]

For example, integrated optical acoustooptic deflection, optical waveguide lenses, and an integrated waveguide-detector such as described herein can be used to perform wide band spectrum analysis of electronic signals by employing the configuration shown in Figure 5.[4]
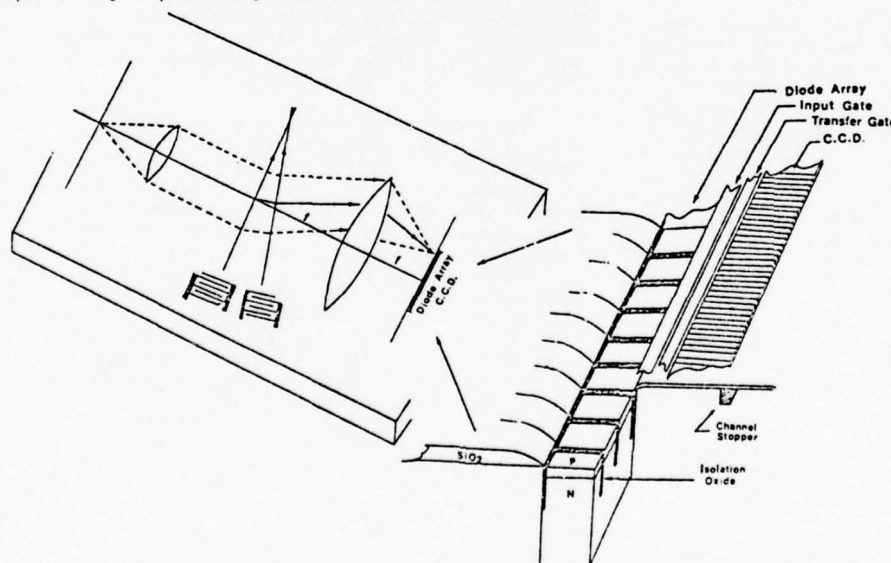
Figure 5. Integrated optical spectrum analyzer configuration.

206
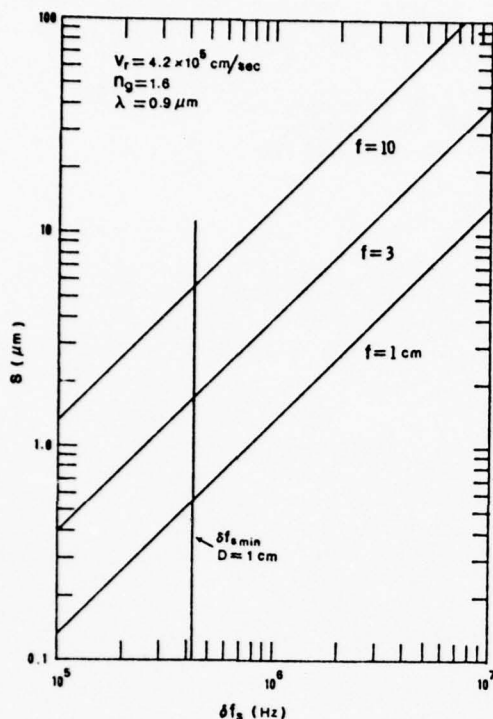
Figure 6. Detector array center-to-center spacing
as a function of spectrum analyzer fre-
quency resolution.

Coherent laser light propagating in a thin-film
waveguide is expanded and collimated prior to being
incident on a surface elastic wave which has been
excited by the incoming signal. Surface elastic
waves can be excited efficiently on silicon using
a ZnO film in the transducer region.[12] Diffrac-
tion of light by the surface elastic wave occurs
in such a way that light is diffracted at dif-
ferent angles corresponding to different signal
frequency components. The signal frequency range
of the spectrum analyzer corresponds to the band-
width of the surface elastic wave transducer con-
figuration. For a range of signal frequencies and
wave intensities, the deflection angle is
linearly proportional to the signal frequency and
the diffracted light amplitude is linearly pro-
portional to the signal surface elastic wave
amplitude. A waveguide lens is then positioned so
as to perform a one-dimensional Fourier transform.
Signal spectral information which is represented
by the angular composition of light emerging from
the surface elastic wave region then becomes repre-
sented by the transverse spatial variation of light
in the Fourier transform plane. The intensity of
the light spatial distribution in the transform
plane corresponds to the signal power density
spectrum and can then be converted to an electrical
signal by means of a detector array. With the
presence of a CCD in the detector array, trans-
formation of the electrical signal from a parallel
format into a serial format occurs in a natural
and simple way.

Information capacity of integrated optical

signal processing devices will be limited by beam
diffraction or array resolution and detector dynamic
range.[4] In particular, the nature of acoustooptic
deflection and of the Fourier transform property
of lenses causes the optical diffraction pattern
in the lens transform plane to be displaced by a
distance s for a signal frequency deviation δf_s,
where [4]

$$s = \frac{f\lambda}{n_e v_r} \delta f_s . \qquad (4)$$

In (4) f is the lens focal length, λ is the optical
wavelength, n_e is the waveguide mode effective
refractive index, and v_r is the Rayleigh wave
velocity. If the detector array in Figure 5 is
spacing of s, then λf_s is the frequency difference
which can be resolved by the spectrum analyzer.
The relationship between center-to-center spacing
and frequency resolution is illustrated in Figure
6 for several focal lengths and typical parameters.
As expected, smaller center-to-center spacings are
required to resolve smaller frequency differences.
The vertical ine in Figure 6 corresponds to the
diffraction-limited frequency resolution for a 1
cm. aperture. Once this assymptote has been reach-
ed, further reduction in detector center-to-center
spacing cannot improve frequency resolution. As
the presence of optical scattering will reduce both
spectrum analyzer frequency resolution and dynamic
range, integration of the array into the optical
waveguide, and therby minimizing scattering
occuring in waveguide-detector coupling, will allow
superior performance as compared with the use of
an external detector array.

The integrated waveguide-CCD detector array
may find additional applications based on its
inherent property of parallel entry of signal in-
formation into a CCD shift register. Optical
injection of parallel signals into CCDs offers
significant advantages over electrical injection
techniques, in that for the latter sophisticated
stabilized charge injection circuits would likely
be required for each entry tap. Furthermore,
capacitive coupling limits both the proximity of
adjacent taps and the maximum usable signal fre-
quency for parallel electrical injection. Parallel
optical signal injection using bulk optical waves
along with a mask to implement a fixed tap weight
transversal filter has previously been demonstrated[13]
We anticipate that the use of integrated optical
channel waveguide-detector structures could yield a
programmable device with potentially a large
channel density and almost complete channel isola-
tion. Parallel integrated optical signal injection
into CCDs may also find application in multi-
plexing, other types of programmable filtering,
and memory devices.

IV. SUMMARY

Successful fabrication and operation of a
linear CCD image array integrated into an optical
waveguide structure have been described. Data have
been presented with regard to the optimum array
element size required for the light wave to be
efficiently coupled into the detector region.
Minimal excessive scattering in the region where

coupling of light from the waveguide to the detector occurs was observed. The integrated structure that has been described herein is expected to serve as a basic element in integrated optical signal processing devices and to provide a method for parallel entry of information into CCDs.

REFERENCES

1. J. T. Boyd and C. L. Chen, "Integrated Optical Silicon Photodiode Array," Appl. Opt. Vol. 15, pp 1389-1393, 1976.

2. W. F. Kosonocky and J. E. Carnes, "Two Phase Charge-Coupled Devices with Overlapping Polysilicon and Aluminum Gates," RCA Rev. Vol. 34, pp 164-202, 1973.

3. M. F. Tompsett, G. F. Amelio, W. J. Bertram, R. R. Backley, W. J. McNamara, J. C. Mikkelsen, and D. A. Sealer, "Charge Coupled Imaging Devices: Experimental Results," IEEE Trans. Electr. Dev. Vol. ED-18, pp 992-996, 1971.

4. D. B. Anderson, J. T. Boyd, M. C. Hamilton, and R. R. August, "Integrated Optics Approach to the Fourier Transform," to be published.

5. P. K. Tien, and R. Ulrich, "Theory of Prism-Film Coupler and Thin Film Light Guides," J. Opt. Soc. Am. Vol. 60, pp 1325-1337, 1970.

6. M. Born and E. Wolfe, Principles of Optics, Second Edition, Pergamon Press, 1964.

7. R. W. Brodersen, D. D. Buss, and A. F. Tasch, "Experimental Characterization of Transfer Efficiency in Charge-Coupled Devices," IEEE Trans. Electr. Dev. Vol. ED-22, pp 40-46, 1975.

8. C. H. Sequin and M. F. Tompsett, Charge Transfer Devices, Academic Press, 1975.

9. C. S. Tsai, M. A. Alhaider, L. T. Nguyen, and B. Kim, "Wideband Guided-Wave Acoustooptic Bragg Diffraction and Devices Using Multiple Tilted Surface Acoustic Waves," Proc. IEEE, Vol. 64, pp 318-328, 1976.

10. C. S. Tsai and P. Saunier, "Ultrafast Guided-Light Beam Deflection/Switching and Modulation Using Simulated Electro-optic Prism Structures in $LiNbO_3$ Waveguides," Appl. Phys. Lett. Vol. 27, pp 248-250, 1975.

11. R. Shubert and J. H. Harris, "Optical Guided Wave Focusing and Diffraction," J. Opt. Soc. Amer., Vol. 61, pp 154-161, 1971.

12. F. S. Hickernell, "Zinc Oxide Thin-Film Surface Wave Transducers," Proc. IEEE, Vol. 64, pp 631-635, 1976.

13. M. A. Copeland, D. Roy, J. D. E. Beynon, and F. Y. K. Dea, "An Optical CCD Convolver," IEEE Trans Electr. Dev. Vol. ED-23, pp 152-155, 1976.

APPENDIX E

Inhomogeneous optical waveguide lens analysis*

W. H. Southwell
Electronics Research Division
Rockwell International
Anaheim, California 92803

Abstract

Gradient-index ray-tracing techniques are used to evaluate performance of inhomogeneous optical waveguide lenses. Using the thin-film waveguide parameters including the lens thickness profile, the phase error and diffraction pattern are derived. The procedure is applied to a classical Luneburg index profile for which exact results are known. The results indicate that better than diffraction-limited accuracy is achievable with reasonable computer running times. A second example demonstrates the procedure on lens profiles approximating generalized Luneburg lenses (focal length > diameter).

INTRODUCTION

The optical waveguide lens technology[1] is being developed with the expectation of performing signal processing functions using the transform properties of lenses in an integrated optics format. From an optical design consideration, the problem presents new degrees of freedom as well as some constraints. Aside from dealing with one-dimensional apertures, perhaps the most significant difference results from the ability to create inhomogeneous refractors using homogeneous materials in the thin-film integrated optics format. Furthermore, these lenses function in an immersed region of nonunity index. Thus, it becomes possible to utilize the perfect imaging properties of the Luneburg lenses which have been known for many years.[2]

The basic techniques involving the focusing properties of gradient-index media have been known and utilized in the microwave antenna art. Achieving the diffraction-limited potential of planar waveguide lenses in the optical region, however, may not be an easy task in practice. Thus, it is necessary as in the case of standard optical design to have an analysis and design capability. The present paper addresses this issue.

Using the differential equation for ray paths in inhomogeneous media, a waveguide lens ray-trace algorithm is derived from which the optical imaging quality may be ascertained from given or measured waveguide thickness profiles. The associated phase errors are derived using Hamilton's angular characteristic function, from which the image diffraction pattern is calculated. Various numerical techniques employed are described, and some numerical examples illustrating the procedure are included.

WAVE PROPAGATION IN LAYERED MEDIA

The basis of the effective index for optical propagation is contained in a consideration of the electric field modes in the dielectric waveguide layers.[3] In particular, we will consider the four-layer structure shown in Fig. 1. The layers shown represent a planar structure with optical propagation to the right. The propagating modes are the solutions to Maxwell's equations subject to the appropriate boundary conditions. We present here the results for the case $n_2 > n_3 > n_1, n_4$.

Application of the boundary conditions yields the following equations:

$$\tan(hkt + \phi) = -h/p \tag{1}$$

$$\tan\phi = (h/\ell) \tan \gamma \tag{2}$$

$$\tan(-\ell kd + \gamma) = \ell/q \quad , \tag{3}$$

where $k = 2\pi/\lambda$ and

$$p = \sqrt{n_e^2 - n_1^2} \tag{4}$$

$$h = \sqrt{n_2^2 - n_e^2} \tag{5}$$

$$q = \sqrt{n_e^2 - n_4^2} \tag{6}$$

$$\ell = \begin{cases} \sqrt{n_3^2 - n_e^2} & \cdot n_e < n_3 \\ \sqrt{n_e^2 - n_3^2} & n_e \geq n_3 \quad , \end{cases} \tag{7}$$

where n_e is the effective index for the optical propagation mode.

Using various trigonometric identities, the boundary conditions (1), (2) and (3) may be combined into the following transcendental equation:

$$F(n_e) = \frac{[1 - \frac{\ell}{q} \tan(\ell kd)] \tan(hkt) + \frac{h}{\ell} [\frac{\ell}{q} + \tan(\ell kd)]}{1 - \frac{\ell}{q} \tan(\ell kd) - \frac{h}{\ell} [\frac{\ell}{q} + \tan(\ell kd)]\tan(hkt)} + \frac{h}{p}$$

$$n_e < n_3,$$

or

$$F(n_e) =$$

$$\frac{\left[\left([q + \ell]\, e^{2\ell kd} + q-\ell\right)\tan(hkt) + \frac{h}{\ell}\left([q + \ell]\, e^{2\ell kd} - q + \ell\right)\right]}{[q + \ell]\, e^{2\ell kd} + q - \ell - \frac{h}{\ell}\tan(hkt)\left([q + \ell]\, e^{2\ell kd} - q + \ell\right)} + \frac{h}{p} \qquad (8)$$

$$n_e \geq n_3.$$

The solution n_e of the equation $F(n_e) = 0$ is the desired effective index. The numerical solution may be obtained by iteration from a starting value $n^{\circ}{}_e$ using Newton's method,

$$n_e{}^{i+1} = n_e{}^{i} - \frac{F\left(n_e{}^{i}\right)}{\frac{dF}{dn}} , \qquad (9)$$

where the derivation dF/dn is also evaluated at $n_e{}^{i}$. Although an analytical expression may be derived for dF/dn using implicit differentiation, it is computationally more efficient to obtain a numerical derivative. The numerical derivative requires only one additional evaluation of $F(n_e)$, whereas the analytical derivative appears to be much more complicated.

We have thus established a means to evaluate the effective index n_e in terms of the waveguide parameters and the overlay thickness t, shown in Fig. 1. Due to the possibility of higher order modes in the waveguide, multiple solutions for n_e may result. Care should be taken to assure that the initial starting value for n_e in Eq. (9) is close to the desired solution. Generally, when "stepping" through a changing overlay profile, the previous solution may be used as a starting point for the next adjacent step. This provides rapid convergence and propagation follows the same mode. All of the analysis in this paper assumes a single mode propagation.

Having established the means to provide the effective index, we are now in a position to outline the procedure for tracing a ray through a

212

eguide region of changing overlayer thickness. For regions of uniform verlayer, the effective index is uniform and propagation follows a straight line. In one step the optical path is described using conventional geometrical optics for these regions having no index changes.

As the ray encounters a region of a gradient index, the ray will begin to execute a curved path. We next address the problem of determining this curved path.

GRADIENT-INDEX RAY TRACE

We restrict our interest in this paper to waveguide profiles (and consequently index profiles) having circular symmetry. Consider the ray path shown in Fig. 2. The position vector r is described in a coordinate system with its origin at the center of symmetry of the index profile. The position of the ray is described by the components of r. The direction of the ray s is given by the instantaneous tangent to the curve,

$$r = x\,\hat{i} + y\,\hat{j}$$

$$S = \lim_{\Delta s \to 0} \frac{\Delta r}{\Delta s} = \alpha\,\hat{i} + \beta\,\hat{j} \ .$$

The quantities α and β are also called the direction cosines of the ray. The ray tracing procedure described here follows, with some modifications, that published by L. Montagnino.[4]

Suppose we know the initial ray position (x_0, y_0) and direction (α_0, β_0) at one point in space. To find the position in a close neighborhood, we expand r(s) in a Taylor's series about the known point. The argument s is the scalar distance along the path. The vector s is a unit vector in the direction of the tangent.

213

$$r(s_0 + \Delta s) = r(s_0) + \frac{dr}{ds}\bigg|_{s=s_0} \Delta s + \frac{1}{2!} \frac{d^2r}{ds^2}\bigg|_{s=s_0} (\Delta s)^2 + \frac{1}{3!}\frac{d^3r}{ds^3}(\Delta s)^3 + \ldots \quad (10)$$

The first derivative dr/ds is the ray vector s, and the second derivative is the curvature vector $K = d^2r/ds^2 = ds/ds$. Thus, the ray vector obeys the expansion

$$s(s_0 + \Delta s) = s(s_0) + K(\Delta s) + \frac{1}{2}\frac{dK}{ds}(\Delta s)^2 + \ldots \quad (11)$$

The required derivatives are obtained from the differential equation for the ray position in a gradient index medium,

$$\frac{d}{ds}\left[n \frac{dr}{ds} \right] = \nabla n, \quad (12)$$

where ∇n is the index gradient

$$\nabla n = \frac{\partial n}{\partial x}\hat{i} + \frac{\partial n}{\partial y}\hat{j} . \quad (13)$$

Expanding Eq. (12), we obtain the curvature vector

$$K = \frac{1}{n}\left[\Delta n - (\nabla n \cdot s) s \right] . \quad (14)$$

Before obtaining the last required derivative dK/ds, we rewrite Eq. (14), making use of the symmetry in n

$$K = f(r)\left[r - (r \cdot s) s \right] , \quad (15)$$

where

$$f(r) = \frac{1}{nr}\frac{dn}{dr} . \quad (16)$$

Differentiating Eq. (15), we have

$$\frac{dK}{ds} = \frac{1}{r}\frac{df}{dr}(s \cdot r)[r - (r \cdot s)s] - f[(r \cdot K)s + (r \cdot s)K] , \quad (17)$$

214

where we have used the general relationships,

$$\frac{dg}{ds} = s \cdot \nabla g, \quad \nabla g(r) = \frac{1}{r} \frac{dg}{dr} r \ . \qquad (18)$$

The ray tracing algorithm, therefore, is as follows:

(1) From the known position and directions $(x_0, y_0, \alpha_0, \beta_0)$ and index gradient, evaluate the curvature K and its derivative, Eqs. (14) and (17) at that point.

(2) Select an incremental step size Δs and evaluate the new position and angle from Eqs. (10) and (11).

(3) Considering our new position and angle as known, go back to Step (1) and repeat the sequence until the exit surface is reached or until the region is encountered when the index gradient vanishes.

We note that this algorithm requires the index, the gradient dn/dr, and the second derivative d^2n/dr^2 at each point. It is necessary to discuss how these are obtained.

The assumption is that the only known quantities are the waveguide parameters of Fig. 1, including the outerlayer profile. This thickness profile is either taken from measurements or otherwise specified.

The previous section describes how the index is evaluated as a function of the planar position of the ray. The required index derivatives are perhaps most easily provided using numerical derivative approximations,

$$\frac{dn}{dr} = \frac{1}{2\Delta t} \quad [n(t + \Delta t) - n(t - \Delta t)] \qquad (19)$$

$$\frac{d^2n}{dr^2} = \frac{1}{(\Delta t)^2} \quad [n(t + \Delta t) - 2n(t) + n(t - \Delta t)] \qquad (20)$$

where $t = t(r)$ is the given thickness profile.

215

EXIT BOUNDARY LOCATION

It is necessary to consider the problem of precisely locating the ray position as it exits the lens region. For computational efficiency, the step size Δs is large compared to the required ray tracing tolerances. Thus, an interpolation is required once the ray has stepped outside the lens.

The procedure we take for locating the edge is as follows. We first define the function F

$$F = r_o^2 - r^2 , \tag{21}$$

where r_o is the lens radius and $r^2 = x^2 + y^2$ as determined by the ray position. By considering the last point inside the lens as the base point, we see that r becomes a function of the step size Δs. The function F then may be considered a function of Δs, $F = F(\Delta s)$. The problem of locating the edge is then solved by finding the root Δs that makes $F(\Delta s) = 0$. This may be done using Newton's method

$$(\Delta s)_e = (\Delta s)_o - F \Big/ \frac{dF}{d(\Delta s)}\bigg|_{\Delta s = \Delta s_o} . \tag{22}$$

Since the functional dependence of F on Δs is given through Eq.(10), we have

$$\frac{\partial F}{\partial(\Delta s)} = -2r \cdot \frac{dr}{d(\Delta s)} = -2r \cdot s . \tag{23}$$

Initially $(\Delta s)_o = 0$ at our base point inside the lens and the derivative in Eq. (22) has already been evaluated. It is thus a simple matter to apply Eq. (22) until $|F| < 10^{-8}$ or some prescribed small quantity.

We have now established the general procedure for ray tracing through the waveguide lens. But we have not, as yet, specified a value for the step size Δs. To do this, let us return to a discussion of the convergence properties of the above ray tracing algorithm.

216

CONVERGENCE AND AN EXTRAPOLATION TECHNIQUE

There are two factors to be considered when determining a value for the step size Δs. They are computing time and accuracy. It is important to know the accuracy of the ray heights as they leave the lenses. If the rays are being plotted and visual accuracy is sufficient, then the step size is easily determined. The ray trace may be repeated, each time reducing the step size a factor of 2, until no changes are visible on the plot.

However, when tracing diffraction-limited systems, it is necessary to have confidence that the ray trace will provide an exit height accurate to some fraction of a wavelength. This may require extremely small step size and, consequently, long computing time. We, therefore, suggest the following extrapolation technique for achieving the desired accuracy with reasonable step sizes.

For simplicity, let $h = \Delta s$ be the step size. Consider the ray exit height y as a function of the (small) step size h, $y = y(h)$. The problem is to estimate the value of y for the limit as h approaches zero. This suggests a Taylor's expansion.

$$y(h) = y(0) + \frac{dy}{dh} h + \frac{1}{2} \frac{d^2 y}{dh^2} h^2 + \ldots \tag{24}$$

If we assume h is small enough that the first three terms of the expansion suffice, then we may pick an h, trace the ray and determine $y(h) = y_1$. But there are three unknowns in Eq. (24). Thus, we perform two more ray traces, each time reducing h by a factor of 2, to give us y_2 and y_3. This gives us the set of linear equations:

$$y_1 = a_1 + a_2 h + a_3 h^2$$
$$y_2 = a_1 + a_2 h/2 + a_3 h^2/4 \tag{25}$$
$$y_3 = a_1 + a_2 h/4 + a_3 h^2/16 \; .$$

In matrix notation,

$$y = Ha , \tag{26}$$

which has a solution

$$a = H^{-1} y, \tag{27}$$

where the matrix H is

$$H = \begin{pmatrix} 1 & h & h^2 \\ 1 & h/2 & h^2/4 \\ 1 & h/4 & h^2/16 \end{pmatrix} . \tag{28}$$

If we choose h = 0.025, then

$$H^{-1} = \begin{pmatrix} 1/3 & -2 & 8/3 \\ -80 & 400 & -320 \\ 4266.7 & -12800 & 8533.3 \end{pmatrix} . \tag{29}$$

The solution for a_1, which is the desired estimate $y(0)$, is

$$y = y_1/3 - 2y_2 + 8y_3/3 . \tag{30}$$

Equation (30) is the extrapolation formula. Notice that it is a weighted mean of three ray-traced values and that the sum of the weights is unity. Furthermore, it turns out that these weighting factors are the same for any value of h used to trace y_1. The validity of Eq. (30), of course, depends on h being small enough such that the expansion (24) is valid.

To demonstrate the gradient index algorithm and illustrate the extrapolation technique, a classical Luneburg[2] lens index profile was traced. The index profile is given by

$$n = n_0 \sqrt{2 - (r/r_0)^2} , \tag{31}$$

218

where r_0 is the lens radius and n_0 is the immersion index. The example was chosen because all parallel rays incident on the left are known to come to perfect focus on the optical axis at the edge of the lens. Also, the index gradients are higher than those encountered with longer focal length lenses. Figure 3 shows six rays traced through this classical Luneburg lens.

We next investigated the ray exit height for the lower ray shown in Fig. 3. In this case, this exit height also represents the ray trace error since the true height should be zero. Figure 4 is a plot of the ray trace error as a function of the ray trace step size for a Luneburg lens with a radius of 2 cm (the computation of all the work reported in this paper was performed on a Hewlett Packard 9830A calculator). The tabulation in Table I shows the results of the first three ray traces of that ray.

TABLE I. Exit height y for various step sizes h

h(cm)	y(cm)
0.1	8.65078×10^{-3}
0.05	4.18073×10^{-3}
0.025	2.05583×10^{-3}

Using the extrapolation (30), we obtain $y = 4.3466 \ 10^{-6}$ cm. This result is well within diffraction-limited ray trace accuracy.

Being satisfied that the numerical ray trace procedure is capable of diffraction-limited accuracies, we next proceed to determine the diffraction patterns in the image surface.

WAVEFRONT ERROR

For systems which are near diffraction limited, the spot diagrams determined by ray tracing are not adequate for comparisons to actual measured image patterns. This occurs because the ray trace itself does not account for diffraction effects. We surmount this problem by employing a technique to determine the phase errors from the ray trace data. These phase errors are then expressed in a pupil function (which is a function of the pupil coordinates). The pupil function is then Fourier transformed and squared to form the image diffraction pattern.

To derive the wavefront errors from ray trace intercept data, we draw upon the theory of Hamilton's angle characteristic function.[5] The angular characteristic function $T(\beta)$ represents the optical path length along the path through the system described by the entrance height y_0. This function is also expressed as a function of the exit angle β. The theory states that the ray intercept error y in the image plane is given by

$$y = -\frac{\partial T}{\partial \beta} \quad . \tag{32}$$

To utilize this theory, we assume that the optical path length may be expressed as a power series in the exit angle coordinate β,

$$T = c_1\beta^2 + c_2\beta^4 + c_3\beta^6 + \ldots \tag{33}$$

Since we are dealing with symmetric systems we consider only even powers of β (the coefficients in this expansion are related to the usual aberrations; that is, the quadratic error, c_1 corresponds to defocus and the other coefficients are related to various orders of spherical aberration).

To determine these coefficients, we trace a number of rays and record the intercepts and the exit angles y_i, β_i. These data points are then fit in a least-squares fashion to the function

220

$$\frac{\partial T}{\partial \beta} = (2c_1\beta + 4c_2\beta^3 + 6c_3\beta^5 + \ldots) \ . \tag{34}$$

This procedure determines the c coefficients for the optical path length in Eq. (33).

Prior to fitting the intercept data to the expression (34), it is convenient to first normalize the β's. By doing this, the wavefront error function (33) is then automatically expressed in terms of normalized aperture coordinates. The preceding statement is valid strictly for systems with a linear relationship between aperture and exit angle. Although this is only approximately true, it is sufficiently close for our case

The phase error is $2\pi/\lambda$ times the optical path error. Figure 5 is a plot of the phase error of the Luneburg lens of Fig. 3 using the extrapolation Eq. (30) on the rays with $\Delta s = 0.1$ cm for the initial step size. Since we expect zero phase error, the amount shown represents the residual ray tracing error. We note that it is considerably less than $\pi/4$ and consequently represents a diffraction-limited wavefront.

The pupil function is given by the expression

$$P = \exp[i2\pi T(y/y_0)/\lambda], \tag{35}$$

where the function T is expressed in terms of aperture position y.

It may be shown[6] that the square of the Fourier transform of P yields the irradiance diffraction pattern in the image plane. This is performed using the discrete fast Fourier transform algorithm. Figure 6 is the diffraction pattern for the Luneburg lens as traced in Figs. 3 and 5.

To further test the system, we moved the detector plane slightly away from the edge of the lens and repeated the evaluation. The corresponding phase error is shown in Fig. 7 and its diffraction pattern in Fig. 8.

221

EXAMPLE OF THE GENERAL PROCEDURE ON A WAVEGUIDE PROFILE

We conclude by presenting an example of how this ray trace technique may be used to illustrate the effects of various waveguide profiles on image quality.

Suppose we have a profile described by the relationship $t=t_0 \cos^{.18} (\pi r/2r_0)$ as shown in Fig. 9. This profile yields an approximation to the index distribution for the generalized Luneburg lens given by Morgan.[7] The exact solution would give a perfect focus in an image surface outside of the lens boundary. Using the techniques described in this paper and the waveguide parameters shown in the figure caption, a number of rays were traced through the system. Figure 10(a) is a plot of these rays. We next alter the lens profile to follow a $\cos^{.25} (\pi r/2r_0)$ dependence. The results of the trace are plotted in Fig. 10(b). We see how the effects of the shape of the knee of the lens profile affect the spherical aberration. Finally, we plot the lens profile with a $\cos^{.211} (\pi r/2r_0)$ dependence shown in Fig. 11(c).

CONCLUSIONS

The above example demonstrates the potential of this analysis technique in designing and fabricating waveguide lenses. When used in conjunction with laboratory measurements, the skill in producing waveguide lenses with desired properties is greatly enhanced. Both the input qualities (the lens profiles) and the output quantities (ray plots and image diffraction patterns) are in terms of measured quantities.

The algorithms presented are designed to be computationally efficient and have diffraction-limited accuracy.

REFERENCES

1. D. B. Anderson, R. L. Davis, J. T. Boyd and R. R. August, "Comparison of Optical Waveguide Lens Technologies," to be published in J. Quantum Electronics, Special Issue Integrated Optics, April 1977.

2. R. K. Luneburg, <u>Mathematical Theory of Optics</u> (University of California Press, Berkeley, 1966), p. 187.

3. P. K. Tien, "Light Waves in Thin Films and Integrated Optics," Appl. Opt. <u>10</u>, 2395 (1971).

4. L. Montagnino, "Ray Tracing in Inhomogeneous Media," J. Opt. Soc. Amer. <u>58</u>, 1667 (1968).

5. M. Born and E. Wolf, <u>Principles of Optics</u> (Pergamon Press, Ltd., London, 1970), p. 137.

6. J. W. Goodman, <u>Introduction to Fourier Optics</u> (McGraw-Hill, New York, 1968), p. 61.

7. S. P. Morgan, "General Solution of the Luneburg Lens Problem," J. Appl. Phys. <u>29</u>, 1358 (1958). The exact overlayer profiles yielding Morgan's solutions for the generalized Luneburg lens will be published in a forthcoming paper by Southwell.
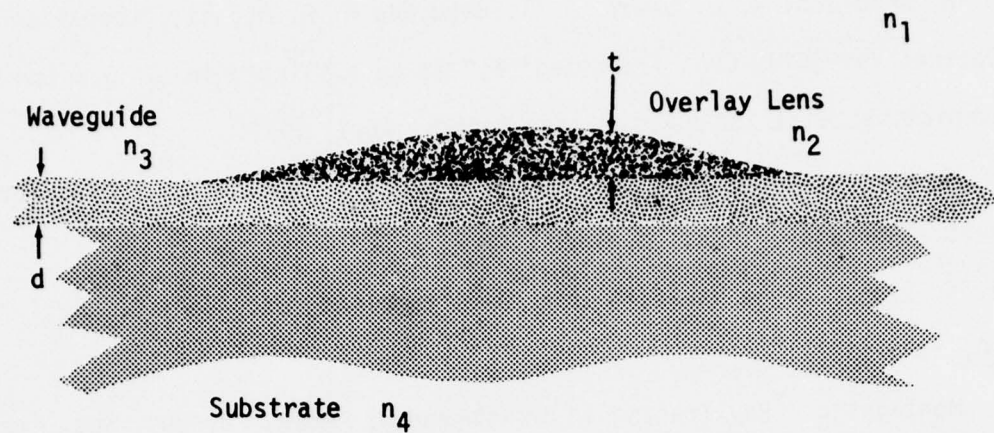
Figure 1E. Cross-Section of Multilayer Planar Dielectric Waveguide. Optical propagation is from left to right.
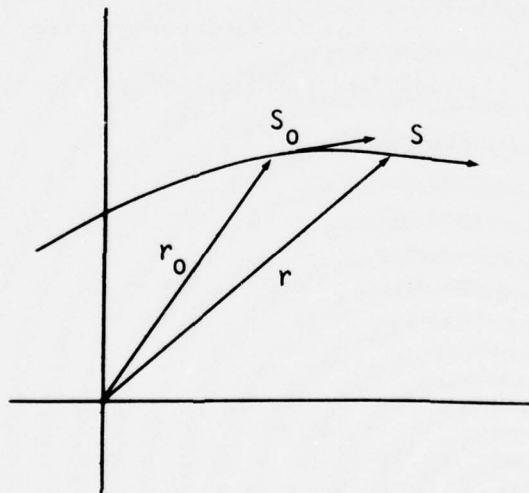
Figure 2E. Ray Path Geometry Showing Ray Position Vector r and the Ray Vector s. The Scalar s is the distance Along the Path and the Vector s is a Unit Vector Tangent to the Path.

224
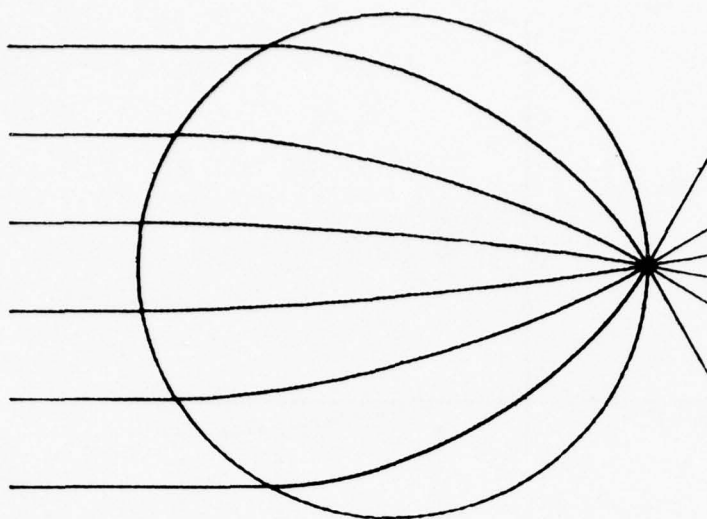
Figure 3E. Plot of the Ray Paths Traced Through the Classical Luneburg Lens Described by Eq. (31).
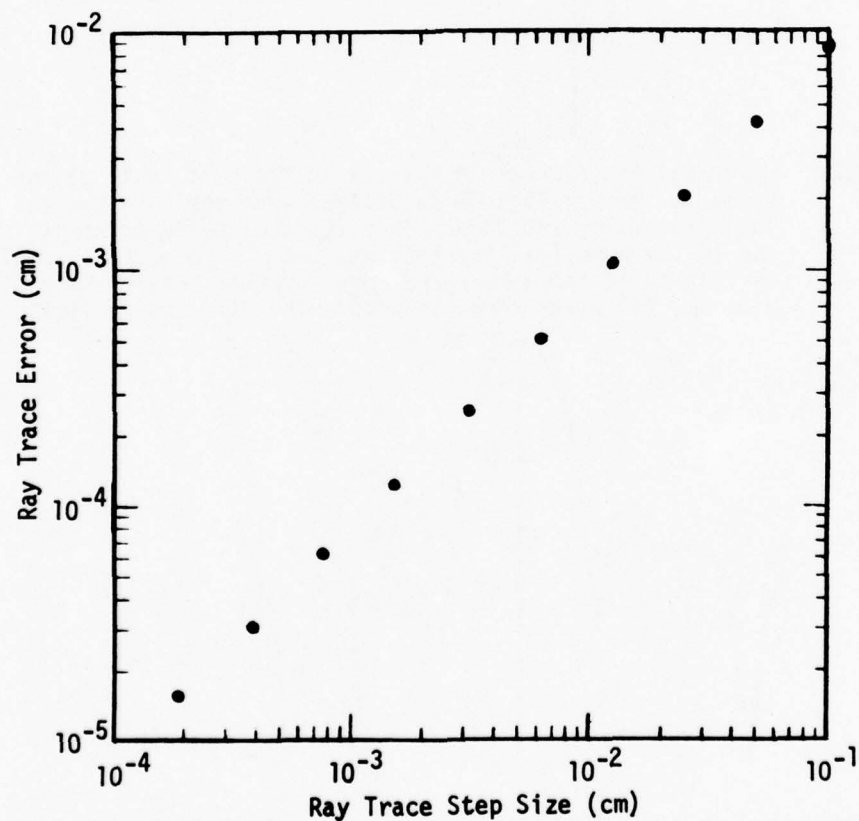
Figure 4E. Plot of the Ray Trace Error as a Function of the Step Size Δs for a 2 cm Radius Classical Luneburg Lens Shown in Fig. 3E. It is Shown that Extrapolation Techniques can Yield Required Accuracy without Using Extremely Small Step Size.

225
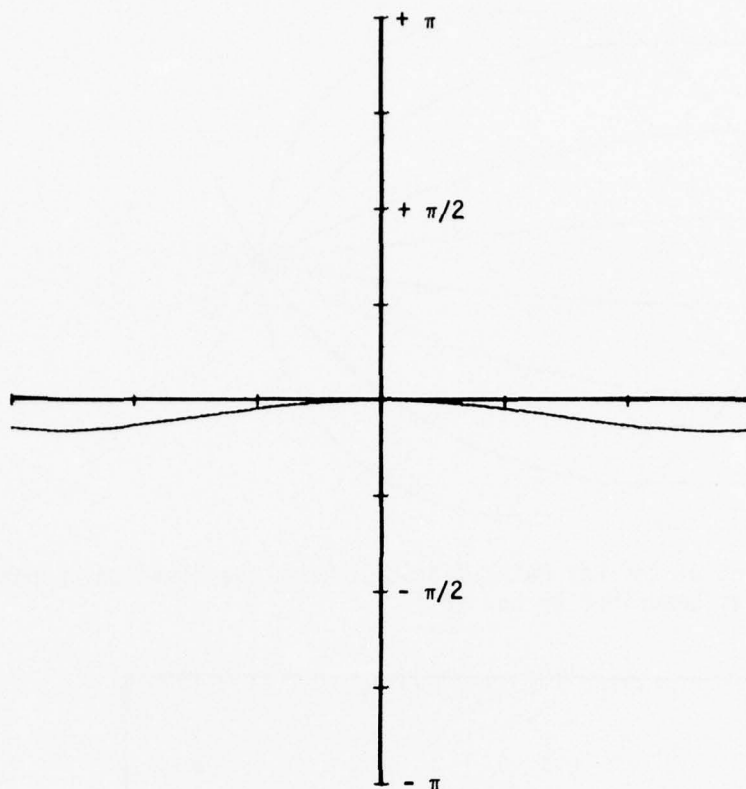
Figure 5E. Wavefront Phase Error in Radians in the Exit Pupil of the
            Luneburg Lens of Fig. 3E as Derived from the Ray-Trace
            Technique Using λ=0.633μ. This residual phase error is
            due to the numerical ray-tracing, but may be made as small
            as desired at the expense of more computer running time.
            However, the error shown is within the diffraction limit.
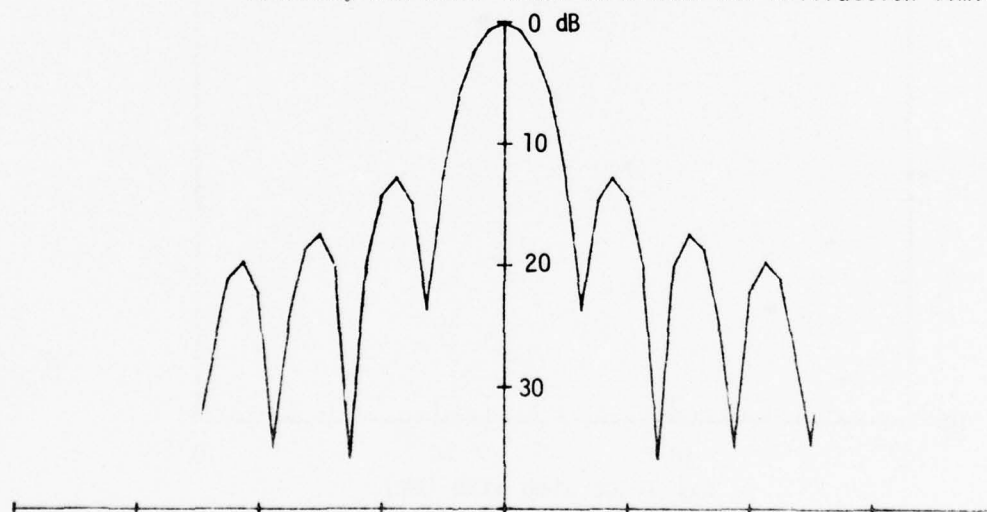
Figure 6E. Diffraction Pattern Showing the Log of the Intensity in the
            Image Surface for the Luneburg Lens of Figs. 3E and 5E.
            This pattern agrees with the sinc function squared.

226
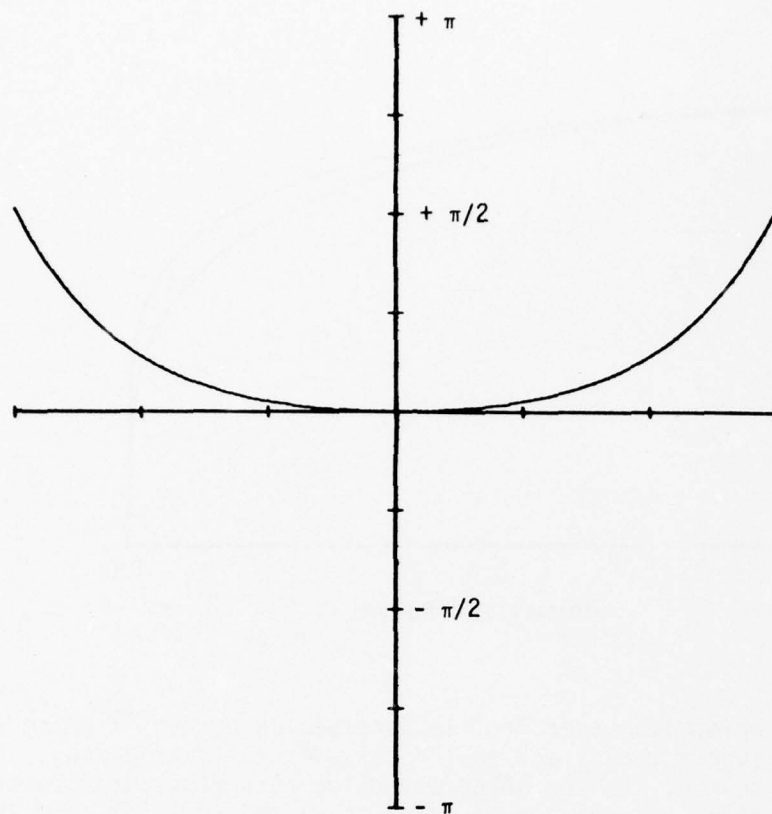
Figure 7E. Phase Error of the Luneburg Lens of Fig. 3E Defocused by 0.5μ.
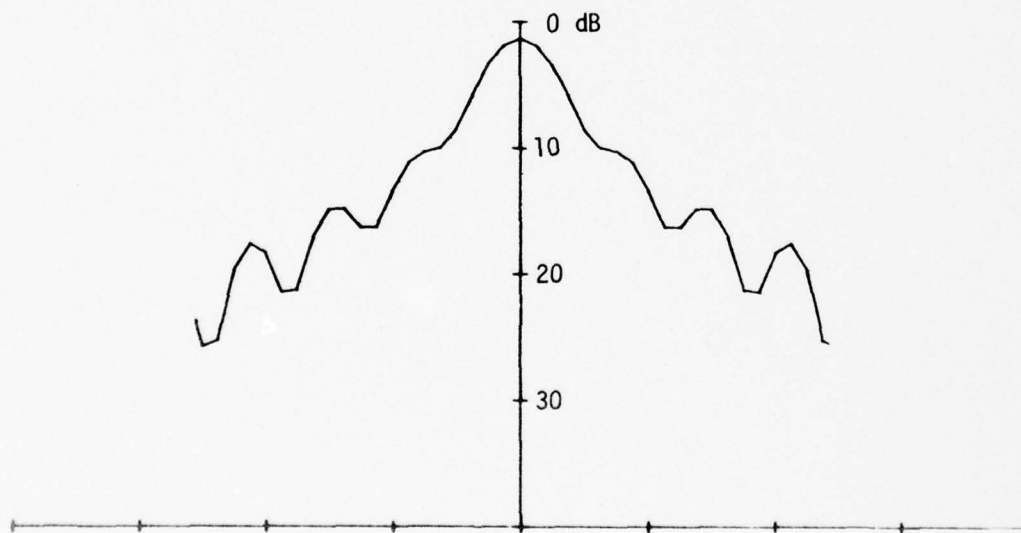
Figure 8E. Diffraction Pattern Resulting from Defocused Luneburg Lens Shown in Fig. 7E. A 64-point fast Fourier transform algorithm was used to generate this pattern.

227
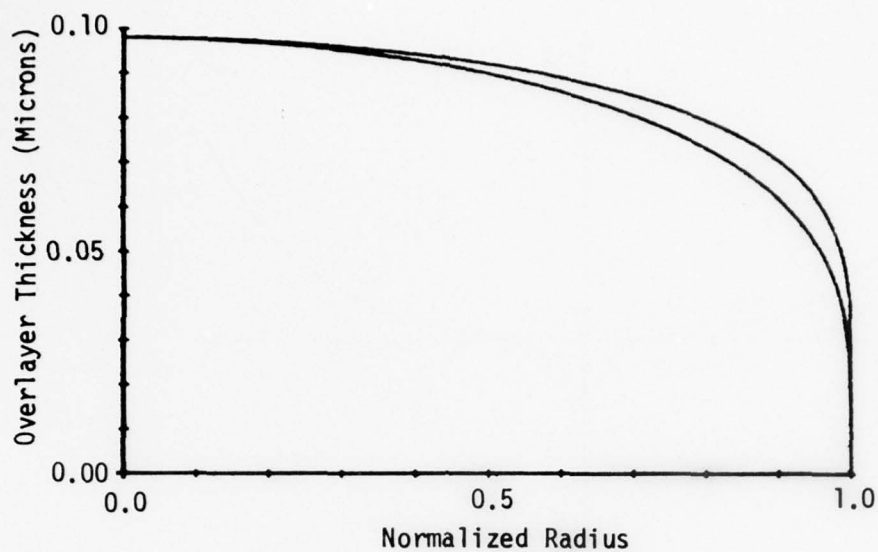
Figure 9E. Waveguide Layer Profile Represented by $\cos^{.18}$ Dependence
(upper curve) and $\cos^{.25}$ Dependence (lower curve). Referring
to Fig. 1E, the other waveguide parameters used to trace
this lens are: $n_1=1$, $n_2=2$, $n_3=1.565$, $n_4=1.47$, $d=0.75\mu$, and
$\lambda=0.633\mu$.

228
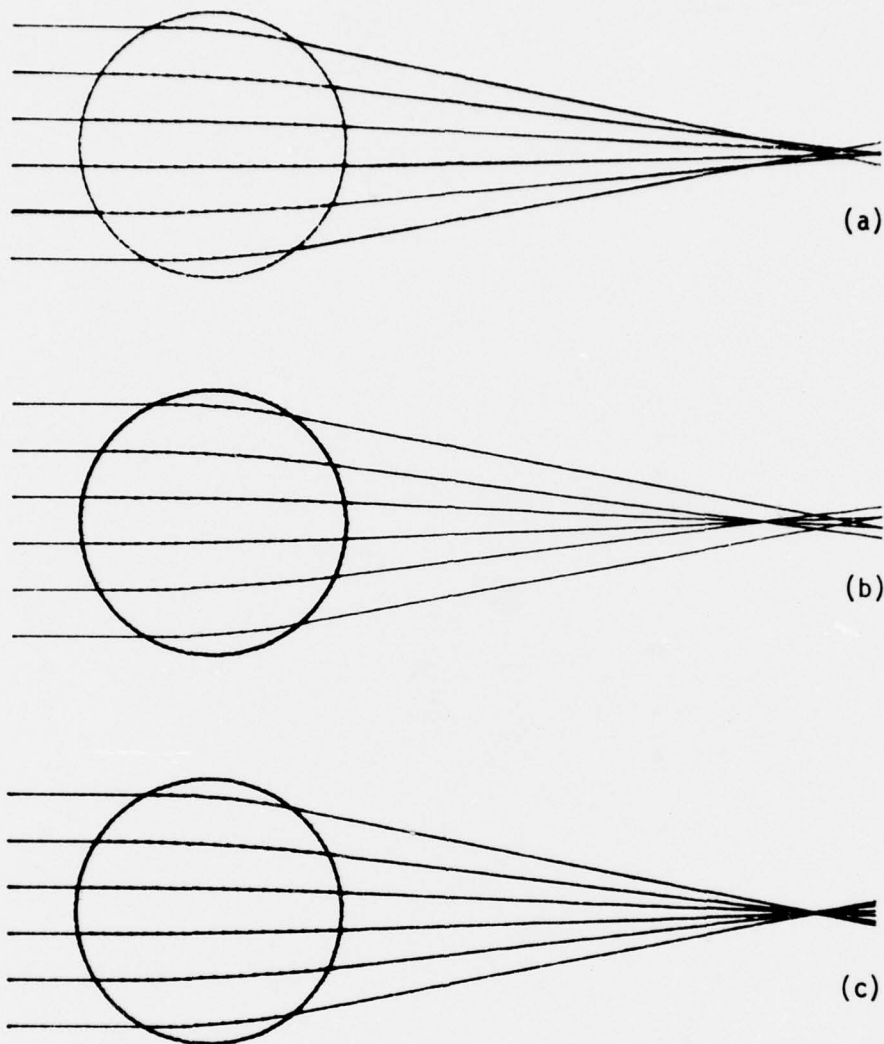
Figure 10E.   Ray Plots of Waveguide Lens Described in Fig. 9E: (a) with cos.^{18} dependence profile; (b) with cos.^{25} dependence profile; (c) with cos.^{211} dependence profile.

229

APPENDIX F

Index and waveguide thickness profiles
for
generalized Luneburg lenses*

W. H. Southwell
Electronics Research Division
Rockwell International
Anaheim, California 92803

ABSTRACT

An analytical approximation is derived which provides a
transcendental relationship for the spherically symmetric in-
homogeneous index distribution which perfectly focuses infinite
objects. Using this expression, the index profiles (called
generalized Luneburg lenses) were calculated for lenses having
f-numbers down to f/1. It is shown through a ray-tracing ex-
ample that these profiles have sufficient accuracy to provide
diffraction-limited performance in the optical wavelength
region. An expression is also derived for the lens overlay film
thickness profile on an optical waveguide in terms of these
generalized Luneburg lens index profiles.

INTRODUCTION

In general[1], a Luneburg lens is a variable-index, spherically symmetric refracting structure which will form perfect geometrical images of two given concentric spheres on each other. One of the spheres may be of infinite radius, in which case the lens will perfectly focus a parallel beam of rays. Luneburg[2] derived an integral equation for these symmetric index profiles. He then solved it explicitly for the case of focusing a parallel beam to an image surface coincident with the edge of the lens. We refer to this well-known refractive index distribution, $n = \sqrt{2-r^2}$, where both n and r are normalized to unity at the edge of the lens radius, as the "classical" Luneburg lens. By "generalized" Luneburg lenses, we refer to those having image surfaces located at distances greater than one lens radius from the center of the lens.

Morgan[1] formalized the problem more generally than Luneburg by allowing index discontinuities. His solutions are also expressed in terms of integral equations.

Interest in these generalized Luneburg lenses has arisen in integrated optics for application to Fourier transform signal processing functions[3,4]. Zernike[5] demonstrated a classical Luneburg lens on an optical waveguide. Variations in waveguide overlay thickness result in changes in the effective refractive index for optical propagation in the waveguide. Such thickness changes provide the index gradients required for the thin-film Luneburg lenses. This is, in effect, a means of obtaining the rather large index inhomogeneities needed using a homogeneous optical medium. Generalized Luneburg lenses have been demonstrated as waveguide beam expansion systems and as Fourier transform lenses.[4,5]

232

The problem which we address in this paper is to specify the Luneburg lens index profile and, subsequently, to specify the corresponding over-lay waveguide thickness profile. Figure 1 illustrates the optical wave-guide parameters.

We report in this paper an analytical approximation for Luneburg's integral equation from which the index profile for the generalized Luneburg lens may be extracted to sufficient accuracy to ray-trace optical wavelengths to diffraction-limited performance. This expression was derived as an ex-pansion based on a consideration of known behavior at certain limits. The expression consists of five parameters which depend on the focal length. Two of these parameters may be determined from the "boundary" limits and the others are determined using a least-squares procedure. This analytical expression provides a convenient means for obtaining the index at any r for ray-tracing purposes. It also provides a means of conveniently determining integrated optics Luneburg lens thickness profiles.

Plots and tabulated values for Luneburg lens index and waveguide over-lay thickness profiles are presented. Using a ray-trace procedure described in another paper[6] the example herein demonstrates that the phase errors resulting from these index profiles are less than diffraction limited.

NUMERICAL INTEGRATION OF THE INTEGRAL EQUATION FOR GENERALIZED LUNEBURG LENSES

A spherically symmetric index distribution n(r) which gives a perfect image of an infinite object satisfies[2] the integral equation

$$n = \exp[\omega(\rho,s)], \qquad\qquad (1)$$

where $\rho = rn$ and

233

$$\omega(\rho,s) = \frac{1}{\pi} \int_{\rho}^{1} \frac{\sin^{-1}(x/s)}{(x^2-\rho^2)^{1/2}} \, dx \qquad . \qquad (2)$$

It is assumed that r is normalized with respect to the radius of the lens region such that $0 \leq r \leq 1$. It is also assumed that the lens is immersed in a homogeneous waveguide medium of n_o and that n above is normalized with respect to n_o such that $1 \leq n$. The quantity s is the image distance as measured from the center of the lens, so that $1 \leq s$. The full aperture f-number for these lenses turns out to be s/2 for $2 \leq s$.

For the case s=1, where the image surface is located at the edge of the lens itself, the above integral may be evaluated in closed form. This yields the "classical" Luneburg lens

$$n = \sqrt{2-r^2} \qquad (3)$$

For generalized Luneburg lenses (longer focal lengths), we must deal with the integral in Eq. (2) directly. To do this, we first perform a change of variables,

$$\omega(\rho,s) = \frac{1}{\pi} \int_{0}^{1-\rho} \frac{\sin^{-1}\left(\frac{y+\rho}{s}\right)}{(y+2\rho)^{1/2} y^{1/2}} \, dy \qquad . \qquad (4)$$

We may now remove the $y^{-1/2}$ singularity by performing an integration by parts,

234

$$\omega(\rho,s) = \frac{1}{\pi}\left[\; 2\,\sin^{-1}\left(\frac{1}{s}\right)\frac{(1-\rho)^{1/2}}{(1+\rho)^{1/2}} \;-\int_0^{1-\rho}\left(\left[s^2-(y+\rho)^2\right]^{-1/2}\right.\right.$$

$$\left.\left. - \frac{\sin^{-1}\left(\frac{y+\rho}{s}\right)}{(y+2\rho)}\right)\frac{y^{1/2}dy}{(y+2\rho)^{1/2}}\right] \quad . \tag{5}$$

Although Eq. (5) appears more complicated, it is actually "well-behaved" and may be easily evaluated numerically. Table I is a tabulation of the quantity $\omega(\rho,s)$ for various values of ρ and s. The integration was performed by dividing the interval into four equal regions and using a 32-point Gaussian quadrature[7] on each region. The numbers given are believed accurate to better than one part in the sixth decimal place.

AN ANALYTICAL APPROXIMATION FOR $\omega(\rho,s)$

At this point, we observe that performing an extremely accurate numerical integration to evaluate $\omega(\rho,s)$ is cumbersome. Furthermore, the quantity obtained is not the index as a function of radial position r, but is a function of $\rho=rn$. Thus, the desired index distribution is still imbedded.

It is desirable to derive an analytical expression to represent or approximate the function $\omega(\rho,s)$ to the required accuracy. To gain some insight into the functional form of such an expression, we investigate the limiting behavior of Eq. (5) as $\rho\to1$, which is near the edge of the lens. The integrand in the integral of Eq. (5) approaches zero as $y^{1/2}\to0$, thus the integral portion behaves as $(1-\rho)^{3/2}$. But this is a higher order term compared to the first term on the right side of Eq. (5). Thus, in the limit as $\rho\to1$, $\omega(\rho,s)$ behaves as

235

$$\omega(\rho,s) \underset{\rho \to 1}{=} \frac{\sqrt{2}}{\pi} \sin^{-1}\left(\frac{1}{s}\right)(1-\rho)^{1/2} \qquad . \tag{6}$$

Furthermore, we are led to believe that the next order term will have a $(1-\rho)^{3/2}$ behavior which suggests the form

$$\omega(\rho,s) = p_1(1-\rho)^{1/2} + p_2(1-\rho)^{3/2} + p_3(1-\rho)^{5/2} + p_4(1-\rho)^{7/2} + p_5(1-\rho)^{9/2} \tag{7}$$

We have already established that

$$p_1 = \frac{\sqrt{2}}{\pi} \sin^{-1}\left(\frac{1}{s}\right) \qquad . \tag{8}$$

Another constraint is that the function must reduce to the correct value at $\rho=0$. From Eq. (4), this value is

$$\omega(o,s) = \frac{1}{\pi} \int_0^{1/s} \frac{\sin^{-1}x}{x} \, dx, \tag{9}$$

where we have applied another change of variables. The inverse sine in Eq. (9) may be expanded in a series and the integration performed term by term. This leads to

$$\omega(o,s) = \frac{1}{\pi} \left[s^{-1} + \frac{1}{2\cdot3\cdot3} s^{-3} + \frac{1\cdot3s^{-5}}{2\cdot4\cdot5\cdot5} + \frac{1\cdot3\cdot5s^{-7}}{2\cdot4\cdot6\cdot7\cdot7} + \dots \right] \qquad . \tag{10}$$

The function $\omega(o,s)$ also determines the value of the index at the center of the lens through the relation $n=\exp[\omega(o,s)]$ which is also its maximum value. Table II is a tabulation of $\omega(o,s)$ using Eq. (10) and the maximum index values.

236

We note that the values of $\omega(o,s)$ using Eq. (10) agree with the values obtained by numerical integration of Eq. (5) as listed in the $\rho=o$ row of Table I.

Returning to Eq. (7), we see that $\omega(o,s)$ equals the sum of the coefficients. Thus, we may specify

$$p_5 = \omega(o,s) - p_1 - p_2 - p_3 - p_4 \quad . \tag{11}$$

With Eqs. (8) and (11), only three of the p coefficients are as yet unspecified. To determine these remaining coefficients, we fit the data given in Table I to the function $\omega(\rho,s)$ given by Eq. (7). The problem is a linear least-squares curve-fit and the solution is readily obtained. Notice that more points are included near the $\rho=1$ region in order to more heavily weight the region when the greatest change is occurring. Table III is a tabulation of the results of the curve-fit for the 29 "data" points determined from the numerical integration of Eq. (5). In performing the curve-fit, p_1 was also allowed to vary in order to economize the fit. We note, however, that the best-fit value for p_1 agrees very well with the value predicted by Eq. (8).

GENERALIZED LUNEBURG LENS INDEX PROFILES

Having an analytical expression for $\omega(\rho,s)$, we are now in a position to extract n(r) numerically for any specified value of r. To do this, we define a function F,

$$F(n) = \exp[\omega(\rho,s)] - n. \tag{12}$$

For a given r, we extract the value of n that makes F(n) vanish using Newton's iterative method. A tabulation of results is given in Table IV. Plots of

237

these profiles are shown in Fig. 2.

The ability to provide a numerical value of n for a given r is useful for ray tracing these generalized Luneburg lenses.   In addition to a numerical value of n, the ray-trace algorithms[6] also require values for dn/dr and d^2n/dr^2. Even though the above procedure provides only a numerical value for n(r), we are able to derive analytical expressions for dn/dr and d^2n/dr^2 in terms of r and the numerical value for n. This is done using implicit differentiation of Eq. (12) using Eq. (7) for $\omega(\rho,s)$. The results are

$$\frac{dn}{dr} = \frac{-n^2 G}{2(1-rn)^{1/2}+nrG} \quad , \tag{13}$$

$$\frac{d^2n}{dr^2} = \frac{2n^3\left[G^2(1-rn)^{1/2}+H\right]}{\left[2(1-rn)^{1/2}+nrG\right]} + \frac{2}{n}\left(\frac{dn}{dr}\right)^2 \quad , \tag{14}$$

where

$$G = p_1 + 3p_2(1-rn) + 5p_3(1-rn)^2 + 7p_4(1-rn)^3 + 9p_5(1-rn)^4 \quad , \tag{15}$$

and

$$H = -p_1 + 3p_2(1-rn) + 15p_3(1-rn)^2 + 35p_4(1-rn)^3 + 63p_5(1-rn)^4. \tag{16}$$

WAVEGUIDE LENS THICKNESS PROFILES

The equations[6] governing the relationship between the effective index of refraction n for the TE mode and the lens overlay thickness t (see Fig. 1) on

an integrated optics planar waveguide are,

$$
-\frac{h}{p} = \begin{cases} \dfrac{\left[1 - \frac{\ell}{q}\tan(\ell kd)\right]\tan(hkt) + \frac{h}{\ell}\left[\frac{\ell}{q} + \tan(\ell kd)\right]}{\left[1 - \frac{\ell}{q}\tan(\ell kd)\right] - \frac{h}{\ell}\left[\frac{\ell}{q} + \tan(\ell kd)\right]\tan(hkt)} & n < n_3 \\[3em] \dfrac{\left[(q+\ell)e^{2\ell kd} + q-\ell\right]\tan(hkt) + \frac{h}{\ell}\left[(q+\ell)e^{2\ell kd} - q+\ell\right]}{\left[(q+\ell)e^{2\ell kd} + q-\ell\right] - \frac{h}{\ell}\tan(hkt)\left[(q+\ell e^{2\ell kd} - q+\ell\right]}, & n \geq n_3 \end{cases}
\tag{17}
$$

where $k = 2\pi/\lambda$, d is the waveguide thickness, and

$$
\begin{aligned}
p &= \sqrt{n^2 - n_1^2} \\[0.5em]
h &= \sqrt{n_2^2 - n^2} \\[0.5em]
q &= \sqrt{n^2 - n_4^2} \\[0.5em]
\ell &= \begin{cases} \sqrt{n_3^2 - n^2} & n < n_3 \\[1em] \sqrt{n^2 - n_3^2} & n \geq n_3 \, . \end{cases}
\end{aligned}
\tag{18}
$$

The indices used in Eq. (18) are as follows:

n_1 is the outer index (n_1 = 1, usually air), n_2 is the bulk index of the lens overlay material, n_3 is the bulk index of the waveguide material, and n_4 is the substrate index.

Although Eq. (17) is a transcendental equation when determining n for a given t, it may be solved explicitly for t as a function of n,

$$
t = \begin{cases} \tan^{-1}\left[\dfrac{h\left[1 - \frac{\ell}{q}\tan(\ell kd)\right] + \frac{ph}{\ell}\left[\frac{\ell}{q} - \tan(\ell kd)\right]}{\frac{h^2}{\ell}\left[\frac{\ell}{q} - \tan(\ell kd)\right] - p\left[1 - \frac{\ell}{q}\tan(\ell kd)\right]} \right] & n < n_3 \\[20pt] \tan^{-1}\left[\dfrac{h\left[(q + \ell)e^{2\ell kd} + q - \ell\right] + \frac{ph}{\ell}\left[(q + \ell)e^{2\ell kd} - q + \ell\right]}{\frac{h^2}{\ell}\left[(q + \ell)e^{2\ell kd} - q + \ell\right] - p\left[(q + \ell)e^{2\ell kd} + q - \ell\right]} \right] & n \geq n_3. \end{cases}
\tag{19}
$$

Consequently, with the above numerical determination of $n(r)$, the lens thickness profile is given by Eq. (19). Table V is a tabulation of the overlay thickness for the waveguide parameters shown. The refractive indices in decreasing value are representative of Ta_2O_5, Corning 7059 glass and SiO_2. Figure 3 is a plot of these profiles.

DISCUSSION

From an examination of the sum of the residual errors for the best-fit parameters as shown in Table III, we see that better fits are obtained for the larger values of s. This means that fewer terms in the expansion in Eq. (7) could be used and still provide adequate accuracy for the larger s values.

It also appears that it may be possible to parameterize all the p-coefficients as functions of s. This may be done by either considering higher order terms in the expansion of Eq. (5) or by a curve-fitting process of the best-fit parameters.

We have not pursued the above suggestions for further simplifications. The   parameter formulation and the technique for determining their values have proven to be quite satisfactory.

To test the accuracy of the approximation of Eq. (7), we ray-traced the s=2 case using a recently developed procedure[6] that provides phase errors

240

and image diffraction patterns. Figure 4 is a plot showing six rays traced through the lens. Nineteen rays were traced and the resulting pupil phase error at $\lambda = 0.9\mu$ was determined. The result is shown in Fig. 5. The corresponding intensity diffraction pattern is shown on a logarithmic scale in Fig. 6. We note that the index as derived from Eq. (7) produces diffraction-limited results. The phase errors for the higher values of s are even less.

ACKNOWLEDGMENT

REFERENCES

1. S. P. Morgan, "General Solution of the Luneburg Lens Problem," J.
    Appl. Phys. 29, 1358 (1958).

2. R. K. Luneburg, Mathematical Theory of Optics (University of
    California Press, Berkeley, 1966), p. 187.

3. M. C. Hamilton, D. A. Wille, and W. J. Miceli, "An Integrated
    Optical RF Spectrum Analyzer," IEEE 1976 Ultrasonic Symposium
    Proceedings, Annapolis, MD.

4. D. B. Anderson, R. L. Davis, J. T. Boyd and R. R. August,
    "Comparison of Optical Waveguide Lens Technologies," to be published
    in J. Quantum Electronics, Special Issue Integrated Optics, April 1977.

5. F. Zernike, "Luneburg Lens for Optical Waveguide Use," Optics Commun.,
    Vol. 12, pp 379-381, 1974.

6. W. H. Southwell, "Inhomogeneous optical waveguide lens analysis,"
    J. Opt. Soc. Am.

7. V. J. Krylov, Approximate Calculation of Integrals (Macmillian, New York
    1962) pp 100-111 and 337-340.

TABLE I. THE FUNCTION $\omega(\rho,s)$ USING NUMERICAL INTEGRATION OF EQ. (5)

$\rho = nr$	Focal Length (from center of lens)			
	s=2	s=3	s=5	s=9
0	0.161532974	0.106778890	0.063805003	0.035392104
0.05	0.161342261	0.106648497	0.063725803	0.035347899
0.10	0.160769336	0.106256851	0.063487944	0.035215145
0.15	0.159808733	0.105600483	0.060389404	0.034992731
0.20	0.158451834	0.104673946	0.062527016	0.034678922
0.25	0.156686071	0.103469292	0.061796158	0.034271183
0.30	0.154494419	0.101975755	0.060890568	0.033766077
0.35	0.151854652	0.100179276	0.059802058	0.033159113
0.40	0.148738270	0.098061820	0.058520124	0.032444524
0.45	0.145108972	0.095600405	0.057031366	0.031614952
0.50	0.140920465	0.092765706	0.055318671	0.030660993
0.55	0.136113226	0.089519984	0.053359994	0.029570529
0.60	0.130609596	0.035813951	0.051126507	0.028327704
0.65	0.124306009	0.081581790	0.048579670	0.026911308
0.70	0.117060059	0.076732851	0.045666328	0.025292067
0.75	0.108667412	0.071136813	0.042309951	0.023427811
0.80	0.098816687	0.064594618	0.038393469	0.021253986
0.85	0.086989077	0.056773724	0.033720994	0.018662513
0.90	0.072186077	0.047032184	0.027913781	0.015444290
0.91	0.068702784	0.044746660	0.026553125	0.014690614
0.92	0.064982368	0.042308139	0.025102071	0.013887006
0.93	0.060981056	0.039688340	0.023543894	0.013024222
0.94	0.056638918	0.036848515	0.021855673	0.012089597
0.95	0.051869952	0.033733031	0.020004490	0.011064939
0.96	0.046542594	0.030256728	0.017939945	0.009922388
0.97	0.040436101	0.026276641	0.015577406	0.008615163
0.98	0.033121510	0.021514796	0.012752276	0.007052273
0.99	0.023495253	0.015255661	0.009040778	0.004999423
1.00	0	0	0	0

TABLE II.   THE FUNCTION $\omega(o,s)$ USING EQ. (10) $n_{max} = \exp[\omega(o,s)]$

s	$\omega(o,s)$	$n_{max}(r=0)$
2	0.161532974	1.17531121
3	0.106778890	1.11268820
4	0.0798585731	1.08313387
5	0.0638050027	1.06588453
6	0.0531341389	1.05457109
7	0.0455246840	1.04657684
8	0.0398234213	1.04062701
9	0.0353921041	1.03602586
10	0.0318487205	1.03236132
17	0.0187277137	1.01890418

244

TABLE III. RESULTS OF FITTING EQ. (7) TO THE DATA IN TABLE I.

The values listed for SUM are the sum of the squares of the errors for the 29 points. p_5 was determined by Eq. (11).

	s=2	s=3	s=5	s=9
SUM	3.9101×10^{-11}	5.8134×10^{-12}	1.7893×10^{-12}	5.3512×10^{-13}
p_1	0.235687835	0.152976535	$.0906399959$	$.0501194645$
p_2	$-7.47500358 \times 10^{-2}$	$-4.22494061 \times 10^{-2}$	$-2.34300068 \times 10^{-2}$	$-1.26356394 \times 10^{-2}$
p_3	$6.72894476 \times 10^{-3}$	$-1.93175172 \times 10^{-3}$	$-2.51100017 \times 10^{-3}$	$-1.63934418 \times 10^{-3}$
p_4	$-5.14447054 \times 10^{-3}$	$-8.25244897 \times 10^{-4}$	$-1.49192458 \times 10^{-4}$	$-4.07947091 \times 10^{-5}$
p_5	$-9.89299661 \times 10^{-4}$	$-1.19124255 \times 10^{-3}$	$-7.44793717 \times 10^{-4}$	$-4.11582122 \times 10^{-4}$

TABLE IV. NORMALIZED REFRACTIVE INDEX PROFILES FOR GENERALIZED LUNEBURG LENSES

r	s=2	s=3	s=5	s=9
0	1.175311212	1.112688200	1.065884534	1.036025859
0.05	1.174999407	1.112507930	1.065788087	1.035976411
0.10	1.174071705	1.111969546	1.065500332	1.035828873
0.15	1.172521576	1.111069129	1.065018948	1.035581965
0.20	1.170340993	1.109801290	1.064340603	1.035233817
0.25	1.167519780	1.108158811	1.063460759	1.034781859
0.30	1.164044879	1.106132212	1.062373426	1.034222692
0.35	1.159899514	1.103709214	1.061070836	1.033551908
0.40	1.155062156	1.100874045	1.059543028	1.032763858
0.45	1.149505212	1.097606509	1.057777265	1.031851324
0.50	1.143193243	1.093880684	1.055757219	1.030805062
0.55	1.136080437	1.089663045	1.053461790	1.029613132
0.60	1.128106836	1.084909633	1.050863316	1.028259883
0.65	1.119192434	1.079561599	1.047924746	1.026724355
0.70	1.109227400	1.073537799	1.044594938	1.024977603
0.75	1.098054844	1.066721643	1.040800259	1.022977928
0.80	1.085437716	1.058935566	1.036428193	1.020661529
0.85	1.070987513	1.049884988	1.031290974	1.017921692
0.90	1.053981685	1.039009952	1.025027636	1.014552365
0.91	1.050159236	1.036524794	1.023580201	1.013768729
0.92	1.046155078	1.033902395	1.022045349	1.012935510
0.93	1.041942017	1.031119755	1.020407545	1.012043672
0.94	1.037484456	1.028146025	1.018645667	1.011080865
0.95	1.032734249	1.024938133	1.016729693	1.010029408
0.96	1.027623448	1.021432662	1.014614324	1.008862349
0.97	1.022050589	1.017529080	1.012225136	1.007534739
0.98	1.015851602	1.013049431	1.009422596	1.005960167
0.99	1.008726930	1.007614146	1.005874179	1.003921693
1.00	1	1	1	1

TABLE V.   OVERLAY THICKNESS IN MICRONS FOR OPTICAL WAVEGUIDE LUNEBURG LENSES

The waveguide parameters are n_1=1, n_2=2.1, n_3=1.565, n_4=1.47, d=1.0665μ, and λ=0.9μ

| r (cm)	s=2	s=3	s=5	s=9
0	0.2191	0.1591	0.1223	0.0979
0.05	0.2187	0.1590	0.1222	0.0979
0.10	0.2177	0.1585	0.1220	0.0978
0.15	0.2160	0.1578	0.1216	0.0975
0.20	0.2135	0.1567	0.1211	0.0972
0.25	0.2105	0.1554	0.1204	0.0968
0.30	0.2068	0.1537	0.1196	0.0963
0.35	0.2024	0.1518	0.1186	0.0957
0.40	0.1975	0.1495	0.1174	0.0949
0.45	0.1920	0.1469	0.1160	0.0940
0.50	0.1860	0.1440	0.1141	0.0930
0.55	0.1794	0.1406	0.1126	0.0918
0.60	0.1722	0.1370	0.1105	0.0905
0.65	0.1646	0.1328	0.1081	0.0888
0.70	0.1563	0.1282	0.1054	0.0869
0.75	0.1472	0.1229	0.1022	0.0846
0.80	0.1374	0.1169	0.0983	0.0817
0.85	0.1262	0.1097	0.0935	0.0780
0.90	0.1130	0.1006	0.0870	0.0727
0.91	0.1099	0.0984	0.0853	0.0713
0.92	0.1067	0.0960	0.0835	0.0697
0.93	0.1031	0.0933	0.0814	0.0679
0.94	0.0993	0.0903	0.0790	0.0657
0.95	0.0949	0.0869	0.0762	0.0632
0.96	0.0898	0.0827	0.0728	0.0601
0.97	0.0835	0.0774	0.0682	0.0559
0.98	0.0749	0.0699	0.0616	0.0499
0.99	0.0597	0.0562	0.0496	0.0395
1.00	0	0	0	0
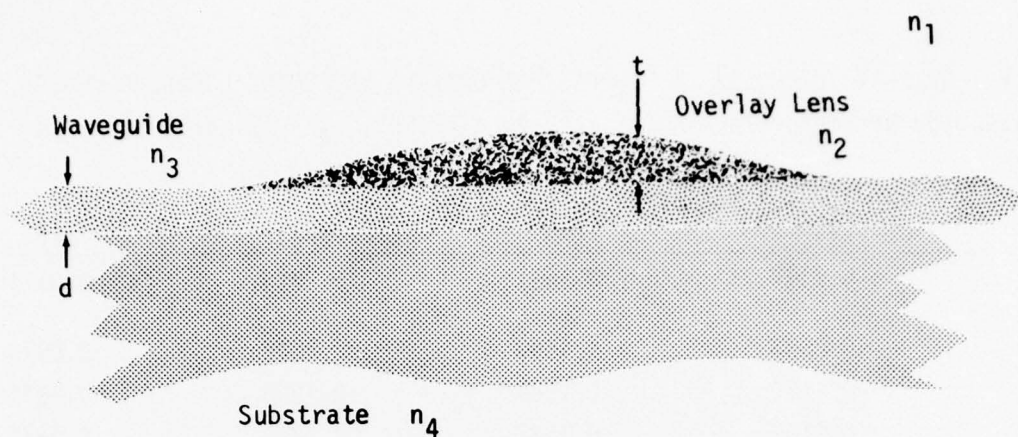
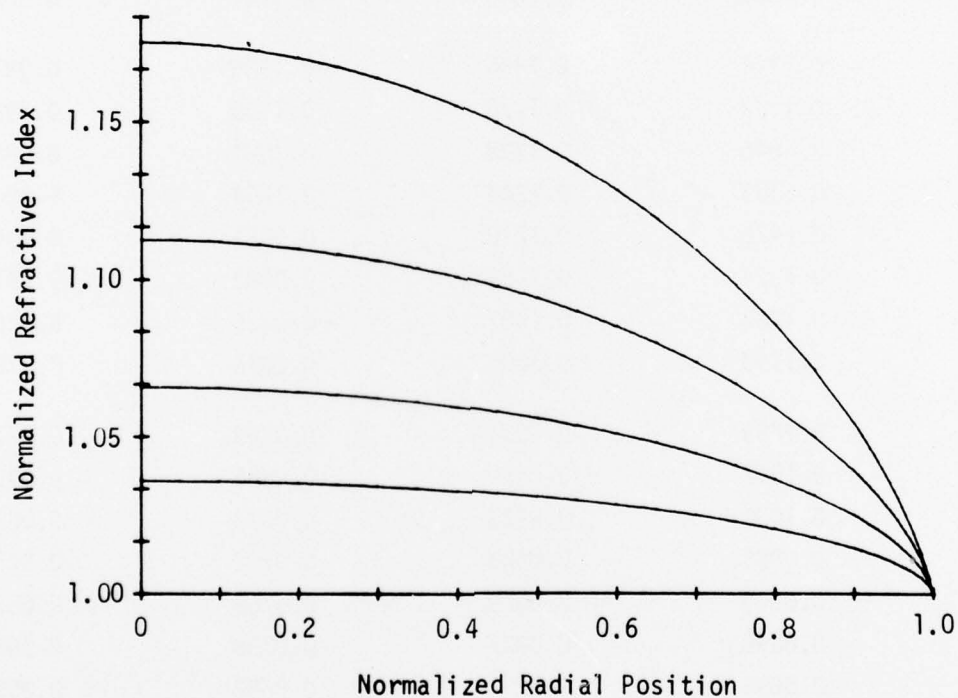Figure 1F.   Cross-Section of Multilayer Planar Dielectric Waveguide.

Figure 2F.   Index Profiles for Generalized Luneburg Lenses. From top to bottom, the lenses have full aperture f-numbers of f/1, f/1.5, f/2.5, and f/4.5.
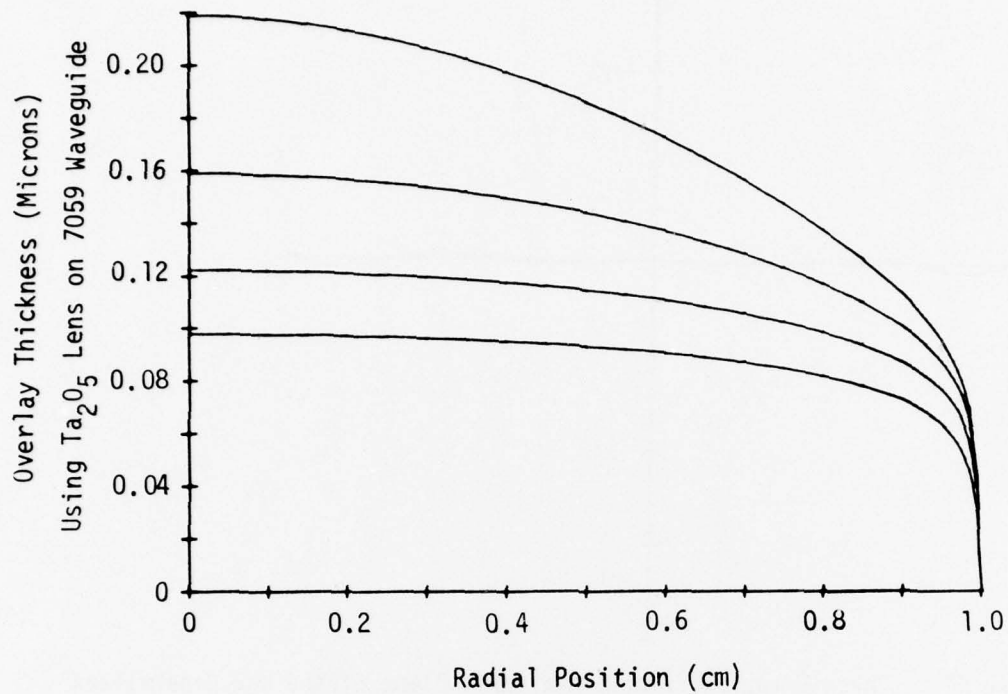
Figure 3F.   Waveguide Overlay Thickness Profiles for the Generalized
             Luneburg Lens Profiles Shown in Fig. 2F for the Waveguide
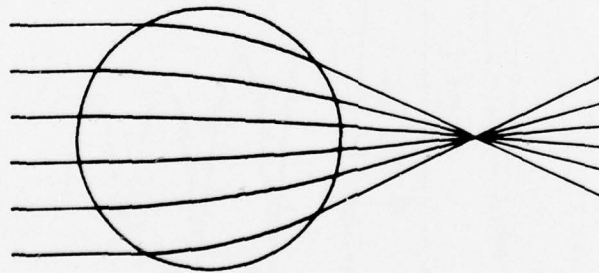   Parameters Listed in Table V.

Figure 4F.   Ray Trace of the s=2 Generalized Luneburg Lens Using the
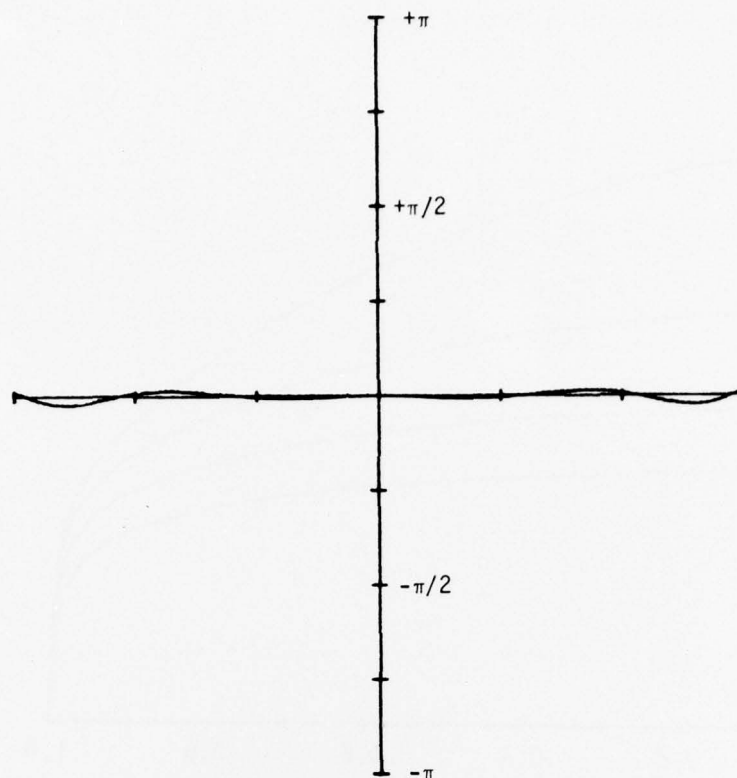   Index Profile Derived from Eq. (7).

Figure 5F.   Phase Error Profile in the Pupil Plane of the s=2 Generalized
Luneburg Lens Using the Approximation Eq. (7) to Derive the
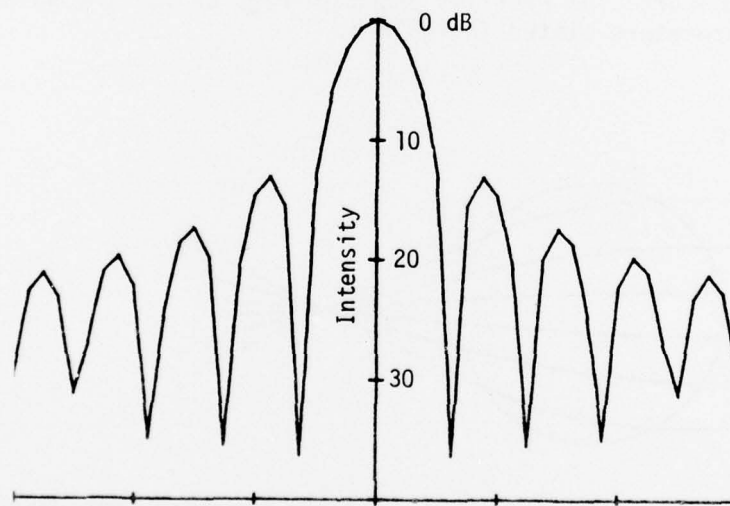Index Profile.

Figure 6F.   Intensity Diffraction Pattern Using Logarithmic Scale in
the Image Surface for the Luneburg Lens of Figs. 4F and 5F.
(Note that this coincides with a diffraction-limited distri-
bution).

IV. REFERENCES

1. M. C. Hamilton and D. A. Wille, "Acousto-Optic Diffraction in Optical Waveguides," Digest of Technical Papers, Topical Meeting on Integrated Optics, New Orleans, Louisiana, January 21-24, 1974.

2. M. C. Hamilton, D. A. Wille, and W. J. Miceli, "An Integrated Optical RF Spectrum Analyzer," IEEE 1976 Ultrasonic Symposium Proceedings, Annapolis, Maryland.

3. L. J. Cutrona, E. N. Leith, C. J. Palermo and J. J. Porcello, "Optical Data Processing and Filtering," IRE IT-6, 386 (1960).

4. J. T. Tippett, D. A. Berkowitz, L. C. Clapp, C. J. Koester and A. Vanderburgh, Editors, Optical and Electro-Optical Information Processing, MIT Press 1965.

5. K. Preston, Jr., Coherent Optical Computers, McGraw-Hill 1972.

6. D. B. Anderson, et al, "Thin Film Light Sources for Integrated Optics," Final Technical Report, AFAL Contract F33615-73-C-1041, Rockwell International Report C73-292.23/501, November 1974.

7. D. B. Anderson, R. R. August and J. E. Coker, "Distributed-Feedback Double-Heterostructure GaAs Injection Laser with Fundamental Grating," Appl. Opt. 13, 2742 (1974).

8. R. G. Hunsperger, "Optimized Thin Film Light Sources," Final Report on Contract F33615-75-C-1024, August 1976.

9. D. A. Wille and M. C. Hamilton, "Acousto-Optic Deflection in Ta_2O_5 Waveguides," Appl. Phys. Lett. 24, 159 (1974).

10. E. G. H. Lean, J. M. White, and C. D. W. Wilkinson, "Thin-Film Acousto-Optic Devices," Proc. IEEE, Vol. 64, 779 (1976).

11. Y. Omachi, "Acousto-Optical Light Diffraction in Thin Films," J. Appl. Phys. 44, 3928 (1973).

12. C. S. Tsai, M. A. Alkaider, L. T. Nguyen, and B. Kim, "Wideband Guided-Wave Acousto-Optic Bragg Diffraction and Devices Using Multiple Tilted Surface Acoustic Waves," Proc. IEEE 64, 318 (1976).

251

13. T. G. Giallorenzi and A. F. Milton, "Light Deflection in Multimode Waveguides Using the Acousto-optic Interaction," J. Appl. Phys., Vol. 45, pp 1762-1774, 1974.

14. W. S. C. Chang, "Acoustooptical Deflection in Thin Films," IEEE J. Quant. Electron., Vol. QE-7, pp 167-170, 1971.

15. J. T. Boyd and C. L. Chen, "Integrated Optical Silicon Photodiode Array," Appl. Opt., Vol. 15, pp 1389-1393, 1976.

16. D. B. Anderson, R. L. Davis, J. T. Boyd, R. R. August, and R. E. Eisile, "Optical Waveguide Lenses I," Final Report on Contract F33615-75-C-1017, AFAL-TR-76-54, Mar. 1976.

17. F. S. Hickernell "Zinc-Oxide Thin-Film Surface-Wave Transducers," Proc. IEEE Vol. 64, pp 631-635, 1976.

18. F. S. Hickernell, "The Acoustic Properties of Oxide Films and Their Application to Acoustic Surface Wave Devices," J. Sol. St. Chem. Vol. 12, pp 225-231, 1975.

19. F. S. Hickernell, "DC Triode Sputtered Zinc Oxide Surface Elastic Wave Transducers," J. Appl. Phys. Vol. 44, pp 1061-1071, 1973.

20. N. Chubachi, J. Kushibiki, and Y. Kikuchi, "Monolithically Integrated Bragg Deflector for an Optical Guided Wave Made of Zinc-Oxide Film," Elec. Lett. Vol. 9, pp 193-194, 1973.

21. K. W. Loh, W. S. C. Chang, W. R. Smith, and T. Grudkowski, "Bragg Coupling Efficiency for Guided Acoustooptic Interaction in GaAs," Appl. Opt. Vol. 15, pp 156-166, 1976.

22. G. S. Kino and R. S. Wagers, "Theory of Interdigital Couplers on Nonpiezoelectric Substrates," J. Appl. Phys. Vol. 44, pp 1480-1488, 1973.

23. J. W. Goodman, Introduction to Fourier Optics, McGraw-Hill 1968.

24. L. D. Dickson, "Characteristics of a Propagating Gaussian Beam," Appl. Phys., Vol. 9, pp 1854, 1970.

25. E. G. H. Lean, "Interaction of Light and Acoustic Surface Waves," in _Progress in Optics_, E. Wolf, Ed., Vol. 11, pp 123-166, North Holland, 1973.

26. N. Uchida and N. Niizeki, "Acousto-optic Deflection Materials and Techniques," Proc. IEEE, Vol. 61, pp 1073-1092, 1973.

27. B. Kim and C. S. Tsai, "High-Performance Guided-Wave Acousto-optic Scanning Devices Using Multiple Surface Acoustic Waves," Proc. IEEE, Vol. 64, pp 788-793, 1976.

28. R. V. Schmidt, "Acoustooptic Interactions Between Guided Optical Waves and Acoustic Surface Wave," IEEE Trans. Son. and Ultrason., Vol. SU-23, pp 22-32, 1976.

29. E. I. Gordon, "A Review of Acoustooptical Deflection and Modulation Devices," Proc. IEEE, Vol. 54, pp 1391-1401, 1966.

30. C. L. Chen, "Thin Film Optical Waveguide and Integrated Photodetector," MS Thesis, Department of EE, Univ. of Cincinnati, 1975.

31. D. H. Hensler, J. D. Cuthbert, R. J. Martin, and P. K. Tien, "Optical Propagation in Sheet and Pattern Generated Films of Ta_2O_5," Appl. Opt., Vol. 10, pp 1037-1042, 1971.

32. P. K. Tien, R. J. Martin, and G. Smolinsky, "Formation of Light-Guiding Interconnections in an Integrated Optical Circuit by Composite Tapered-Film Coupling," Appl. Opt., Vol. 12, pp 1909-1916, 1973.

33. P. K. Tien, G. Smolinsky, and R. J. Martin, "Radiation Fields of a Tapered Film and a Novel Film-to-Fiber Coupler," IEEE Trans. Vol. MIT-23, pp 79-85, 1975.

34. T. Tamir Ed., _Integrated Optics_, Springer-Verlag (1975)(Chapter 2).

35. F. Zernike, "Luneburg Lens for Optical Waveguide Use," Optics Commun., Vol. 12, pp 379-381, 1974.

36. M. Born and E. Wolfe, _Principles of Optics_, Pergamon Press, New York (1964).

37. R. K. Luneburg, _The Mathematical Theory of Optics_, University of California Press, Berkeley, California (1954).

253

38. S. P. Morgan, "General Solution of the Luneburg Lens Problem," J. Appl. Phys., Vol. 29, pp 1358-1369, 1958.

39. O. N. Stavroudis, The Optics of Rays, Wavefronts and Caustics, Academic Press, New York (1972) p 118.

40. H. Jasik, "Fundamentals of Antennas," Antenna Engineering Handbook, McGraw Hill, Chapter 2, 2-1 (1961).

41. W. T. Welford, Aberrations of the Symmetrical Optical System, Academic Press, Chapter 11, (1974).

42. E. H. Linfoot, Sc.D., Fourier Methods in Optical Image Evaluation, The Focal Press (1964).

43. W. F. Kosonocky and J. E. Carnes, "Two Phase Charge-Coupled Devices with Overlapping Polysilicon and Aluminum Gates," RCA Rev. Vol. 34, pp 164-202, 1973.